

Investigating Stimulated Wave-Particle Interaction of Radiation Belt Particles With Space-Borne Whistler Mode Transmitters

**P. Song
B. W. Reinisch
X. Huang
G. S. Sales
J. Tu
V. V. Paznukhov**

**University of Massachusetts Lowell
Center for Atmospheric Research
600 Suffolk Street
Lowell, MA 01854**

Final Report

30 March 2009

Approved for public release; distribution unlimited.



**AIR FORCE RESEARCH LABORATORY
Space Vehicles Directorate
29 Randolph Road
AIR FORCE MATERIEL COMMAND
HANSCOM AFB, MA 01731-3010**

AFRL-RV-HA-TR-2009-1121

Using Government drawings, specifications, or other data included in this document for any purpose other than Government procurement does not in any way obligate the U.S. Government. The fact that the Government formulated or supplied the drawings, specifications, or other data, does not license the holder or any other person or corporation; or convey any rights or permission to manufacture, use, or sell any patented invention that may relate to them.

This report is published in the interest of scientific and technical information exchange and its publication does not constitute the Government's approval or disapproval of its ideas or findings.

This technical report has been reviewed and is approved for publication.

/ signed /

Daniel Elsner, 1Lt, USAF
Contract Manager

/ signed /

Dwight T. Decker, Chief
Space Weather Center of Excellence

This report has been reviewed by the ESC Public Affairs Office (PA) and is releasable to the National Technical Information Service (NTIS).

Qualified requestors may obtain additional copies from the Defense Technical Information Center (DTIC). All other requestors should apply to the National Technical Information Service (NTIS).

If your address has changed, if you wish to be removed from the mailing list, or if the addressee is no longer employed by your organization, please notify AFRL/RVIM, 29 Randolph Road, Hanscom AFB, MA 01731-3010. This will assist us in maintaining a current mailing list.

Do not return copies of this report unless contractual obligations or notices on a specific document require that it be returned.

REPORT DOCUMENTATION PAGE				Form Approved OMB No. 0704-01-0188	
The public reporting burden for this collection of information is estimated to average 1 hour per response, including the time for reviewing instructions, searching existing data sources, gathering and maintaining the data needed, and completing and reviewing the collection of information. Send comments regarding this burden estimate or any other aspect of this collection of information, including suggestions for reducing the burden to Department of Defense, Washington Headquarters Services Directorate for Information Operations and Reports (0704-0188), 1215 Jefferson Davis Highway, Suite 1204, Arlington VA 22202-4302. Respondents should be aware that notwithstanding any other provision of law, no person shall be subject to any penalty for failing to comply with a collection of information if it does not display a currently valid OMB control number.					
PLEASE DO NOT RETURN YOUR FORM TO THE ABOVE ADDRESS.					
1. REPORT DATE (DD-MM-YYYY) 25-03-200		2. REPORT TYPE Scientific, Final		3. DATES COVERED (From - To) 26 Jun 05 – 30 Jun 09	
4. TITLE AND SUBTITLE Investigating Stimulated Wave-Particle Interaction of Radiation Belt Particles with Space-Borne Whistler Mode Transmitters				5a. CONTRACT NUMBER F19628-05-C-0070	
				5b. GRANT NUMBER 	
				5c. PROGRAM ELEMENT NUMBER 63278E	
6. AUTHORS P. Song, B. Reinisch, X. Huang, G.S. Sales, J. Tu, and V. V. Paznukhov				5d. PROJECT NUMBER DARP	
				5e. TASK NUMBER RR	
				5f. WORK UNIT NUMBER 57	
7. PERFORMING ORGANIZATION NAME(S) AND ADDRESS(ES) Center for Atmospheric Research, University of Massachusetts 600 Suffolk Street Lowell, MA				8. PERFORMING ORGANIZATION REPORT NUMBER UMLRF-003	
9. SPONSORING/MONITORING AGENCY NAME(S) AND ADDRESS(ES) Air Force Research Laboratory /RVBXR 29 Randolph Road Hanscom AFB, MA 01731-3010				10. SPONSOR/MONITOR'S ACRONYM(S) AFRL/RVBXR	
				11. SPONSOR/MONITOR'S REPORT NUMBER(S) AFRL-RV-HA-TR-2009-1121	
12. DISTRIBUTION/AVAILABILITY STATEMENT Approved for public release; distribution unlimited					
13. SUPPLEMENTARY NOTES 					
14. ABSTRACT <p>We study the feasibility of transmitting whistler mode waves in space for stimulating wave-particle interaction in the radiation belts. We investigated both theoretically and experimentally the antenna-plasma interaction, the whistler waves radiated from a space-borne transmitter, and the VLF waves radiated from ground-based transmitters. We have developed a one-dimensional model of the high-voltage-antenna-sheath-plasma both analytically and numerically, and compared the results with the space transmission experiments made by the Radio Plasma Imager on the IMAGE satellite. We have developed a general theory for whistler wave radiation in space. Our results have shown that previous antenna sheath theories need significant modifications and the previous whistler wave radiation theory contains substantial mathematical errors and flaws. The model developed a few decades ago to describe the whistler waves penetrating through the ionosphere and propagating in the magnetosphere also needs significant improvements. This project has laid solid foundation for further investigations and modeling of space-borne whistler transmissions.</p>					
15. SUBJECT TERMS . Whistler wave transmission, Antenna-plasma interaction, Space whistler transmission, High-voltage antenna in space, VLF wave, Plasma sheath, Radio Plasma Imager, Active experiment, Whistler radiation resistance					
16. SECURITY CLASSIFICATION OF:			17. LIMITATION OF ABSTRACT UNL	18. NUMBER OF PAGES	19a. NAME OF RESPONSIBLE PERSON Daniel J. Elsner, 1Lt, USAF
a. REPORT UNCL	b. ABSTRACT UNCL	c. THIS PAGE UNCL			19b. TELEPHONE NUMBER (Include area code)

CONTENTS

1. INTRODUCTION	1
2 PROGRESS	2
2.1. High Voltage Antenna-plasma Interaction in Whistler Wave Transmission: Plasma Sheath Effects	2
2.2 Plasma sheath structures around a radio frequency antenna.....	3
2.3 Kinematics of Ions in the Sheath Surrounding a High Power Transmitting Antenna in the Plasmasphere.....	4
2.3.1 Introduction.....	4
2.3.2 Results.....	5
2.3.2 Summary	15
2.4 Radiation Theory in Magnetized Plasma.....	16
2.5 Impedance Characteristics of an Active Antenna Transmitting in the Whistler Mode	16
2.6 VLF Station Monitoring in Space with the RPI Instrument	17
2.6.1 Introduction.....	17
2.6.2 VLF signal detection with the RPI.....	17
2.6.3 Results and Discussion	23
2.6.4 Summary and conclusion.....	27
3 CONCLUSIONS.....	28
4 FUTURE STUDIES.....	28
REFERENCES	31
APPENDIX A.....	33
APPENDIX B	47
APPENDIX C	61
APPENDIX D.....	139

FIGURES

- Figure 1. a) The two components of charge on Element 1 of the dipole antenna 4
The blue horizontal line at 1×10^{-7} (C) represents the space charge accumulated on the antenna. The black curve is the sinusoidal time variation of the antenna current driven charge. The red curve is the sum of the space charge and the driven charge and is always negative, b) The time variation of the total charge on the two elements of the dipole antenna illustrating the phase relationship.
- Figure 2. Illustrated cross-section of the ion-sheath 5
- Figure 3. Electric field strength as a function of distance from the antenna 8
The maximum radius of the ion-sheath under the assumed conditions was 2.82m. It was assumed that neutral plasma exists outside the sheath.
- Figure 4. The time dependent position of the ions starting at different radii. The red curve 8
defines the radius of the sheath during the RF-period of 29.4 ns. Each curve represents ions beginning at 10 cm in steps of 10 cm. Ions do not begin to move until the sheath reaches a radius equal to the initial position of the ion.
- Figure 5. The time variation of the antenna charge during one RF-cycle. The black curve is 9
the combined current driven charge and the space charge the keeps the antenna negative over the complete period. The red curve is the positive charge deposited on the antenna from the hydrogen ion current attracted to the negatively charged antenna. The green curve is the sum of the two charges resulting in a positive phase towards the end of the RF-cycle.
- Figure 6. Terminal velocity of sheath ions reaching the antenna within one RF-cycle as a 11
function of starting position of the ions. All velocities are negative (directed inward towards the antenna). The second iteration show a reduced terminal velocity and a smaller starting position at the outer boundary of the sheath.
- Figure 7. Arrival time of Hydrogen ions at antenna relative to the start of the RF-cycle 12
- Figure 8. Hydrogen-ion current reaching the antenna as a function of time during an RF- 12
period for four driven antenna currents.
- Figure 9. Peak ion current into the antenna element as a function of the driven antenna 13
current.
- Figure 10. Ion current into antenna element as a function of time for one RF-period. 13
The black (square points) curve is for a plasma density $n_0 = 1.5 \times 10^9 \text{ m}^{-3}$ and the red curve (dots) for $n_0 = 1.5 \times 10^8 \text{ m}^{-3}$.
- Figure 11. Magnitude of the electric field strength during the positive phase. The field 14
strengths at four times during this phase are presented.

Figure 12. Arrival time of electrons during the positive phase of charge on the antenna. 15
The distances correspond to the arrival times of all the 10 cm shells out to 1.4 m.

Figure 13. Top panel: an example RPI dynamic spectrogram showing signal from the NLK..... 19
station. The characteristic upper hybrid (fuh) and gyro frequency (fce) resonance lines are also
shown. Signal from the NLK station is indicated. This record was made on 21 April 2001.
Bottom panel: corresponding IMAGE satellite projection traced along the magnetic field line as
a function of time.

Figure 14. NLM station observations made during years 2001 and 2002. Each circle in the 20
plot corresponds to a single measurement, with the location of the circle corresponding to the
satellite magnetic footprint (traced northward) while the size and color of the circle are
modulated by the observed signal amplitude.

Figure 15. Magnetic footprints (circles) of IMAGE satellite and wave amplitudes 21
(color-coding) received by RPI at the frequency channel corresponding to the DHO station
operating frequency.

Figure 16. An example of the RPI measurements in the dynamic spectrogram mode with 22
new settings.

Figure 17. Observations of the NML station made in 2003. The position of each circle 23
corresponds to the location of the magnetic footprint of the IMAGE satellite shown in
geographic coordinates. The black star indicates the location of NML.

Figure 18. Observations of the NML station made from northern geomagnetic hemisphere 24
(left panel) and southern hemisphere (right panel). Satellite footprints are shown in geomagnetic
coordinates.

Figure 19. Signal amplitude as a function of the IMAGE Satellite Position. Circles represent.. 25
individual measurements.

Figure 20. Signal decays for daytime and nighttime conditions. Signal amplitude is shown as . 26
a function of the distance between the satellite footprint and the location of the DHO station.

TABLES

Table 1. Locations and main parameters of the most powerful VLF stations observed by the... 18
RPI

1. INTRODUCTION

The effort under this contract is to enhance our understanding of the physical processes involved in transmitting whistler mode waves into the radiation belt. The enhanced wave-particle interaction stimulated by these waves may artificially reduce the lifetime of the sturdily trapped relativistic electrons in the radiation belt. The target electrons are in the energy range of 0.5~3.0 MeV in the region between $L = 1.7\sim 2.2$, where L is the equatorial distance of a field line in R_E , and the objective is to reduce the lifetime to about 1/50 of the natural diffusion time. Although many schemes have been proposed to artificially reduce the lifetimes of the radiation particles, our approach focuses on using space-transmitted whistler waves to pitch-angle diffuse the electrons into the loss-cone, i.e., to precipitate the relativistic electrons into the neutral atmosphere. There are several reasons for this choice. First, the wave-particle interaction theory has been developed and tested in many previous studies. Pitch-angle diffusion of the particles does occur as reported. Second, technologies of whistler mode waves transmission have recently been developed both on-ground and in space [Reinisch *et al.*, 2000; Sonwalker *et al.*, 2004]. However, the applications of these technologies and theories to transmitting sufficient power, large enough to produce significantly enhanced pitch-angle diffusion, remain challenging because several physical processes become important when the power and voltage of the transmitter are high. These processes are not currently well understood. The major issue is how to most efficiently radiate enough power in the whistler mode frequency range into the region in space where the wave-particle interaction can occur.

We address a number of scientific/technological problems in order to reach the goal of transmitting large whistler mode power into the radiation belt.

1. Understand and model the physical processes occurring in a region called plasma sheath, a region of net electric charges near the antenna, between a high-voltage antenna and space plasma in whistler mode transmission. These processes appear to be critical and limit high-power transmission in space.
2. Understand and model the radiation process. The previously developed radiation theory in anisotropic media, one of which is the whistler mode transmission in magnetized plasma, has been found to contain mathematical errors. A new theoretical model is necessary to describe the radiation power and pattern as well as radiation characteristics as functions of plasma conditions.
3. Validate the theoretical models discussed above using whatever observations and experiments available. The radio plasma imager (RPI) on the IMAGE satellite will be used as a primary test bed.
4. Conduct feasibility analyses for two possible orbits of space-borne transmitters: a low-inclination and mid-altitude orbit [e.g., Inan *et al.*, 2003], and a low-altitude and high-inclination orbit. The latter is proposed by UMass Lowell and referred to as the Low-earth Orbit Relativistic Electron Remediation System (LORERS). Because of the reduction in the funding of the program, the LORERS portion of the investigation is not carried out.

5. Integrate the knowledge gained in the above items into designs of a space-borne transmission system.

In addition to the above central scheme, we also study how VLF waves transmitted from ground-based stations are coupled into the magnetosphere through the ionosphere using space observations. These observations will be compared with raytracing models. These analyses will determine the controlling factors of the coupling between the ionosphere and magnetosphere, and the propagation characteristics of whistler waves in space, verify the raytracing models, and provide guidance for raytracing model improvements when necessary. Correctly modeling whistler wave propagation in the magnetosphere as functions of plasma conditions and wave frequency is crucial to determining the orbital characteristics of a space-borne system. This study will include an evaluation of the efficiency and feasibility for ground-based systems.

2 PROGRESS

We carried out investigations listed in items 1, 2, 3, and 5 above and the additional item. Because of the partial funding support of the program, item 4 has not been carried out. We published two papers in *J. Geophys. Res.* on items 1 and 3. We submitted a paper to *J. Geophys. Res.* for publication in which we integrated the knowledge we learned through the project and compare it with the experimental results, items 3 and 5. We developed a comprehensive theory on the radiation in magnetized plasmas, with whistler mode transmission as one of the examples. This work is now completed and will be written into 2 papers for publication. We conducted analyses of the signals observed in space from ground VLF transmitters and contributed a paper published in *J. Geophys. Res.*

In this report, we include the abstracts of the publications in the main body and the full articles in the Appendices.

2.1. High Voltage Antenna-plasma Interaction in Whistler Wave Transmission: Plasma Sheath Effects

This is an analytical study of the sheath problem, item 1 in the introduction. The theory is compared with the experiment, item 3. This paper is published in *J. Geophys. Res.* and the full article is attached in Appendix A. Below is the abstract.

We study the plasma sheath surrounding an antenna that transmits whistler mode waves in the inner magnetosphere in order to investigate the feasibility of conducting controlled experiments on the role of wave-particle interactions in the pitch angle diffusion of relativistic radiation belt electrons. We propose a model for such an antenna-sheath-plasma system for an antenna much shorter than the wavelength, i.e., an electrically short antenna, assuming that the transmission frequency, for the whistler mode, is below the electron characteristic frequencies and much higher than the ion characteristic frequencies so that the ion current can be neglected. In our model, the sheath is free of electrons and conduction current. The antenna is charged to a large negative potential during a steady transmission. Positive charge occurs in the sheath. The net charge on the antenna and in the sheath is zero. The volume, or the radius in a cylindrical

case, of the sheath varies in response to the charge variation on the antenna. The oscillating radius of the sheath translates to a current in the plasma. We analytically solve a time-dependent 1-dimensional situation by neglecting the effects of the magnetic field. The sheath is similar to a co-axial cable with an electrically leaky and time-varying radius outer shell. At the sheath-plasma boundary, the electric field is near zero, but the voltage is not. The current associated with the motion of the sheath boundary is the current that radiates waves into the plasma. This radiation current is more normal and less tangential to the boundary surface at the boundary. The sheath radius varies 90° out of phase with the driving current around an equilibrium radius, which is determined by the DC charge on the antenna. A whistler wave transmission experiment conducted by the RPI-IMAGE has shown that the model may describe the most important physical processes occurring in the system. It shows no evidence for significant sheath current or sheath resistance. From the experiment, the antenna is most likely to be charged to a substantial negative potential as described by the model. Quantitatively, the model may underestimate the sheath capacitance by about 20%.

2.2 Plasma sheath structures around a radio frequency antenna

This is a numerical simulation of the sheath problem, item 1. In addition to validating the code and the analytical theory described in section 2.1, the ion effects that are neglected in the analytical theory are included. This paper is published in J. Geophys. Res. and the full article is attached in Appendix B. Below is the abstract.

A one-dimensional particle-in-cell (PIC) simulation code is developed to investigate plasma sheath structures around a high-voltage transmitting antenna in the inner magnetosphere. We consider an electrically short dipole antenna assumed to be bare and perfectly conducting. The oscillation frequency of the antenna current is chosen to be well below the electron plasma frequency but higher than the ion plasma frequency. The magnetic field effects are neglected in the present simulations. Simulations are conducted for the cases without and with ion dynamics. In both cases, there is an initial period, about one-fourth of an oscillation cycle, of antenna charging because of attraction of electrons to the antenna and the formation of an ion plasma sheath around the antenna. With the ion dynamics neglected, the antenna is charged completely negatively so that no more electrons in the plasma can reach the antenna after the formation of the sheath.

When the ion dynamics are included, the electrons impulsively impinge upon the antenna while the ions reach the antenna in a continuous manner. In such a case, the antenna charge density and electric field have a brief excursion of slightly positive values during which there is an electron sheath. The electron and ion currents collected by the antenna are weak and balance each other over each oscillation cycle. The sheath-plasma boundary is a transition layer with fine structures in electron density, charge density, and electric field distributions. The sheath radius oscillates at the antenna current frequency. The calculated antenna reactance is improved from the theoretical value by 10%, demonstrating the advantage of including the plasma sheath effects self-consistently using the PIC simulations. The sheath tends to shield the electric field from penetrating into the plasma. There is, however, leakage of an electric field component with significant amplitude into the plasma, implying the applicability of the high-voltage antennas in whistler wave transmission in the inner magnetosphere.

2.3 Kinematics of Ions in the Sheath Surrounding a High Power Transmitting Antenna in the Plasmasphere

This analysis is also aimed at the antenna-sheath interaction, item 1, but more from an engineering point of view. It combines the knowledge we learned in theory with the circuit simulation model, an important tool to understand the responses of the transmitter to the sheath effects and predict the characteristics of the system under various conditions.

2.3.1 Introduction

A space-charged (negative) high-voltage transmitting antenna system forms a positive ion-sheath that surrounds both elements of a dipole antenna (*Shkarofsky*, (1972); *Song et al.*, 2007, *Tu et al.*, 2008). During each period of the transmitted frequency, the radius of the cylindrical sheath grows and decays as the current in the antenna oscillates and the total charge on each element varies from zero (when the driven antenna current is combined with the space charge) to a negative maximum. Figure 1 illustrates first the variation of the charge on one element of the dipole antenna. The total charge on each element is always negative and the two elements are 180° out of phase with respect to each other as illustrated in the second panel.

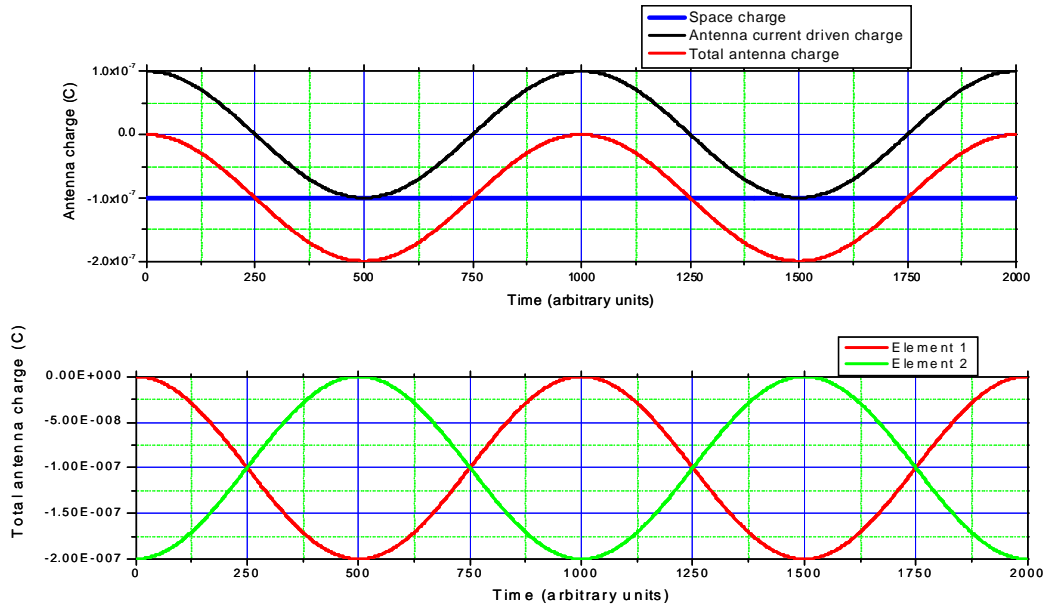


Figure 1. a) The two components of charge on Element 1 of the dipole antenna. The blue horizontal line at 1×10^{-7} (C) represents the space charge accumulated on the antenna. The black curve is the sinusoidal time variation of the antenna current driven charge. The red curve is the sum of the space charge and the driven charge and is always negative, b) The time variation of the total charge on the two elements of the dipole antenna illustrating the phase relationship.

As the charge on each element increases from zero to a negative maximum, the sheath grows in radius such that the positive charge within the surrounding sheath is equal to the negative

charge on that element. At the time of the maximum charge on the element the sheath reaches its maximum radius and then the radius decreases as the charge on that element decreases until the net charge is zero and the radius of the sheath is also zero. The positive charge within the sheath is always equal to the negative charge on the antenna.

The aim of this work is to determine the electric field strength inside the sheath and with that, the motion of the positive ions within the sheath as they respond to this electric field. The antenna elements, being negatively charged, initially drive out the electrons within the plasma surrounding the antenna elements, leaving behind the positive ion-sheath with a radius such that the total positive charge within the sheath is equal to the negative charge on the antenna. The radius of the sheath depends first on the quantity of negative charge on the antenna element and then on the ion density in the plasma surrounding the antenna. As the driven electron current in the antenna flows from one element of the dipole to the other, and as the total charge on the element varies, the radius of the sheath changes, though the balance between the antenna charge and the sheath charge is always maintained.

2.3.2 Results

This analysis assumes a cylindrical ion-sheath along the length of the antenna element and that the radius of the sheath is small compared to its length. It is also assumed that there is cylindrical symmetry around the antenna element. These assumptions simplify the analysis and make it possible to treat the problem of determining the sheath electric field as a 2-D problem. The configuration used here is illustrated in Figure 2, showing the cross-section of the sheath.

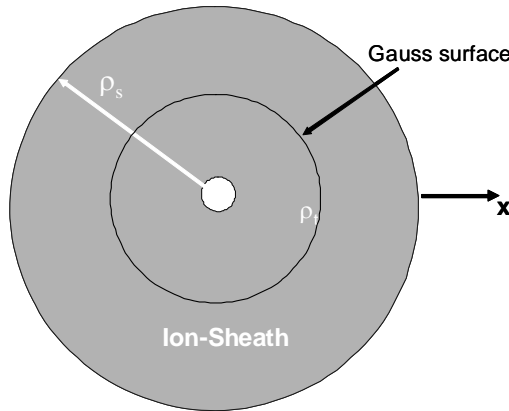


Figure 2. Illustrated cross-section of the ion-sheath.

Here the sheath radius is ρ_s , the ambient plasma density is n_o (m^{-3}) and the antenna wire radius is “ a ” (white inner circle) which is negatively charged. Although initially the ion density is assumed uniform as in the surrounding plasma, as the ions begin to move inward under the influence of the electric field, the ion density increases as the distance to the antenna element decreases. As is discussed later, a simple model for the ion density variation is derived. For now, the variation of ion density as a function of ρ is given as:

$$n_i(\rho) = n_o \times \left(\frac{\rho_s}{\rho} \right)$$

This density function means that since the differential cylindrical volume elements increase as ρ , this just compensates for the decreasing density and the resulting variation of charge, within the differential volume, with radius is essentially constant.

Given the azimuthal symmetry for the dipole antenna, the field strength variation along any radial is the same and using Gauss's law it is relatively simple to calculate the electric field strength as a function of distance from the antenna element. Because of the symmetry, the electric field vector will have only a radial component inside the sheath. The Gaussian surface chosen is a cylinder along the antenna axis with radius ρ . For $\rho < \rho_s$ the calculated field is inside the sheath. The total charge within the positive ion-sheath of radius ρ_s , as a function of time, is given as:

$$Q(t)_s = 2e\pi L n_o \rho_s(t) (\rho_s(t) - a)$$

while the charge inside the Gaussian surface is:

$$Q_{in} = 2e\pi L n_o \rho_s (\rho - a)$$

where e is the charge on the ion and L is the length of the antenna element.

Under the influence of the electric field, the positive ions move towards the antenna element and upon contact with the surface charge (electrons) they reduce the total negative charge on the antenna. This analysis also calculates the ion velocity as they reach the antenna, the charge deposited on the antenna and the positive ion current contacting the antenna. Because of the nature of the approach taken here, the effect of the ions on the antenna electric field and ion motion was done iteratively. That is, we first calculated the ion motion neglecting the effect of the arriving positive charge as they alter the antenna electric field and then in the next iteration the effect of the accumulated positive charge on the antenna is used to recalculate the ion motion and currents.

Before correcting for the positive ion charge accumulating on the antenna during the RF-cycle, the electric field strength at a distance ρ is given as:

$$E_\rho(\rho, t) = \frac{e n_o}{\epsilon_o} \rho_s(t) - Q_o \frac{(1 - \cos(\omega t))}{2\pi \epsilon_o L \rho} \quad \text{for } \rho < \rho_s$$

$$\text{and } E_\rho(\rho, t) = 0 \quad \text{for } \rho > \rho_s$$

$$\text{where } \rho_s(t) = \frac{a}{2} + \left[\left(\frac{a}{2} \right)^2 + \frac{Q_o (1 - \cos(\omega t))}{2\pi e n_o L} \right]^{\frac{1}{2}}$$

Note that Q_o is related to the antenna current as detailed below.

For all subsequent calculations the following parameters were used.

$$N_o = 1.5 \times 10^9 \text{ m}^{-3} \quad (\text{electron/ion density in ambient plasma})$$

$$i_o = 160 \text{ mA} \quad (\text{maximum antenna current})$$

$$f_o = 34 \text{ kHz} \quad (\text{transmitted frequency})$$

$$\omega_o = 2\pi f_o \quad (\text{angular frequency})$$

$$T = \frac{1}{f_o} \quad (\text{wave period})$$

$$Q_o = \frac{i_o}{\omega_o} = 4.7 \times 10^{-6} \text{ C} \quad (\text{maximum antenna driven charge})$$

$$L = 125 \text{ m} \quad (\text{antenna length})$$

$$\text{ion} = \text{hydrogen}$$

$$a = 0.0002 \text{ m} \quad (\text{antenna radius})$$

$$m_e = 9.11 \times 10^{-31} \text{ kg} \quad (\text{mass of the electron})$$

$$e = 1.60 \times 10^{-19} \text{ C} \quad (\text{electron charge})$$

$$m_i = 1836 m_e \quad (\text{mass of the proton})$$

MATHECAD was used to carry out these calculations. The results for the electric field during the first iteration (neglecting the changes induced by the positive ion-charge accumulating on the antenna) are shown in Figure 3. This figure shows the variation of the electric field with distance from the antenna, within the sheath ($\rho < \rho_s$) at three different times during the growth of the sheath. At $t=0$, the sheath radius and field are zero and maximum when $t=T/2$. The E-field (negative pointing inward) is strongest close to the antenna element where the negative charge is less affected by the surrounding positive ion charge within the sheath. At 10 cm from the antenna wire, the field reaches $-2 \times 10^4 \text{ V/m}$ when the negative antenna charge is a maximum. Within the sheath the electric field decreases as ρ^{-1} when the distance to the antenna is small. At a distance of 1m from the antenna the field strength has decreased by almost two orders of magnitude and continues to decrease to zero as the boundary of the sheath is approached. It should be remembered that the sheath radius is changing with time.

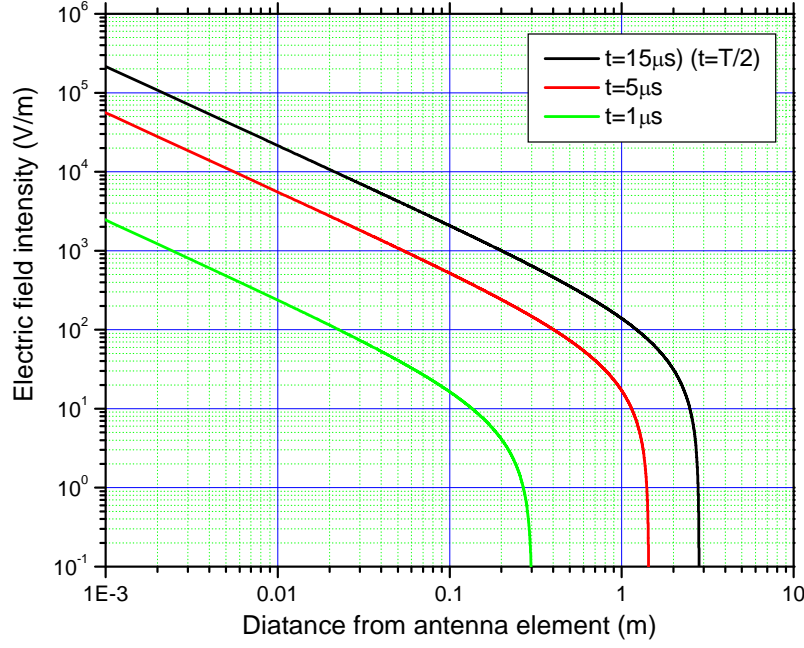


Figure 3. Electric field strength as a function of distance from the antenna. The maximum radius of the ion-sheath under the assumed conditions was 2.82m. It was assumed that neutral plasma exists outside the sheath.

Physically, the decrease in field strength results from the increasing quantity of positive charge included within the Gaussian cylinder of radius equal to the distance of the field point, ρ . By Gauss' law the charges outside this radius do not contribute to the field at the Gaussian surface.

Having computed the electric field intensity within the sheath, it is now possible to calculate the motion of the positive ions within the sheath. The positive ions are attracted towards the negatively charged antenna element. The motion of the hydrogen ions in this case was found by solving the equation of motion:

$$\frac{d^2 \rho}{dt^2} = \frac{e}{m_i} E_\rho(\rho, t)$$

where $\rho = \rho(t)$

Figure 4 is a plot of the position of the ions located in the beginning every 10 cm as a function of time during one RF-period. The origin of these ions is identified by the starting radius in the figure. All ions out to a radius 1.48m (the outer-most curve) reaches the antenna within the period of the RF-cycle. Hydrogen ions outside this radius do not reach the antenna within that time and in some cases barely begin to move before the sheath shrinks to a radius

smaller than these outer ions. The most inner ions, say at 10 cm, reach the antenna in about $4\mu\text{s}$ after the start of the cycle while the ions at 1m reach the antenna after $18\mu\text{s}$. The ions at 1.48m, reach the antenna after the full period of $29.4\mu\text{s}$. Ions inside 1.48m that reach the antenna constitute about 48% of the ions within the sheath at maximum radius. The positive charge that accumulates on the antenna begins slowly at the beginning of the RF-cycle and increase through the entire cycle depositing a total charge of $6.98 \times 10^{-7} \text{ C}$ compared to the maximum negative charge of $1.38 \times 10^{-6} \text{ C}$ on the antenna which includes the space charge.

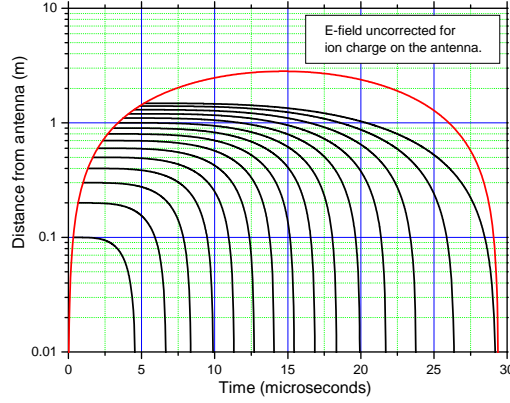


Figure 4. The time dependent position of the ions starting at different radii. The red curve defines the radius of the sheath during the RF-period of $29.4\mu\text{s}$. Each curve represents ions beginning at 10 cm in steps of 10 cm. Ions do not begin to move until the sheath reaches a radius equal to the initial position of the ion.

Figure 5 shows the two components of the charge on the antenna during an RF-cycle. The green curve, which represents the sum of the two components, shows the time when the net charge on the antenna is zero which is then followed by a positively charged phase. The zero point has moved from the end of the RF-cycle ($29.4\mu\text{s}$) when only the current driven charge and negative space charge is considered to about $23.1\mu\text{s}$ when the ion current is added to the antenna charge.

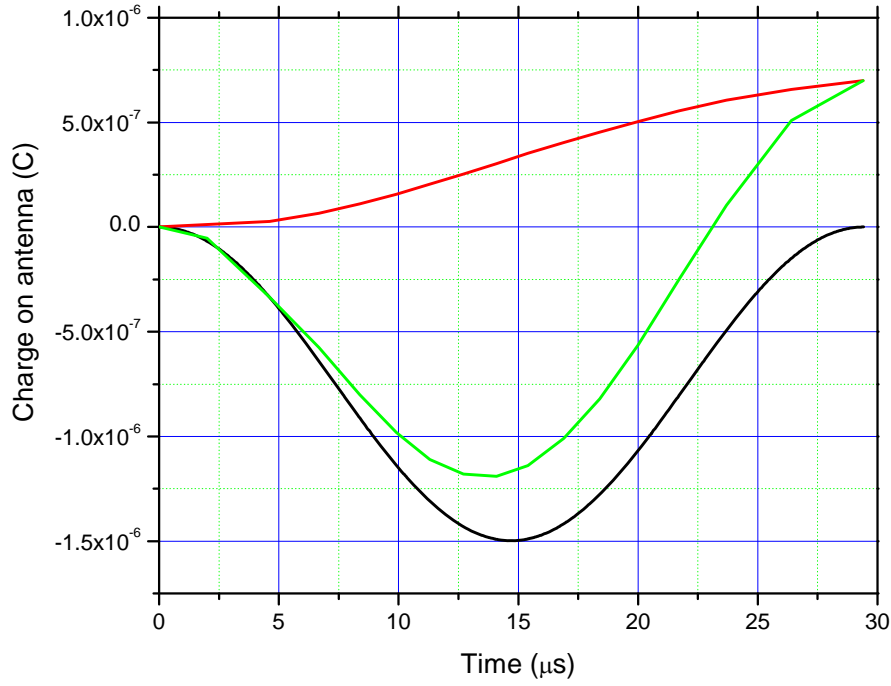


Figure 5. The time variation of the antenna charge during one RF-cycle. The black curve is the combined current driven charge, and the space charge the keeps the antenna negative over the complete period. The red curve is the positive charge deposited on the antenna from the hydrogen ion current attracted to the negatively charged antenna. The green curve is the sum of the two charges resulting in a positive, towards the end of the RF-cycle.

Using the results of the calculated ion position to determine the positive charge deposited on the antenna as a function of time, it is possible to now recalculate the electric field and ion motion using the combined positive and negative antenna charge as illustrated by the green curve in Figure 5. A simple mathematical function was fit to the positive ion curve (red) and the new fields computed based on the modified antenna charge. The results are not greatly different for this iteration, though the ions in the sheath now move somewhat more slowly, the electric field being weaker. Fewer ions are therefore removed from the sheath and deposited on the antenna. For the first iteration the ions out to 1.48m reached the antenna in one RF-period and now only out to 1.45m reach the antenna in the same time. The hydrogen ion terminal velocity (Figure 6) shows this effect. At the beginning of the cycle the difference between the two iterations is essentially zero since little positive charge has reached the antenna at those early times (small distance from the antenna).

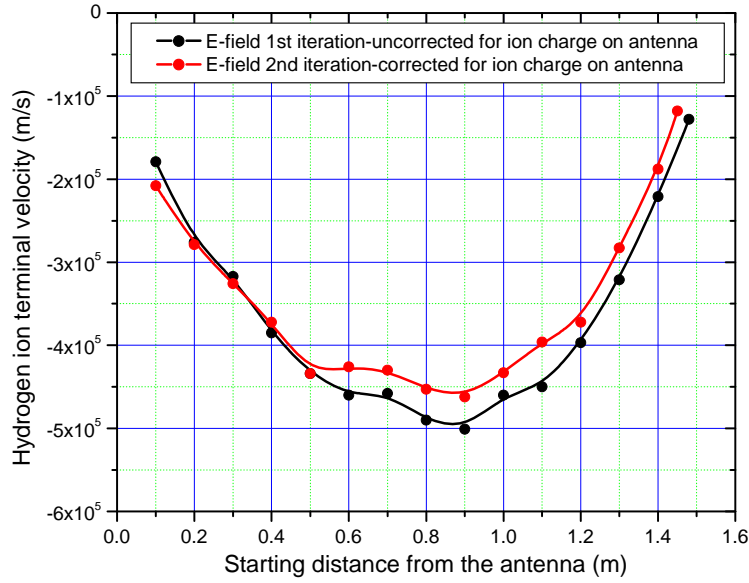


Figure 6. Terminal velocity of sheath ions reaching the antenna within one RF-cycle as a function of starting position of the ions. All velocities are negative (directed inward towards the antenna). The second iteration show a reduced terminal velocity and a smaller starting position at the outer boundary of the sheath.

It is interesting to note that the ion terminal velocity is greatest in the middle region. For the close-in regions the terminal velocity is small, although the electric field is strongest, because the ions reach the antenna quickly and they do not have the time to increase their speed. At the longer distances, the electric field is much weaker and the ion acceleration is small and the ions never reach a high terminal velocity. Only in the middle region is the field sufficiently strong and the acceleration time long enough for the ions to reach the maximum negative velocity (inward).

Finally the hydrogen-ion current into the antenna is calculated from the quantity of charge arriving at the antenna (Figure 5) and the time of arrival (derived from Figure 4) and shown in Figure 7.

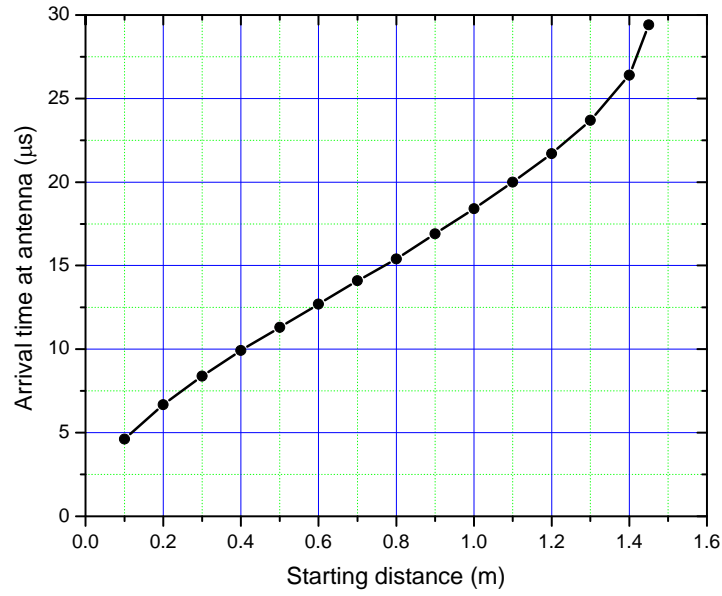


Figure 7. Arrival time of Hydrogen ions at antenna relative to the start of the RF-cycle.

Using the quantity of positive charge arriving at the antenna and the arrival times in Figure 7, it was possible to calculate the ion current into the antenna as a function of time and the magnitude of the driven current. Using the plasma parameters listed earlier (particularly for ambient plasma density of $1.5 \times 10^9 \text{ m}^{-3}$) and for four driven antenna currents from 80mA to 320mA, the ion currents as a function of time are shown in Figure 8.

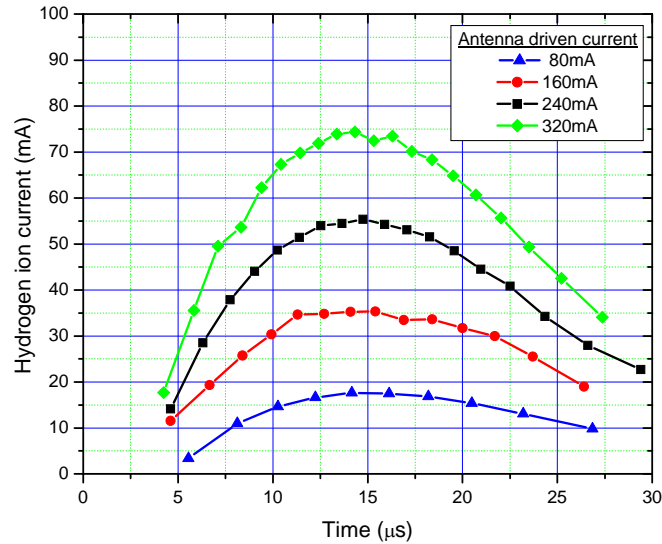


Figure 8. Hydrogen-ion current reaching the antenna as a function of time during an RF-period for four driven antenna currents.

The same variation as for the ion terminal velocity is seen here, where the current peaks near the middle of the period. The peak current at time $t = \frac{T}{2}$ increases linearly with the increasing magnitude of the driven current. This is illustrated in Figure 9.

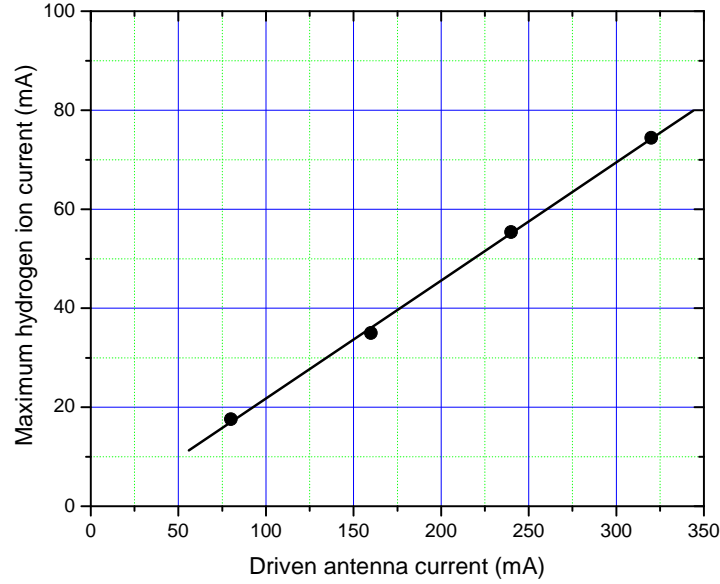


Figure 9. Peak ion current into the antenna element as a function of the driven antenna current.

Finally a comparison was made of the ion current for two plasma densities differing by an order of magnitude. These results are shown in Figure 10.

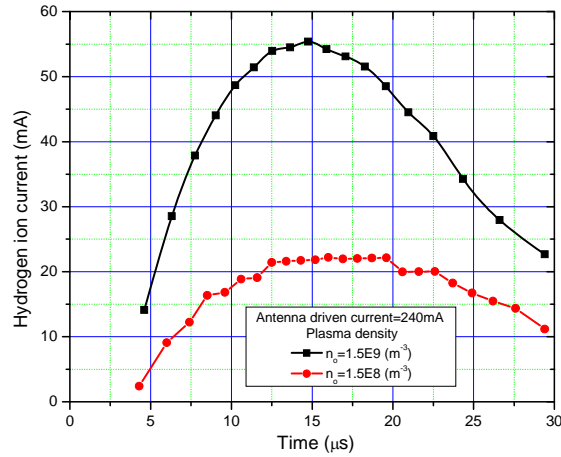


Figure 10. Ion current into antenna element as a function of time for one RF-period. The black (square points) curve is for a plasma density $n_0 = 1.5 \times 10^9 \text{ m}^{-3}$ and the red curve (dots) for $n_0 = 1.5 \times 10^8 \text{ m}^{-3}$.

The peak ion current decreases from 55 mA to only 22 mA for the low density plasma, while the maximum radius of the ion-sheath increases from 3.4m for the high density plasma to 10.9m for the low density plasma. For all the calculations with the high density plasma approximately 50% of the ions in the maximum sheath reach the antenna within the RF-period compared to 21% for the low density plasma.

During the positive phase, that is, when the ions being attached the antenna element is greater than the negative charge on the dipole element, the antenna begins to attract electrons from the ambient plasma outside the sheath. The light weight electrons, compared to the protons, begin to arrive quickly at the antenna. No electron sheath can form during this short time, that is, the positive ions cannot move out because, first, the electric field is considerably weaker than the field associated with the negatively charged antenna and secondly, the heavy ions do not move significantly during the short time available before the arriving electrons neutralize the positive charge on the antenna. The fall-off of the antenna the electric field strength (Figure 11) with distance during the positive phase is different than for the negatively charged antenna because during this positive phase no electron sheath or sheath boundary is formed.

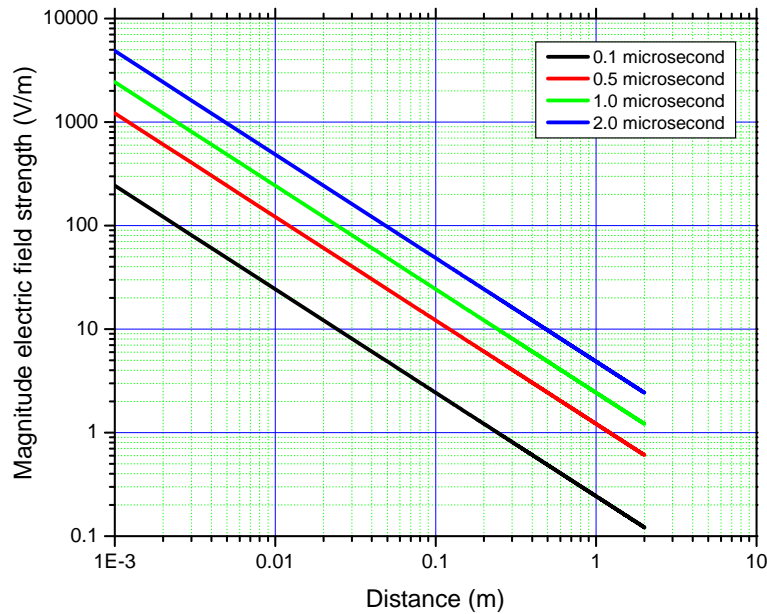


Figure 11. Magnitude of the electric field strength during the positive phase. The field strengths at four times during this phase are presented.

The field is directed outward away from the antenna during this positive phase. The times associated with the electron flow are significantly shorter than during the large portion of the RF-cycle while the antenna is negatively charged, because as will be shown shortly, the electrons reach the antenna and neutralize the positive charge very quickly. The quantity of electrons out to a radius of 1.4 m is of course exactly the same as charge carried by the protons during the RF-cycle. The arrival time of these electrons is shown in Figure 12. Here we see that in just under 3 μ s all the electrons necessary to neutralize the positive charge that arrived during the entire RF-

cycle, i.e., 2×10^{-7} C. At the end of the RF period the antenna has returned to zero net charge and is ready to begin the next cycle just as at the start of the previous cycle.

The issue of the continuous increase of net charge on the antenna during each cycle, in spite of maintaining neutrality, is addressed here. Apparently, 2×10^{-7} C positive ions and 2×10^{-7} C electrons accumulate on the antenna each cycle. Does this process go on continuously? We propose that the positive ions and electrons recombine on the antenna and escape as neutral hydrogen gas into the environment around the antenna. Actually, the ions and electrons have considerable kinetic energy as they arrive at the antenna and transfer some of this energy to the antenna wire and some remains with the components of the hydrogen atom. When the hydrogen gas reenters the plasma region, solar ionization takes place and the quantity of plasma is restored. Now this process can continue indefinitely. The energy carried away from the antenna by the hydrogen atoms represents warm plasma in the region around the antenna.

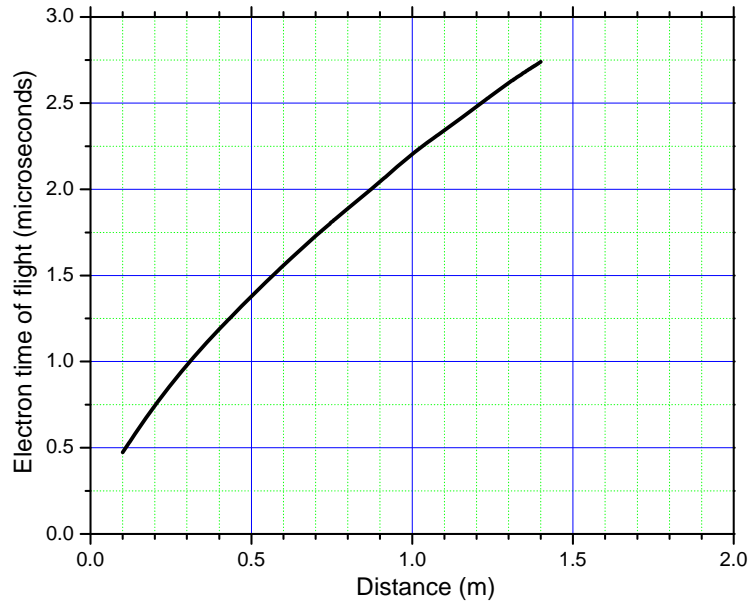


Figure 12. Arrival time of electrons during the positive phase of charge on the antenna. The distances correspond to the arrival times of all the 10 cm shells out to 1.4 m.

2.3.2 Summary

Although the methods used here are not truly self-consistent as was the work of J. Tu on the same subject, this effort describes well the physics of the process of sheath formation and ion and electron motions in the vicinity of the antenna. One issue that was examined here was the effect of oxygen ions as compared to the protons. These calculations were carried out and it was determined that the heavy oxygen ions contribute only a small fraction to the ion current at the antenna compared to the proton ions and the oxygen ion contribution has been neglected here. Finally, the question of losses in the sheath growth and decay process, an important issue which as of this writing, has not been fully addressed. It appears that the only energy expended by the transmitter power supply is in the formation of the ion sheaths, which theoretically should be

recovered when the sheaths collapse at the end of the RF-cycle. However, the accelerated ion motion results in their carrying a large kinetic energy which is lost in the form of heat, first the antenna wire and then to the hot hydrogen released at the antenna after ion-electron recombination. This is the next area for our investigation and future updates will include a discussion of the energy loss mechanisms.

2.4 Radiation Theory in Magnetized Plasma

This is a comprehensive theoretical investigation of the radiation in magnetized plasma. We demonstrate in Appendix C-F that the previous whistler radiation theories were seriously flawed. The most obvious evidence is that they predicted the radiation power to be greater for shorter antennas. Our investigation has arrived at the opposite conclusion. The work involves massive mathematical development. We are still in the process to simplify it for eventual publications. We include the full details in Appendix C and its sub-appendices C-A, C-B, C-C, C-D, C-E, and C-F.

2.5 Impedance Characteristics of an Active Antenna Transmitting in the Whistler Mode

The main body of this study is the data analyses of the second RPI whistler transmission experiment. Because the satellite and the instrument were severely damaged after over 5 years of operation in its extended mission period, there are many uncertainties in the state of condition of the satellite and instrument. To interpret the results was extremely challenging. We have been able to successfully remove most uncertainties. We further compare the results with theoretical predictions. A clear picture emerges of instrument operation and physics that controlled the processes. This paper is submitted to *J. Geophys. Res.*, and the full article is attached in Appendix D. Below is the abstract.

We use the Radio Plasma Imager on the IMAGE satellite to investigate the characteristics of whistler wave transmission by an electric antenna in space plasma. A dedicated experiment was carried out on 21-22 September 2005, for two orbits in the plasmasphere. The input impedance characteristics of the dipole antenna submerged in plasma is determined for whistler mode transmission. These results are consistent with a physical model in which the plasma around each antenna element forms an ion sheath with a time-varying radius while the antenna itself is negatively charge to a large voltage. Within the plasmasphere, these sheaths are a part of the antenna-plasma system and represent a capacitive component of the tuned antenna circuit. It is shown that inside the plasmasphere the RPI antenna capacitance varied from 430 pF to 480 pF. Comparison to model calculations shows good agreement with a relative error smaller than 5%. Measurements of the antenna input resistance showed that inside the plasmasphere its value was between 200 Ω and 500 Ω , varying considerably with changes in the ambient electron density and cyclotron frequency. A comparison to model calculations suggests that a large part of the antenna input resistance represents the antenna radiation resistance.

2.6 VLF Station Monitoring in Space with the RPI Instrument

This investigation is aimed at addressing the additional item mentioned in the introduction. We have gained much knowledge about the wave power in space from the VLF ground transmitters. We question the validity of the previous theories on the coupling of the ionosphere and the raytracing results based on our observations. We are very pleased with the publication of the *Starks et al.* [2008] J. Geophys. Res. paper, to which we contributed. We summarize below some other observations on this issue.

2.6.1 Introduction

Recently, there has been a significant interest in studying characteristics of the whistler waves in the Earth's plasmasphere [e.g., *Green et al.*, 2005; *Bortnik et al.*, 2003; *Starks et al.*, 2008]. Whistlers are usually defined as ordinary electromagnetic waves with the frequency smaller than the plasma gyrofrequency [*Budden*, 1985], a condition that puts them in an audio frequency range. The major sources for the whistler waves in the plasmasphere are plasmaspheric hiss, chorus, lightning discharges, and ground-based transmitters [*Abel and Thorn*, 1998a; 1998b]. When propagating in the Earth's plasmasphere, these waves are capable of affecting the pitch angle distribution of energetic particles which are potentially harmful to low Earth orbit satellites [*Lyons et al.*, 1971; 1972].

This section presents results of the observations of the whistler waves produced by powerful ground-based very low frequency (VLF) transmitters. At present there are a significant number of such transmitters operating in a frequency range of 10-50 kHz. In addition to the main active sounding mode, the RPI was also capable of detecting the thermal radio emissions through the entire operating frequency range in a passive mode. This mode was also found to be suitable for observations of the whistler waves [e.g., *Galkin et al.*, 2004] propagating in the plasmasphere. In this work, the RPI data, routinely collected in the passive operating mode was used to study signals produced by ground based VLF transmitters. Complementing the analysis of routinely collected data, a specially designed RPI program of operation intended for the reception of the signals from the ground-based VLF transmitters has been developed and executed over a significant period of time that made it possible to collect reasonable amount of data and analyze parameters of the VLF signals originating from the ground in greater details.

2.6.2 VLF signal detection with the RPI

In 2002, it was first realized that in the passive mode of operation typically used for thermal noise measurements, the RPI instrument is detecting transmissions from ground-based stations. In the 10-30 kHz frequency range there is number of stations operating around-the-clock. Some of the most powerful among the known ones are listed in the Table 1.

Table 1. Locations and main parameters of the most powerful VLF stations observed by the RPI

Freq. (kHz)	Station Identifier	Power (kW)	Location	Geographic Lat.	Geographic Long.	L- shell
19.8	NWC	1000	Exmouth, NWC, Australia	21.8 S	114.1 E	1.41
20.9	HWU	1000	Rosnay, France	46.7 N	1.3 E	1.79
21.4	NPM	566	Laulaulie, Hawaii	21.4 N	201.9 E	1.45
23.4	DHO	500	Randerfehn, Germany	51.2 N	7.9 E	2.15
24.0	NAA	1000	Cutler, Maine, USA	44.7 N	292.7 E	2.87
24.8	NLK	250	Arlington, WA, USA	48.2 N	239.0 E	2.89
25.2	NML	500	La Moure, ND, USA	46.4 N	261.7 E	3.26

In the passive operation mode, the RPI operating frequency was stepped from 3 kHz to 1 MHz in increments of 400 Hz, which corresponds to the system bandwidth. The amplitudes for each frequency bin are then plotted as functions of time, resulting in the so-called RPI dynamic spectrogram. A time interval between two consecutive measurements in this operational mode was typically 2 min. More technical details of the signal processing in this regime can be found in [Reinisch *et al.*, 2001; 2000]. An example of such dynamic spectra recorded on 21 April 2001, when among several noise sources transmission from the NLK station was detected is shown in Figure 13.

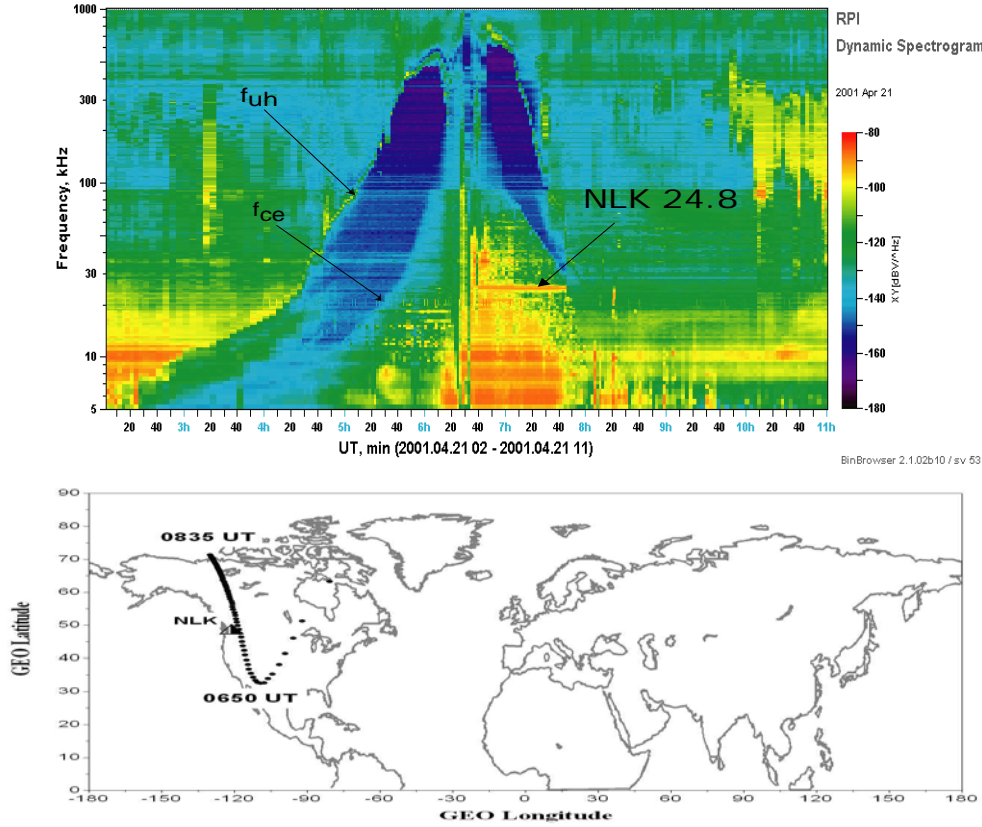


Figure 13. Top panel: an example RPI dynamic spectrogram showing signal from the NLK station. The characteristic upper hybrid (f_{uh}) and gyro frequency (f_{ce}) resonance lines are also shown. Signal from the NLK station is indicated. This record was made on 21 April 2001. Bottom panel: corresponding IMAGE satellite projection traced along the magnetic field line as a function of time.

The figure presents a dynamic spectrogram with the displayed frequency range from 5 kHz to 1000 kHz and a time span of 9 hours. This record was made with the IMAGE satellite passing near its perigee. A number of characteristic features can be seen in the spectrogram. First, note the plasma gyrofrequency, f_{ce} , as well as the upper hybrid resonance line, f_{uh} ($f_{uh}^2 = f_{ce}^2 + f_{pe}^2$, where f_{pe} is the electron plasma frequency, e.g., [Benson *et al.*, 2004]) are indicated in the plot. The region of the spectrogram between these two frequencies is characterized by very low amplitude of the recorded signals, since there are no propagating waves in this frequency range [Budden, 1985]. The spectral pattern evolves as the satellite travels along the orbit and the frequencies of the local plasma resonances change. At approximately 0300 UT the satellite enters the plasmasphere on the dayside, and the local plasma frequency (which is very close to the upper hybrid resonance line, as long as f_{ce} is small) starts to increase rapidly. At 0630 UT the satellite passes above the Earth's South Pole and goes into the night-side plasmasphere. During that time (from 0635 to 0750 UT) the recorded signal amplitude in the 24.8 kHz frequency channel (corresponding to the NLK station operating frequency) shows significantly higher

amplitude, as seen in the figure. Note that the signal enhancement is observed only over a relatively narrow frequency band (less than 1 kHz) that suggests that the signal source has a constant frequency. The magnetic footprint of the satellite (the satellite projection traced down to the Earth's surface along the magnetic field line passing through the satellite) during each individual measurement made in the passive mode is shown in Figure 1b. Clearly, during the time of interest the satellite footprints were in the close vicinity of the NLK confirming that the observed signal was originating from this ground-based station. In general, we were able to clearly see the VLF station signals only when the satellite was inside the plasmasphere.

For a better understanding of the distribution of the signal amplitude as a function of satellite position with respect to the VLF ground station, a special type of presentation was made. Figure 14 presents two years of passive observations for the 25.365 kHz frequency channel (within 400 Hz system bandwidth) which is the closest to the NML station operating frequency (25.2 kHz). Each circle in the plot corresponds to a single measurement, with the location of the circle corresponding to the satellite magnetic footprint (traced northward) while the size and color of the circle are modulated by the observed signal amplitude. Thus, signals below certain noise threshold (set as 0 dB level) amplitudes are not visible. Totally, there were about 100,000 individual measurements of interest made during 2001-2002.

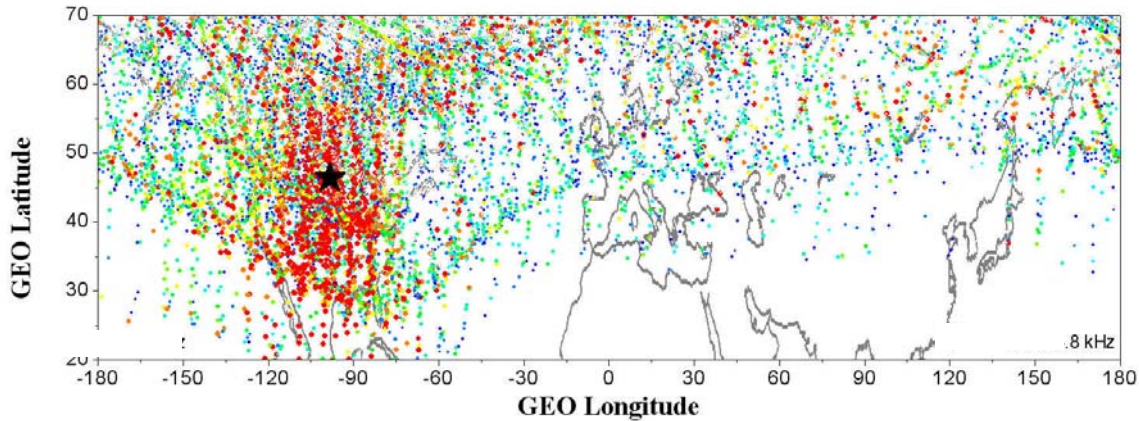


Figure 14. NLM station observations made during years 2001 and 2002. Each circle in the plot corresponds to a single measurement, with the location of the circle corresponding to the satellite magnetic footprint (traced northward) while the size and color of the circle are modulated by the observed signal amplitude.

The pattern made of all the footprints has a peculiar shape because it is determined by the configuration of the satellite's orbit. Since the satellite never flew below ~1000 km altitude, the equatorial regions with very low L-shell values were not covered. Also, because the footprint tracing was performed along the magnetic field, the lower boundary of the pattern varies with the longitude and its shape is determined by the Earth's geomagnetic field. Figure 14 clearly demonstrates that the signals with largest amplitudes were predominantly observed in the region near the NLM station thus confirming their origin. There are a number of other scattered measurements with strong amplitudes observed in the figure which is not very surprising given the statistical nature of the data presented. It should also be noted that the instrument's

bandwidth was rather wide (~ 400 Hz) making it impossible to limit the received signal to a narrow band around the known operating frequency. Note that there were a significant number of the large amplitudes observed in the latitudes above approximately 60° , which are most likely caused by the auroral activity.

Figure 15 shows observations presented in the same format as Figure 14 for the DHO station (23.4 kHz frequency channel). Here, however, the measurements are separated into nighttime (top panel) and daytime (bottom panel) observations. The time of the day is determined for the location of the station. Clearly, the difference between the two observations is dramatic. During the daytime measurements, the observed signal is confined to a small region around the station, which is 3-4 times smaller than that for the nighttime observations. We attribute this effect to a larger absorption of the VLF signal in the Earth-ionosphere waveguide during the daytime. In these plots the observations presented were limited to the satellite location within the plasmasphere to avoid displaying the effects of the auroral activity. This limitation puts the upper boundary on the data presented.

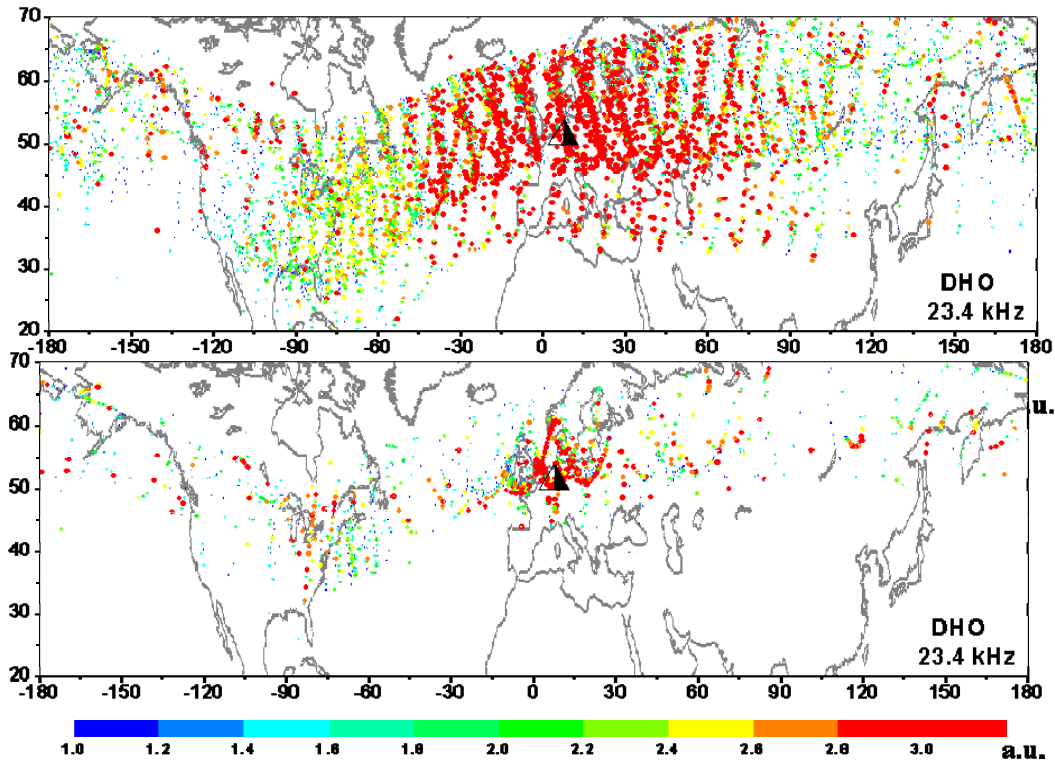


Figure 15. Magnetic footprints (circles) of IMAGE satellite and wave amplitudes (color-coding) received by RPI at the frequency channel corresponding to the DHO station operating frequency.

After comprehensive analysis of the signal amplitudes during this period, it was concluded that the recorded VLF signals from the ground-based stations were, in fact, saturating the RPI receiver for most of the observations. That happened because this passive mode was originally designed for receiving relatively weak natural emission signals in space and accordingly the receiver was programmed with the highest gain settings. Thus, even though in this retrospective

analysis we were able to successfully identify VLF signals from the ground-based stations detected by the RPI instrument, the fact of the signal saturation made it impossible to determine any quantitative characteristics of the VLF signal trans-ionospheric propagation. Because of that, in early 2003 it was decided to perform VLF station monitoring using a specifically designed program with a lower gain setting of the RPI receiver. With approximately two months of data collected under testing conditions, it was possible to identify a gain setting that was near optimum in terms of the ambient noise level and minimal saturation. Unfortunately, because of the schedule limitations of the instrument operation, it was not possible to run this newly designed program round-o-clock and to collect as much data as it was collected in the regular passive observation mode aimed at studying thermal noise emission. Instead, the VLF station monitoring was done on a campaign basis, with a several series of observations carried out during September-November 2003, June-September 2004 and March-August 2005. In this special program for the VLF study, the RPI dynamic spectrogram was made in a rather small frequency range, from 18 kHz to 32 kHz, which was of interest for the observation of the VLF transmitters. Figure 16 presents an example of the NLK station observation made with the use of this special RPI program. Clearly, this plot shows a signal from VLF station in greater details compare to the original data collected in 2001-2002. Also note two vertical lines corresponding to the time of the satellite's passage through the auroral regions.

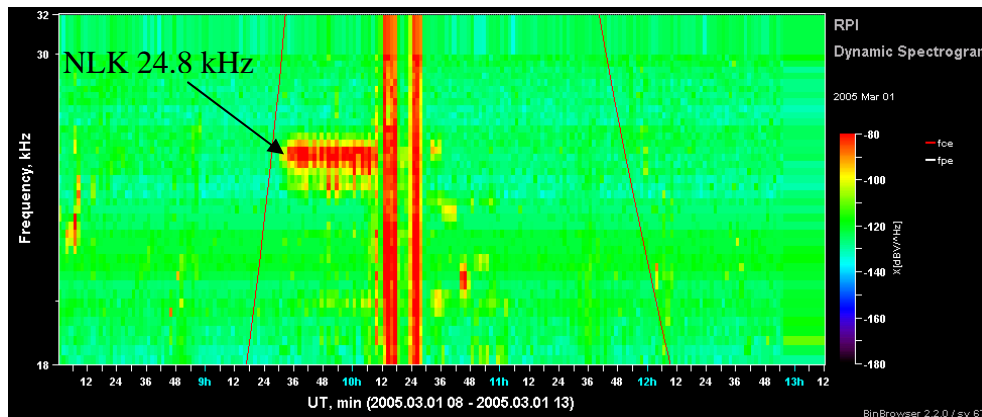


Figure 16. An example of the RPI measurements in the dynamic spectrogram mode with new settings.

As in the case of earlier observations, the signals from the VLF stations were detected mostly when the satellite was inside Earth's plasmasphere. Because of the satellite's orbit configuration, most of the data were collected for the following three stations: NML, NLK, DHO. The satellite's orbit configuration restricted the time of the observations. Thus, in 2003 there were mainly dayside observations, in 2004 there were dawn and dusk observations, and in 2005 there mainly daytime observations.

Figure 17 presents observations of the NML transmissions made in September-November 2003. The format of this figure is same as in Figures 14 and 15, i.e., the position of each circle corresponds to the location of the magnetic footprint of the IMAGE satellite in geographic coordinates, and amplitude of the detected signal is shown both with the circle color and size. It is evident that in the specially designed program for the VLF station observations, the RPI

instrument has reliably detected the signals from the ground-based NML station with the signal to noise ratio of over 30 dB. The noise level in this case is the typical signal amplitude in the 25.2 kHz frequency channel for the observations made away from the NML station location. Again, note the strong signals concentrated in the latitudes approximately above 60°, which corresponds to the satellites passing through the auroral regions, during which a wide-band signal enhancement is observed as seen in Figure 16, for example.

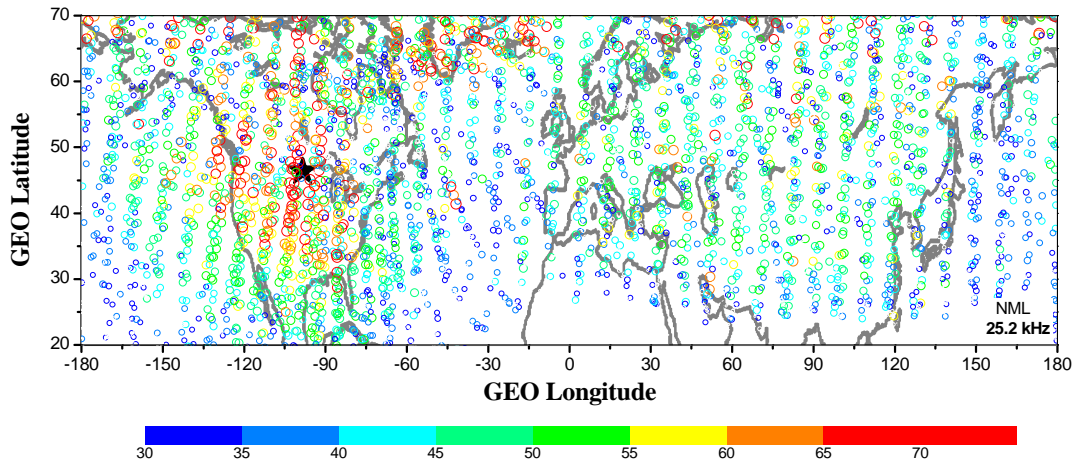


Figure 17. Observations of the NML station made in 2003. The position of each circle corresponds to the location of the magnetic footprint of the IMAGE satellite shown in geographic coordinates. The black star indicates the location of NML.

2.6.3 Results and Discussion

A generally accepted model of the VLF signal propagation consists of three different propagation stages [e.g., *Helliwell* 1965, *Ginzburg*, 1967]. At the first stage the VLF signal emitted by the transmitter propagates in the Earth-ionosphere wave-guide. Primarily in the vicinity of the station a fraction of signal energy “leaks” through the ionosphere into the plasmasphere. At present, little is known about the specifics of the “leakage” mechanism as there have not been many dedicated experiments to understand how much signal propagates through the ionosphere. It is important to stress that since the signal frequency is very low (<30 kHz), then outside of the ionosphere, in the plasmasphere where plasma frequencies are significantly higher (>50 kHz) such waves can only propagate in the whistler mode. This first of all means that outside of the ionosphere VLF signal propagates essentially along the magnetic field line [e.g., *Davies*, 1980]. In this work the data collected has been analyzed with this three-stage propagation model in mind. First, this model gives a key to understanding the difference between the daytime and nighttime observations presented (see Figure 15). Obviously, during the daytime, the VLF signals emitted by a ground-based station, experience a significantly more severe absorption in the Earth-ionosphere waveguide than during the nighttime. Therefore, it is not surprising that the RPI data show that VLF signals with strong amplitudes collected during

the daytime are much more “confined” to the vicinity around the station than those collected during the nighttime.

Figure 17 also suggests that the “illuminated” region around the station (positions of the satellite’s footprints where strong signals were detected) is somewhat displaced southward with respect to the station (i.e., towards lower L-shells). This effect was investigated in more detail by separating the data collected according to the satellite position. Figure 18 presents a portion of the NML observation data shown in Figure 17, with the satellite footprints limited to the vicinity of the station. This plot is now presented in geomagnetic coordinates. The left panel shows the observations made when the satellite itself was located in the northern hemisphere (in geomagnetic sense), while the right panel presents the measurements made when the IMAGE satellite was positioned in the southern hemisphere. It is evident that for the northern hemisphere observations the strongest signals were observed during the closest approach of the footprint to the station location. However, for the observations in the southern hemisphere the maximal signals appear to be offset towards the lower magnetic latitudes.

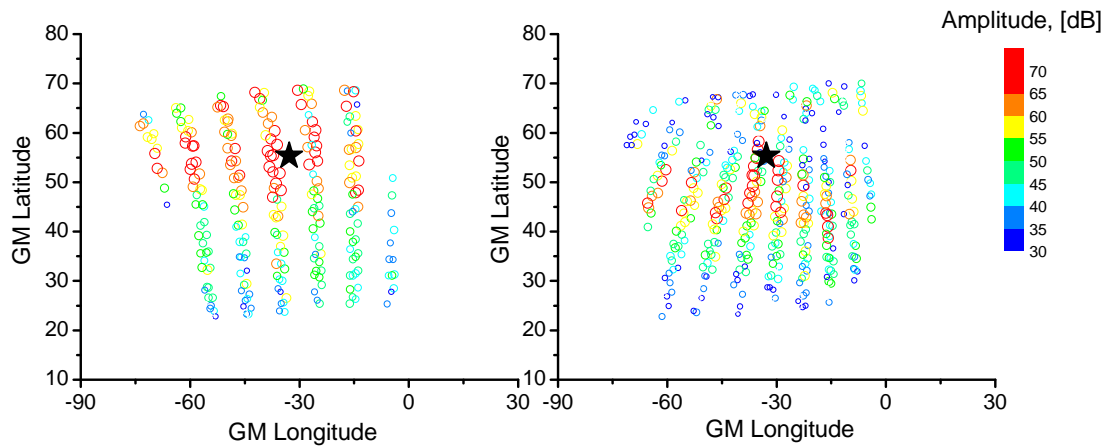


Figure 18. Observations of the NML station made from northern geomagnetic hemisphere (left panel) and southern hemisphere (right panel). Satellite footprints are shown in geomagnetic coordinates.

This interesting effect was investigated further and is illustrated with the following figure. Figure 19 presents an effect of apparent migration of VLF signals towards lower magnetic latitudes. This composite plot presents detected NML signal amplitudes as a function of the satellite position in geomagnetic coordinates. Scattered circles show the received signal amplitudes, with the red curve as the best fit smoothed median amplitude; the blue curve shows the magneto ionic Y-parameter (ratio of the gyro frequency and signal frequency, f_{ce}/f) calculated at the equator for the L-shell corresponding to the satellite position. Regions where the magnetic footprint of the satellite falls in the close vicinity of the station (a box of 5° in geomagnetic latitude and 30° in geomagnetic longitude) are shown as the shaded columns. This plot, in fact, shows the same offset effect introduced in Figure 18 in greater detail, demonstrating the displacement of the strongest signals measured in the southern hemisphere towards the lower latitudes. It also shows that the VLF signal indeed propagates to the satellite positioned in the

southern hemisphere by leaking through the ionosphere in the vicinity of the station and then traveling in the plasmasphere along the magnetic field line. An alternative VLF signal path would be for the signal to propagate in the Earth-ionosphere wave-guide all the way south to the magnetically conjugate point and then penetrate through the ionosphere and continues into the plasmasphere. But if this were the case, such a strong drop in the signal's amplitude seen in the equatorial region would have not been observed.

The signal amplitude distribution shown in Figures 18 and 19 at first appears surprising. It seems to be contradicting to the commonly accepted picture of VLF signal propagation, where in the plasmasphere VLF waves propagate nearly along magnetic field lines in a so-called “ducted” mode, with a slight migration to the higher L-shells along the path [Thomson, 1987]. The calculated Y value, also presented in Figure 19, however, provides a key to understanding the mechanism of the observed effect.

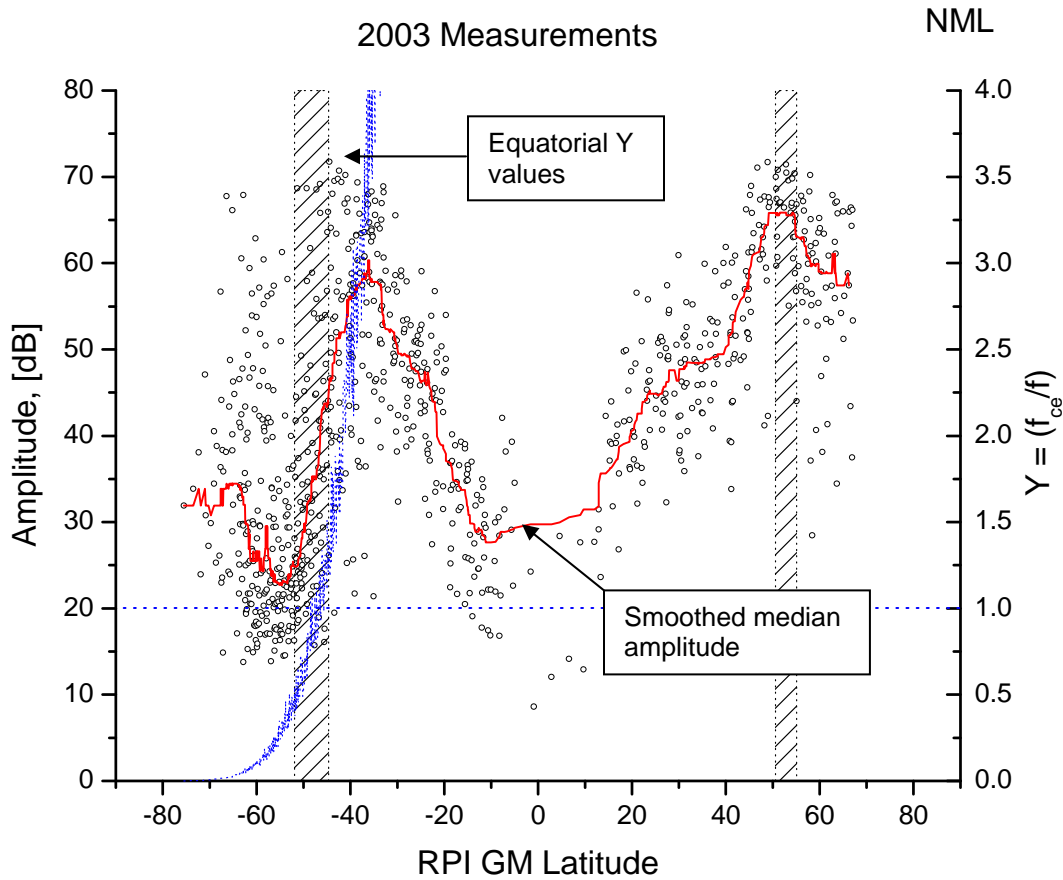


Figure 19. Signal amplitude as a function of the IMAGE Satellite Position. Circles represent individual measurements.

By definition, whistler waves can exist only when the wave frequency is lower than the gyro frequency (*i.e.*, $Y > 1$). The signal originating from the ground station on its way along the field line from the northern to the southern hemisphere goes through the equatorial region with the

weakest magnetic field, and therefore, lowest gyro frequency. For this particular case of observing the signals from the NML station operating at the frequency of 25.2 kHz, the wave frequency becomes greater than the gyro frequency at the equator, as illustrated by Figure 7 (regions for which the corresponding equatorial value of Y is smaller than unity). Clearly, for the satellite positions at about -50° magnetic latitude (this is also the location where the satellite magnetic footprint is in the closest vicinity of the NML station, and therefore, the strongest signal is expected) the corresponding equatorial Y value is near unity and, therefore, the signal cannot propagate across the equator. This explains why the NML signals are not observed at this satellite position. When the satellite is at the lowest geomagnetic latitudes, the corresponding equatorial Y -values are significantly larger allowing for the signal penetration into the southern hemisphere. This results in an apparent “offset” of the region associated with the strongest signal amplitude towards lower latitudes.

The signal “migration” was not observed for the DHO signals, but was detected for the NLK signals in good agreement with the gyro frequency values calculated for the corresponding magnetic tubes. A similar effect was also observed in CRRES and DEMETER measurements of the VLF transmissions [Clilverd *et al.*, 2008].

Using the data collected in these 2003 and 2005 observations, a comparison between signal decays during daytime and nighttime observations has been made. Figure 20 presents individual (circles) and averaged (lines) measurements of the signal decays for the DHO station observations. The reason for selecting the DHO station was the orbit configuration which has the largest area around the station covered with observations. Only the cases when the satellite was located in the northern hemisphere were selected to exclude weaker signals collected in the opposite hemisphere.

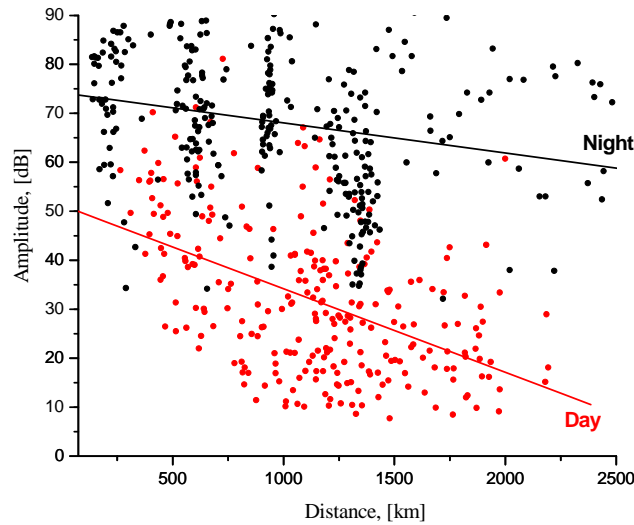


Figure 20. Signal decays for daytime and nighttime conditions. Signal amplitude is shown as a function of the distance between the satellite footprint and the location of the DHO station.

The two curves in Figure 20 show the average signal decay rates for these two conditions. Signal amplitudes are shown as a function of the distance between the satellite footprint and the

location of the DHO station. It is evident that during the daytime the observed signal amplitude is about 20 dB smaller than during the nighttime periods. Signal decay rates are 10 dB/1000 km for night time observations, while for the daytime ones it is about 20 dB/1000km. These values are close to those derived from ground-based monitoring of VLF signals, supporting the assumption that the main VLF signal attenuation on its transionospheric path comes from the propagation in the Earth-ionosphere waveguide.

It is important to stress that the observed daytime confinement of the signal to a small region around the station supports the fact that outside of the ionosphere VLF signals propagate predominately along the magnetic field lines. If this were not the case, then no matter how small the region in the ionosphere “illuminated” by the VLF transmitter, the RPI would always “see” a large spread of the signal around the station. This absence of the significant signal migrations across the magnetic field lines suggests that in the plasmasphere the VLF waves favor the ducted mode of propagation.

We have also made an effort to estimate the total power of the observed VLF signals in space. This, in fact proved to be quite a challenge, since this estimate requires the knowledge of the absolute value of the electric field strength which can only be derived from the measurements if the effective antenna length and the receiver gain were precisely calibrated. Using estimated effective antenna lengths and the laboratory calibration of the receiver, our measurements show that the peak VLF signal amplitude is of the order of 200 $\mu\text{V/m}$, corresponding to a Poynting flux of about $2.6 \times 10^{-10} \text{ W/m}^2$ within a flux-tube of 2000 km radius. Since the typical power of the ground based transmitters is of the order of 0.5-1 MW (see Table 1) this would mean that less than 1% of the total power radiated by the ground-based VLF station is transmitted through the Earth’s ionosphere into the plasmasphere.

The data collected in the specially designed passive mode of observations with the low receiver gain were also used for simulation of the IMAGE/RPI VLF measurements which showed a reasonable agreement between the observations and the model for the VLF station observations in the middle latitudes [Starks *et al.*, 2008].

2.6.4 Summary and Conclusion

The RPI instrument onboard of the IMAGE satellite was capable of detecting VLF signals from ground-based transmitters operating in the frequency range of 10-30kHz. Using the specially designed passive mode of observations with low gain settings some characteristics of the transionospheric propagation of VLF signal were determined. Results obtained show evidence for the validity of commonly accepted mechanism of the VLF wave propagation. It was shown that the nighttime observations are significantly different from the daytime ones. This effect is attributed to the stronger radiowave absorption in the Earth-ionosphere waveguide (i.e., at the first stage of the VLF signal transionospheric propagation). It was also possible to estimate the VLF signal decay rate as a function of the distance resulting in the value of 10dB/1000 km and 20dB/1000 km for nighttime and daytime measurements correspondingly. No significant signal migrations across the magnetic field line were observed suggesting that ducted modes of the VLF propagation inside the plasmasphere are common. It was also shown that the low values of the geomagnetic field at the equator act effectively as a “cut-off” frequency thus preventing

some VLF signals from penetrating one hemisphere into the other (when the condition for the whistler mode $Y > I$ is not satisfied at the equator). Finally, it is estimated that less than 1% of the total transmitted power leaks to the space through the ionosphere.

3 CONCLUSIONS

Through the course of the investigation, we have gained a great deal of knowledge about the transmission of whistler waves in space. The understanding is based on the combination of theoretical studies and observational data analyses, as well as computer simulations and circuit simulations.

The physical picture emerging from the investigation is that when transmitting in space, the antenna will be charged negatively to a voltage similar to the amplitude of the oscillation of antenna voltage. This highly charged antenna behaves similar to a leaky capacitor. The transmitted power is the “leakage”. In order to increase the radiation power, the transmitter needs a tuner to counter-balance the capacitance and to increase the current. Fixed tuning can be realized in steady state transmission. The notion that the variation in the radius of the sheath during a wave cycle would prohibit the system from being properly tuned is a misunderstanding of the problem and unsupported by experiments. Similarly, the notion that the antenna properties vary during a prolonged charge process is also unfounded and unsupported by simulations. Our studies have indicated that the charge process takes place rapidly within a few wave cycles.

The capacitive reactance of the antenna-sheath-plasma is the dominant effect while the radiation resistance is secondary. This is different from certain reports that the reactance is much less than the resistance.

4 FUTURE STUDIES

The theoretical understanding needs to be more quantitative and more realistic. We can divide the studies in three components: sheath and near fields, far fields, and the circuit simulation.

A full particle simulation code can be developed to simulate both electric and magnetic fields in three-dimensions. We have developed such a code for electrostatic condition in 1-D. Without the magnetic field component, the radiation effects cannot be represented. In order to derive the magnetic field, the code has to be 3-D because the current on the antenna decreases along the antenna which requires the second dimension. The variation of the magnetic field along the antenna requires the third dimension in the electric field. Therefore, to fully understand the system 3-D electromagnetic code is required. We have witnessed failed attempts using a fluid code developed in another group. Therefore, a full particle code is the approach that is most likely to succeed.

The general radiation theory has been developed, including the whistler mode application. There are four issues that need to be addressed by such a theory: the radiation resistance, the angular distribution of the radiation, the polarization of the waves which is needed to calculate

the pitch angle scattering, and the optimal orientation of the antenna with respect to the background magnetic field.

The circuit simulation model is crucial to our understanding of our system's responses to the transmission and its dependence on the plasma conditions. Our tests of the DSX system have indicated that the equivalent circuit may be more complicated than our original simple equivalent circuit under certain conditions. We need to develop more realistic equivalent circuits to simulate the possible plasma conditions.

All theoretical investigations should use the DSX parameters and settings as a target model. Any predictions learned should contribute to the developments of the next generation of systems as outlined in item 4 in the introduction which we proposed to study but could not carry out because of the lack of funding.

In addition to theoretical investigations, the most important tasks bearing on the UML team is the data analyses and interpretations. We need to incorporate the knowledge we gained from theories and simulations into the data analyses. We need to anticipate the more complicated effects that may affect our measurements and interpretations. Before the launch of the DSX, we can analyze the results from the several tests conducted on the ground.

REFERENCES

- Abel, B. and R. M. Thorne, Electron scattering loss in the Earth's inner magnetosphere: 1. Dominant physical processes, *J. Geophys. Res.*, **103**, 2385, 1998a.
- Abel, B. and R. M. Thorne, Electron scattering loss in the Earth's inner magnetosphere: 2. Sensitivity to model parameters, *J. Geophys. Res.*, **103**, 2397, 1998b.
- Benson, R. F., P. A. Webb, J. L. Green, L. Garcia, and B. W. Reinisch, Magnetospheric electron densities inferred from upper-hybrid band emissions, *Geophys. Res. Lett.*, **31**(20), L20803, doi:10.1029/2004GL020847, 2004
- Bortnik, J., U. S. Inan, and T. F. Bell, Frequency-time spectra of magnetospherically reflecting whistlers in the plasmasphere, *J. Geophys. Res.*, **108**(A1), 1030, doi:10.1029/2002JA009387, 2003.
- Budden, K.G., The propagation of radio waves. The theory of radio waves of low power in the ionosphere and magnetosphere. Cambridge University Press, Cambridge- New York, 1985
- Burch, J.L. et al., Views of Earth's magnetosphere with the IMAGE satellite, *Science*, **291**, 541, 2001.
- Clilverd, M. A., C. J. Rodger, R. Gamble, N. P. Meredith, M. Parrot, J.-J. Berthelier, and N. R. Thomson (2008), Groundbased transmitter signals observed from space: Ducted or nonducted?, *J. Geophys. Res.*, **113**, A04211, doi:10.1029/2007JA012602
- Davies, K., Ionospheric Radio. IEE Electromagnetic Waves Series 31. Peter Peregrinus Ltd., London, 1990.
- Galkin, I., B. W. Reinisch, G. Grinstein, G. Khmyrov, A. Kozlov, X. Huang, and S. F. Fung, Automated exploration of the radio plasma imager data, *J. Geophys. Res.*, **109**(A12), A12210, doi:10.1029/2004JA010439, 2004
- Ginzburg, V.L., Propagation of Electromagnetic Waves in Plasma, Nauka, Moscow, 1967.
- Green, J. L., S. Boardsen, L. Garcia, W. W. L. Taylor, S. F. Fung, and B. W. Reinisch, On the origin of whistler mode radiation in the plasmasphere, *J. Geophys. Res.*, **110**, A03201, doi:10.1029/2004JA010495, 2005.
- Helliwell, R. A., Whistlers and Related Ionospheric Phenomena, Stanford Univ. Press, Stanford, California, 1965.
- Lyons, L. R., R. M. Thorne, and C. F. Kennel, Pitch-angle diffusion of radiation belt electrons within the plasmasphere. *J. Geophys. Res.*, **77**, 3455 – 3474, 1972
- Lyons, L. R., R. M. Thorne, and C. F. Kennel, Electron pitch-angle diffusion driven by oblique whistler-mode turbulence., *J. Plasma Phys.*, **6**, 589 – 606, 1971
- Reinisch, B.W. et al., The radio plasma imager investigation on the IMAGE spacecraft, *Space Sci. Rev.*, **91**, 319, 2000
- Reinisch, B.W. et al., First results from the radio plasma imager in IMAGE, *Geophys. Res. Lett.*, **28**, 1167, 2001.
- Shkarofsky, I. P. (1972), Nonlinear sheath admittance, currents, and charges associated with high peak voltage drive on a VLF/ELF dipole antenna moving in the ionosphere, *Radio Sci.*, **7**, 503–523.
- Song, P., B. W. Reinisch, V. > Paznukhov, G. Sales, D. Cooke, J.-N. Tu, X. Huang, K. Bibl, and I. Galkin (2007), High voltage antenna–plasma interaction in whistler > wave transmission: Plasma sheath effects, *J. Geophys. Res.*, **112**(A3), A03205, doi:10.1029/2006JA011683.

- Starks, M. J., R. A. Quinn, G. P. Ginet, J. M. Albert, G. S. Sales, B. W. Reinisch, and P. Song, Illumination of the plasmasphere by terrestrial very low frequency transmitters: Model validation, *J. Geophys. Res.*, **113**, A09320, doi:10.1029/2008JA013112, 2008.
- Thomson, N. R., Ray-tracing the paths of very low latitude whistler-mode signals, *J. Atmos. Terr. Phys.*, **49**, 321– 338, doi:10.1016/0021-9169(87)90028-6, 1987.
- Tu, J., Paul Song, and Bodo W. Reinisch, Plasma sheath structures around a radio frequency Antenna, *J. Geophys. Res.*, **113**, A07223, doi:10.1029/2008JA013097, 2008

APPENDIX A

High Voltage Antenna-plasma Interaction in Whistler Wave Transmission: Plasma Sheath Effects

P. Song, B. W. Reinisch, V. Paznukhov, G. Sales, D. Cooke, J.-N. Tu, X.Huang, K. Bibl, and I. Galkin

(see reprint attached)

High-voltage antenna-plasma interaction in whistler wave transmission: Plasma sheath effects

P. Song,^{1,2} B. W. Reinisch,^{1,2} V. Paznukhov,² G. Sales,² D. Cooke,³ J.-N. Tu,² X. Huang,² K. Bibl,² and I. Galkin²

Received 20 February 2006; revised 5 October 2006; accepted 30 October 2006; published 17 March 2007.

[1] We study the plasma sheath surrounding an antenna that transmits whistler mode waves in the inner magnetosphere in order to investigate the feasibility of conducting controlled experiments on the role of wave-particle interactions in the pitch angle diffusion of relativistic radiation belt electrons. We propose a model for an electrically short antenna-sheath-plasma system with transmission frequencies below the electron characteristic frequencies and much higher than the ion characteristic frequencies. The ion current is neglected. We analytically solve a time-dependent one-dimensional situation by neglecting the effects of the wave's magnetic field. In our model, the antenna is charged to a large negative potential during a steady transmission. Positive charge occurs in the sheath and the sheath is free of electrons and conduction current. The net charge on the antenna and in the sheath is zero. The volume, or the radius in a cylindrical case, of the sheath varies in response to the charge/voltage variation on the antenna. The oscillating radius of the sheath translates to a current in the plasma, which radiates waves into the plasma. A whistler wave transmission experiment conducted by the RPI-IMAGE has shown that the model may describe the most important physical processes occurring in the system. The system response is predominately reactive, showing no evidence for significant sheath current or sheath resistance. The negligibly small sheath conduction electron current can be understood if the antenna is charged to a substantial negative potential, as described by the model. Quantitatively, the model may underestimate the sheath capacitance by about 20%.

Citation: Song, P., B. W. Reinisch, V. Paznukhov, G. Sales, D. Cooke, J.-N. Tu, X. Huang, K. Bibl, and I. Galkin (2007), High-voltage antenna-plasma interaction in whistler wave transmission: Plasma sheath effects, *J. Geophys. Res.*, *112*, A03205, doi:10.1029/2006JA011683.

1. Introduction

[2] With the increasing use of spaceborne technologies, we are becoming more and more vulnerable to space weather phenomena, among which the extremely energetic electrons in the radiation belt are a major threat [e.g., Song *et al.*, 2001]. These particles are trapped in the radiation belts with lifetimes as long as a few years, posing long-lasting threats to space-borne technologies and humans in space. Pitch angle diffusion by the wave-particle interaction is a mechanism that systematically reduces the pitch angles of the particles so that they precipitate into the atmosphere along the magnetic field lines. Theoretical investigations have shown that whistler mode waves are very efficient in pitch angle diffusion and are considered a primary candidate

to reduce the relativistic electrons in the radiation belts [Kennel and Petschek, 1966; Lyons *et al.*, 1972; Abel and Thorne, 1998a, 1998b; Albert *et al.*, 2001; Inan *et al.*, 2003; James, 2003]. Placing a transmitter in the radiation belt to transmit whistler mode waves may be among the most direct approaches to determine the wave particle interaction.

[3] For spaceborne transmission, different from vacuum conditions, the antenna is submerged in the surrounding plasma, which is electrically highly conductive because of the low collision rate among particles in space. Here we are concerned with the case in which the plasma will allow the whistler mode to propagate. The whistler mode frequencies lie between the electron gyrofrequency and the lower-hybrid frequency when the electron plasma frequency is higher than the electron gyrofrequency [e.g., Kivelson and Russell, 1995]. When the antenna transmits, the two branches of a dipole antenna, if electrically insulated from the surrounding plasma, are charged alternately with equal but opposite voltages, forming an electric field surrounding the antenna from one branch to the other and in the surrounding space. The charged particles move in response to the electric field; the electrons are attracted to the positively charged branch of the antenna and the ions to the negatively charged

¹Environmental, Earth, and Atmospheric Sciences Department, University of Massachusetts, Lowell, Massachusetts, USA.

²Center for Atmospheric Research, University of Massachusetts, Lowell, Massachusetts, USA.

³Air Force Research Laboratory, Space Vehicles Directorate, Hanscom Air Force Base, Massachusetts, USA.

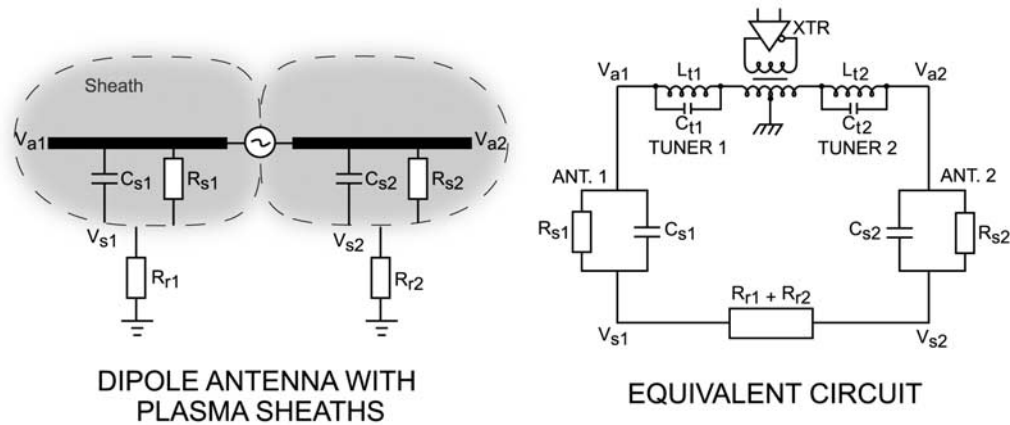


Figure 1. A transmitter-antenna-sheath-plasma system (left) and its equivalent circuit (right). In the right panel, the transmitter is expanded to include a transmitter source and a couple of tuners, the function of which is discussed in section 4. R_r is the radiation resistance, C_s and R_s are the sheath capacitance and resistance, and V_a and V_s are voltages at the antenna and at the boundary between the sheath and plasma, respectively. Note that only the circuit current, the antenna voltage V_a , and the voltage at the transmitter source (before tuner) can be measured.

branch. Furthermore, the transmission current, which flows along the antenna, generates a magnetic field. The magnetic field in turn affects the motion of the charged particles. The theories of whistler mode wave transmission in plasma can be found in numerous studies [e.g., *Arbel and Felsen*, 1963; *Balmain*, 1964; *Wang and Bell*, 1972]. Nonetheless, these theories treated regions far from the antenna.

[4] For whistler mode transmission, a substantial space-charge sheath will form around the antenna because of the different speeds with which the ions and electrons respond to the varying electric field. The quasi-neutrality approximation used in plasma theory, such as in VLF wave radiation and propagation, is no longer valid in the sheath. Figure 1 illustrates such a transmitter-antenna-sheath-plasma system and its equivalent circuit, assuming that the transmitter drives the antennas through a transformer. In the right panel, the equivalent circuit, the transmitter is expanded to a transmitter source and a couple of tuners. The tuners are not important for the discussion of the physical processes of the sheath, but they are important for transmission experiments that will be discussed in section 4. The sheath confines the electric field and functions as a shield that hinders the electromagnetic field from being transmitted. In a steady transmission, this shielding leaves only displacement currents, a small sheath leakage (conduction) current, and the magnetic component to couple to the plasma. Quantitative understanding of the sheath processes and the controlling factors is crucial to the design of a space-borne whistler wave transmitter.

[5] With a bare antenna that is not insulated from the surrounding plasma, two important processes take place: conduction currents flowing in and out of the antenna and electric charging of the antenna. Most existing theories treat a single conductor [e.g., *Laframboise and Parker*, 1973]. A transmission antenna has an active internal driver. During transmission, the positive branch collects electrons and the negative branch collects ions. Owing to the difference in ion and electron masses, electrons move faster and carry more currents than ions. The evolving DC negative antenna potential, which reduces the electron current while increas-

ing the ion current, maintains overall charge conservation. If the two branches of the antenna are DC connected, they will share the same DC voltage. Their DC voltages can be different if they are not DC connected and are made of different materials. In our discussion below, we assume the two branches are made of the same material of high electric conductivity and are DC connected as shown in Figure 1. In a highly simplified picture, the current balance between identical positive and negative elements will be achieved at a voltage ratio of $-(m_e/m_i)^{1/2}$, for a two-branch antenna system at the peak of a wave cycle. In this case, the DC negative voltage thus can be close to the amplitude of the AC voltage. The real situation can involve other effects, such as charge collection by the spacecraft body, transition to a spherical sheath at high voltage, overlapping-sheaths, and electron emission by the negative branch due to secondary and photoelectrons, but the average or common potential is still overwhelmingly negative. The antenna-driving current now couples to the plasma through both conducted particle currents and a displacement or reactive current through the sheath capacitance. For simplicity of language we identify this reactive current with radiation into the whistler modes, while recognizing that there still remains a formidable problem to quantify the partition of the reactive current into radiating and dissipating components beyond the sheath. The electric charging of the antenna substantially changes the processes surrounding the antenna, the electrical characteristics of the antenna, and the satellite environment. Therefore to understand antenna charging is extremely important for antenna and satellite-system designs. A precise determination of the common potential requires a three-dimensional numerical analysis (e.g., *Mandel*, private communication, 2002, for electrostatic cases).

[6] Our present theoretical understanding of the plasma sheath processes for whistler mode transmission is built upon earlier work by *Mlodnosky and Garriott* [1962], *Despain* [1966], *Miller* [1967], *Grard and Tunaley* [1968], *Johnston* [1969], and especially that of *Shkarofsky* [1972]. *Shkarofsky* used the *Langmuir and Mott-Smith*

[1924] method to calculate the electric potential surrounding a one-dimensional static high-voltage antenna. In his model, particles are accelerated by the electric field, and particle motions produce currents. From the relationship between the current and voltage, the sheath capacitance and resistance are derived. *Oliver et al.* [1970] conducted some experiments and found substantial differences between the experiments and theory.

[7] The physical processes we will describe are fundamentally different from the previous models. Most of these models are electrostatic in which the electric field is treated as constant. In a time dependent process, such as a wave, a model not only has to describe an instant but also the very next moment in a continuous manner. To illustrate the inadequacy of a static model, let us consider the moment of maximum voltage at the antenna when all electrons in the sheath are collected by the positively charged antenna branch. In the next moment when the branch voltage is still positive but decreases and the sheath radius decreases, there are no more electrons in the sheath available for the antenna to collect any current. This is an inconsistency in a static model where the time dependence is not self-consistently included in the model because it still predicts a large current. Our model also treats the boundary conditions at the antenna surface to allow surface charging. Most importantly, our model describes a completely different physical process for the radiation current. For simplicity, in our model the ion density is approximated as frozen at the ambient density, allowing for only a small ion current to still be conducted. This particular situation allows the formation of well-defined plasma sheaths, which in our model can be treated by analytic methods and electrically approximated with a lumped circuit model as illustrated in Figure 1.

[8] In section 2 of this paper, we outline the general treatment and boundary conditions for such an antenna-plasma system. Since it is nearly impossible to solve the equation set analytically in three-dimensions, we solve the time-depend equation set in one-dimension in section 3 by neglecting the effects of the magnetic field and ions, but including antenna charge and radiation load which were not included in previous models. In section 4, we present the results from a space transmission experiment and compare them with theory.

2. General Treatment and Physical Model

2.1. Governing Equations

[9] There are three domains in the antenna-plasma system: the antenna, the sheath, and the plasma. The governing equations are different in the three domains. The solutions for each domain depend on the boundary conditions with its neighboring domains. This dependence is important because the solutions in the plasma, when calculating radiation for example, depend on the current at the sheath boundary and not the currents at the antenna surface. Between the sheath and plasma, a transition called presheath is often discussed in the literature, but for our purpose, we assume that the transition between the two domains is sharp, of the order of an electron gyroradius.

[10] Different from previous works, we take a first-principles approach, starting with Maxwell's equations

and the momentum equation of electrons, neglecting the ion motion,

$$m_e d\mathbf{u}_e/dt = -e(\mathbf{E} + \mathbf{u}_e \times \mathbf{B}), \quad (1)$$

where m_e , e , \mathbf{u}_e , \mathbf{E} , and \mathbf{B} are electron mass, elementary electric charge, the electron velocity, and the electric and magnetic fields, respectively. We assume that the current is carried by electrons and neglect the thermal motion of the electrons. Note that the momentum equation describes the motion of the particles in the plasma or sheath but not on the antenna. Because the spatial scale of the sheath is limited, electrons in the regions far from the sheath-plasma boundary in the sheath would hit the antenna or be pushed out of the sheath in no time. The electron momentum equation describes the motion of an electron for only a small fraction of the time of interest, during which ions are barely moved.

[11] The electric scalar potential Φ and the magnetic vector potential \mathbf{A} , from Maxwell's equations and the Coulomb gauge, satisfy

$$\begin{aligned} \nabla^2 \Phi &= e(N - N_0)/\varepsilon_0 \\ \nabla^2 \mathbf{A} - \varepsilon_0 \mu_0 \frac{\partial^2 \mathbf{A}}{\partial t^2} - \varepsilon_0 \mu_0 \frac{\partial \nabla \Phi}{\partial t} &= -\mu_0 \mathbf{J}, \end{aligned} \quad (2)$$

where N_0 , N , \mathbf{J} , ε_0 , and μ_0 , are the number density of the ion or background plasma number density, electron density, electric current, dielectric constant, and magnetic permeability in vacuum. We have assumed that ions are singly charged. The electric charge conservation equation can be obtained from the combination of Ampere's law and Poisson's equation and is

$$\partial \rho_q / \partial t + \nabla \cdot \mathbf{J} = 0, \quad (3)$$

where $\rho_q = e(N_0 - N)$ is the net electric charge density.

2.2. Boundary Conditions at the Antenna Surface

[12] The boundary conditions at the antenna surface are crucial to describe the antenna charging and have not been treated in previous models [e.g., *Shkarofsky*, 1972]. Inside the antenna, both the electric and magnetic fields are zero if one assumes that the antenna is perfectly conducting. The current flows and electric charges occur on the surface of the antenna. At the antenna surface, the boundary conditions are

$$\begin{aligned} E_{na^+} - E_{na^-} &= E_{na^+} = \sigma_a / \varepsilon_0 \\ \mathbf{E}_{Ta^+} &= \mathbf{E}_{Ta^-} = 0 \\ B_{na^+} &= B_{na^-} = 0 \\ \mathbf{B}_{Ta^+} - \mathbf{B}_{Ta^-} &= \mathbf{B}_{Ta^+} = \mu_0 \alpha_a \times \mathbf{n}, \end{aligned} \quad (4)$$

where subscripts T and n denote the components tangential and normal to the antenna surface, the plus and minus signs denote values on the sheath and antenna sides of the boundary, respectively, σ_a is the surface charge density on the antenna, and vectors \mathbf{n} and α_a are the normal direction of the antenna surface and the surface current density on the antenna, respectively.

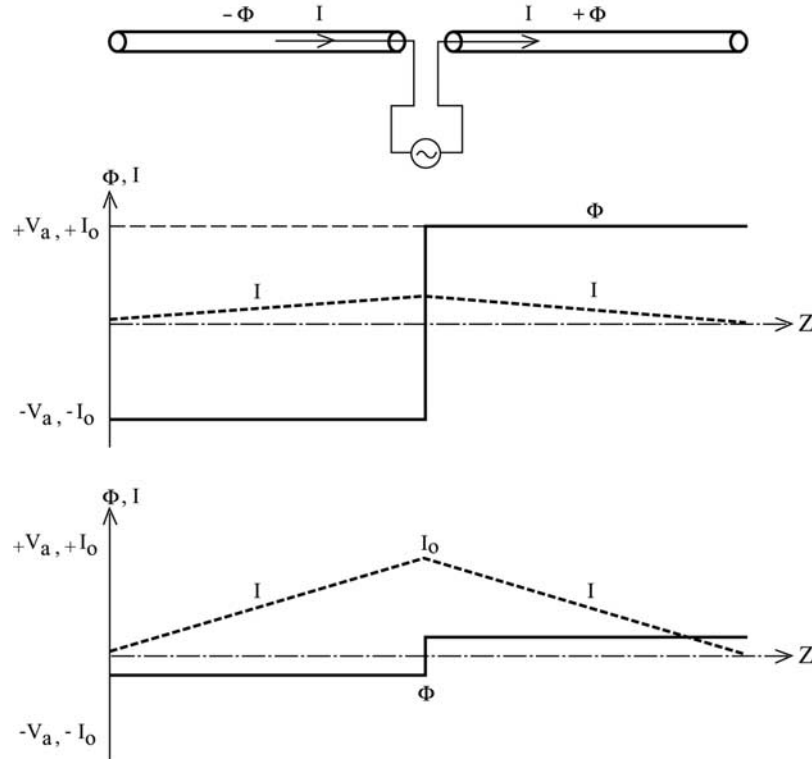


Figure 2. Temporal and spatial variations of the voltage and current on the antenna. Top panel shows the transmitter and antenna system. The transmitter, which includes the driving source and the tuners, drives a current into the antenna. The two lower panels show the current (thick dashed lines) and voltage (thick solid lines) at different times as functions of z along the antenna.

[13] For an antenna that is much shorter than the wavelength and is driven by a sinusoidal voltage oscillation of amplitude V_0 , the antenna voltage is

$$V_a(z, t) = \text{sgn}(z) V_0 e^{j\omega t} + V_{a0}, \quad (5)$$

where V_{a0} is the DC floating voltage of the antenna, noting that each branch of the antenna is at equipotential. In the following discussion, for convenience, we discuss the positive branch of the antenna and drop the sign function in (5). For a short antenna, the antenna current, flowing on the surface of the antenna, can be approximated as linearly decreasing toward the tips of the antenna, when the end effects are neglected, or

$$I_a(z, t) = I_0(1 - |z|/l)e^{j(\omega t - \delta)}, \quad -l < z < l, \quad (6)$$

where l is the antenna half-length. There is a phase shift δ between the current and the voltage when the circuit is not purely resistive. Figure 2 illustrates the temporal and spatial relations. The top panel shows a dipole antenna at the potentials $\pm\phi$ and the resulting current, which is approximately 90° out of phase with the potential when the antenna is predominately reactive. The middle panel shows the voltage and current as functions of distance from the center along the antenna at $t = 0$, assuming zero DC electric current. The lower panel shows the situation at a later time when the current peaks.

[14] At the antenna, for either an insulated surface or a bare-metal conducting surface in steady state transmission, the radial component of the electric current is negligible, as

discussed later for a thin antenna. Assuming azimuthal symmetry, integrating the charge conservation equation (3) over the cross section of the antenna yields

$$I_0 e^{j(\omega t - \delta)} = 2\pi r_a l \frac{\partial \sigma_a}{\partial t} = j\omega 2\pi r_a l \sigma_{ai}, \quad (7)$$

where r_a is the radius of the antenna and $\sigma_a = \sigma_0 + \sigma_{ai}$. Here σ_0 and σ_{ai} are the DC and AC components, respectively. The DC component is associated with the antenna charging and the AC component due to the driving current. The AC charge is uniformly distributed on the surface and varies $\sim 90^\circ$ out of phase with the driving current and an amplitude of $I_0/2\pi r_a \omega l$. The cylindrical components of the electric field immediately outside of the antenna are

$$\begin{aligned} E_{ra^+} &= \frac{\sigma_0}{\epsilon_0} + \frac{I_0 e^{j(\omega t - \delta)}}{j\omega \epsilon_0 2\pi r_a l} \\ E_{\phi a^+} &= 0 \\ E_{za^+} &= 0. \end{aligned} \quad (8)$$

The electric field is uniform along z when the end effects are neglected. Integrating the z -component of Ampere's law over the cross section of the antenna yields, noting from (8) that E_{za^+} is zero,

$$\begin{aligned} B_{ra^+} &= 0 \\ B_{\phi a^+} &= \frac{\mu_0}{2\pi r_a} I_a = \frac{\mu_0}{2\pi r_a} I_0(1 - |z|/l)e^{j(\omega t - \delta)}, \quad -l < z < l \\ B_{za^+} &= 0. \end{aligned} \quad (9)$$

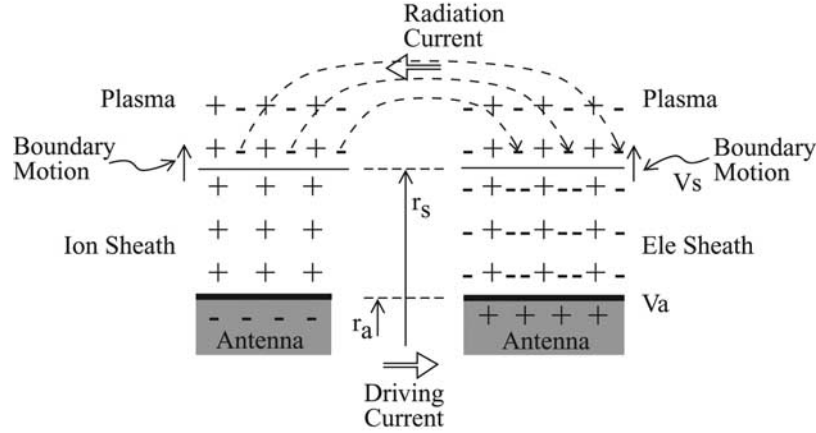


Figure 3. Physical processes in the plasma sheath surrounding an (insulated) antenna. The antenna is in a process with increasingly positive (negative) voltage on the positive (negative) branch. Dashed lines with arrowheads indicate the electron motion at a moment when the boundary between the plasma and the sheath moves up. The direction of the electric current is indicated by open arrowheads. For illustration purposes, we have made the two sheaths symmetric. In fact, the electron sheath is thinner than the ion sheath.

2.3. Electric Charging of a Bare Antenna

[15] Before we discuss the processes around a bare antenna, it is instructive to first examine the processes occurring around a perfectly insulated antenna that has no DC connection to the spacecraft body. For such antenna, because there is no conduction current flowing into the antenna from the sheath, the electrons that are pushed out from the ion-sheath side form the electron sheath on the other side (Figure 3). The temporal variation of the antenna surface charge translates into the variation of the thickness of the sheath. The electron motion in the plasma, not in the sheath, associated with the motion of the boundary produces a current in the plasma. This current corresponds to the radiation current of the antenna in a free-space setting. Since, from equation (7), the surface charge has a 90° phase shift from the driving current, the phase shift between the antenna voltage and the driving current, δ , is nearly 90° when the radiation resistance is small compared to the sheath reactance. In this case, the sheath functions in the same way as a capacitor: the two branches of the antenna are the two plates of a capacitor. The difference from a common capacitor is that the distance between the plates varies in time. The current coupled through the sheath can be interpreted as a displacement current.

[16] For a bare antenna, on the other hand, the processes near the antenna surface are different. In the first few wave cycles, there are two processes taking place: current exchange between the sheath and antenna, and electric charging of the antenna associated with the electrons that flow into or stay on the surface of the antenna.

[17] On the positively charged side, electrons are accelerated by the electric field and hit the antenna surface in no time and are stopped. The kinetic energy of the electrons is converted into thermal energy and heats the antenna. The electron sheath does not occur, given that the acceleration time for the electrons hitting the antenna is much shorter than a wave cycle. As the electrons flow into the antenna, the charge on the positively charged side is reduced. In the next half wave cycle when the voltage of the branch is

negative, if photoelectron emissions are absent, the electrons will not leave the antenna and reemit into space [e.g., Garrett, 1985], if we neglect the possibility of ion collection from the sheath. The whole antenna becomes negatively charged with a DC voltage V_{a0} . The negative charging of the antenna enlarges the size of the ion sheath.

[18] The charging process is expected to complete in a few wave cycles. The system then reaches an equilibrium at which the minimum thickness of the ion sheath during a wave cycle is close to zero. At the moment of the minimum thickness, we note that the antenna is charged with a negative DC voltage close to the amplitude of the AC voltage and that the AC antenna voltage is nearly 90° out of phase with the current; therefore the antenna has nearly zero output in power because the driving current is near zero when the AC voltage reaches its maximum. In the equilibrium state of the transmission, the conduction current in the sheath is near zero because the sheath is nearly free of electrons as discussed before. In reality, when ion motion is included, small leakage currents may exist and satisfy,

$$\int I_i dt + \int I_e dt = 0, \quad (10)$$

where I_i and I_e are ion and electron conduction currents, respectively. It will be discussed later that the DC current is negligible.

3. One-Dimensional Cylindrical Solutions

3.1. Weak Magnetic Field Approximation

[19] In a thin cylindrical antenna (neglecting end effects), the magnetic field produced by the driving current is in the azimuthal direction varying in phase with the current and its strength decreases toward the tips of the antenna as the current becomes weaker, e.g., see equation (9). In other words, when the magnetic field is included, the magnetic field coupling makes the system no longer one-dimensional (1-D). One may easily verify from the radial component of Ampere's law that this magnetic field spatial change is due to

the displacement current associated with the antenna surface charge, while the magnetic field itself is associated with the driving current. Therefore a weak magnetic field approximation is necessary for a 1-D model. In the following we examine the order of magnitude of the magnetic field effect in the momentum equation and in Maxwell's equations.

[20] For an antenna voltage of 10^3 V and the spatial scale of the sheath of $r \sim 10^0$ m, the electric field is of the order of 10^3 V/ 10^0 m $\sim 10^3$ V/m. Note that this is the electric field in the sheath and is not that in the plasma wave radiated into the plasma, which is much smaller. The electron velocity is of the order of the speed accelerated by the antenna voltage, or $u_e \sim 10^7$ m/s. The amplitude of the magnetic field in the sheath associated with the antenna current is of the order of $\mu_0 I_0 / 2\pi r \sim 10^{-7}$ T, assuming $I_0 \sim 10^0$ A. The magnetic field is therefore dominated by Earth's magnetic field, which is about 10^{-5} T depending on the altitude of the transmitter. The Coulomb force is about an order of magnitude larger than the $\mathbf{u}_e \times \mathbf{B}$ force. The effect of the wave's magnetic field in the momentum equation (1) can therefore be neglected in a zeroth-order treatment.

[21] The timescale of the acceleration of electrons is the electron plasma oscillation period when the electric field is the dominant term. An ion sheath becomes electron-free in a timescale of $r/u_e \sim 10^0/10^7 \sim 10^{-7}$ s. This is the timescale of the formation of the sheath, during which electrons are either pushed out of the sheath on one side or hit the antenna on the other side. In comparison, the period of the wave is 10^{-4} s. Essentially, there are no electrons in the ion sheath.

[22] For a transmission frequency of 10^4 Hz, the component of the electric field associated with the vector potential in (2) is of an order of 10^{-3} V/m, given the magnetic field generated by the antenna current $\mu_0 I_0 / 2\pi r \sim 10^{-7}$ T. If the component associated with the scalar potential is of the order of 10^3 V/m, the magnetic field term in Faraday's law can be neglected.

[23] For Ampere's law, the magnetic field spatial variations in the radial direction and along the antenna are of the order of $\sim 10^{-8 \sim 9}$ T/m. The current and displacement term are of the order of 10^{-8} T/m and 10^{-9} T/m, respectively. Therefore the magnetic field term cannot be simply neglected. However, from the divergence of Ampere's law, the magnetic field term vanishes and we obtain the charge conservation equation (3). In other words, different from an electrostatic model, we include Ampere's law in our treatment. The electric field is solved with the two equations in which the time independence is implicit. The time-dependent effects are incorporated from the antenna driving boundary conditions, the charge conservation, and, to some degree, the momentum equation when it is applied to the sheath-plasma boundary, which oscillates with the driving current/voltage.

3.2. Time-Dependent Solution for Charged Bare Antenna

[24] For a thin antenna, which will be discussed, of 0.2 mm in radius and 125 \sim 250 m long, the one-dimensional approximation is valid. The sheath potential equation becomes

$$\frac{1}{r} \frac{\partial}{\partial r} r \frac{\partial \Phi}{\partial r} = -\frac{eN_0}{\varepsilon_0}, \quad (r_a < r < r_s), \quad (11)$$

where r_s is the sheath radius. Note that the sheath is free of electrons, as we discussed in section 2 and the previous subsection. Also note that the equation applies only to the sheath region. A major issue for solving the problem is that the location of the sheath-plasma boundary is unknown and is a function of time. Outside of the sheath, the governing equation is different. How to determine the sheath-plasma boundary location will be discussed in section 3.3. The general solutions of the electric potential in the sheath are

$$\Phi = -\frac{eN_0}{\varepsilon_0} \left(\frac{r^2}{4} + C_1 \ln r \right) + C_2. \quad (12)$$

With the boundary conditions, (8),

$$\begin{aligned} \frac{\partial \Phi(r_{a+})}{\partial r} &= -\frac{\sigma_0}{\varepsilon_0} - \frac{I_0 e^{j(\omega t - \delta)}}{j\omega 2\pi r_a l \varepsilon_0} \\ \Phi(r_{a+}) &= V_a \end{aligned} \quad (13)$$

the electric potential is

$$\begin{aligned} \Phi(r) &= V_a - \frac{eN_0}{4\varepsilon_0} \left[r^2 - r_a^2 + \left(\frac{4\sigma_0 r_a}{eN_0} - j2a^2 e^{j(\omega t - \delta)} - 2r_a^2 \right) \right. \\ &\quad \left. \cdot \ln \left(\frac{r}{r_a} \right) \right], \end{aligned} \quad (14)$$

where $r_a < r < r_s$ and

$$a^2 = \frac{I_0}{\pi \omega l e N_0}. \quad (15)$$

For the DC component

$$\Phi_0(r) = V_{a0} - \frac{eN_0}{4\varepsilon_0} \left[r^2 - r_a^2 + \left(\frac{4\sigma_0 r_a}{eN_0} - 2r_a^2 \right) \ln \left(\frac{r}{r_a} \right) \right]. \quad (16)$$

The radius of the static sheath r_{s0} , at which the static voltage and static electric field go to zero, and the corresponding the surface charge and DC voltage of the antenna satisfy

$$\begin{aligned} V_{a0} &= \frac{eN_0}{4\varepsilon_0} \left[r_{s0}^2 - r_a^2 - 2r_{s0}^2 \ln \left(\frac{r_{s0}}{r_a} \right) \right] \\ r_{s0}^2 &= r_a^2 - \frac{2\sigma_0 r_a}{eN_0}. \end{aligned} \quad (17)$$

The first expression is the same as the static result derived by *Shkarofsky* [1972]. The relationship between the DC voltage and static sheath radius as functions of plasma frequency is given in Figure 4. When the voltage is higher, the static sheath is thicker. The sheath is thinner when the plasma density is higher. From the second expression, it is obvious that the surface charge σ_0 is negative. The second expression states the fact that the total positive charge within the sheath equals the total negative charge on the antenna surface. If the antenna is very thin and the current is strong, the potential in the regions far away from the antenna is

$$\begin{aligned} \Phi(r, z, t) &\approx \text{sgn}(z) V_0 e^{j\omega t} + V_{a0} - \frac{eN_0}{4\varepsilon_0} \left[r^2 \right. \\ &\quad \left. + \left(\frac{4\sigma_0 r_a}{eN_0} - j2a^2 e^{j(\omega t - \delta)} \right) \ln \left(\frac{r}{r_a} \right) \right], \end{aligned} \quad (18)$$

where $r_a \ll r < r_s$.

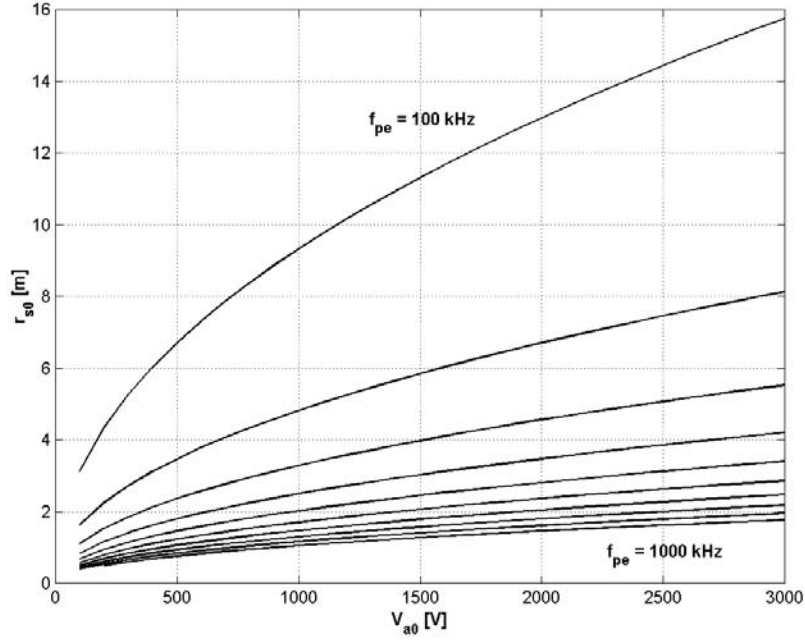


Figure 4. The relationship between the DC voltage and the static sheath radius as functions of plasma frequency. The antenna radius is assumed as 0.2 mm.

3.3. Sheath-Plasma Boundary Conditions

[25] Equation (14) gives the potential and thus the electric field throughout the sheath. It is also valid at the sheath-plasma boundary where the governing equation changes because of the presence of electrons in the plasma. However, since the location of the sheath is not defined yet, it does not specify the values at the boundary. In earlier models [e.g., *Shkarofsky*, 1972], the potential as well as electric field are taken to be zero at the sheath boundary. When there is radiation, both cannot be zero at the same time. Let us derive the boundary conditions at the sheath-plasma boundary.

[26] From the discussion above and Figure 3, the boundary is in constant motion, which translates to an electric current. Take a small column normal to and near the sheath-plasma boundary and let the boundary move from the bottomside of the column, r_s , to the topside, $r_s + dr_s$, in dt . The change in the total charge within the column during dt is $eN_0S dr_s$, where S is the cross section of the column. Since the height of the column dr_s is infinitely small, the current flows only normally to the sheath boundary. From the charge conservation (3), the current density flowing out of the column is

$$J_s = -eN_0 \frac{dr_s}{dt}. \quad (19)$$

The negative sign is due to the negative electron charge.

[27] Similarly, if taking a volume that coincides with the maximum size of the sheath of one branch of the antenna, the current flows into the volume along the antenna and out along the surface of r_{sm} , which is the maximum radius of the sheath. The current flowing into the surface equals that flowing out of it, according to Figure 1. It follows that while the sheath boundary oscillates within the volume, the net

total charge within the volume is determined according to (3). At the moment when the current is zero, the total net charge is zero; namely, the negative charge on the antenna surface equals the total ion charge in the sheath. This zero net-charge condition holds throughout a wave cycle and it is

$$2\pi r_a l \left(-\sigma_0 - \frac{I_0 e^{j(\omega t - \delta)}}{j\omega 2\pi r_a l} \right) = eN_0 l \pi (r_s^2 - r_a^2). \quad (20)$$

Combining (20) with (17) yields

$$r_s^2 = r_{s0}^2 + ja^2 e^{j(\omega t - \delta)}. \quad (21)$$

The sheath thickness is 90° out of phase with the current and, however, is not exactly in phase with the voltage when there is radiation resistance. The total current flowing from the sheath into the plasma equals the radiation current, and is, by combining (21), (19), and (15),

$$I_{rad} = I_s = \int_0^l 2\pi r_s J_s dz = I_0 e^{j(\omega t - \delta)}. \quad (22)$$

In other words, the radiation current equivalence to that defined in radiation theory without the plasma sheath is now the current associated with the sheath boundary motion and equals the total driving current. In 1-D and neglecting the end effects, the sheath current is uniformly distributed along the extent of the antenna instead of having a decreasing magnitude toward the tips as on the antenna surface, as specified in (6). Furthermore, it is normal instead of tangential to the surface for a thin antenna.

[28] The electric field at the boundary appears to be zero when combining (21) with the derivative of (14) with

respect to r . The electric potential at the sheath boundary is, however, not zero and is

$$V_s = \Phi(r_s) = V_a - \frac{eN_0}{4\epsilon_0} \left[r_s^2 - r_a^2 + \left(\frac{2\sigma_0 r_a}{eN_0} - ja^2 e^{j(\omega t - \delta)} - r_a^2 \right) \cdot \ln \left(\frac{r_s^2}{r_a^2} \right) \right] = V_0 e^{j\omega t} + \frac{eN_0}{4\epsilon_0} \left[-ja^2 e^{j(\omega t - \delta)} - r_{s0}^2 \ln \left(\frac{r_{s0}^2}{r_a^2} \right) + \left(r_{s0}^2 + ja^2 e^{j(\omega t - \delta)} \right) \ln \left(\frac{r_{s0}^2 + ja^2 e^{j(\omega t - \delta)}}{r_a^2} \right) \right]. \quad (23)$$

3.4. Sheath Reactance and Radiation Resistance

[29] In our circuit, Figure 1, neglecting the sheath loss, the AC voltages and current at a frequency ω satisfy

$$\begin{aligned} V_a - V_{a0} &= V_0 e^{j\omega t} = (R_r + jX_s) I_0 e^{j(\omega t - \delta)} \\ V_s &= V_{s0} e^{j(\omega t - \delta)} = R_r I_0 e^{j(\omega t - \delta)} \\ R_r + jX_s &= \sqrt{R_r^2 + X_s^2} e^{j\delta}, \end{aligned} \quad (24)$$

where $X_s = -1/\omega C$ and R_r are the reactance of the sheath and the radiation resistance of a branch, respectively. Separating the real and imaginary parts in (23) and combining with (24) yields

$$\begin{aligned} V_{s0} &= \frac{R_r}{\sqrt{R_r^2 + X_s^2}} V_0 = R_r I_0 \\ X_s &= -\frac{1}{2\pi\omega l \epsilon_0} \left[\ln \left(\frac{r_s}{r_a} \right) - \frac{1}{2} \right]. \end{aligned} \quad (25)$$

We have assumed that the temporal variation in the logarithm of the sheath radius affects only the amplitude and not the phase. When the sheath is much thicker than the antenna, the capacitance of the sheath is similar to that of a coaxial cable with a radius r_s . Since the radius of the cable in this case varies during a wave cycle, the capacitance of each branch varies with time. When the two branches are treated as a single system, the two capacitances vary out of phase and the total capacitance varies less dramatically.

[30] The radiation resistance of a branch of the antenna is

$$R_r^2 = \left(\frac{V_0}{I_0} \right)^2 - X_s^2. \quad (26)$$

The two branches of the antenna may not be the same in length. However, their DC voltages are the same as discussed earlier in the introduction, assuming that they are made of the same highly conducting materials. Since the amplitude of the sheath radius is a function of length, the sheaths may oscillate at different ranges for the two branches. For a fully charged antenna, the minimum of the sheath radius is limited by the antenna radius, or

$$r_{sm}^2 = r_{s0}^2 - a_m^2 \geq r_a^2, \quad (27)$$

where a_m is the amplitude of the shorter branch l_m . For the shorter (longer) branch, the equal (greater than) sign applies.

As the two sheath reactances are in series and vary both in time with a 180° phase difference, the average reactance is

$$\bar{X}_s = \frac{1}{T_w} \int_0^{T_w} (X_{s1} + X_{s2}) dt, \quad (28)$$

where $T_w = 1/f$ is the period of the wave. Combining with (28), (25), and (21), the total sheath reactance is

$$\bar{X}_s = -\frac{1}{\omega C} = -\frac{1}{4\pi\omega\epsilon_0} \left(\frac{1}{l_1} + \frac{1}{l_2} \right) \left[\ln \left(\frac{I_0}{\pi\omega l_m e N_0 r_a^2} + 2 \right) - 1 \right]. \quad (29)$$

4. Sheath Capacitance Measurements: Space-Borne VLF Transmission Experiment

[31] In order to verify the theoretical model, we conducted an experiment using the Radio Plasma Imager (RPI) [Reinisch *et al.*, 2000] on the IMAGE satellite [Burch *et al.*, 2001] operating in the inner magnetosphere. The RPI antenna is cylindrical and was made of copper. Its radius r_a is 0.2 mm and the two branches are 250 m and 125 m long, respectively. The RPI antennas share a common DC ground with the satellite. As the antenna is charged, the satellite will be charged to the same voltage. The RPI tuners consist of a combination of inductors and capacitors selected in a way that minimizes the relay switching requirements when the transmitter frequency varies over the frequency range from 3 to 200 kHz. The net reactance of the tuner is positive (inductive) to “tune out” the negative (capacitive) reactance of the antenna. The objective of the experiment was to measure the sheath impedance during whistler wave transmission by varying the tuner inductance and transmission frequency and looking for “tuned transmission,” during which the antenna current maximizes and, as a consequence, generates a voltage maximum at the antenna. Figure 5 shows the RMS antenna AC currents and voltages at the two antenna branches, +X and −X, for frequencies between 8 and 22 kHz during a 3-hour transmission period. The RPI design does not allow changing the tuner inductance without changing the frequency, so we were forced in our experiment to change the frequency. Each frequency was transmitted with a fixed inductance, and inductances at different frequencies may be different. Therefore unfortunately, the frequency and inductance effects are intertwined. In the experiment, RPI stepped through a set of inductances in 1.25 min, and repeated the procedure every 4 min. For each inductance (and frequency), more than 800 wave cycles were transmitted. If the antenna charging took a few wave cycles, the transient processes during charging contributed little to the measurements, which were therefore assumed to be made when the antenna was charged. Between two scans, regular sounding and dynamic spectra were made in order to determine the plasma conditions at the spacecraft location. The plasma frequency and electron gyrofrequency measured by local resonances [Reinisch *et al.*, 2001; Benson *et al.*, 2003] are given in Figure 6.

[32] Clear enhancements in the current and voltage amplitudes are seen at some frequencies (inductances) in Figure 5. As discussed before, the enhancements at these frequencies

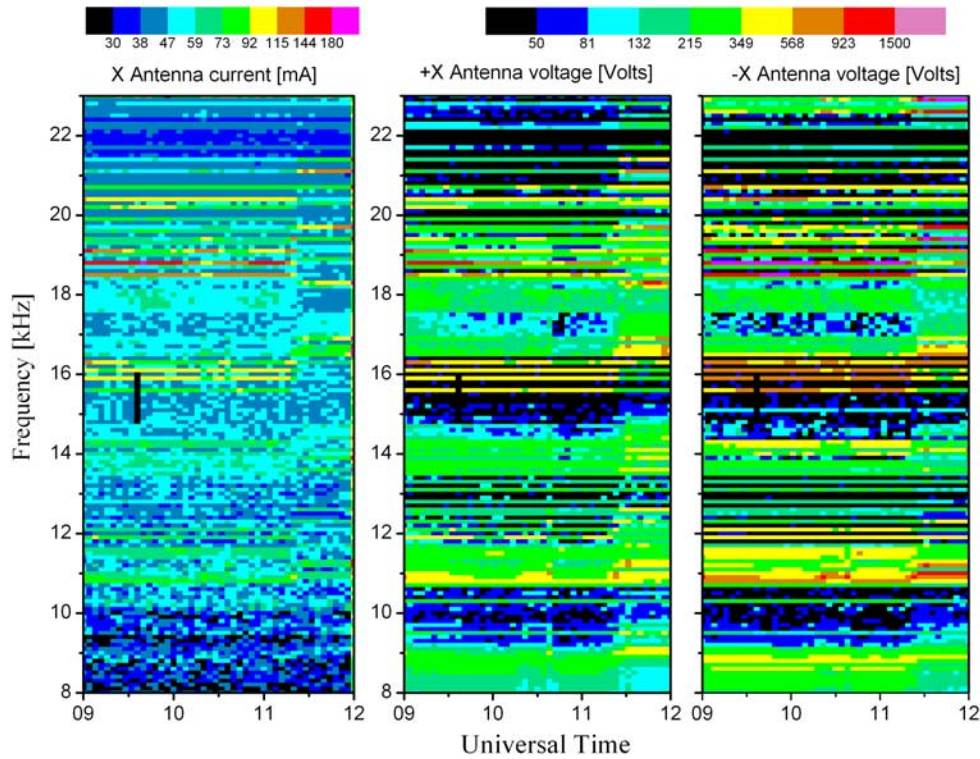


Figure 5. Current and voltages as functions of frequency (inductance) and time on the X-antenna, measured by RPI on 29 September 2004 during a whistler wave transmission experiment. The color-coding shows the RMS amplitude.

were the result of specific inductance/frequency combinations. In addition, the plasma conditions varied as the satellite moved from one region to another as shown in Figure 6. Between 0930 and 1130 UT the transmission frequencies satisfy the whistler mode condition. The analysis provided below separates the effects of the frequency and plasma density.

[33] RPI does not measure the phase between the current and voltage. The absolute values of the amplitudes are not precisely calibrated, but the relative variations are real. Nevertheless, since the sheath reactance depends only on

the logarithm of the current, the uncertainty in the absolute value of the current will not significantly affect the results of the analysis. When the antenna is correctly tuned, the maximum current into the antenna was measured as 0.2 A when the antenna voltage was close to 3 kV. If the sheath admittance were dominated by the sheath conductance ($1/R_s$ in Figure 1) and the susceptance were relatively small, i.e., if $\omega C_s \ll 1/R_s$, the antenna voltage and current would approximately be in phase and the power dissipation in the antenna close to 600 VA, split between R_s , the tuner resistance R_t , the radiation resistor with $R_t + R_r \ll R_s$.

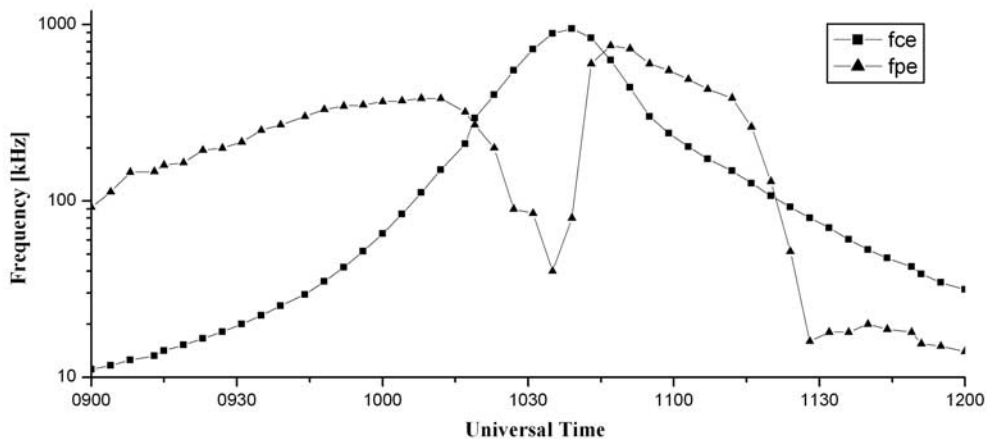


Figure 6. Plasma and electron gyro-frequencies measured by RPI on 29 September 2004.

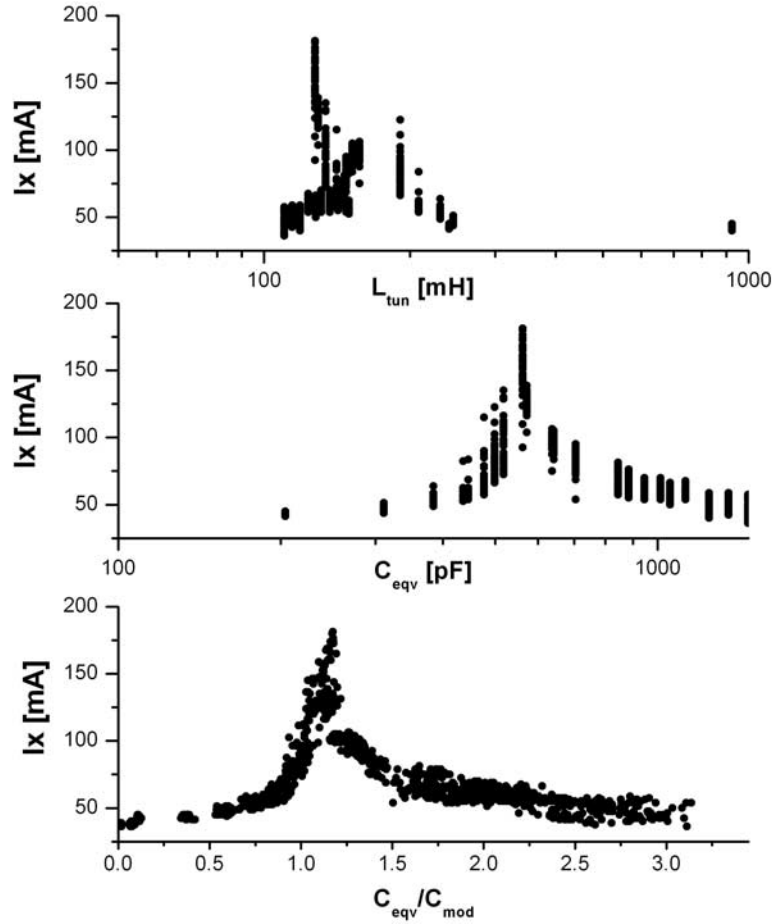


Figure 7. Current in the X-antenna as a function of the tuner inductance L_{tun} (top panel), equivalent capacitance $C_{\text{eqv}} = 1/\omega^2 L_{\text{tun}}$ (middle panel), and the normalized equivalent capacitance with respect to the model capacitance (lower panel).

However, the RPI transmitter supplies a maximum of 2 A at 50 V (Figure 1), i.e., 100 W of power. Therefore the current must be substantially out of phase with the voltage V_a on the antenna, leading to the conclusion that the antenna is highly reactive with a negligible current through the sheath conductance (sheath losses), or $1/\omega C_s \ll R_s + R_t + R_r$. It follows that the sheath reactance is around $3 \text{ kV}/0.2 \text{ A} = 15 \text{ k}\Omega$. At the frequency with maximum transmission, 19 kHz, the corresponding sheath capacitance is around 560 pF under the plasma condition when the maximum transmission occurred.

[34] One feature evident in Figure 5 is the positive correlation between the amplitudes of the antenna current and voltages as expected. The top panel of Figure 7 shows the current as a function of tuner inductance, L_{tun} , when each current value was measured. Each of the measurements satisfies the whistler mode condition; namely, the transmission frequency is less than both the local plasma and electron gyrofrequencies. Measurements with currents less than 0.05 A are not shown. Because there are only a limited number of inductances, there can be more than one measurement at each point on this plot. Similarly, since the transmission frequencies spread over a factor of 3, Figure 5, the currents at a single inductance correspond to several

frequencies, different by up to a factor 3. The antenna was “in tune” when maximum current amplitudes were measured. The in-tune condition occurs when $L_{\text{tun}}C = 1/\omega^2$, where C and ω are the (total) sheath capacitance and the transmission angular frequency, respectively. The upper panel shows a complicated dependence of the current as a function of inductance because several frequencies shared the same inductance and only some of them were tuned to the system. An equivalent capacitance C_{eqv} is defined according to the in-tune condition. It represents the sheath capacitance only at current peaks. When the current is weak, it has no real physical meaning. The middle panel of Figure 7 shows the current as a function of equivalent capacitance. Because $C_{\text{eqv}} = 1/L_{\text{tun}}\omega^2$, different frequencies that shared the same inductance are now separated. A clear concentration of the in-tune condition appears in a range of the equivalent capacitances.

[35] The lower panel of Figure 7 shows the equivalent capacitance normalized by the capacitance based on our model, equation (29). If the model were perfect, there would be a single sharp peak at 1.0 of normalized capacitance in the lower panel. The first feature observation to note is that the normalization narrows the peak. The width of the peak, say the width at 100 mA, divided by the center value is

about 100% in the inductance panel and 40% in the equivalent capacitance panels, but it narrows to 30% for the normalized capacitance. The narrowing of the width of the peak from the top panel to the middle panel indicates that the effects due to different frequencies are removed to a certain degree. The further narrowing in the bottom panel indicates that the model capacitance correctly describes the capacitance as a function of plasma density. Note that the relatively smaller improvement from the middle panel to the lower panel is a result of the logarithmic dependence of the sheath capacitance on the plasma density, as shown in (15) and (25). The peak of the normalized capacitance is at about 1.2, indicating the model may underestimate the capacitance or overestimate the reactance by about 20%.

[36] The above comparison is based on the assumptions that the antenna was charged to a negative voltage close to the amplitude of the AC voltage (-3 kV) and that there is no electron sheath. Under these conditions, the cold electrons cannot penetrate the sheath and reach the antenna; hence the current in the sheath is negligible, there is no significant sheath conductance in the equivalent circuit (Figure 1). If the antenna were not fully charged, electrons would be accelerated when they move toward the branch with positive voltage and form the sheath current. This high-speed particle stream would bombard the antenna surface and produce heat on the antenna surface as the kinetic energy becomes thermal energy. According to the bare but uncharged antenna surface model, the equivalent resistance, referred to as sheath resistance in parallel with the sheath capacitance, is of the same order as the sheath reactance. In the experiment, the in-tune antenna current is about 0.2 A and the source voltage is 100 V at the secondary of the transmitter output transformer (Figure 1). The total equivalent circuit resistance, including the tuner resistance, leakage current effects, and radiation resistance, is $500\ \Omega$. The inductor resistance is known to be $250\ \Omega$. If the radiation resistance is of the order of $200\ \Omega$ based on the formula of Balmain [1964], the radiated power was $I^2 R_r = 8$ W. When the antenna and the satellite are charged to -3 kV, the corresponding DC current associated with the ion motion attracted to the antenna and satellite is less than 2 mA (in parallel with the sheath capacitor and resistor, not shown in Figure 1), negligibly small compared with the transmission current. The approximation of neglecting the ion motion is therefore valid.

5. Summary and Discussion

[37] We have developed a first-principles-based model of the plasma sheath surrounding a bare antenna during whistler mode wave transmission. In this model, the antenna is negatively charged with a voltage similar to the amplitude of the driving voltage. An ion sheath is formed on each side of the antenna. The sheath is electron-free with little conduction current flowing through it. During a wave cycle, the radius of the sheath oscillates, translating to a current. This current is the current that radiates the wave into plasma. This picture is consistent with the displacement current of a capacitor. In addition to the DC electric charge to the bare antenna, the antenna charge also varies in time as the current decreases from the center to the tips. Differing from a conventional capacitor, for which the distance

between the two plates is fixed, there is only one physical plate, which in our case is the antenna surface. On the other side, one may imagine a leaky surface of the sheath-plasma boundary which may play a similar role as a capacitor. However, the location of this surface oscillates in response to the charge variation on the antenna. Positive charges occur in the sheath. The net charge on the antenna and in the sheath is zero. On the plasma side, conduction current forms and radiates the wave.

[38] Equations are solved time-dependently in one-dimension by neglecting the magnetic field. The mathematical treatment includes the antenna DC charge and the radiation resistance. At the sheath-plasma boundary the voltage and the electric field cannot be zero at the same time or there would be no radiation. The analysis shows that at the sheath boundary, the electric field is zero. The electrons at the boundary will continue to move. As they are moving, the electric field is modified and so are the motions. Accordingly, the boundary moves at a varying speed. This motion of the boundary or the electron speed at the boundary gives the current for radiation.

[39] A whistler wave transmission experiment with the RPI instrument on IMAGE has shown that the model may describe the most important physical processes occurring in the system. It shows no evidence for any significant sheath (conduction) current or sheath conductance because the system appears to be highly reactive. The antenna is most likely charged to a substantial negative potential. Quantitatively, the model may underestimate the sheath capacitance by about 20%, leaving room for improvements.

[40] **Acknowledgments.** We thank G. Cheney of UML for implementing the RPI experiment and L. Chen of UC Irvine for helpful discussion. This work was supported by AFRL under contracts F19628-02-C-0092 and FA8718-05-C-0070 and by NASA under subcontract 83822 from SWRI.

[41] Amitava Bhattacharjee thanks Paul Kellogg and Daniel Sheehan for their assistance in evaluating this paper.

References

- Abel, B., and R. M. Thorne (1998a), Electron scattering loss in the Earth's inner magnetosphere: 1. Dominant physical processes, *J. Geophys. Res.*, **103**, 2385.
- Abel, B., and R. M. Thorne (1998b), Electron scattering loss in the Earth's inner magnetosphere: 2. Sensitivity to model parameters, *J. Geophys. Res.*, **103**, 2397.
- Albert, J. M., D. H. Brautigam, R. V. Hilmer, and G. Ginet (2001), Dynamic radiation belt modeling at air force research laboratory, in *Space Weather, Geophys. Monogr. Ser.*, vol. 125, edited by P. Song, H. J. Singer, and G. L. Siscoe, p. 281, AGU, Washington, D. C.
- Arbel, E., and L. B. Felsen (1963), Theory of radiation from sources in anisotropic media part 1: General sources in stratified media, in *Symposium on Electromagnetic Theory and Antenna*, edited by E. C. Jordan, p. 421, Pergamon, New York.
- Balmain, K. G. (1964), The impedance of a short dipole antenna in a magnetoplasma, *IEEE, Trans Antennas Propag.*, **12**, 605.
- Benson, R. F., V. A. Osherovich, J. Fainberg, and B. W. Reinisch (2003), Classification of IMAGE/RPI-stimulated plasma resonances for the accurate determination of magnetospheric electron density and magnetic field values, *J. Geophys. Res.*, **108**(A5), 1207, doi:10.1029/2002JA009589.
- Burch, J. L., et al. (2001), Views of Earth's magnetosphere with the IMAGE satellite, *Science*, **291**, 541.
- Despain, A. M. (1966), Antenna impedance in the ionosphere, *Rep. 3, AFCRL-66-412*, Upper Air Res. Lab., Univ. of Utah, Salt Lake City, Utah.
- Garrett, H. B. (1985), The charging of spacecraft surfaces, in *Handbook of Geophysics and the Space Environment*, edited by A. S. Jursa, p. 1–7, Air Force Geophys. Lab., location?.

- Grard, R. J. L., and J. K. E. Tunaley (1968), The impedance of the electric dipole aerial on the FR-1 satellite, *Ann. Geophys.*, **24**, 1.
- Inan, U. S., T. F. Bell, J. Bortnik, and J. A. Albert (2003), Controlled precipitation of radiation belt electrons, *J. Geophys. Res.*, **108**(A5), 1186, doi:10.1029/2002JA009580.
- James, H. G. (2003), Electromagnetic whistler-mode radiation from a dipole in the ionosphere, *Radio Sci.*, **38**(1), 1009, doi:10.1029/2002RS002609.
- Johnston, T. W. (1969), The low-frequency nonlinear current voltage characteristic for long dipoles mounted on ionospheric satellites, in *A Study of the VLF/ELF Satellite*, Res. Rep., 7-801-80, RCA, Montreal.
- Kennel, C. F., and H. E. Petschek (1966), Limit on stably trapped particle fluxes, *J. Geophys. Res.*, **71**, 1.
- Kivelson, M. G., and C. T. Russell (1995), *Introduction to Space Physics*, 568 pp., Cambridge Univ. Press, New York.
- Laframboise, J. G., and L. W. Parker (1973), Probe design for orbit-limited current collection, *Phys. Fluids*, **16**, 629–636.
- Langmuir, I., and H. M. Mott-Smith (1924), Studies of electric discharges in gases at low pressure, *Gen. Elec. Rev.*, **27**, 449–455.
- Lyons, L. R., R. M. Thorne, and C. F. Kennel (1972), Pitch-angle diffusion of radiation belt electrons within the plasmasphere, *J. Geophys. Res.*, **77**, 3455.
- Miller, E. K. (1967), The admittance of an infinite cylindrical antenna in a lossy incompressible anisotropic plasma, *Can. J. Phys.*, **45**, 4019–4038.
- Mlodnosky, R. F., and O. K. Garriott (1962), The v.l.f. admittance of a dipole in lower ionosphere, paper presented at International Conference on the Ionosphere (London), Inst. of Phys. and Phys. Soc., Dorking, UK.
- Oliver, B. M., R. M. Clements, and P. R. Smy (1970), The rf floating double probe as a plasma diagnostic, *J. Appl. Phys.*, **41**, 2117.
- Reinisch, B. W., et al. (2000), The radio plasma imager investigation on the IMAGE spacecraft, *Space Sci. Rev.*, **91**, 319.
- Reinisch, B. W., et al. (2001), First results from the radio plasma imager in IMAGE, *Geophys. Res. Lett.*, **28**, 1167.
- Shkarofsky, I. P. (1972), Nonlinear sheath admittance, currents, and charges associated with high peak voltage driven on a VLF/ELF dipole antenna moving in the ionosphere, *Radio Sci.*, **7**, 503.
- Song, P., H. J. Singer, and G. L. Siscoe (Eds.) (2001), *Space Weather*, *Geophys. Monogr. Ser.*, vol. 125, AGU, Washington, D. C.
- Wang, T. N., and T. F. Bell (1972), VLF/ELF radiation patterns of arbitrarily oriented electric and magnetic dipoles in a cold lossless multicomponent magnetoplasma, *J. Geophys. Res.*, **77**, 1174.

K. Bibl, I. Galkin, X. Huang, V. Paznukhov, B. W. Reinisch, G. Sales, P. Song, and J.-N. Tu, Center for Atmospheric Research, University of Massachusetts, Lowell, 600 Suffolk Street, Lowell, MA 01854-3629, USA.
D. Cooke, Air Force Research Laboratory, Space Vehicles Directorate, 29 Randolph Road, Hanscom Air Force Base, MA 01731-3010, USA.

APPENDIX B

Plasma sheath structures around a radio frequency antenna

Jiannan Tu, Paul Song, and Bodo W. Reinisch

(see reprint attached)

Plasma sheath structures around a radio frequency antenna

Jiannan Tu,¹ Paul Song,^{1,2} and Bodo W. Reinisch^{1,2}

Received 14 February 2008; revised 4 April 2008; accepted 18 April 2008; published 31 July 2008.

[1] A one-dimensional particle-in-cell (PIC) simulation code is developed to investigate plasma sheath structures around a high-voltage transmitting antenna in the inner magnetosphere. We consider an electrically short dipole antenna assumed to be bare and perfectly conducting. The oscillation frequency of the antenna current is chosen to be well below the electron plasma frequency but higher than the ion plasma frequency. The magnetic field effects are neglected in the present simulations. Simulations are conducted for the cases without and with ion dynamics. In both cases, there is an initial period, about one-fourth of an oscillation cycle, of antenna charging because of attraction of electrons to the antenna and the formation of an ion plasma sheath around the antenna. With the ion dynamics neglected, the antenna is charged completely negatively so that no more electrons in the plasma can reach the antenna after the formation of the sheath. When the ion dynamics are included, the electrons impulsively impinge upon the antenna while the ions reach the antenna in a continuous manner. In such a case, the antenna charge density and electric field have a brief excursion of slightly positive values during which there is an electron sheath. The electron and ion currents collected by the antenna are weak and balance each other over each oscillation cycle. The sheath–plasma boundary is a transition layer with fine structures in electron density, charge density, and electric field distributions. The sheath radius oscillates at the antenna current frequency. The calculated antenna reactance is improved from the theoretical value by 10%, demonstrating the advantage of including the plasma sheath effects self-consistently using the PIC simulations. The sheath tends to shield the electric field from penetrating into the plasma. There is, however, leakage of an electric field component with significant amplitude into the plasma, implying the applicability of the high-voltage antennas in whistler wave transmission in the inner magnetosphere.

Citation: Tu, J., P. Song, and B. W. Reinisch (2008), Plasma sheath structures around a radio frequency antenna, *J. Geophys. Res.*, 113, A07223, doi:10.1029/2008JA013097.

1. Introduction

[2] When an actively transmitting antenna is immersed in a plasma, the particle distributions around the antenna are greatly disturbed because of the electromagnetic field excited by the antenna and/or the current collection by the antenna. In the presence of such antenna–plasma interaction several situations can arise. For a receiving antenna, there is a region of low electron density (ion plasma sheath) when the antenna is in an equilibrium plasma [e.g., *Morin and Balmain*, 1993] or a region of high electron density (electron plasma sheath) when there are photoelectron emissions from the antenna surface [e.g., *Tsutsui et al.*, 1997; *Zhao et al.*, 1996]. In the case of a VLF wave transmission antenna, there may be an ion sheath in the

vicinity of the antenna because of the large difference in the timescales of the ions and electrons with which the ions and electrons respond to the varying electromagnetic field transmitted by the antenna. The plasma sheaths act to modify the antenna impedance and thus change characteristics of the electromagnetic wave transmission from the antenna. This is particularly true when the antenna is driven by a high-voltage source so that the size of the sheath is large [*Shkarofsky*, 1972]. It is necessary to study the interactions between the high-voltage antenna and plasma because of the potential application of a high-voltage whistler wave transmitter in controlled precipitation of the radiation belt electrons [*Inan et al.*, 2003].

[3] In the past 50 years, extensive studies have been conducted to understand the impedance properties of the antennas in plasma, treating the plasma around the antennas as a medium with given constant dielectric tensor [e.g., *Balmain*, 1964; *Kuehl*, 1966; *Nakatani and Kuehl*, 1976; *Nikitin and Swenson*, 2001]. In a recent simulation study, *Ward et al.* [2005] developed a finite difference time domain (FDTD) model to investigate the impedance of a short

¹Center for Atmospheric Research, University of Massachusetts, Lowell, Massachusetts, USA.

²Environmental, Earth, and Atmospheric Sciences Department, University of Massachusetts, Lowell, Massachusetts, USA.

dipole antenna in a magnetized plasma. In the work of *Ward et al.* [2005] the plasma was treated as a multicomponent fluid with the electron density and velocity varying in response to the electromagnetic field excited by the transmitting antenna. Their study revealed that the antenna current distribution deviates significantly from the triangular distribution near the fundamental plasma frequencies. However, the sheath effects were not included due to the large and disparate temporal scale of the sheath compared to the upper hybrid oscillation period [*Ward et al.*, 2005].

[4] A number of early works have included the plasma sheath effects in investigations of the antenna impedance [e.g., *Mlodnosky and Garriott*, 1963; *Shkarofsky*, 1972; *Baker et al.*, 1973]. However, the physics of the antenna–plasma interaction, particularly in the case of the high-voltage antennas, has not been well understood. Thus the effects of the plasma sheath, represented by an additional impedance due to the sheath, were introduced based on predefined sheath models. Those sheath models are essentially electrostatic and are resulted from the boundary conditions that both electric field and potential are zero at the plasma sheath edge [e.g., *Riemann*, 1991 and references therein]. Such boundary conditions may not be valid in the case of transmitting antenna, especially for the case of a high-voltage source [*Song et al.*, 2007]. Adopting such predefined sheath models may be one of the reasons that the theoretical values of the sheath capacitance predicated by, e.g., *Shkarofsky* [1972], were an order of magnitude smaller than the measured ones, as revealed by the experiment–theory comparison made by *Oliver et al.* [1973].

[5] Recently *Song et al.* [2007] proposed an improved model to evaluate the impedance of a high-voltage antenna in the frequency range of whistler waves. In this new model, a bare metal antenna is assumed to be charged to a negative potential based on physical arguments. The plasma sheath (an ion sheath) is formed to satisfy the boundary conditions on the antenna surface, as well as at the plasma sheath boundary where the electric potential is not zero. It is also assumed that the sheath is free of electrons and conduction current when the transmission frequency is much higher than the ion characteristic frequencies but significantly below the electron characteristic frequencies. The sheath–plasma boundary is simply treated with a step function and is defined at the location within which the net charge on the antenna and in the sheath is zero. The radius of this boundary, or the sheath radius, varies in response to the oscillations of the charge/voltage on the antenna. The oscillating sheath radius translates to a current in the surrounding plasma, which radiates waves into the plasma. Compared to the whistler wave transmission experiment conducted using the radio plasma imager (RPI) instrument on the IMAGE satellite [*Reinisch et al.*, 2000], the model describes some important physical processes occurring in the high-voltage antenna–plasma interaction. The sheath capacitance predicted by *Song et al.* [2007] is about 20% lower than that from the RPI experiment, a significant improvement over the previous theoretical studies.

[6] The model by *Song et al.* [2007] treated only the steady-state transmission without self-consistent introduction of the plasma sheath formation and initial antenna charging process. More importantly, the ion dynamics are ignored by assuming a transmission frequency much higher

than the ion characteristic frequencies. The effects of the ion dynamics, however, may be substantial since the frequency of the whistler wave to be transmitted is likely not much higher than the ion characteristics frequencies. For instance, in the plasmasphere the electron gyrofrequency is significantly lower than the electron plasma frequency, leading to a condition in which the whistler wave frequencies are only few times of the ion plasma frequency.

[7] In this paper we for the first time use a particle-in-cell (PIC) simulation code to self-consistently investigate the antenna–plasma interactions for a high-voltage antenna in space plasma. The simulations allow detailed examination of the antenna charging processes and plasma sheath structures that are difficult to tackle analytically. In addition, the simulations can incorporate effects of the ion dynamics on the antenna charging and plasma sheath structures. The simulation results provide new insights to the physical processes occurring in the antenna–plasma interaction in the frequency range below the electron plasma frequency, especially for the case including the ion dynamics. We discuss the numerical simulation model in the next section and present the simulation results for the case without ion dynamics in section 3. The results from the simulation with ion dynamics included are presented in section 4. The final section gives a summary with discussions.

2. Simulation Model

2.1. Numerical Scheme

[8] In this study we consider an electrically short dipole antenna driven by a high-voltage source, as schematically displayed in Figure 1. We consider a cylindrical bare antenna that is perfectly conducting. The antenna is long compared to its thickness and the radial scale of the sheath. We use a cylindrical coordinate system (r, ϕ, z) that has its z axis coincide with the axis of the thin cylindrical antenna and the coordinate origin at the center of the dipole antenna as shown in Figure 1.

[9] As a first step toward developing a comprehensive kinetic simulation model for studying the antenna–plasma interaction, in the present study we adopt some approximations used by the theoretical analysis of *Song et al.* [2007]. These approximations include weak effects of the magnetic field compared to the electric field induced by the high-voltage source, cold plasma, and negligible end effects at the antenna tips. However, we do not predefine the electron density distribution surrounding the antenna during its time evolution, as *Song et al.* [2007] did, but allow the electron and ion density to vary in response to the electric field force that is self-consistently calculated. As a result, the plasma sheath will be self-consistently formed. We perform simulations with both immobile and mobile ions so that we can examine effects of the ion dynamics, which are excluded by the study of *Song et al.* [2007] study. *Song et al.* [2007] have argued that as long as the antenna is not extremely thin, say less than 0.01 m in radius, the magnetic field effects produced by the antenna driving current can be neglected in a zeroth-order treatment. This is because the magnetic force term in momentum equation and magnetic field term in Faraday’s law are much weaker than the corresponding electric field terms in the case of high-voltage antennas. Adopting this approximation means that

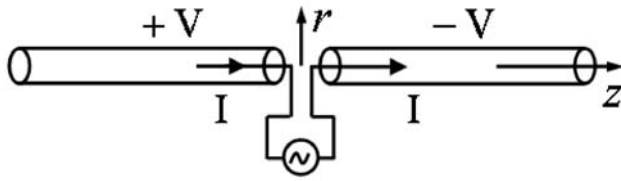


Figure 1. Schematic display of a short dipole antenna system. Arrows indicate the current at a time corresponding to the polarity of the antenna. The r and z axes of the cylindrical coordinates are shown.

we perform quasi-electrostatic simulations in the present study. Neglecting the end effects excludes the z component (in the antenna orientation) of the electric field, which may cause some errors. Nevertheless, this electric field component probably extends only in a distance comparable to the sheath size. Furthermore, the plasma thermal energy is much smaller than the kinetic energy once the charged particles are accelerated by the strong electric field of the transmission voltage, which justifies the cold plasma approximation.

[10] It should be pointed out that in the present simulations the background magnetic field is also excluded, making the plasma isotropic (unmagnetized). Therefore, at the frequency considered there will be actually no electromagnetic wave transmission from the antenna in a cold plasma. This means the present simulations cannot deal directly with the effects of the plasma sheath on the wave transmission. Nevertheless, such simulations can reveal the detail structures of the plasma sheath and provide insights to the physical processes occurring in the antenna–plasma interaction for the high-voltage antenna. The presence of a background magnetic field will alter the plasma sheath structures, e.g., the sheath may show some degrees of asymmetry with respect to the background magnetic field. The alteration of the plasma sheath by the background magnetic field, however, may be slight because the plasma sheath structures are predominantly controlled by the very strong electric field in the vicinity of the high-voltage antenna. Note that the situation we consider here is different from the spacecraft charging in which the electric field is weak and the effects of the geomagnetic field is significant [e.g., *Laframboise and Sonmor*, 1993].

[11] For an electrically short antenna the antenna current, driven by a voltage source and flowing on the antenna surface, can be approximated as a triangular distribution [e.g., *Balmain*, 1964].

$$I_A = I_0(1 - |z|/l)e^{j(\omega t + \delta)}, \quad -l \leq z \leq l \quad (1)$$

where l is the length of each branch of the antenna, ω is the angular frequency of the antenna current, and δ is the initial phase of the current relative to the driving voltage. This approximation is valid as long as the transmission frequency is not close to the fundamental plasma frequencies [*Ward et al.*, 2005]. The antenna current is the largest at the feeding point of the each branch of the antenna (neglecting the gap between two branches of the antenna) $z = 0$, and zero at the antenna tips $z = \pm l$. The charge on the antenna surface is uniformly distributed along the antenna according to the charge conservation for such a linear distribution of the

current. The electric field on the antenna surface is thus perpendicular to the antenna surface except at the antenna tips and in the gap between the feeding points of the two branches of the antenna. If the end effects at the antenna tips and in the gap of the two branches are neglected, all the physical parameters, except the antenna current, do not vary along the z coordinate. Plus the azimuthal symmetry, the problem to be solved becomes 1D. Neglecting the end effects is a crude approximation, particularly in the gap of the two antenna branches, and may be an important cause of the difference between theoretical value of the antenna capacitance by *Song et al.* [2007] and that from the RPI experiments.

[12] With above approximations adopted, the simulation model solves the time-dependent, 1D electric field through Gauss's law

$$\frac{\partial E_r}{\partial r} = \frac{\rho}{\epsilon_0} \quad (2)$$

where E_r is the component of the electric field perpendicular to z axis, ρ is charge density and ϵ_0 is vacuum permittivity. The electron and ion simulation particles (or super-particles), which represent a number of real electrons and ions, respectively [*Hockney and Eastwood*, 1988], are advanced through equations of motion, after neglecting the weak Lorentz force

$$\frac{d\gamma_s m_s v_s}{dt} = q_s E_r \quad (3)$$

where m_s is the mass of a simulation particle of species s in the rest frame, v_s and q_s are the velocity component in r direction and charge of the particle, respectively, $\gamma_s = 1/\sqrt{1 - (v_s/c)^2}$, and c is the speed of light in vacuum.

With symmetry about the z axis, the electric field has only an E_r component, and particles move only in the r direction when the magnetic field is neglected.

[13] The spatial domain is from r_0 to maximum radial distance r_m , where r_0 is the radius of a cylindrical antenna. The spatial domain is divided into m cells, and N_s pairs of simulation electrons and ions are initially loaded with a uniform number density n_0 . At each time step the charge density distribution ρ_j on the cell grids r_j ($j = 0, 1, 2, \dots, m$) is calculated with linear weighting. That is, for particles located in the cell $[r_j, r_{j+1}]$, the part of the charge assigned to grid j is given by [*Birdsall and Langdon*, 1983]

$$Q_j = \sum_{s,i} q_s \frac{r_{j+1}^2 - r_i^2}{r_{j+1}^2 - r_j^2} \quad (4)$$

and the part assigned to $j + 1$ is

$$Q_{j+1} = \sum_{s,i} q_s \frac{r_i^2 - r_j^2}{r_{j+1}^2 - r_j^2} \quad (5)$$

where r_i is the particle location, q_s is the charge of the particle in unit length along z axis, and summation is over

all species and all particles of each species in the cell. The electric fields on the grids are then calculated by integrating Gauss's law

$$2\pi r_{j+1}E_{j+1} - 2\pi r_jE_j = \frac{Q_j + Q_{j+1}}{2\epsilon_0} \quad (6)$$

where Q_j represents the charge (not charge density) in unit length along z axis assigned onto the grid j .

[14] The simulation particles represent a number of real particles [Hockney and Eastwood, 1988]. This number, referred to as the weight of the simulation particles, is determined by the number of simulation particles of each species, the size of the simulation spatial domain, number of cells, and the initial density of the species. At each time $t = n\Delta t$ (Δt is time step), the simulation particles are advanced using a leapfrog algorithm [Birdsall and Langdon, 1983]

$$(\gamma_s v_s)^{n+1/2} = (\gamma_s v_s)^{n-1/2} + \left(\frac{q_s E_{ri}}{m_s} \right)^n \Delta t \quad (7)$$

$$r_i^{n+1} = r_i^n + v_s^{n+1/2} \Delta t \quad (8)$$

where E_{ri} is the electric field acting on the particle at location r_i (within cell $[r_j, r_{j+1})$) at $t = n\Delta t$. The superscript n in equations (7) and (8) denotes values at n th time step, and $n + 1/2$ indicates at a half time step (between $n\Delta t$ and $(n + 1)\Delta t$). Since the electric fields, E_j , solved from equation (6), are located on the spatial grids, the electric field E_{ri} must be interpolated from E_j ($j = 0, 1, 2, \dots, m$). We apply the same linear weighting for charge assignment to calculate E_{ri} from the electric fields at r_j and r_{j+1} in order to conserve particles' momentum [Birdsall and Langdon, 1983; Hockney and Eastwood, 1988]. With the leapfrog algorithm, $(\gamma_s v_s)$ is advanced from $t = (n - 1/2) \Delta t$ to $t = (n + 1/2) \Delta t$, while the particle location r_i is advanced from $t = n\Delta t$ to $t = (n + 1) \Delta t$. Thus we need $(\gamma_s v_s)$ and velocity v_s at $t = - (1/2) \Delta t$, which are calculated by pushing $(\gamma_s v_s)$ and v_s at $t = 0$ back to $t = - (1/2) \Delta t$ using the electric field at $t = 0$ and initial (at $t = 0$) velocity v_s .

2.2. Boundary Conditions

[15] Boundary conditions, for both the electromagnetic fields and particles, have crucial influences on the particle simulation results [Dum, 1984]. In the present study, the simulation domain is from r_0 (inner boundary, on the antenna surface) to r_m (outer boundary). The boundary condition for the electric field at r_0 (on the surface of the bare antenna) is dictated by the surface charge density on the antenna, σ_A , i.e.,

$$E_A = E_r(r_0) = \frac{\sigma_A}{\epsilon_0} \quad (9)$$

for a perfectly conducting antenna.

[16] The antenna surface charge density includes the contribution from both the antenna current and the charged particles that impinge and reside on the antenna surface. Because of the azimuthal symmetry, the antenna surface charge density due to the antenna current is obtained by

integrating the charge conservation equation over the antenna cross-section. Using the antenna current distribution of equation (1), we obtain for one of the antenna branches

$$\sigma_{ai} = \frac{I_0}{2\pi\omega r_0 l} e^{j(\omega t + \delta + 3\pi/2)} \quad (10)$$

Equation (10) (taking the real part of the right hand side) is used to calculate the oscillating charge density on the antenna surface. The collected charge density, σ_c , from the contribution of the charged particle bombardment onto the antenna is obtained by collecting the particles that reach the antenna surface from $t = 0$ to the current time step. The total charge density on the antenna surface at the current time step is then $\sigma_A = \sigma_{ai} + \sigma_c$, which is used in equation (9) to determine the electric field on the antenna surface. According to Gauss's law the electric field on any grid r_j is determined by the charge enclosed within the circle of a radius r_j (see equation (6)). The electric field at the outer boundary $r = r_m$ can be calculated from equation (6) when the charges on grids r_j ($j = 0, 1, 2, \dots, m$) are known. Therefore we do not need an outer boundary condition for the electric field. However, we need a boundary condition for charge Q_m at the outermost grid r_m .

[17] The specification of Q_m at r_m appears to be difficult. From equations (4) and (5), we see that the charge Q_m at the outer boundary r_m includes the contribution of the particles in both cell m and those outside the outer boundary. Since the locations of those particles outside the simulation domain are unknown, Q_m cannot be fully determined. Therefore, at each time step, we approximate Q_m by Lagrangian extrapolation of the charges Q_j ($j = 0, 1, 2, \dots, m - 1$) to r_m . Note that the evaluation of charges assigned to all grids are done after the particle removal at the inner boundary r_0 and particle injections at the outer boundary r_m described in the following subsection.

2.3. Particle Removal and Injections

[18] The simulation particles may move outside the simulation box because of either hitting the antenna surface at $r = r_0$ or moving beyond $r = r_m$. Those particles are removed from the active particle list in the simulation domain. The charges of the particles that hit the antenna are collected and included as the antenna surface charge. At the outer boundary r_m , particles may inject into the simulation domain from the outside. However, we do not have a priori knowledge to determine the velocities of the injected particles and their locations in the simulation domain. Such a difficulty arises from the fact that we only can simulate a limited portion of the plasma and that the electric fields beyond the outer boundary are unknown. In the case of a high-voltage antenna, the electric fields beyond the outer boundary are significant and their effects on the particles outside the simulation domain are not negligible when considering the particle injections. The particle injections at the outer boundary thus have to be treated approximately. In the present simulations, we treat the particle injections at the outer boundary with the following method.

[19] First of all we notice that the total current (conduction plus displacement current) in the plasma is independent

of r in the 1D problem that only has r dependence. From the divergence of Ampere's law

$$\nabla \cdot \nabla \times \mathbf{B} \equiv 0 = \nabla \cdot \left(\mu_0 \mathbf{J} + \epsilon_0 \mu_0 \frac{\partial \mathbf{E}}{\partial t} \right) \quad (11)$$

where \mathbf{B} is magnetic field, \mathbf{J} is conduction current density, and μ_0 is vacuum susceptibility, we have that the sum of the conduction and displacement current is independent of r

$$I_{total}(r, t) = I(r, t) + 2\pi r \epsilon_0 \frac{\partial E(r, t)}{\partial t} = \text{const.} \quad (12)$$

where $I(r, t) = 2\pi r J(r, t)$ is the conduction current flowing through the cylindrical surface of radius r with unit length in the z direction. Because of condition (12), the total current evaluated at the grid r_m should be equal to that at the grid r_{m-1} , i.e., $I_{total}(r_m, t) = I_{total}(r_{m-1}, t)$ at any given time. An imbalance between $I_{total}(r_m, t)$ and $I_{total}(r_{m-1}, t)$ indicates that a number of electrons or ions should be injected into the simulation domain because the total current is equivalent to the charges passing through the cylindrical surface in unit time. Specifically, the number of particles to be injected at any time step is given by

$$N_{inj} = (I_{total}(r_m, t) - I_{total}(r_{m-1}, t))(\Delta t / q_s) \quad (13)$$

If $I_{total}(r_m, t) < I_{total}(r_{m-1}, t)$, N_{inj} is the number of electrons (then q_s is the electron charge) to be injected to compensate for the larger current flowing through cylindrical surface of radius $r = r_{m-1}$. Otherwise, N_{inj} is the number of ions to be injected.

[20] As mentioned previously, there is no precise way to determine the velocities and the locations of the injected particles. The procedure adopted in the present simulations is that at each time step the velocities of the injected particles are calculated using the electric field at the outer boundary and then multiplied by a random number in the range of 0–1

$$\gamma_s v_s = -|q_s E(r_m) / m_s| \Delta t \text{ rand}() \quad (14)$$

The injected particles are then calculated using

$$r_i = r_{m-1} + v_s \Delta t \text{ rand}() \quad (15)$$

[21] We have tested several different methods of the particle injection and specification of Q_m . For example, we have set the velocities of the injected particles to zero with their locations randomly distributed in cell m , and used linear extrapolation of the charges inside the outer boundary to specify Q_m . It is found that the simulation results in 12 oscillating periods are essentially the same for the different methods we have tested, suggesting that the effects of the particle injections and the outer boundary condition for the charge distribution propagate only slowly inward.

[22] Randomly assigning velocities to the injected particles introduces an effective temperature to the electrons and ions. We note that the amplitude of the electric field at the outer boundary is about 1 V/m, as will be shown by the simulation results. Using 1 V/m in equation (14) and values

for charge, mass, and time step ($\Delta t = \sim 8.3 \times 10^{-8}$ s) introduced in section 3, the energies assigned to the injected electrons and ions are in the range of $0 - 6 \times 10^{-4}$ eV and $0 - 3 \times 10^{-7}$ eV, respectively. Taking the energy spread as the measure of the temperature, the effective temperatures of the electrons and ions are thus about 6×10^{-4} eV and 3×10^{-7} eV, respectively, which are very low. Therefore the randomness in injecting the particles essentially does not lead to a warm plasma in the simulation domain.

2.4. Initial Conditions

[23] At $t = 0$ the simulation electrons and ions are loaded into the simulation box with a uniform density. Initially individual pairs of electron and ion are placed at the same location so that the charge density in the simulation domain is zero at $t = 0$. The initial electric field distribution is determined by the surface charge on the antenna surface at $t = 0$, using equations (6) and (9). The velocities of the electrons and ions at $t = 0$ are set to zero. The leapfrog algorithm requires that initial velocities of the electrons and ions (if ions are mobile in the simulation) are set at $t = -(1/2) \Delta t$, which are calculated using equation (3) with one half time step backward.

3. Simulation Results With Immobile Ions

[24] In this section we describe the simulation results when the ions are assumed as fixed background of the positive charge. We use the following parameter values for the simulations. The antenna radius is $r_0 = 0.2$ m and simulation domain expands to $r_m = 200.2$ m. This simulation domain is divided into $m = 1000$ cells uniformly and thus the spatial resolution is $\Delta r = 0.2$ m. The initial electron and ion densities are set to be uniform with a value of $n_0 = 500 \text{ cm}^{-3}$ ($5 \times 10^8 \text{ m}^{-3}$). Initially 2.5×10^7 pairs of simulation electrons and ions are loaded into the simulation domain, with their velocities and temperatures set to be zero. The number of the simulation particles in cell 1 is smallest because it is the cell with smallest area: there are 75 simulation electrons and 75 simulation ions initially. The number of simulation particles increases in the cells further away from the antenna. The weight of the simulation particles (the number of real particles represented by a simulation particle) is $w = \sim 2.51 \times 10^6$. The charge of a simulation electron and ion is $\mp 1.6 \times 10^{-19} w$ Coulomb, respectively. The mass of a simulation ion is $1.67 \times 10^{-27} w$ kg while the mass of a simulation electron is $9.1 \times 10^{-31} w$ kg. The mass ratio of ion to electron is thus 1843 (real mass ratio). The real mass ratio is used to avoid difficulty in scaling simulation parameters to physical quantities (one of our objectives, for example, is to know physically how large the plasma sheath radius is). The time step is set as $\omega_p \Delta t = 0.1047197$, where $\omega_p^2 = \omega_{pe}^2 + \omega_{pi}^2$, ω_{pe} and ω_{pi} are electron and ion plasma frequency in rad/s, respectively. The length of each antenna branch is 100 m. The amplitude of the antenna current at $z = 0$, driven by the high-voltage source, is $I_{a0} = 0.4$ A, and the oscillating frequency of the current is $f = 30$ kHz, which is lower than the electron plasma frequency $f_{pe} \approx 200.64$ kHz but higher than the ion plasma frequency $f_{pi} \approx 4.68$ kHz. The simulation focuses on one branch of the antenna (another branch is 180° out of phase). The initial phase of the current is set

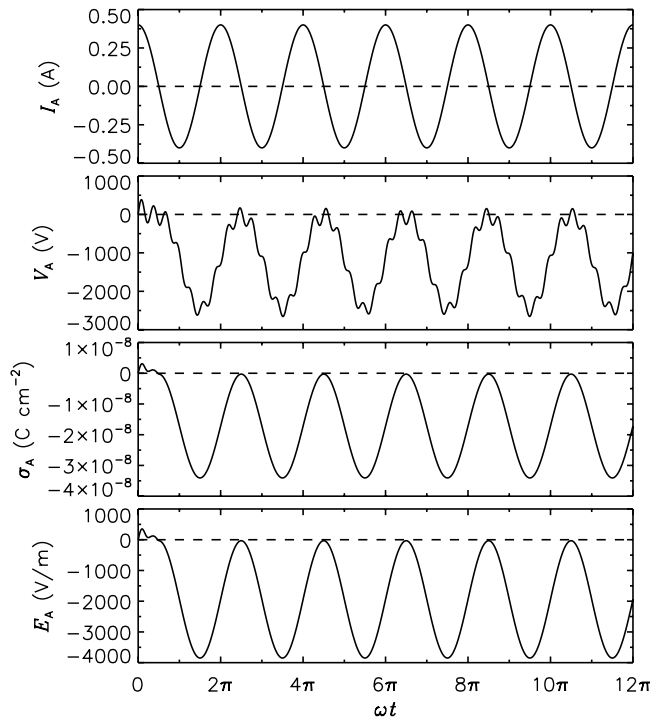


Figure 2. Time variations of the antenna current (input current to the antenna), antenna potential, antenna surface charge density, and normal electric field on the antenna surface (first to last panels) from the simulation neglecting the ion dynamics.

to $\delta = 0$ (the initial phase of the current on another antenna branch is $\delta + 180^\circ$). It should be pointed out that using different values of δ does not affect the simulated physical processes. We conduct simulations at only one frequency because the emphasis of the present study is to reveal the physical processes occurring in the antenna–plasma interaction for the high-voltage–driven antenna.

3.1. Antenna Charging and Impedance

[25] We first examine the antenna charging process in the simulation with the ion dynamics ignored. In Figure 2 we display, from the first to the last panels, the time variations of the antenna current (at the antenna feed point), the electric potential on the antenna surface, the surface charge density, and the normal electric field on the antenna surface. Note that the electric field, potential, and the charge density on the antenna surface are uniformly distributed along the antenna on the basis of 1D assumption. The potential reference position is set at r_m . It is seen that the antenna charging occurs in a transit dynamic process, and is completed in about one-fourth of an antenna current oscillation period because of the fast response of the light electrons. Without negative charging the antenna charge density should keep on increasing to reach its maximum value at one-fourth cycle. After negatively charged, the antenna surface charge density σ_A oscillates steadily, varying between about $-2.87 \times 10^{-10} \text{ C cm}^{-2}$ and $-3.41 \times 10^{-8} \text{ C cm}^{-2}$, while the electric field on the antenna surface oscillates between about -3848.6 V/m and -32.4 V/m . The maximum value of the electric field is less than zero (-32.4 V/m). This is because the antenna is overly charged: the maximum antenna surface charge density is less

than zero. We will discuss this issue later when discussing the causes of the antenna charging. The oscillation frequency of both antenna surface charge density and electric field is 30 kHz, the same as that of the antenna driving current. The antenna potential essentially lies below zero because of the charging and also oscillates at the antenna current frequency. The slight positive value of the antenna potential are due to the arbitrary selection of the potential reference point at the outer boundary. The potential there may actually not be zero with respect to the potential of the ambient plasma. The DC voltage associated with the antenna charging is about -1225.7 V .

[26] Figure 2 shows that the phase of the antenna current is nearly 90° in advance of the antenna potential, indicating that the antenna impedance is mainly capacitive. The phase difference between the antenna potential and current, averaged over 6 oscillating cycles, is about -88.59° . From the relationship between the antenna potential and current, we can calculate the antenna reactance X_s . The potential (relative to the reference point at $r_m = 0$) of the other antenna branch is 180° out of phase, and the potential difference (or voltage) between the two antenna branches is just the potential shown in Figure 2 with the DC component removed. The peak-to-peak potential difference, averaged for 6 oscillating periods shown in Figure 2, is 2789.8 V. The peak-to-peak antenna current is 0.8 A. The antenna reactance is thus calculated to be $X_s = -3486.2 \Omega$. Compared to that given by equation (29) in the study by Song *et al.* [2007] ($X_s = -3175 \Omega$) using the same parameter values, the reactance from the simulation is about 10% larger than that from the theoretical model. This is an improvement over the analytical value but still underestimates the IMAGE RPI experiment value by about 10%.

[27] The antenna charging is caused by the electrons in the plasma that attach to the surface of the antenna, as shown by Figure 3, which displays the time history of the number of electrons that are attracted onto the antenna. Within the first one-fourth of an oscillating period, there are a large number of electrons reaching the antenna. After that short period, no more electrons can reach the antenna surface because of the negative antenna surface charge density, and hence the negative (directed toward the antenna) electric field on and near the antenna surface. Note that the antenna charging does not stop at the time when the antenna surface charge σ_A density becomes zero. Instead, it stops when σ_A becomes negative ($-2.87 \times 10^{-10} \text{ C cm}^{-2}$). The reason for extra charging is that some electrons in the plasma, which are accelerated toward the antenna, have finite kinetic energies to overcome the negative potential and reach the antenna. Only when the negative charge density on the antenna is large enough (in value), all the electrons, including those that have been accelerated toward the antenna, can no longer reach the antenna. It will be shown later that when the ion motion is allowed the antenna will not be completely charged to negative charge density through a whole oscillation cycle.

3.2. Plasma Sheath Structures

[28] After the antenna is negatively charged, the antenna surface electric field becomes negative. This negative electric field repels electrons away from the proximity of the antenna, leaving a region with extra ions (positive charges). This region is an ion sheath, which is observed in the

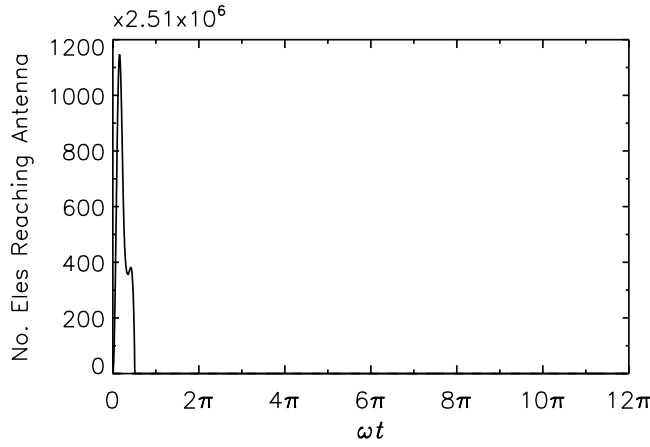


Figure 3. Number of electrons that reach the antenna from the surrounding plasma as a function of time.

electron and charge density distributions at individual time steps. Figure 4, which displays sample snapshots of the electron density distribution and the charge density distribution at $\omega t = 34.31$ (dashed line) and $\omega t = 36.62$ (solid line), clearly shows the ion sheath and its spatial structures. Around the antenna is a region where the electron density is greatly depleted (essentially zero, see top panel) and the background ions provide a constant positive charge density of $8 \times 10^{-17} \text{ C cm}^{-3}$ (see the bottom panel). Outside the sheath, the electron density remains around its initial value of 500 cm^{-3} with fluctuations of small amplitudes because of the limited number of simulation particles. The boundary from the ion sheath to the plasma (hereafter we refer to it the sheath–plasma boundary) is a transition region with a finite length of about 7 m. Both the electron and charge densities have sharp gradients at the inner edge of the sheath–plasma boundary so that the step function description of the electron and charge density is a very good approximation [Song *et al.*, 2007], if the fine structures of the electron and charge density in the transition region are neglected. Immediately away from the sharp gradient, the electron density at $\omega t = 36.62$ shows an overshoot and then gradually returns to 500 cm^{-3} . Correspondingly, the charge density in the same region is negative and then keeps essentially zero further away from the sheath. The electron density enhancement is

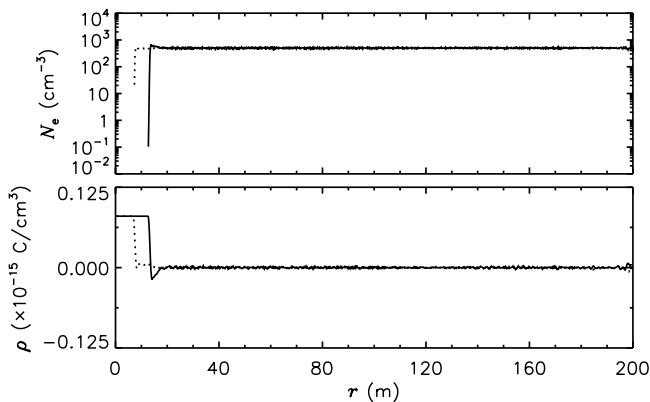


Figure 4. Electron density distribution (top panel) and charge density distribution (bottom panel) at $\omega t = 34.31$ (dashed line) and $\omega t = 36.62$ (solid line).

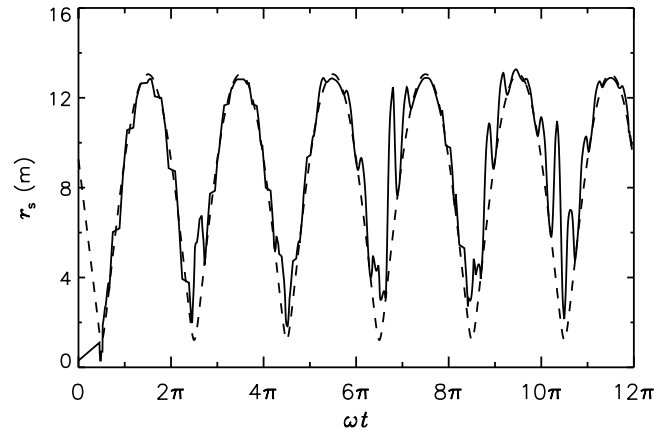


Figure 5. Oscillations of the radius of the sheath–plasma boundary. The dashed line is the time variation of the sheath–plasma boundary calculated using the theoretical model of Song *et al.* [2007].

due to a pileup of electrons in the transition layer at this time. Note that the electric fields in the sheath always direct toward the antenna (negative values) even though the electric fields oscillate at the frequency of the antenna current. The electric field in the transition region and in the plasma, on the other hand, primarily oscillates at the plasma frequency and has positive and negative phases, as will be shown in Figure 7. The pileup occurs when the electric field in the transition region is in its negative phase, e.g., at $\omega t = 36.62$ (corresponding to the second vertical dashed line in Figure 7). The electrons at the inner edge of the boundary are strongly pushed outward by the stronger electric field in the transition region while the electrons further away experience much weaker electric field force. When the electric field in the transition region is in its positive phase, e.g., at $\omega t = 34.31$ (first vertical dashed line in Figure 7), the electron density overshoot almost disappears. The transition region, which has been neglected in the analytical treatment of Song *et al.* [2007], may be one of the causes of the small difference in the antenna reactance between the simulated and theoretical values.

[29] The sheath size, or the sheath radius in a cylindrical case, oscillates with the antenna current frequency as can be seen in Figure 5, which displays the time variation of the sheath–plasma boundary radius r_s . The boundary is defined at where the charge enclosed inside the boundary is equal (but with opposite sign) to that on the antenna surface, in unit length in the z direction. The dashed line represents the sheath–plasma boundary variation calculated using equation (21) in the study of Song *et al.* [2007]. In calculating the theoretical values of r_s , the antenna surface charge density from the simulation is used to evaluate the static sheath radius in equation (17) in the study of Song *et al.* [2007] because the antenna surface charge density is not calculated in the theoretical model. The spikes in the simulated boundary radius are caused by the noise in the charge density, which sometimes results in the fluctuations in determining the boundary location. It is found that the simulated sheath–plasma boundary radius is in good agreement with the theoretical values when the antenna surface charge density from the simulation is used. Both oscillate at

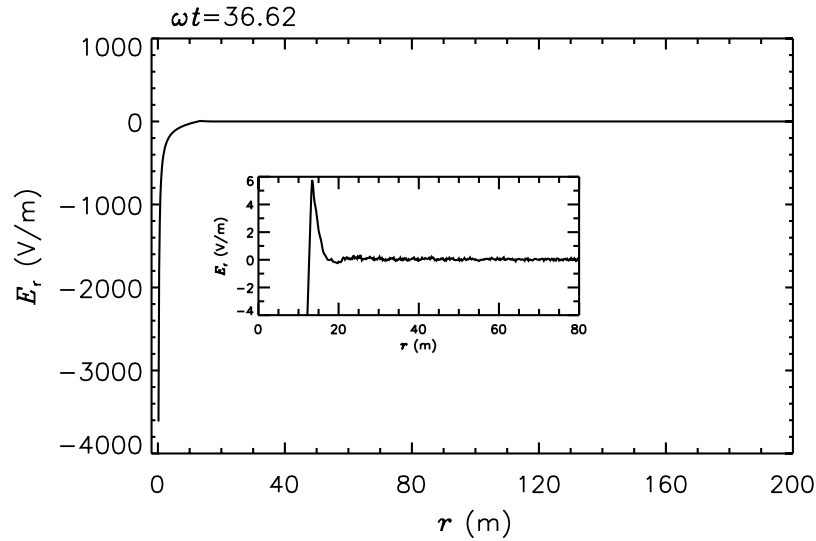


Figure 6. The electric field distribution at $\omega t = 36.62$. The inserted figure displays fine structures of the electric field around the sheath–plasma boundary at this time.

the antenna current frequency. It is also interesting to note that once formed the sheath region maintains a minimum radius above 1.5 m. It never shrinks to the antenna surface during its oscillations. This is because the antenna is negatively charged and the electric field near the antenna is always negative. Note that the theoretical formula for r_s is valid only after the antenna charging process is completed. The theoretical values, therefore, are different from the simulated within the first one-fourth oscillating period when the antenna charging is ongoing.

3.3. Electric Shielding by Plasma Sheath

[30] The plasma sheath acts as a shield to the antenna electric field so that it is expected that the electric field is significantly weaker outside the sheath. This is indeed the case by examining the spatial distribution of the electric field at all time steps. As an example, we show in Figure 6 the spatial distribution of the electric field at $\omega t = 36.62$. It is seen that there is a very strong electric field in the sheath region, but a much weaker electric field outside. The inserted panel on Figure 6 reveals the fine structure of the electric field around the sheath–plasma boundary. A positive spike at the inner edge of the sheath–plasma boundary layer is observed followed by a weak negative excursion, which are the electric field structures of the transition region. The positive spike can be explained by the charge density distribution shown in Figure 4 also for the time moment of $\omega t = 36.62$. The charge density inside the sheath is positive, which tends to weaken the strength of the negative electric field when moving away from the antenna. Thus the electric field increases rapidly to positive values at the inner edge of the boundary layer. The charge density then suddenly drops to negative values because of the pileup of the electrons in the transition layer as discussed in the previous subsection. Therefore the electric field rapidly decreases, forming a spike in the transition layer.

[31] It is also interesting to examine the time variations of the electric field. In Figure 7, we show the time variation of the electric field at three different locations: inside the sheath close to the antenna at $r = 0.3$ m; around the

sheath–plasma boundary at $r = 12.1$ m; and far away from the sheath at $r = 36.1$ m. Since the minimum sheath radius is above 1.5 m, the location $r = 0.3$ m is always inside the sheath. The electric field in the sheath is strong and oscillates with the antenna current frequency because the sheath region is free of electrons and the ions are fixed (thus no oscillating charges inside the minimum sheath radius of $r_s < \sim 1.5$ m). At $r = 12.1$ m, which is close to the maximum radius (~ 13.5 m) of the sheath–plasma boundary, the electric field either primarily oscillates with the plasma frequency when the sheath–plasma boundary is within $r = 12.1$ m or has a stronger amplitude and varies with the antenna current frequency when the sheath–plasma boundary is outside $r = 12.1$ m. Away from the maximum radius of the sheath–plasma boundary, the electric field primarily oscillates at the plasma frequency but modulated by the antenna current frequency.

[32] The plasma oscillations are caused by the penetration of the electric field into the plasma before the plasma sheath is formed. In the simulation, the penetrated electric field perturbs the electrons and causes the electron plasma oscillations. The sheath acts to shield the antenna electric field, as discussed before. However, such shielding is not perfect. Therefore the antenna electric field, which oscillates at the antenna current frequency, can leak into the plasma even after the sheath is formed. This component at the antenna current frequency modulates the plasma oscillations as seen in Figure 7. It is noted that in the present simulation there is no transmitted wave since we actually considered an unmagnetized cold plasma. In the unmagnetized cold plasma the waves that can propagate must have a frequency higher than the plasma frequency. Note that we have argued that the random injection of the particles from the outside of the simulation domain does not introduce substantial warm plasma.

[33] Although the electric field beyond the sheath–plasma boundary is weak compared to that in the sheath, its oscillating amplitude is significant. The electric field beyond the sheath primarily oscillates at the plasma frequency but modulated by the antenna current frequency. The amplitude of this modulated component is around

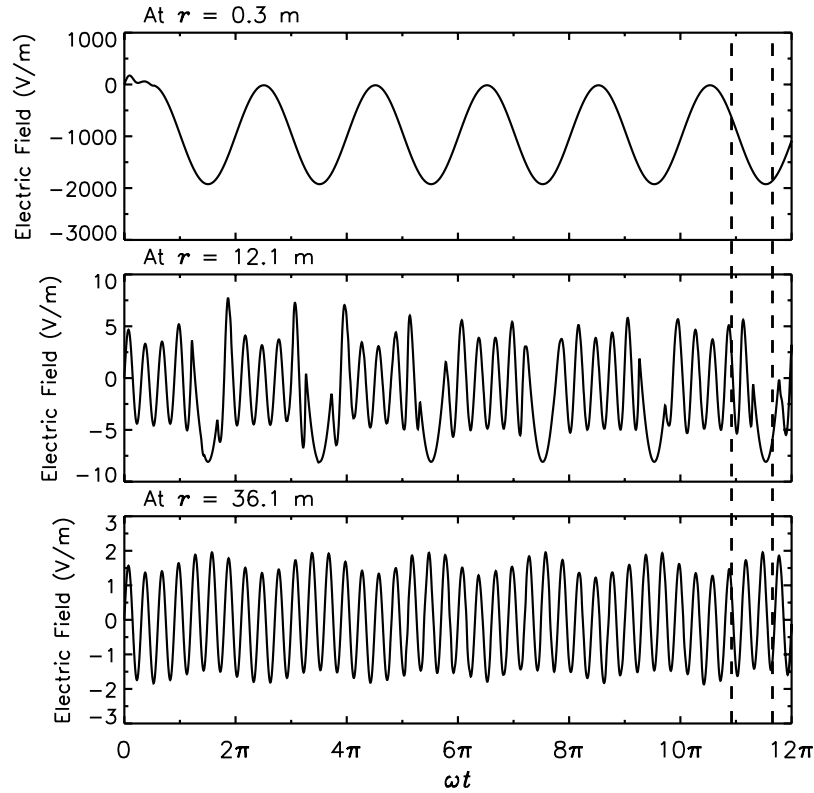


Figure 7. Time variation of the electric field at three selected locations as labeled from the simulation neglecting the ion dynamics. Two dashed vertical lines indicate two time moments: $\omega t = 34.31$ and $\omega t = 36.62$.

0.25 V/m as demonstrated in Figure 7. The strength of this component will be larger when the higher voltage is applied to the antenna. If this value was the electric field amplitude of the transmitted whistler wave, it would be much stronger than the electric field amplitude of the natural whistler waves in the inner magnetosphere, which is typically in the order of mV/m [e.g., *Helliwell*, 1965; *Meredith et al.*, 2001]. Note that once the whistler waves are excited in the plasma around the antenna, the wave energy is confined in a small angle with respect to geomagnetic field lines and is not damped very much along its field-aligned guided propagation path. Thus it may be feasible to use the whistler wave transmitted from high-voltage antennas in the magnetosphere for controlled precipitation of relativistic electrons in the radiation belts. We should, however, keep in mind that a definite conclusion cannot be derived from the present simulation which is quasi-static in nature. We will further examine this issue with the simulations that include the magnetic fields and thus can deal with the wave transmission directly.

4. Effects of Ion Dynamics on Antenna–Plasma Interaction

[34] The simulation results shown above reproduce the theoretical predictions by *Song et al.* [2007], indicating that the simulation model is reliable. Such a simulation without the ion dynamics is illustrative and is valid if the frequency of the antenna current is much higher than the ion characteristic frequencies. As argued in the Introduction, in the inner magnetosphere the VLF wave frequencies may not be

much higher than the ion characteristic frequencies so that ion dynamics should be included. In this section we examine how the ion dynamics affects the antenna–plasma interaction. In the present simulation, both the ions and electrons move in response to the time-dependent electric field. We use the same simulation parameters described at the beginning of section 3. The oscillating frequency of the antenna current utilized, 30 kHz, is only about 6 times the ion plasma frequency (~ 4.8 kHz for the given plasma density of 500 cm^{-3}). The effects of the ion dynamics thus should be clearly observable in the simulation.

[35] We first examine how the antenna charging is affected by the ion dynamics. Figure 8 shows, in the same format as that of Figure 2, the results from the simulation with the ion dynamics included. The antenna charging is still completed within about one-fourth of an oscillating period as can be seen from the time variation of the antenna charge density. A readily noticeable feature is that, in contrast to the case without the ion dynamics, the peak value of the antenna charge density is slightly positive in the present simulation. Consequently, the antenna electric field from the simulation with mobile ions has a short excursion of small positive values in each oscillation cycle. The positive excursion of the antenna charge density and electric field is caused by the ion current collected by the antenna from the plasma as will be discussed later.

[36] Same as in the case without the ion dynamics, it is demonstrated by Figure 8 that the antenna potential is also nearly -90° out of phase with the antenna current. Averaged over 6 oscillation periods, the potential–current phase difference is about -88.79° and the peak-to-peak antenna

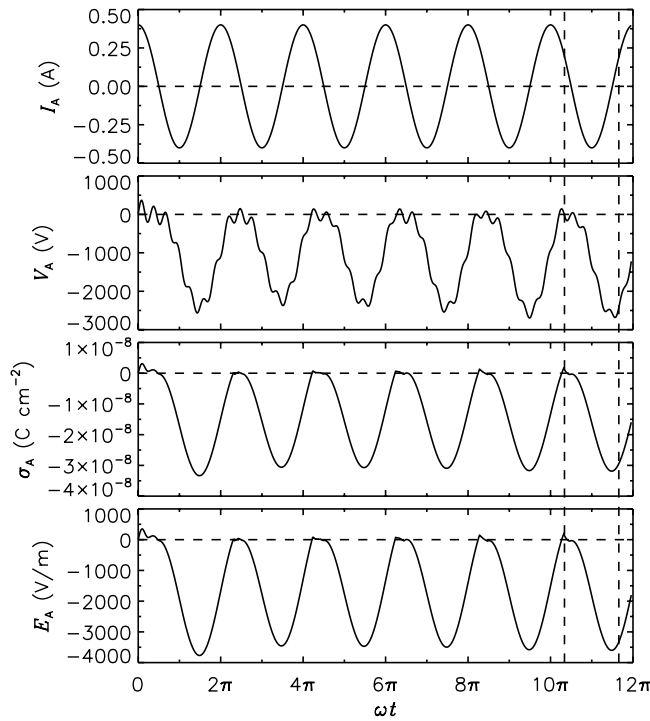


Figure 8. The same format as that of Figure 2 but for the simulation with the ion dynamics included. Two dashed vertical lines indicate two time moments: $\omega t = 32.48$ and $\omega t = 36.62$.

potential difference is about 2741.48 V. The antenna reactance is then calculated to be about 3426.1 Ω , close to the reactance (3486.2 Ω) obtained from the simulation without the ion dynamics included. Including the ion dynamics in the simulation, therefore, does not significantly affect the antenna reactance for the simplified 1D and quasi-static situation.

[37] In Figure 9 we display electron (solid line) and ion (dotted line) current collected by the antenna because of the electrons and ions impinging on the antenna surface. Also plotted, as stars, is the total (electron plus ion) current

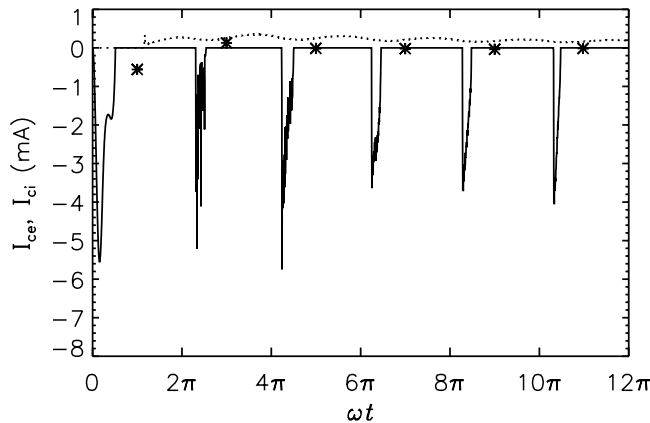


Figure 9. Electron (solid line) and ion (dashed line) current collected by the antenna as a function of time. Stars represent the total (electron plus ion) current averaged over each oscillation period.

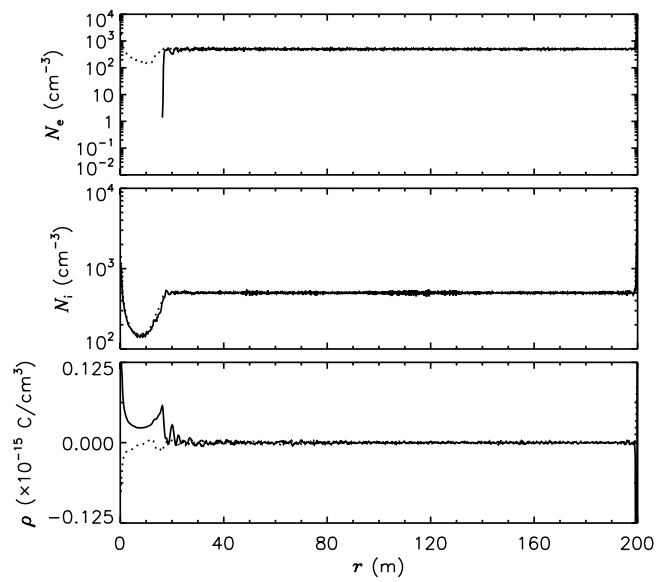


Figure 10. Electron density (first panel), ion density (second panel), and charge density (third panel) distribution at $\omega t = 32.48$ (dotted line) and $\omega t = 36.62$ (solid line), corresponding to the time moments indicated by two dashed vertical lines in Figure 8.

averaged over each oscillation period. First of all we note that the electron current (or the electron impinging to the antenna) is impulsive with the oscillation period of the antenna current. The first pulse occurs in the first one-fourth period, which causes the negative charging of the antenna. The negative charging results in a negative electric field that repels the electrons away but attracts the ions toward the antenna. After the first half oscillation cycle of the antenna current, the ion current starts with a small peak value. The ion current is continuous since the collection of ions by the antenna is continuous. The ion collection does not stop even when the total charge density (sum of ions and electrons attracted from the plasma and charge from the antenna current) on the antenna becomes positive. The reason is that the ions response to the electric field (and its change) slowly as a result of their large inertial compared to that of the electrons. Only when the positive charge density (so the positive electric field) lasts long enough, will the ion current disappear. Once the antenna charge density becomes positive, however, a large number of electrons rapidly flow to and reside on the antenna surface in response to the positive electric field, decreasing the antenna charge density to negative in a short time, less than one-fourth of a period. Afterward the ion current collection increases again before it completely disappears. It is also found that both the electron and ion currents collected by the antenna, are in the order of 1 mA, which is very weak compared to the peak antenna current of 0.4 A. Finally, it is shown by the stars in Figure 9 that after about 1 oscillation period, the ion current basically balances the electron current averaged over each oscillation period. Thus, after the antenna charging is finished, there is no significant net conduction current to the antenna from the sheath, which is consistent with the IMAGE RPI experiment discussed by *Song et al.* [2007].

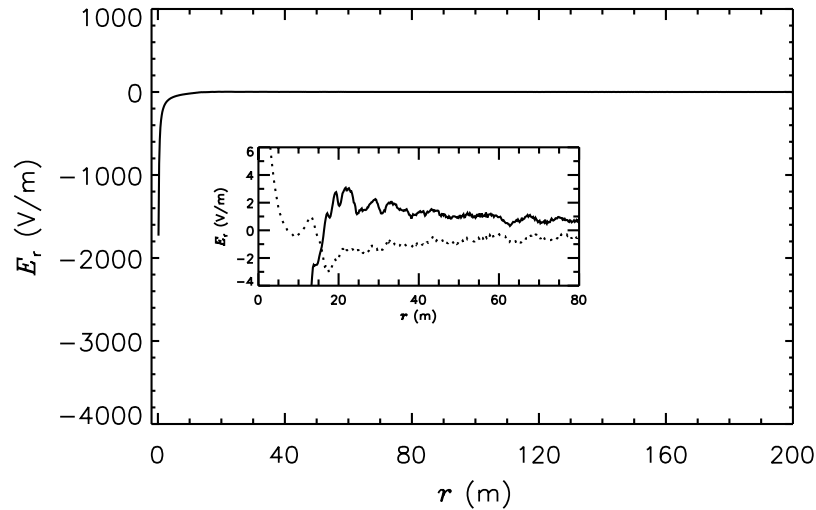


Figure 11. The electric field distribution at $\omega t = 31.30$ from the simulation with the mobile ions. The inserted figure displays fine structures of the electric field around the sheath–plasma boundary at $\omega t = 31.30$ (solid line) and $\omega t = 32.48$ (dotted line).

[38] Next we examine how the plasma sheath structures are affected by the ion dynamics. It is found by scrutinizing the individual density snapshots that the electron density distribution consists of similar structures to those in the simulation without the ion dynamics, when the antenna charge density (and also the antenna electric field) is negative. There is a region of the deeply depleted electron density (essentially zero) with a sharp density gradient at the outer boundary. The boundary moves in and out when the negative charge density on the antenna decreases and increases in magnitude. However, the electron density distribution is distorted substantially from above picture during the positive excursion of the antenna charge density. As an example, we show in Figure 10, from the first to the last panels, the electron density, ion density and charge density distribution at $\omega t = 32.48$ (dotted line) and $\omega t = 36.62$ (solid line), corresponding to the time moments indicated by the two dashed lines in Figure 8, respectively. The deeply depleted region in the electron density distribution is observed at $\omega t = 36.62$ similar to that shown in Figure 4. Nevertheless, at $\omega t = 32.48$ when the antenna charge density becomes positive, the electron density distribution is quite different: the deeply depleted region is now filled in with the electrons although the density inside the region is still lower than the background. Filling the depleted region is simply due to the inward attraction of the electrons by the positive electric field. The U-shaped structure is caused by the rapid attraction of the electrons in the vicinity of the antenna while slower supply of the electrons from background plasma region where the electric field is much weaker. The charge density at $\omega t = 32.48$ in the U-shaped region is negative because of the extra electrons. In other words, there is an electron plasma sheath at this moment. This is different from the situation without the ion dynamics where there always exists an ion plasma sheath.

[39] The ion density distribution is also U-shaped: decreased in the center of the region while enhanced (above its background value) in the immediate proximity of the antenna. The enhanced ion density near the antenna is

caused by the negative electric field which attracts the ions toward the antenna. The valley of the ion density is a result of attraction of the ions to the vicinity of the antenna and the slow supply of the ions to the valley region from the plasma. Such an ion density structure is quite stable as demonstrated by comparing the ion density distributions at $\omega t = 32.48$ (dotted line) and $\omega t = 36.62$ (solid line) shown in Figure 10. The persistence of the U-shaped structure during the positive excursion of the electric field is resulted from the finite response time of the ions to the electric field and the short period of the positive electric field.

[40] As in the case without the ion dynamics, the plasma sheath tends to shield the electric field from penetrating into the plasma. The shielding, however, is even less perfect in the present simulation. A significant electric field, which has a component oscillating at the frequency of the antenna current, extends farther into the plasma. Figure 11 demonstrates the electric field distributions at $\omega t = 31.30$. The fine structures of the electric field around the plasma sheath boundary is also shown for the time of $\omega t = 31.30$ (solid line) and $\omega t = 32.48$ (dotted line) by the inserted panel. It is seen again the strength of the electric field quickly decreases away from the antenna and becomes weak beyond the plasma sheath. As shown by the inserted panel, the amplitude of the electric field is around 1 V/m, which is significant. Note that at $\omega t = 32.48$ the electric field in the sheath is positive because of the positive antenna charge density at that time.

5. Summary and Discussions

[41] We have applied a PIC simulation code to investigate the antenna–plasma interaction in space plasma. We performed the simulations for cases without and with ion dynamics included. By assuming that ions do not move, the simulation performed with our 1D code basically reproduces the theoretical predications by *Song et al.* [2007], namely, antenna charging, ion plasma formation, and the oscillation of the sheath radius. The simulation also reveals the details of the antenna charging process and the

fine structures of the plasma sheath, which are not tractable by the analytical methods. It is seen from the simulation that the antenna charging and the plasma sheath formation is a transit dynamic process that is completed in about one-fourth of an oscillation cycle. The sheath radius oscillates with the frequency of the antenna driving current and has a finite minimum value. Furthermore, the electric field oscillations at the plasma frequency in the plasma, which are not expected in the analytical model, are clearly demonstrated by the simulation. The simulation including the ion dynamics reveals a number of new features of the antenna–plasma interaction. These features include a brief excursion of the positive antenna charge density and electric field, the impulsive electron and continuous ion currents collected by the antenna, electron plasma sheath during the excursion of the positive antenna charge density, and stable U-shaped ion density structure in the plasma sheath region. The antenna reactance evaluated from the simulations with and without the ion dynamics are nearly the same. The simulations improve the reactance value from the theoretical estimate given by Song *et al.* [2007] by about 10%. Such improvement demonstrates the advantage of the PIC simulation models that can include the plasma sheath effects self-consistently in studying the antenna–plasma interaction.

[42] In the simulations, the plasma sheath is formed as a result of the negative antenna charging. This is similar to the formation of a Debye sheath around an electrode (or a probe) in the plasma. However, the sheath size (or radius in cylindrical geometry) is controlled primarily by the strong electric field excited by the antenna charge instead of the Debye length (or plasma temperature) because the transmission antenna is actively driven. That is, the sheath formation is caused by the kinetic force of the applied electric field rather than the difference between the thermal motions of the electrons and ions. As shown by Figure 5, although the plasma is assumed cold, the simulated sheath size is of a spatial scale comparable to the Debye length of a 1-keV warm plasma with the same density as that used in the simulations (500 cm^{-3}). In addition, different from the case of the Debye sheath, the potential and electric field are not zero at the plasma sheath boundary, which itself oscillates with the antenna current frequency. Actually there is an electric field component with a significant amplitude ($\sim 0.3 \text{ V/m}$) oscillating at the frequency of the antenna current because of the partial penetrating of the electric field into the plasma. If this is the amplitude of the transmitted whistler wave, it is strong compared to the amplitude (typically in the order of mV/m) of the natural whistler waves in the magnetosphere [Helliwell, 1965; Meredith *et al.*, 2001], implying the applicability of the high-voltage antennas in whistler wave transmission. Nevertheless, simulations that include the magnetic fields are necessary for a definite conclusion on this issue.

[43] The simulations provide significantly improved understanding of the antenna–plasma interaction in the context of high-voltage antennas in the inner magnetosphere, although they were performed on the basis of several assumptions, namely, cold plasma, negligible end effects at the antenna tips, weak effects of the magnetic field, and thus the 1D approximation. Including those effects neglected in the present simulations will allow more accurate evaluation of the impedance properties of the antennas

and comprehensive understanding of the antenna transmission characteristics in the presence of the plasma sheath.

[44] **Acknowledgments.** This work was supported by AFRL under contracts F19628-02-C-0092 and FA8718-05-C-0070. J. Tu thanks X. Huang for many thoughtful discussions. The authors greatly appreciate the suggestive comments from the reviewers.

[45] Amitana Bhattacharjee thanks Paul J. Kellogg and another reviewer for their assistance in evaluating this paper.

References

- Baker, D. J., H. Weil, and L. S. Bearce (1973), Impedance and large signal excitation of satellite-borne antennas in the ionosphere, *IEEE Trans. Antennas Propag.*, **21**, 672–679.
- Balmain, K. G. (1964), The impedance of a short dipole antenna in a magnetoplasma, *IEEE Trans. Antennas Propag.*, **12**, 605–617.
- Birdsall, C. K., and A. B. Langdon (1983), *Plasma Physics via Computer Simulation*, 479 pp., McGraw-Hill Book Company, New York.
- Dum, C. T. (1984), Simulation models for space plasmas and boundary conditions as a key to their design and analysis, in *Computer Simulation of Space Plasmas*, edited by H. Matsumoto and T. Sato, pp. 303–375, Terra Scientific Publishing, New York.
- Helliwell, R. A. (1965), *Whistlers and Related Ionospheric Phenomena*, 368 pp., Stanford Univ. Press, Stanford, Calif.
- Hockney, R. W., and J. W. Eastwood (1988), *Computer Simulation Using Particles*, 540 pp., Taylor and Francis, New York.
- Inan, U. S., T. F. Bell, J. Bortnik, and J. M. Albert (2003), Controlled precipitation of radiation belt electrons, *J. Geophys. Res.*, **108**(A5), 1186, doi:10.1029/2002JA009580.
- Kuehl, H. H. (1966), Resistance of a short antenna in a warm plasma, *Radio Sci.*, **1**, 971–976.
- Laframboise, J. G., and L. J. Sonmor (1993), Current collection by probes and electrodes in space magnetoplasmas: A review, *J. Geophys. Res.*, **98**, 337–357.
- Meredith, N. P., R. B. Horne, and R. R. Anderson (2001), Substorm dependence of chorus amplitudes: Implications for the acceleration of electrons to relativistic energies, *J. Geophys. Res.*, **106**, 13,165–13,178.
- Mlodnosky, R. F., and O. K. Garriott (1963), The v.l.f. admittance of a dipole in the lower ionosphere, in *Proc. Int. Conf. Ionosphere*, pp. 484–491, Inst. Phys. and Phys. Soc., Dorking, U. K.
- Morin, G. A., and K. G. Balmain (1993), Plasma sheath and presheath waves: Theory and experiment, *Radio Sci.*, **28**, 151–167.
- Nakatani, D. T., and H. H. Kuehl (1976), Input impedance of a short dipole antenna in a warm anisotropic plasma: 1. Kinetic theory, *Radio Sci.*, **11**, 433–444.
- Nikitin, P., and C. Swenson (2001), Impedance of a short dipole antenna in a cold plasma, *IEEE Trans. Antennas Propag.*, **49**, 1377–1381.
- Oliver, B. M., R. M. Clements, and P. R. Smy (1973), Experimental investigation of the low-frequency capacitive response of a plasma sheath, *J. Appl. Phys.*, **44**, 4511–4517.
- Reinisch, B. W., et al. (2000), The radio plasma imager investigation on the IMAGE spacecraft, *Space Sci. Rev.*, **91**, 319–359.
- Riemann, K.-U. (1991), The Bohm criterion and sheath formation, *J. Phys. D: Appl. Phys.*, **24**, 493–518.
- Shkarofsky, I. P. (1972), Nonlinear sheath admittance, currents, and charges associated with high peak voltage drive on a VLF/ELF dipole antenna moving in the ionosphere, *Radio Sci.*, **7**, 503–523.
- Song, P., B. W. Reinisch, V. Paznukhov, G. Sales, D. Cooke, J.-N. Tu, X. Huang, K. Bibl, and I. Galkin (2007), High voltage antenna–plasma interaction in whistler wave transmission: Plasma sheath effects, *J. Geophys. Res.*, **112**(A3), A03205, doi:10.1029/2006JA011683.
- Tsutsui, M., I. Nagano, H. Kojima, K. Hashimoto, H. Matsumoto, S. Yagitani, and T. Okada (1997), Measurements and analysis of antenna impedance aboard the Geotail spacecraft, *Radio Sci.*, **32**, 1101–1126.
- Ward, J., C. Swenson, and C. Furse (2005), The impedance of a short dipole antenna in a magnetized plasma via finite difference time domain model, *IEEE Trans. Antennas Propag.*, **53**, 2711–2718.
- Zhao, H., R. Schmidt, C. P. Escoubet, K. Torkar, and W. Riedler (1996), Self-consistent determination of the electrostatic potential barrier due to the photoelectron sheath near a spacecraft, *J. Geophys. Res.*, **101**, 15,653–15,659.

B. W. Reinisch, P. Song, and J. Tu, Center for Atmospheric Research, University of Massachusetts–Lowell, 600 Suffolk Street, Lowell, MA 01854-3629, USA. (jiannan_tu@uml.edu)

APPENDIX C

Radiation Theory in Magnetized Plasma
X. Huang

Radiation Theory in Magnetized Plasma

1. Physical Model and Assumptions

When an antenna is embedded in an anisotropic medium and driven by a sinusoidal steady current at the fed point, sinusoidal varying electromagnetic fields will be stimulated around the antenna. The theoretical study of the radiation problem is to find the solution from the radiation equation derived from the Maxwell equation system

$$\nabla \times (\nabla \times \mathbf{E}(\mathbf{r})) - k_0^2 \boldsymbol{\kappa} \cdot \mathbf{E}(\mathbf{r}) = -j\mu_0 \omega \mathbf{J}(\mathbf{r}') \quad (1.1)$$

where ω is the angular frequency, $\mathbf{J}(\mathbf{r}')$ the complex amplitude of the driving current density at a point \mathbf{r}' in the antenna region, $\mathbf{E}(\mathbf{r})$ and $\mathbf{H}(\mathbf{r})$ the complex amplitudes of the electric and magnetic fields at any observing point \mathbf{r} , respectively, $\boldsymbol{\kappa}$ the relative dielectric tensor of the anisotropic medium, and $k_0 = \omega/c$ is the wave number in free space. The relationship of the speed of light in free space, c , the permittivity of free space, ϵ_0 , and the permeability of free space, μ_0 , is $c = (\epsilon_0 \mu_0)^{-1/2}$. The time factor $e^{j\omega t}$ is used in the analysis but, in general, omitted in the expressions. Bold letters denote vectors or tensors and this notation convention applies throughout the text.

It is very difficult to derive a rigorous analytical solution from Equation (1.1) for the general situation. It is advisable to establish a physics model to simplify the analysis, making sure that the model is a good approximation of the real radiation problem.

At first, it is assumed that the magnetoplasma is uniform and can be treated as a fluid. When the z-axis is set along the direction of the ambient field, \mathbf{B}_0 , under the condition of the cold plasma approximation the relative dielectric tensor can be expressed in matrix form

$$\boldsymbol{\kappa} = \begin{bmatrix} \epsilon_1 & -j\epsilon_2 & 0 \\ j\epsilon_2 & \epsilon_1 & 0 \\ 0 & 0 & \epsilon_3 \end{bmatrix}$$

$$\epsilon_1 = 1 - \frac{XU}{U^2 - Y^2}, \quad \epsilon_2 = \frac{XY}{U^2 - Y^2}, \quad \epsilon_3 = 1 - \frac{X}{U} \quad (1.2)$$

$$X = \frac{\omega_{pe}^2}{\omega^2}, \quad Y = \frac{\omega_{ce}}{\omega}, \quad U = 1 - jZ, \quad Z = \frac{\nu}{\omega}$$

where ν denotes the electron-neutral collision frequency, ω_{pe} the electron plasma frequency, and ω_{ce} the electron gyro-frequency

$$\omega_{pe} = (N_e e^2 / \epsilon_0 m_e)^{1/2}$$

$$\omega_{ce} = |e| B_0 / m_e \quad (1.3)$$

which are dependent on the plasma density (N_e), electron charge (e) and mass (m_e), and amplitude of the ambient magnetic field (B_0). It should be noted that the ion effects have been ignored in Equation (1.2) although it is not necessary in the analysis of this study.

Equation (1.2) represents the general case with collision effects included. For practical applications the collision can, in general, be ignored. However, solutions that start with setting $\nu = 0$ in equation 1.2 may differ from the limit of the general solution for collisional plasma. In fact, the dissipation-free case is not realistic and the limitation principle should be used: the physically meaningful result for collision-free plasma is the limit of the general solution when the collision rate approaches zero. The limitation principle is widely used in physics, for example, in fluid dynamics where the viscosity should be, at first, included to get the general solution, and then taking the limit to get the solution for viscosity-free fluid. Accordingly, we always deal with collisional plasma in the analysis and regard the collisionless plasma as the limiting case so that the derived results are applicable to collisionless plasma.

We assume a center-fed thin wire dipole antenna with finite length $2L$ and with an orientation angle Ψ relative to the ambient field direction. The length and orientation of the antenna are arbitrary in the analysis.

As shown in Figure 1, the origin of the coordinate system is located at the center of the antenna. The z' -axis for the current source coordinate system is along the antenna wire and located in the xz -plane. In addition to the Cartesian coordinate system, the spherical and cylindrical coordinate systems are used according to the convenience of analysis. The components of a current source point and an observing point are

$$\begin{aligned}\mathbf{r}' &= (x', y', z') = (r', \alpha', \beta') = (\rho', \beta', z') \\ \mathbf{r} &= (x, y, z) = (r, \alpha, \beta) = (\rho, \beta, z)\end{aligned}\tag{1.4}$$

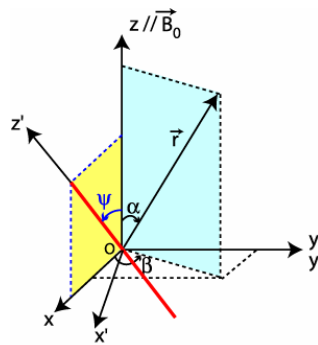


Figure 1. Coordinate system

Strictly speaking, the source current in Equation (1.1) is unknown in the problem. One can only assume the current at the feed point of the antenna and the current density distribution in the antenna region should be determined in such a way that it satisfies the boundary condition at the surface of the antenna. In this study the antenna is assumed infinitely thin and a line current

along the antenna is reasonably prescribed and the stimulated field surrounding the antenna satisfied the boundary condition in a very good manner of approximation.

While this study concentrates on whistler radiation, the analysis is not limited to it because:

- (1) It is found that no special treatment for whistler transmission is needed in finding general solutions, and the derived results can be applied for transmission for any plasma parameters as long as the cold plasma assumptions are valid.
- (2) In practice, for the transmit antenna on a satellite in the magnetosphere or ionosphere, the plasma parameters vary over very large ranges. The general solution can give directions on system design and explain the obtained data.
- (3) The radiation problem for a linear antenna in free space or an isotropic medium has been solved, and the results can be found in any antenna book. The results of the general analysis presented in this study show the convergence of the solution to the classical cases when the plasma density and/or the ambient magnetic field approaches zero.

The fluid plasma theory cannot describe the phenomena of cutoff and resonance which occur under the following conditions

$$\begin{aligned}
 X &= 1 \\
 Y &= 1 \\
 X &= 1 - Y \\
 X &= 1 + Y \\
 X &= 1 - Y^2
 \end{aligned}
 \tag{1.5}$$

Except for these special parameters there is no other limitation in the analysis of this study. The parameters for cold plasma can be divided into eight regions by the lines defined by Equation (1.5) to construct the CMA parameter diagram as shown in Figure 2. The divided 8 regions are:

- Region 1: $0 < X < 1 - Y$, $0 < Y < 1$
- Region 2: $1 - Y < X < 1 - Y^2$, $0 < Y < 1$
- Region 3: $1 - Y^2 < X < 1$, $0 < Y < 1$
- Region 4: $1 < X < 1 + Y$, $0 < Y < 1$
- Region 5: $1 + Y < X$, $0 < Y < 1$
- Region 6: $0 < X < 1$, $Y > 1$
- Region 7: $1 < X < 1 + Y$, $Y > 1$
- Region 8: $X > 1 + Y$, $Y > 1$

As is well known, the topological property of the refractive index surface of plane waves in a region is the same but may vary greatly when transitioning from one region to another. It will be shown in this study that the CMA diagram also gives a very good description for radiation property.

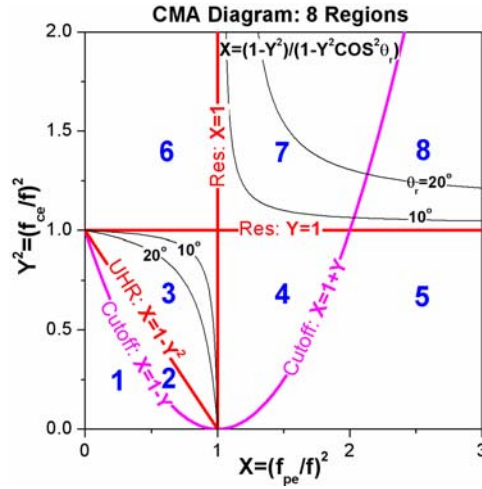


Figure 2. CMA diagram for cold plasma

2. General Solution

When the driving current density in the antenna is given, a rigorous solution of Equation (1.1) can be derived with the Green's function method. The Green's function takes the form

$$\mathbf{G}(\mathbf{r}, \mathbf{r}') = \mathbf{G}(\mathbf{r} - \mathbf{r}') = \frac{j\mu_0\omega k_0^3}{(2\pi)^3} \Lambda \int \frac{e^{-jk_0\mathbf{n}\cdot(\mathbf{r}-\mathbf{r}')}}{\det(\mathbf{\Gamma})} d\mathbf{n} \quad (2.1)$$

The detailed derivation is given in Appendix A. In Equation (2.1), $\int \dots d\mathbf{n}$ is a simplified notation of the three-dimensional integral $\iiint \dots dn_x dn_y dn_z$ over the entire n -space. The refractive index vector of plane wave, \mathbf{n} , is defined proportional to the wave vector, \mathbf{k} , with

$$\mathbf{k} = k_0 \mathbf{n} \quad (2.2)$$

The coordinate axes of the n -space are set parallel to that of the observing or the source coordinate system so that

$$\begin{aligned} \mathbf{n} &= (n_x, n_y, n_z) = (n, n_\theta, n_\phi) = (n_\rho, n_\phi, n_z) \\ \mathbf{n} &= (n_{x'}, n_{y'}, n_{z'}) \end{aligned} \quad (2.3)$$

In Equation (2.1) Λ is a differential operator with respect to the coordinates of the observing point, \mathbf{r} , and its expression in the Cartesian coordinate system is given in a matrix form as shown by Equation (A26) in Appendix A. The expression of the determinant $\det(\mathbf{\Gamma})$ is given in spherical coordinates as

$$\det(\mathbf{\Gamma}) = k_0^6 \begin{bmatrix} (\varepsilon_1 \sin^2 \theta + \varepsilon_3 \cos^2 \theta) n^4 \\ + ((\varepsilon_2^2 - \varepsilon_1^2) \sin^2 \theta - \varepsilon_1 \varepsilon_3 (1 + \cos^2 \theta)) n^2 \\ + (\varepsilon_1^2 - \varepsilon_2^2) \varepsilon_3 \end{bmatrix}, \quad (2.4a)$$

and in the cylindrical coordinate system as

$$\det(\Gamma) = k_0^6 \begin{bmatrix} \varepsilon_3 n_z^4 + ((\varepsilon_1 + \varepsilon_3) n_\rho^2 - 2\varepsilon_1 \varepsilon_3) n_z^2 \\ + \varepsilon_1 n_\rho^4 + (\varepsilon_2^2 - \varepsilon_1^2 - \varepsilon_1 \varepsilon_3) n_\rho^2 \\ + (\varepsilon_1^2 - \varepsilon_2^2) \varepsilon_3 \end{bmatrix} \quad (2.4b)$$

Then the solution of Equation (1.1), the electric field, takes the form

$$\mathbf{E}(\mathbf{r}) = \int_S \mathbf{G}(\mathbf{r}, \mathbf{r}_s) \cdot \mathbf{J}_s(\mathbf{r}_s) d\mathbf{r}_s = \frac{j\mu_0 \omega k_0^3}{(2\pi)^3} \int_S \left[\Lambda \int \frac{e^{-jk_0 \mathbf{n} \cdot (\mathbf{r} - \mathbf{r}_s)}}{\det(\Gamma)} d\mathbf{n} \right] \cdot \mathbf{J}_s(\mathbf{r}_s) d\mathbf{r}_s \quad (2.5)$$

where the integration is over the antenna current source region S.

The evaluation of the transmitted field as expressed in Equation (2.5) involves three computational operations: a differential operation with respect to the observing point, integration over the whole n -space, and integration over the source current region. These three operations are independent and the computation order is optional. Since, in general, the differential operation is easier than integration, and a function after a differential operation turns out to be even more complicated, here we always do the differential operation last to keep the integrand in the integrations as simple as possible. Then there are two ways to evaluate the electric field, i.e.,

$$\mathbf{E}(\mathbf{r}) = \Lambda \cdot \frac{j\mu_0 \omega k_0^3}{(2\pi)^3} \int_S d\mathbf{r}' \left\{ \mathbf{J}(\mathbf{r}') \int d\mathbf{n} \left[\frac{e^{-jk_0 \mathbf{n} \cdot (\mathbf{r} - \mathbf{r}')}}{\det(\Gamma)} \right] \right\} \quad (2.7)$$

or

$$\begin{aligned} \mathbf{E}(\mathbf{r}) &= \Lambda \cdot \frac{j\mu_0 \omega k_0^3}{(2\pi)^3} \int d\mathbf{n} \left\{ \frac{e^{-jk_0 \mathbf{n} \cdot \mathbf{r}}}{\det(\Gamma)} \mathbf{J}(\mathbf{n}) \right\} \\ \mathbf{J}(\mathbf{n}) &= \int_S d\mathbf{r}' \left[e^{-jk_0 \mathbf{n} \cdot \mathbf{r}'} \mathbf{J}(\mathbf{r}') \right] \end{aligned} \quad (2.8)$$

Equation (2.7) has a clear physical meaning: the inner integration over the n -space represents the contribution of a “point source” at \mathbf{r}' , and the total transmitted field at an observing point \mathbf{r} is the superposition of all contributions from the current source. In Equation (2.8), the Fourier transform is performed first for the current source, and the total transmitted field is the superposition of all wave components in the spatial spectrum.

For the radiation problem in an isotropic medium, as is well known, it is very convenient to introduce a vector potential and the transmitted magnetic field can be expressed as a result of differential operation (the curl) acting on the vector potential. For the anisotropic medium, the problem is more complicated, and it is difficult to define a similar gauged vector potential unless some approximations are made. Now in the anisotropic medium, as indicated by Equations (2.7) or (2.8), the transmitted electric field can be expressed by a differential operator acting on a vector,

$$\begin{aligned}\mathbf{E}(\mathbf{r}) &= \mathbf{A} \cdot \mathbf{A}(\mathbf{r}) \\ \mathbf{H}(\mathbf{r}) &= \frac{j}{\mu_0 \omega} \nabla \times \mathbf{E}(\mathbf{r})\end{aligned}\tag{2.9}$$

The vector $\mathbf{A}(\mathbf{r})$ is referred to as the general vector potential,

$$\mathbf{A}(\mathbf{r}) = \frac{j\mu_0\omega k_0^3}{(2\pi)^3} \int d\mathbf{n} \left\{ \frac{e^{-jk_0\mathbf{n}\cdot\mathbf{r}}}{\det(\Gamma)} \int_S d\mathbf{r}' \left[e^{-jk_0\mathbf{n}\cdot\mathbf{r}'} \mathbf{J}(\mathbf{r}') \right] \right\}\tag{2.10}$$

or

$$\begin{aligned}\mathbf{A}(\mathbf{r}) &= \frac{j\mu_0\omega k_0^3}{(2\pi)^3} \int d\mathbf{n} \left\{ \frac{e^{-jk_0\mathbf{n}\cdot\mathbf{r}}}{\det(\Gamma)} \mathbf{J}(\mathbf{n}) \right\} \\ \mathbf{J}(\mathbf{n}) &= \int_S d\mathbf{r}' \left[e^{-jk_0\mathbf{n}\cdot\mathbf{r}'} \mathbf{J}(\mathbf{r}') \right]\end{aligned}\tag{2.11}$$

Equations (2.9) through (2.11) give the general solution of the radiation Equation (1.1) for any prescribed driving current in the physics model. It is found that Equation (2.11) is more convenient for computation of the general vector potential and it will be used in the analysis.

3. Antenna Current Model

The current wave in an infinite long wire immersed in the uniform magnetoplasma has been investigated by [Ishizone et al., 1971] based on wave theory, and the result given in a series form that satisfies the boundary condition on the wire surface. For an electrically thin wire with arbitrary orientation angle ψ , Ishizone's primary term can well be approximated to a line current wave,

$$I(z') = I_A e^{-jk_0\gamma z'}\tag{3.1}$$

With regard to a linear antenna with finite length, the current wave is propagating from the feed point to both ends, and reflected there. The current along the antenna can then be written in the form

$$I(z') = I_1 e^{-jk_0\gamma|z'|} + I_2 e^{+jk_0\gamma|z'|}\tag{3.2}$$

The boundary condition that the current vanishes at the both ends, $I(\pm L) = 0$, requires that $I_2 = -I_1 e^{-j2k_0\gamma L}$. The antenna current is therefore

$$I(z') = I_1 \left(e^{-jk_0\gamma|z'|} - e^{-j2k_0\gamma L} e^{+jk_0\gamma|z'|} \right)\tag{3.3}$$

Without losing generality, it can be rewritten as

$$I(z') = I_A \sin(k_0 \gamma (L - |z'|)), \quad |z'| \leq L$$

$$I_A \equiv \frac{I_0}{\sin(k_0 \gamma L)} \quad (3.4)$$

where the quantity I_0 is the current at the feed point of the antenna.

The above current model is derived based on the transmission line theory and it has been used to estimate the impedance of an antenna in magnetoplasma [Ishizone et al., 1971]. The propagation constant, γ , depends on the plasma parameters and the antenna orientation, and the dependence is different for long and short antennas. The propagation constants for the two limiting cases are given below.

For long antennas:

$$\gamma = \left(\varepsilon_1 (\varepsilon_1 \cos^2 \psi + \varepsilon_3 \sin^2 \psi) \right)^{1/4}, \quad -\pi/2 < \arg(\gamma) \leq 0, \quad (3.5)$$

and for short antennas:

$$\gamma = \left(\varepsilon_1 (\varepsilon_1 \cos^2 \psi + \varepsilon_3 \sin^2 \psi) \right)^{1/2}, \quad -\pi < \arg(\gamma) \leq 0 \quad (3.6)$$

It is not clear what the boundary of the two cases is, and what the expression should be if the antenna is neither long nor short. Anyhow, as this model gives an analytical description of the current, in principle, for any length and any orientation of the antenna, it is used as the antenna current model in this study.

It is interesting to point out that, when the ambient magnetic field vanishes, $\varepsilon_2 = 0$ and $\varepsilon_1 = \varepsilon_3 = \varepsilon$, the model reduces to the isotropic case

$$\gamma = \sqrt{\varepsilon}$$

$$I(z') = \frac{I_0}{\sin(k_0 \sqrt{\varepsilon} L)} \sin(k_0 \sqrt{\varepsilon} (L - |z'|)) \quad (3.7)$$

And when the electron density of the plasma approaches zero, the current distribution reduces to the free space case

$$I(z') = \frac{I_0}{\sin(k_0 L)} \sin(k_0 (L - |z'|)) \quad (3.8)$$

Based on this prescribed current model, the radiation field in free space is well known giving the classical result of antenna theory.

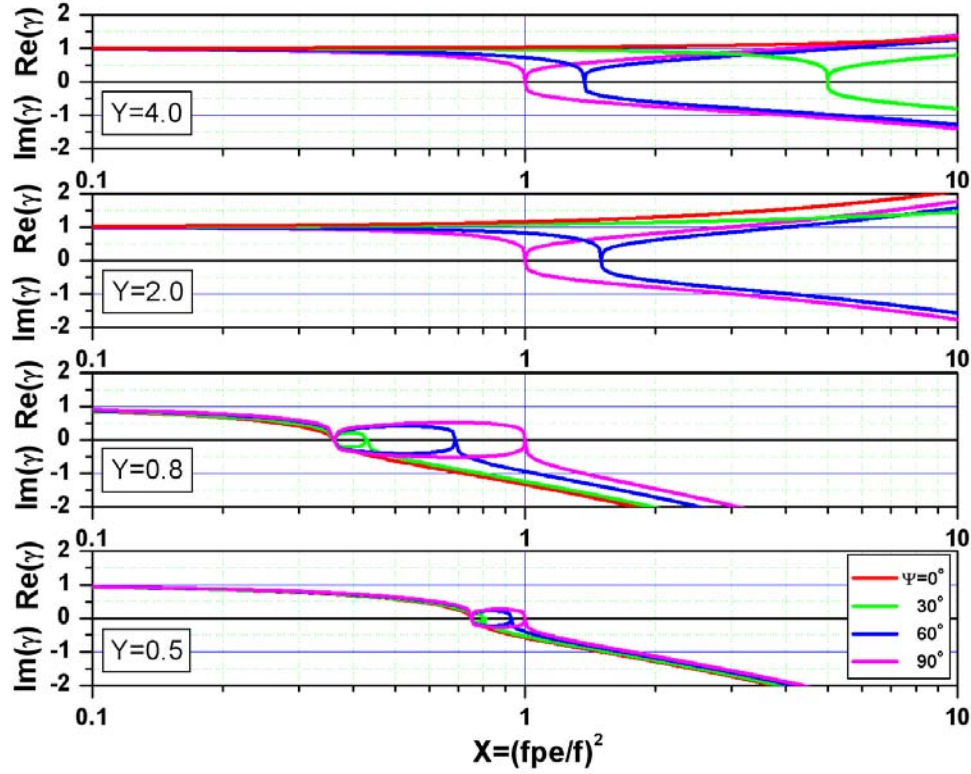


Figure 3. Current model for collisionless plasma

For collisional plasma the current propagation factor is always a non-zero complex number. We are more interested in collisionless electron magnetoplasma and in this case the current propagation factor (3.5) or (3.6) becomes

$$\gamma = \left[\left(1 - \frac{X}{X_{01}} \right) \left(1 - \frac{X}{X_{02}} \right) \right]^u, \quad u = 1/4 \text{ or } 1/2 \quad (3.9)$$

$$X_{01} \equiv 1 - Y^2, \quad X_{02} \equiv \frac{1 - Y^2}{1 - Y^2 \sin^2 \Psi},$$

The real and imaginary parts are plotted in Figure 3 as a function of the variable X with given values of Y and Ψ . Analyzing Equation (3.9) reveals the general features of the current model:

- 1) $\gamma \rightarrow 1$ when $X \rightarrow 0$. It means that for very low plasma densities or very high frequency the antenna current approaches the free space case.
- 2) $\gamma \rightarrow n = (1 - X)^{1/2}$ when $Y \rightarrow 0$. It means that for very weak ambient magnetic field or very high frequency the medium can be treated as isotropic.

- 3) When $X < 1$ and $Y < 1$, there are two zero points: one ($X = X_{01}$) is located where the upper hybrid resonance occurs, and the other ($X = X_{02}$) is dependant on the antenna orientation angle. If the orientation angle $\psi \rightarrow 0$, i.e., the case when the antenna is in the direction of the magnetic field, the two zeroes merge to one. The real and imaginary parts of the factor vary with the plasma parameters.

$$\text{Re}(\gamma) \begin{cases} > 0, \text{ if } X < X_{02} \\ = 0, \text{ if } X \geq X_{02} \end{cases}, \quad \text{Im}(\gamma) \begin{cases} = 0, \text{ if } X \leq X_{01} \text{ or } X = X_{02} \\ < 0, \text{ if } X > X_{01} \end{cases} \quad (3.10)$$

- 4) If $X > 1$ and $Y > 1$, it is a real number for small orientation angles, and has one zero point for larger orientation angles as summarized by

$$\begin{cases} \text{Re}(\gamma) > 0 \text{ and } \text{Im}(\gamma) = 0, \text{ if } X < X_{02} \\ \gamma = 0, \text{ if } X = X_{02} \\ \text{Re}(\gamma) > 0 \text{ and } \text{Im}(\gamma) < 0, \text{ if } X > X_{02} \end{cases} \quad (3.11)$$

In the parameter range of ($X < 1$, $Y < 1$ and $X + Y^2 > 1$) or ($X > 1$ and $Y > 1$), an angle α_{SRC} can be defined by

$$\alpha_{SRC} = \arctan \sqrt{\frac{X + Y^2 - 1}{(1 - X)(1 - Y^2)}} \quad (3.12)$$

If $\psi = \alpha_{RSC}$, then $\gamma = 0$.

It should be stressed that, even for collisionless plasma, the propagation factor may be a complex number and it means that both amplitude and initial phase of the antenna current vary with the distance from the feed point. An example is shown in Figure 4 for a half-wave dipole ($k_0 L = \pi / 2$) in a collisionless magnetoplasma with $X=0.5$, $Y=0.8$. In this figure, the relative amplitude and initial phase $I(z'/L)/I(0)$ are plotted for two antenna orientation angles $\psi = 30^\circ$, 60° . For reference, the current for the free space case is also shown in the figure. When the orientation angle $\psi = 30^\circ$, the factor is a pure imaginary number ($\gamma \approx -0.5j$), and the amplitude decreases exponentially while the initial phase at anywhere at the antenna is the same as at the feed port. In this case, the two branches of the antenna are inversely charged but the charge polarities of any two points in the same branch are always the same. For the case $\psi = 60^\circ$, the factor is a complex number ($\gamma \approx (0.41 - 0.41j)$). The amplitude decreases exponentially and the initial phase varies with the distance from the feed point, which means that the charge polarity at a point in a branch may different from that in its neighborhood at a given time.

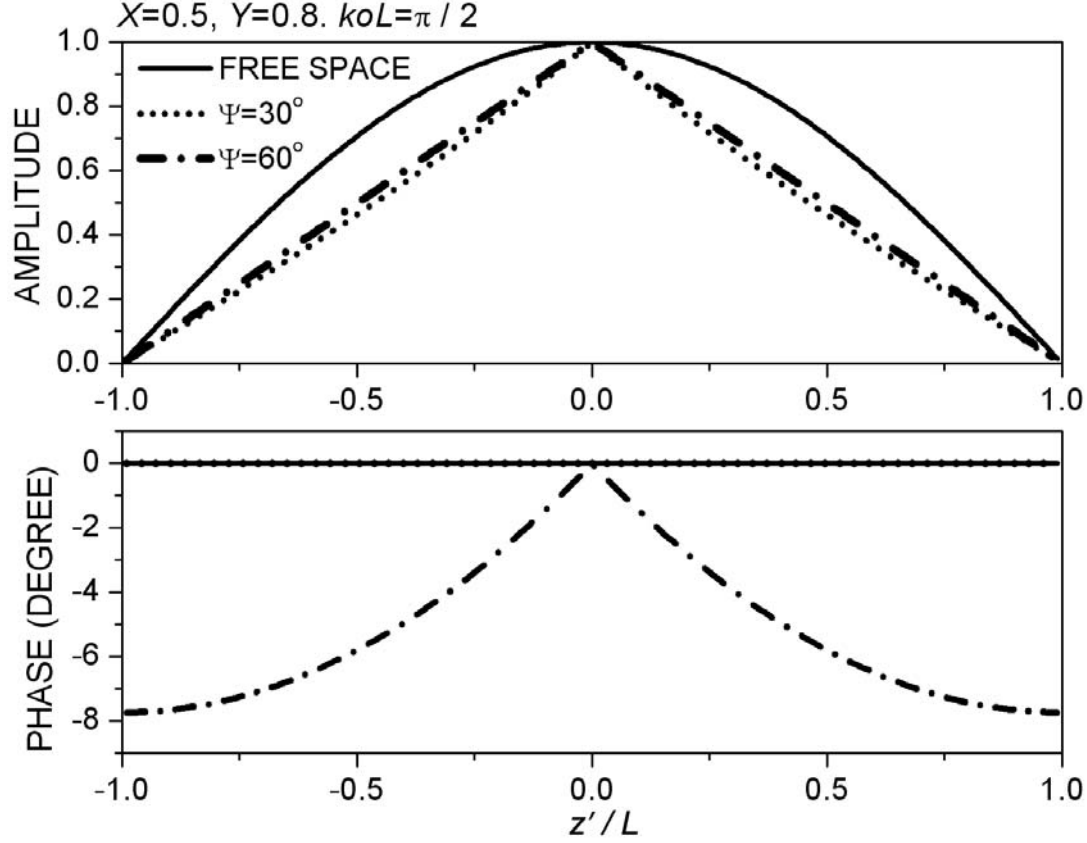


Figure 4. Amplitude and phase at a $\lambda/2$ dipole

4. Evaluation of the General Vector Potential

4.1 Decomposition into two wave modes

The current along the electrically thin antenna is modeled as a line current and the current density in the source coordinate system is a delta-function,

$$\mathbf{J}(\mathbf{r}') = \hat{\mathbf{Z}}_s I_A \sin(k_0 \gamma (L - |z'|)) \delta(x') \delta(y'), \quad -L \leq z' \leq L \quad (4.1)$$

where the vector $\hat{\mathbf{Z}}_s$ denotes a unit vector in the direction of the z' -axis. The Fourier transform of the antenna current is

$$\mathbf{J}(\mathbf{n}) = \int_S d\mathbf{r}' \left[e^{-j\mathbf{k}_0 \mathbf{n} \cdot \mathbf{r}'} \mathbf{J}(\mathbf{r}') \right] = \hat{\mathbf{Z}}_s \frac{2\gamma I_A}{k_0} \frac{\cos(k_0 n_z L) - \cos(k_0 \gamma L)}{\gamma^2 - n_z^2} \quad (4.2)$$

The component of the refractive index vector on the z' -axis, n_z , can be expressed in terms of its spherical components:

$$n_z = n (\sin \theta \cos \varphi \sin \psi + \cos \theta \cos \psi), \quad (4.3)$$

and in the cylindrical coordinate system

$$n_{z'} = n_\rho \cos \varphi \sin \psi + n_z \cos \psi \quad (4.4)$$

With the Fourier transform of the antenna current, Equation (4.2), the general vector potential expressed by Equation (2.11) becomes

$$\mathbf{A}(\mathbf{r}) = \hat{\mathbf{Z}}_s \frac{j\mu_0\omega k_0^3}{(2\pi)^3} \int d\mathbf{n} \left[\frac{e^{-jk_0\mathbf{n}\cdot\mathbf{r}}}{\det(\Gamma)} \frac{2\gamma I_A}{k_0} \frac{\cos(k_0 n_{z'} L) - \cos(k_0 \gamma L)}{\gamma^2 - n_{z'}^2} \right] \quad (4.5)$$

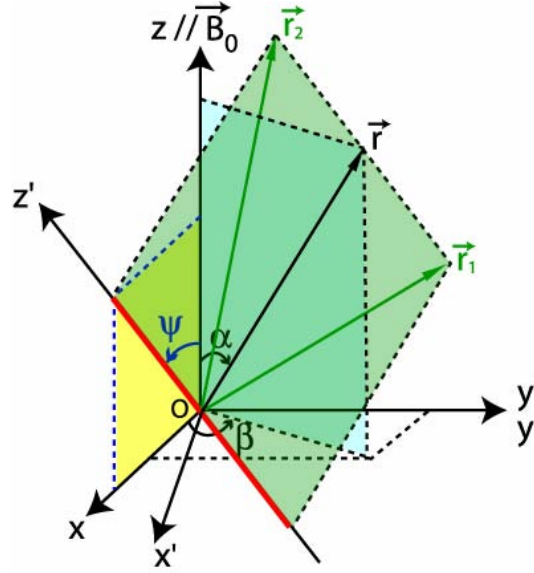


Figure 5. Decomposition of the general vector potential

Introducing the vectors shown in Figure 5:

$$\begin{aligned} \mathbf{L} &= \hat{\mathbf{Z}}_s L \\ \mathbf{r}_1 &= \mathbf{r} - \mathbf{L} \\ \mathbf{r}_2 &= \mathbf{r} + \mathbf{L} \end{aligned} \quad (4.6)$$

and noting that

$$\cos(k_0 L n_{z'}) = \frac{e^{jk_0\mathbf{n}\cdot\mathbf{L}} + e^{-jk_0\mathbf{n}\cdot\mathbf{L}}}{2} \quad (4.7)$$

the general vector potential (4.5) can be expressed as a linear composition of the same functional vector at three points \mathbf{r}_1 , \mathbf{r}_2 and \mathbf{r} ,

$$\mathbf{A}(\mathbf{r}) = \frac{1}{2} \mathbf{A}_0(\mathbf{r}_1) + \frac{1}{2} \mathbf{A}_0(\mathbf{r}_2) - \cos(k_0 \gamma L) \mathbf{A}_0(\mathbf{r}) \quad (4.8)$$

This treatment simplifies the evaluation considerably as only one functional vector depending on the location needs to be analyzed,

$$\mathbf{A}_0(\mathbf{r}) = \hat{\mathbf{Z}}_s \frac{j\mu_0\omega k_0^2 I_A}{(2\pi)^3} \int d\mathbf{n} \left[\frac{e^{-jk_0\mathbf{n}\cdot\mathbf{r}}}{\det(\Gamma)} \frac{2\gamma}{\gamma^2 - n_z^2} \right] \quad (4.9)$$

Furthermore it is evident that the involved integrand is simpler than the one in Equation (4.5).

It should be pointed out that the approach to separate the general vector potential into three parts makes it possible to analyze the radiation problem for an asymmetrical dipole antenna in case the two arms of the antenna were not extended perfectly in space.

It is important to select a proper coordinate system to evaluate the general vector potential. As explained in Appendix F it seems that the spherical coordinate system is not convenient. In fact, because of the symmetrical property of the medium as implied by Equation (1.2), plane waves can propagate along the ambient magnetic field and cylindrical waves in the perpendicular direction. It should therefore be possible to represent the result of Equation (4.9) as a superposition of such waves. In order to do this it is more convenient to use the cylindrical coordinate system and the integration will be performed over the whole \mathbf{n} -space such that $d\mathbf{n} = n_\rho dn_\rho d\varphi dn_z$, $n_\rho \in [0, \infty]$, $\varphi \in [0, 2\pi]$, $n_z \in [-\infty, +\infty]$.

In the cylindrical coordinate system, the expression for the determinant, Equation (2.4b), can be factorized,

$$\det(\Gamma) = k_0^6 \varepsilon_3 \left(n_z^2 - n_{z+}^2 \right) \left(n_z^2 - n_{z-}^2 \right) \quad (4.10)$$

where

$$\begin{aligned} n_{z\pm}^2 &= \frac{2\varepsilon_1\varepsilon_3 - (\varepsilon_1 + \varepsilon_3)n_\rho^2 + q_\pm(n_\rho)}{2\varepsilon_3} \\ q_\pm(n_\rho) &= \sqrt{(\varepsilon_1 - \varepsilon_3)^2 n_\rho^4 - 4\varepsilon_2^2 \varepsilon_3 n_\rho^2 + 4\varepsilon_2^2 \varepsilon_3^2} \\ (-\pi/2 \leq \arg(q_+) < \pi/2, \quad \pi/2 \leq \arg(q_-) < 3\pi/2) \end{aligned} \quad (4.11)$$

Note that $\det(\Gamma) = 0$ is the dispersion relation and Equation (4.11) gives the refractive index of plane waves expressed in the cylindrical coordinate system. There are two wave modes designated by “+” and “-” signs, respectively.

Substituting Equations (4.4) and (4.11) into Equation (4.9) and noting that

$$n_{z+}^2 - n_{z-}^2 = \frac{q_+(n_\rho)}{\varepsilon_3} = -\frac{q_-(n_\rho)}{\varepsilon_3}, \quad (4.12)$$

we can represent \mathbf{A}_0 as:

$$\mathbf{A}_0(\mathbf{r}) = \mathbf{A}_{0+}(\mathbf{r}) + \mathbf{A}_{0-}(\mathbf{r})$$

$$\mathbf{A}_{0\pm}(\mathbf{r}) = \hat{\mathbf{Z}}_s \frac{j\mu_0\omega I_A}{(2\pi)^3 k_0^4} \int_0^\infty dn_\rho \left\{ \frac{n_\rho}{q_\pm(n_\rho)} \int_0^{2\pi} d\varphi \left[e^{-jk_0 n_\rho \rho \cos(\varphi-\beta)} I_{z\pm}(\mathbf{r}; n_\rho, \varphi) \right] \right\} \quad (4.13)$$

$$I_{z\pm}(\mathbf{r}; n_\rho, \varphi) \equiv \int_{-\infty}^{+\infty} dn_z e^{-jk_0 n_z z} \frac{1}{n_z^2 - n_{z\pm}^2} \frac{2\gamma}{\gamma^2 - (n_\rho \cos \varphi \sin \psi + n_z \cos \psi)^2}$$

Equation (4.13) indicates that the general vector potential and thus the transmitted field can be decomposed into two parts related to the two modes of plane wave.

4.2 Integration over n_z

We can now start evaluating the general vector potential in Equation (4.13) by first carrying out the integration over n_z :

$$I_{z\pm}(\mathbf{r}; n_\rho, \varphi) \equiv \int_{-\infty}^{+\infty} dn_z e^{-jk_0 n_z z} \frac{1}{n_z^2 - n_{z\pm}^2} \frac{2\gamma}{\gamma^2 - (n_\rho \cos \varphi \sin \psi + n_z \cos \psi)^2} \quad (4.14)$$

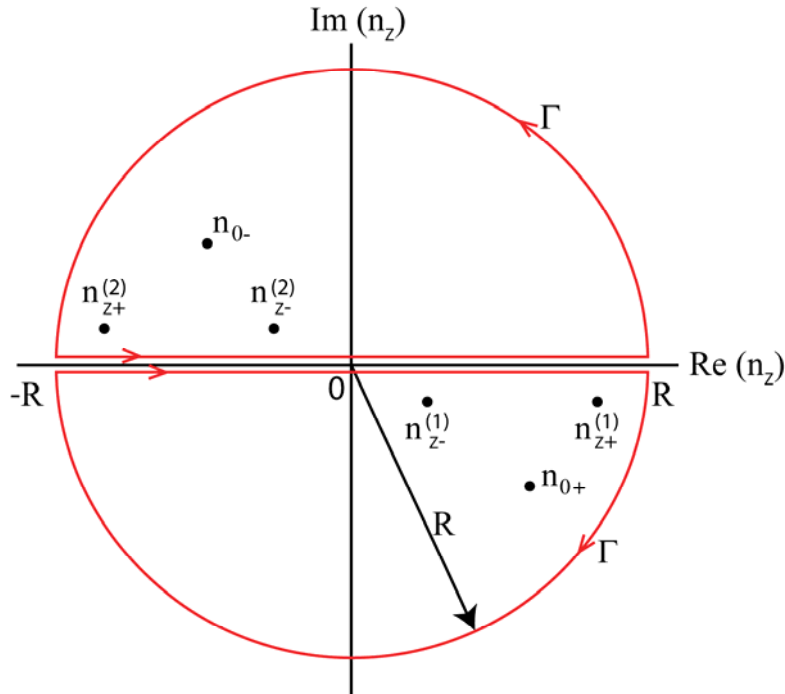


Figure 6. Integration path

For collisional plasma, one can prove that γ and $n_{z\pm}$ are complex numbers. In general, there are six simple poles of the integrand in the complex n_z -plane as illustrated in Figure 6:

$$\begin{aligned}
n_{z\pm}^{(1)} &= \sqrt{\frac{2\varepsilon_1\varepsilon_3 - (\varepsilon_1 + \varepsilon_3)n_\rho^2 + q_\pm^2}{2\varepsilon_3}}, \quad \left(-\pi < \arg(n_{z\pm}^{(1)}) < 0\right) \\
n_{z\pm}^{(2)} &= -n_{z\pm}^{(1)}, \quad \left(0 < \arg(n_{z\pm}^{(2)}) < \pi\right) \\
n_{0+} &= \frac{+\gamma - n_\rho \cos \varphi \sin \psi}{\cos \psi}, \quad n_{0-} = \frac{-\gamma - n_\rho \cos \varphi \sin \psi}{\cos \psi} \\
&\left(\psi \neq \pi/2, \quad -\pi < \arg(n_{0+}) < 0, \quad 0 < \arg(n_{0-}) < \pi\right)
\end{aligned} \tag{4.15}$$

If the antenna is perpendicular to the ambient magnetic field ($\psi = \pi/2$), the last two poles disappear. The integral $I_{z\pm}(n_\rho, \varphi)$ can be found using the residue theorem. As illustrated in Figure 6, when $z > 0$, the closed contour on the lower half plane is selected to yield

$$I_{z\pm}(\mathbf{r}; n_\rho, \varphi) = -2\pi j \times \left\{ \begin{aligned} &\frac{e^{-jk_0 n_{z\pm}^{(1)} z}}{n_{z\pm}^{(1)}} \frac{\gamma}{\gamma^2 - (n_\rho \cos \varphi \sin \psi + n_{z\pm}^{(1)} \cos \psi)^2} \\ &+ \cos \psi \frac{e^{\frac{-jk_0}{\cos \psi} \frac{+\gamma - n_\rho \cos \varphi \sin \psi}{z} z}}{(n_{z\pm}^{(1)} \cos \psi)^2 - (\gamma - n_\rho \cos \varphi \sin \psi)^2} \end{aligned} \right\}, \quad (z > 0) \tag{4.16}$$

When $z < 0$, the closed contour on the upper half plane is selected to yield

$$I_{z\pm}(\mathbf{r}; n_\rho, \varphi) = +2\pi j \times \left\{ \begin{aligned} &\frac{e^{-jk_0 n_{z\pm}^{(2)} z}}{n_{z\pm}^{(2)}} \frac{\gamma}{\gamma^2 - (n_\rho \cos \varphi \sin \psi + n_{z\pm}^{(2)} \cos \psi)^2} \\ &- \cos \psi \frac{e^{\frac{-jk_0}{\cos \psi} \frac{-\gamma - n_\rho \cos \varphi \sin \psi}{z} z}}{(n_{z\pm}^{(2)} \cos \psi)^2 - (\gamma + n_\rho \cos \varphi \sin \psi)^2} \end{aligned} \right\}, \quad (z < 0) \tag{4.17}$$

Introducing a sign function

$$\text{sgn}(z) = \begin{cases} -1, & \text{if } z < 0 \\ 0, & \text{if } z = 0 \\ +1, & \text{if } z > 0 \end{cases} \tag{4.18}$$

and noting that $n_{z\pm}^{(2)} = -n_{z\pm}^{(1)}$, one can combine the two expressions (4.16) and (4.17) to one

$$\begin{aligned}
I_{z\pm}(\mathbf{r}; n_\rho, \varphi) &= -2\pi j \times \left\{ \begin{aligned} &\frac{e^{-jk_0 n_{z\pm} \text{sgn}(z) z}}{n_{z\pm}} \frac{\gamma}{\gamma^2 - (n_\rho \cos \varphi \sin \psi + n_{z\pm} \text{sgn}(z) \cos \psi)^2} \\ &+ \cos \psi \frac{e^{\frac{-jk_0}{\cos \psi} \frac{\text{sgn}(z) \gamma - n_\rho \cos \varphi \sin \psi}{z} z}}{(n_{z\pm} \cos \psi)^2 - (\text{sgn}(z) \gamma - n_\rho \cos \varphi \sin \psi)^2} \end{aligned} \right\}, \\
&\quad (z \neq 0; \quad -\pi < \arg(n_{z\pm}) < 0)
\end{aligned} \tag{4.19}$$

In the above equation, the superscript was omitted while keeping in mind that $n_{z\pm}$ are the singular points located in the lower half of the n_z -plane for either $z>0$ and $z<0$.

For collisionless plasma the singular points are located on the real or imaginary axis of the n_z -plane and the integration results will be different. As sited in Section 1, according to the limitation principle the limit of Equation (4.19) when collision approaches zero is the true solution for collisionless plasma.

The integration result of Equation (4.19) consists of two terms. As mentioned earlier the singular poles arising from the antenna orientation disappear for perpendicular antenna. It is clear that this term vanishes for perpendicular antenna when $\psi = \pi/2$. In fact, as long as the far field is concerned this term can always be disregarded for any arbitrary antenna orientation. With a constant omitted, this term is denoted by $I_{z2\pm}(\mathbf{r}; n_\rho, \varphi)$,

$$I_{z2\pm}(\mathbf{r}; n_\rho, \varphi) = \frac{e^{-jk_0 \frac{\text{sgn}(z)\gamma - n_\rho \cos \varphi \sin \psi}{\cos \psi} z}}{(n_{z\pm} \cos \psi)^2 - (\text{sgn}(z)\gamma - n_\rho \cos \varphi \sin \psi)^2} \quad (4.20)$$

According to Equation (4.6), $z_1 = z - L \cos \psi$, and $z_2 = z + L \cos \psi$, we have

$$\begin{aligned} I_{z2\pm}(\mathbf{r}_1; n_\rho, \varphi) &= \frac{e^{-jk_0 \frac{\text{sgn}(z-L\cos\psi)\gamma - n_\rho \cos \varphi \sin \psi}{\cos \psi} z_1}}{(n_{z\pm} \cos \psi)^2 - (\text{sgn}(z-L\cos\psi)\gamma - n_\rho \cos \varphi \sin \psi)^2} \\ I_{z2\pm}(\mathbf{r}_2; n_\rho, \varphi) &= \frac{e^{-jk_0 \frac{\text{sgn}(z+L\cos\psi)\gamma - n_\rho \cos \varphi \sin \psi}{\cos \psi} z_2}}{(n_{z\pm} \cos \psi)^2 - (\text{sgn}(z+L\cos\psi)\gamma - n_\rho \cos \varphi \sin \psi)^2} \\ 2\cos(k_0 L \gamma) I_{z2\pm}(\mathbf{r}; n_\rho, \varphi) &= \frac{e^{-jk_0 \frac{\text{sgn}(z)\gamma - n_\rho \cos \varphi \sin \psi}{\cos \psi} (z-L\cos\psi)}}{(n_{z\pm} \cos \psi)^2 - (\text{sgn}(z)\gamma - n_\rho \cos \varphi \sin \psi)^2} + \frac{e^{-jk_0 \frac{\text{sgn}(z)\gamma - n_\rho \cos \varphi \sin \psi}{\cos \psi} (z+L\cos\psi)}}{(n_{z\pm}^{(1)} \cos \psi)^2 - (\text{sgn}(z)\gamma - n_\rho \cos \varphi \sin \psi)^2} \end{aligned} \quad (4.21)$$

and the sum

$$\begin{aligned} &I_{z2\pm}(\mathbf{r}_1; n_\rho, \varphi) + I_{z2\pm}(\mathbf{r}_2; n_\rho, \varphi) - 2\cos(k_0 L \gamma) I_{z2\pm}(\mathbf{r}; n_\rho, \varphi) \\ &= \frac{e^{-jk_0 \frac{\text{sgn}(z-L\cos\psi)\gamma - n_\rho \cos \varphi \sin \psi}{\cos \psi} z}}{(n_{z\pm} \cos \psi)^2 - (\text{sgn}(z-L\cos\psi)\gamma - n_\rho \cos \varphi \sin \psi)^2} - \frac{e^{-jk_0 \frac{\text{sgn}(z)\gamma - n_\rho \cos \varphi \sin \psi}{\cos \psi} (z-L\cos\psi)}}{(n_{z\pm} \cos \psi)^2 - (\text{sgn}(z)\gamma - n_\rho \cos \varphi \sin \psi)^2} \\ &+ \frac{e^{-jk_0 \frac{\text{sgn}(z+L\cos\psi)\gamma - n_\rho \cos \varphi \sin \psi}{\cos \psi} z}}{(n_{z\pm} \cos \psi)^2 - (\text{sgn}(z+L\cos\psi)\gamma - n_\rho \cos \varphi \sin \psi)^2} - \frac{e^{-jk_0 \frac{\text{sgn}(z)\gamma - n_\rho \cos \varphi \sin \psi}{\cos \psi} (z+L\cos\psi)}}{(n_{z\pm} \cos \psi)^2 - (\text{sgn}(z)\gamma - n_\rho \cos \varphi \sin \psi)^2} \\ &= 0, \text{ if } |z| \geq L \cos \psi \end{aligned} \quad (4.22)$$

Equation (4.22) indicates that the field represented by the second term vanishes beyond a small region near the perpendicular direction $|z| \geq L \cos \psi$ or $r |\cos \alpha| \geq L \cos \psi$. For a point in the far region with polar angle close to the perpendicular direction, the contribution of the second term is zero as long as the distance is large enough. This suggests that the second term represents the near field and it can be dropped from Equation (4.19) as we are more interested in the far field radiation. Then only remaining term in Equation (4.19) is

$$I_{z\pm}(\mathbf{r}; n_\rho, \varphi) = -2\pi j \times \frac{e^{-jk_0 n_{z\pm} \text{sgn}(z)z}}{n_{z\pm}} \frac{\gamma}{\gamma^2 - (n_\rho \cos \varphi \sin \psi + n_{z\pm} \text{sgn}(z) \cos \psi)^2} \quad (4.23)$$

and Equation (4.13) becomes

$$\begin{aligned} \mathbf{A}_{0\pm}(\mathbf{r}) &= \hat{\mathbf{Z}}_s \frac{\mu_0 \omega I_A}{(2\pi)^2 k_0^4} \int_0^\infty dn_\rho \frac{n_\rho e^{-jk_0 n_{z\pm} \text{sgn}(z)z}}{q_\pm(n_\rho) n_{z\pm}} I_{\varphi\pm} \\ I_{\varphi\pm} &= \int_0^{2\pi} d\varphi e^{-jk_0 n_\rho \rho \cos(\varphi - \beta)} \frac{\gamma}{\gamma^2 - (n_\rho \cos \varphi \sin \psi + n_{z\pm} \text{sgn}(z) \cos \psi)^2} \\ &\quad (z \neq 0; \quad -\pi < \arg(n_{z\pm}) < 0) \end{aligned} \quad (4.24)$$

4.4 Integral representation

To evaluate the integration over the variable φ , one part of the integrand is expanded into a Bessel function series [Stratton, 1941],

$$e^{-jk_0 n_\rho \rho \cos(\varphi - \beta)} = J_0(k_0 n_\rho \rho) + 2 \sum_{u=1}^{\infty} (-j)^u J_u(k_0 n_\rho \rho) \cos u(\varphi - \beta) \quad (4.25a)$$

and the other part into a Fourier cosine series,

$$\frac{\gamma}{\gamma^2 - (n_\rho \cos \varphi \sin \psi + n_{z\pm} \text{sgn}(z) \cos \psi)^2} = \sum_{m=0}^{\infty} d_{m\pm}(n_\rho) \cos m\varphi \quad (4.25b)$$

The coefficients of the Fourier expansion, $d_{m\pm}(n_\rho)$, are determined in Appendix B. Substituting the two expansions into Equation (4.24) yields

$$\begin{aligned} I_{\varphi\pm} &= \int_0^{2\pi} d\varphi \left[J_0(k_0 n_\rho \rho) \sum_{m=0}^{\infty} d_{m\pm} \cos m\varphi \right] \\ &\quad + 2 \int_0^{2\pi} d\varphi \left[\sum_{m=0}^{\infty} d_{m\pm}(n_\rho) \sum_{u=1}^{\infty} (-j)^u J_u(k_0 n_\rho \rho) \cos u(\varphi - \beta) \cos m\varphi \right] \end{aligned} \quad (4.26)$$

It can be proved that the series in Equation (4.26) is uniformly converging with respect to the variables $n_\rho \in (0, +\infty)$ and $\varphi \in (0, 2\pi)$ and so the summation and integration in Equation (4.26) can be exchanged to yield

$$I_{\varphi\pm} = 2\pi \sum_{m=0}^{\infty} d_{m\pm} (-j)^m J_m(k_0 n_\rho \rho) \cos m\beta \quad (4.27)$$

Finally Equation (4.24) takes the form of an integral representation,

$$\mathbf{A}_{0\pm}(\mathbf{r}) = \hat{\mathbf{Z}}_S \frac{\mu_0 \omega I_A}{2\pi k_0^4} \sum_{m=0}^{\infty} (-j)^m \int_0^{\infty} dn_{\rho} \frac{n_{\rho}}{q_{\pm}(n_{\rho})n_{z\pm}} d_{m\pm} e^{-jk_0 n_{z\pm} \text{sgn}(z)z} J_m(k_0 n_{\rho} \rho) \cos m\beta \quad (4.28)$$

We could proceed to perform the integration and represent the result in terms of supergeometric series; however, this has no merits as far as the far field analysis is concerned.

The following formulae summarize our analysis:

$$\begin{aligned} \mathbf{A}(\mathbf{r}) &= \mathbf{A}_+(\mathbf{r}) + \mathbf{A}_-(\mathbf{r}) \\ \mathbf{A}_{\pm}(\mathbf{r}) &= \frac{1}{2} \mathbf{A}_{0\pm}(\mathbf{r}_1) + \frac{1}{2} \mathbf{A}_{0\pm}(\mathbf{r}_2) - \cos(k_0 L \gamma) \mathbf{A}_{0\pm}(\mathbf{r}) \\ \mathbf{r}_1 &= \mathbf{r} - \mathbf{L}, \quad \mathbf{r}_2 = \mathbf{r} + \mathbf{L}, \quad \mathbf{L} = \hat{\mathbf{Z}}_S L \\ \mathbf{A}_{0\pm}(\mathbf{r}) &= \hat{\mathbf{Z}}_S \frac{\mu_0 \omega I_A}{2\pi k_0^4} \sum_{m=0}^{\infty} (-j)^m \cos m\beta \int_0^{\infty} dn_{\rho} \frac{n_{\rho} d_{m\pm}}{q_{\pm}(n_{\rho})n_{z\pm}} e^{-jk_0 \text{sgn}(z)n_{z\pm}z} J_m(k_0 n_{\rho} \rho), \quad (z \neq 0) \\ n_{z\pm} &= \left(\frac{2\varepsilon_1 \varepsilon_3 - (\varepsilon_1 + \varepsilon_3)n_{\rho}^2 + q_{\pm}(n_{\rho})}{2\varepsilon_3} \right)^{1/2}, \quad (-\pi < \arg(n_{z\pm}) < 0) \\ q_{\pm}(n_{\rho}) &= \left((\varepsilon_1 - \varepsilon_3)^2 n_{\rho}^4 - 4\varepsilon_2^2 \varepsilon_3 n_{\rho}^2 + 4\varepsilon_2^2 \varepsilon_3^2 \right)^{1/2} \\ &(-\pi/2 \leq \arg(q_+) < \pi/2, \quad \pi/2 \leq \arg(q_-) < 3\pi/2) \end{aligned} \quad (4.29)$$

The transmitted field is composed of two wave modes. The general vector potential of each mode at any observing point, \mathbf{r} , is expressed as a linear composition of the same functional vectors at the points \mathbf{r}_1 , \mathbf{r}_2 , and \mathbf{r} . Each vector component is given in integral form, as expected, representing a superposition of waves, which look like plane waves along the ambient magnetic field, and like cylindrical waves in the perpendicular direction.

5. Asymptotic Form of the General Vector Potential

We concentrate our interests in the analysis of the transmitted far field. This can be achieved by examining the asymptotic form of the general vector potential.

Substituting the asymptotic form of the Bessel function when $\rho \rightarrow \infty$,

$$J_m(k_0 n_{\rho} \rho) \Rightarrow \left(\frac{2}{\pi k_0 n_{\rho} \rho} \right)^{1/2} \cos \left(k_0 n_{\rho} \rho - \frac{m\pi}{2} - \frac{\pi}{4} \right) \quad (5.1)$$

into Equation (4.29), one obtains

$$\mathbf{A}_{0\pm}(\mathbf{r}) \Rightarrow \hat{\mathbf{Z}}_S \frac{\mu_0 \omega I_A}{2\pi k_0^4} \sum_{m=0}^{\infty} (-j)^m \cos m\beta \left(\frac{1}{2\pi k_0 \rho} \right)^{1/2} \left\{ \begin{aligned} &\int_0^{\infty} dn_{\rho} \frac{\sqrt{n_{\rho}} d_{m\pm}}{q_{\pm}(n_{\rho})n_{z\pm}} e^{+j\frac{m+1/2}{2}\pi} e^{-jk_0(n_{z\pm}|\cos\alpha|+n_{\rho}\sin\alpha)r} \\ &+ \int_0^{\infty} dn_{\rho} \frac{\sqrt{n_{\rho}} d_{m\pm}}{q_{\pm}(n_{\rho})n_{z\pm}} e^{-j\frac{m+1/2}{2}\pi} e^{-jk_0(n_{z\pm}|\cos\alpha|-n_{\rho}\sin\alpha)r} \end{aligned} \right\} \quad (5.2)$$

Here the symbol “ \Rightarrow ” is used to denote an asymptotic relation. Exchanging the variable n_ρ with $-n_\rho$ in the second integral and noting that for even functions

$q_\pm(-n_\rho) = q_\pm(n_\rho)$, $n_{z\pm}(-n_\rho) = n_{z\pm}(n_\rho)$, and $d_m(-n_\rho) = (-1)^m d_m(n_\rho)$, given in Appendix B, one can combine the two terms into one integral over the whole real values of n_ρ from negative to positive infinity:

$$\mathbf{A}_{0\pm}(\mathbf{r}) \Rightarrow \hat{\mathbf{Z}}_s \frac{\mu_0 \omega I_A}{2\pi k_0^4} \sum_{m=0}^{\infty} e^{j\pi/4} \cos m\beta \left(\frac{1}{2\pi k_0 \rho} \right)^{1/2} \int_{-\infty}^{\infty} dn_\rho \frac{\sqrt{n_\rho} d_{m\pm}}{q_\pm n_{z\pm}} e^{-jk_0(n_{z\pm}|\cos\alpha| + n_\rho \sin\alpha)r} \quad (5.3)$$

The sign of square root in Equation (5.3) is not important since the current at the feed point is arbitrary anyway. It should be pointed out that in the above derivation two cases had been excluded: $\alpha = 0$ ($\rho = 0$) and $\alpha = \pi/2$ ($z=0$). For the parallel direction the Bessel asymptotic in Equation (5.1) does not hold and the perpendicular direction is not included in the expression of the general vector potential as shown by Equation (4.29). However, the general vector potential is introduced as an intermediate parameter for computation of the electro-magnetic field and essentially has no direct physical meaning. We have the freedom to choose the values for these two special cases and define them as the limits of the general solution when $\alpha \rightarrow 0$ and $\alpha \rightarrow \pi/2$. From now on the asymptotic expression of the general vector potential, Equation (5.3), is valid for any far point in the observing coordinate system.

A function of refractive index is introduced:

$$\begin{aligned} n_s(n_\rho) &= n_z(n_\rho) |\cos\alpha| + n_\rho \sin\alpha \\ n_z(n_\rho) &= \left[\frac{2\varepsilon_1\varepsilon_3 - (\varepsilon_1 + \varepsilon_3)n_\rho^2 + q(n_\rho)}{2\varepsilon_3} \right]^{1/2} \\ q(n_\rho) &= \left[(\varepsilon_1 - \varepsilon_3)^2 n_\rho^4 - 4\varepsilon_2^2 \varepsilon_3 n_\rho^2 + 4\varepsilon_2^2 \varepsilon_3^2 \right]^{1/2} \end{aligned} \quad (5.4)$$

Then Equation (5.3) becomes

$$\mathbf{A}_{0\pm}(\mathbf{r}) \Rightarrow \hat{\mathbf{Z}}_s \frac{\mu_0 \omega I_A}{2\pi k_0^4} \sum_{m=0}^{\infty} e^{j\pi/4} \cos m\beta \left(\frac{1}{2\pi k_0 \rho} \right)^{1/2} \int_{-\infty}^{\infty} dn_\rho \frac{\sqrt{n_\rho} d_{m\pm}}{q_\pm n_{z\pm}} e^{-jk_0 n_s r} \quad (5.5)$$

The integrand function in Equation (5.5) has no singular points since it can be proved that $q_\pm(n_\rho) \neq 0$ and $n_{z\pm}(n_\rho) \neq 0$ hold for any real n_ρ . The integrand function is analytically extended and the integral path of the real axis is deformed to the steepest descent through the saddle point so as to get the asymptotic form of the integral. This process can use the formula [Felsen, 1995]

$$I(\Omega) = \int f(z) e^{\Omega \Phi(z)} dz \xrightarrow{\Omega \rightarrow \infty} \left(\frac{-2\pi}{\Omega \Phi''(z_s)} \right)^{1/2} f(z_s) e^{\Omega \Phi(z_s)}$$

$$\Phi'(z_s) \equiv \left. \frac{d\Phi(z)}{dz} \right|_{z=z_s} = 0, \quad \Phi''(z_s) \equiv \left. \frac{d^2\Phi(z)}{dz^2} \right|_{z=z_s} \neq 0 \quad (5.6)$$

In Equation (5.6), $z = z_s$ is the saddle point. If there is more than one saddle point, the contributions from all saddle points should be taken into account and the asymptotic solution is the sum of all contributions. But at this moment it is assumed that there is only one single saddle point.

Now the saddle points are the roots of the equation $\frac{dn_s(n_\rho)}{dn_\rho} = 0$, i.e.,

$$n_\rho \left[-(\varepsilon_1 + \varepsilon_3)q(n_\rho) + (\varepsilon_1 - \varepsilon_3)^2 n_\rho^2 - 2\varepsilon_2^2 \varepsilon_3 \right] \cos \alpha + 2\varepsilon_3 n_z(n_\rho)q(n_\rho) \sin \alpha = 0 \quad (5.7)$$

It is clear that the saddle points are symmetric with respect to the perpendicular direction and one need only find the roots for the range $0 \leq \alpha \leq \pi/2$.

The function of refractive index in Equation (5.4) is defined in the whole complex n_ρ -plane. The function is multi-valued and the Riemann surface consists of four sheets, which are connected at the branch points. There are eight branch points: The four branch points are derived from $q(n_\rho) = 0$, referred to as the q -branch points, and the other four from $n_z(n_\rho) = 0$, referred to as the n_z -branch points. The positions of the eight branch points in the complex n_ρ -plane depend on the plasma parameters:

$$n_\rho \Big|_{n_z=0}^{(1,2)} = \pm \sqrt{\varepsilon_3}, \quad n_\rho \Big|_{n_z=0}^{(3,4)} = \pm \sqrt{\frac{\varepsilon_1^2 - \varepsilon_2^2}{\varepsilon_1}}$$

$$n_\rho \Big|_{q=0}^{(1,2,3,4)} = \pm \frac{\sqrt{2\varepsilon_2\varepsilon_3}}{\varepsilon_1 - \varepsilon_3} \sqrt{\varepsilon_2 \pm \sqrt{\varepsilon_2^2 - (\varepsilon_1 - \varepsilon_3)^2}} \quad (5.8)$$

The eight branch points are distinct for collisional plasma and none of them is located on the real or imaginary axis. In the limiting case when collision approaches zero, they may locate on the real or imaginary axis. Note that the four sheets are also joined together at the points: the four roots of the equation $n_s(n_\rho) = 0$ and $n_\rho = \infty$. These five points are not the branch points because a point moving around any of them never goes from one sheet to another.

According to Equation (4.29), the two wave modes are designated by

$$\begin{aligned} -\pi/2 &\leq \arg(q_+) < \pi/2 \\ \pi/2 &\leq \arg(q_-) < 3\pi/2 \\ -\pi &< \arg(n_z) < 0 \end{aligned} \quad (5.9a)$$

With consideration of the limit from collisional to collisionless plasma, the requirement for the argument of n_z for collisionless plasma should be revised to include the real axis,

$$\begin{aligned} -\pi &\leq \arg(n_z) \leq 0 \\ \pi/2 &\leq \arg(q_+) < \pi/2 \\ \pi/2 &\leq \arg(q_-) < 3\pi/2 \end{aligned} \quad (5.9b)$$

In addition, the so-called radiation condition is set to make sure that the transmitted far field is going away from the antenna, possibly with attenuation in a collisional plasma. This condition is necessary for the solution and it can be expressed as that the calculated refractive index must be in the fourth quadrant,

$$-\pi/2 \leq \arg(n_s) \leq 0 \quad (5.10)$$

The equality gives two special cases: one when the refractive index is a positive number describing a progressive wave without attenuation, and the other when it is negative imaginary represents an evanescent wave.

The four sheets can be disconnected by properly setting branch cut lines according to Equation (5.9a) and referred as to “ n_{z+}/q_+ ”, “ n_{z-}/q_+ ”, “ n_{z+}/q_- ” and “ n_{z-}/q_- ” sheet, respectively,

$$\begin{aligned} \text{Sheet } n_{z+}/q_+ : & -\pi/2 \leq \arg(q) < \pi/2; \quad 0 < \arg(n_z) < +\pi \\ \text{Sheet } n_{z-}/q_+ : & -\pi/2 \leq \arg(q) < \pi/2; \quad -\pi \leq \arg(n_z) \leq 0 \\ \text{Sheet } n_{z+}/q_- : & \pi/2 \leq \arg(q) < 3\pi/2; \quad 0 < \arg(n_z) < +\pi \\ \text{Sheet } n_{z-}/q_- : & \pi/2 < \arg(q) < 3\pi/2; \quad -\pi \leq \arg(n_z) \leq 0 \end{aligned}$$

Now the integration (5.5) is conducted on the “ n_{z-}/q_+ ” or “ n_{z-}/q_- ” sheet for a mode along the real axis.

Equation (5.7) is a nonlinear equation and it is difficult to find an explicit analytical solution. Since the required saddle points are located on the “ n_{z-}/q_+ ” or “ n_{z-}/q_- ” sheet of the Riemann surface, if using the direct method, every step of the numerical analysis must be carried out on the right sheet and it takes a lot of attentive care to do it.

An alternate method is introduced next. With square operation on $q(n_\rho)$ and $n_z(n_\rho)$ in Equation (5.7), it can be transformed to a sixth-order polynomial equation

$$\begin{aligned} a_6 \tau^6 + a_5 \tau^5 + a_4 \tau^4 + a_3 \tau^3 + a_2 \tau^2 + a_1 \tau + a_0 &= 0 \\ \tau &\equiv n_\rho^2 \end{aligned} \quad (5.11)$$

The coefficients of the polynomial are derived in Appendix C. Unfortunately, there is no explicit analytical solution, in general, for a sixth polynomial equation but it is convenient to find the six roots numerically using available algorithms, providing twelve values of

$n_\rho = \pm\sqrt{\tau_i}, (i = 1, 2, \dots, 6)$. The required saddle points must be among them. However, two problems arise: (1) In the course of transformation from Equation (5.7) to (5.11), the designation of mode type is lost. Then how can one identify the mode that belongs of a saddle point? (2) Are all the six roots reasonable saddle points?

For collision-free plasma, all the coefficients in Equation (5.11) are real and there are at least two real roots, positive or negative, and other root pairs of conjugation for such an even order polynomial equation. According to the definition of the refractive index, Equation (5.4), all the conjugate pairs should be disregarded as they will lead to solutions with attenuation in the propagation direction, and this is unreasonable for collision-free plasma in which dissipation and non-linear absorptions are not considered. The saddle points are associated with the real roots. With assumed signs for $n_\rho = \sqrt{\tau}$, $q(n_\rho)$, and $n_z(n_\rho)$ for each root, one can always find a proper selection so as to make them best satisfy the original equation (5.7) and the condition (5.10). Use of Equation (5.9b) determines the mode type.

In most cases, Equation (5.11) has only two real roots providing the saddle points for the two modes, respectively. However, there are some cases where multiple real roots exist for Equation (5.11) and it remains suspended whether all the real roots are saddle points. For example, in the parallel direction $\alpha = 0$, Equation (5.7) is reduced to

$$n_\rho \left[-(\varepsilon_1 + \varepsilon_3)q(n_\rho) + (\varepsilon_1 - \varepsilon_3)^2 n_\rho^2 - 2\varepsilon_2^2 \varepsilon_3 \right] = 0 \quad (5.12)$$

The roots are

$$n_\rho^2 = \begin{cases} 0 \\ \frac{2\varepsilon_1 \varepsilon_2^2 \varepsilon_3 \pm \sqrt{\Delta}}{\varepsilon_2 (\varepsilon_1 - \varepsilon_3)^2}, \end{cases} \quad \Delta \equiv \varepsilon_1 \varepsilon_2^2 \varepsilon_3 (\varepsilon_1 + \varepsilon_3)^2 (\varepsilon_2 + \varepsilon_1 - \varepsilon_3)(\varepsilon_2 - \varepsilon_1 + \varepsilon_3) \quad (5.13)$$

The root of zero is the saddle point because it exists even for collisional plasma. Replacing in Equation (4.29) yields

$$\begin{aligned} n_{\rho s\pm} &= 0 \\ q_\pm &= \pm 2\sqrt{\varepsilon_2^2 \varepsilon_3^2}, \quad -\pi/2 \leq \arg(q_\pm) < \pi/2 \\ n_{z\pm} &= \sqrt{\frac{2\varepsilon_1 \varepsilon_3 + q_\pm}{2\varepsilon_3}}, \quad -\pi \leq \arg(n_{z\pm}) \leq 0 \\ n_{s\pm} &= n_{z\pm} \end{aligned} \quad (5.14)$$

They are identical with the refractive index of plane waves.

In the perpendicular direction $\alpha = \pi/2$, the saddle points are found from the equation

$$n_z(n_\rho)q(n_\rho) = 0 \quad (5.15)$$

The same equation determines the branch points. The q -branch points are never real or pure imaginary in CMA regions 6, 7 and 8 and in these cases only the n_z -branch points qualify. In fact, for other CMA regions, also the qualified saddle points coincide with two n_z -branch points, giving the refractive index equal to that for plane waves,

$$\begin{aligned} n_{z\pm} &= 0 \\ q_{\pm} &= \pm \sqrt{(\varepsilon_1 - \varepsilon_2 - \varepsilon_1 \varepsilon_3)^2}, \quad -\pi/2 \leq \arg(q_{\pm}) < \pi/2 \\ n_{\rho s\pm} &= \sqrt{\frac{\varepsilon_1^2 - \varepsilon_2^2 + \varepsilon_1 \varepsilon_3 + q_{\pm}}{2\varepsilon_3}}, \quad -\pi/2 \leq \arg(n_{\rho s\pm}) \leq 0 \\ n_{s\pm} &= n_{\rho s\pm} \end{aligned} \quad (5.16)$$

The problem is even more complicated for other directions. When Equation (5.11) has multiple real roots, the saddle points must be identified carefully. A detailed discussion to identify the qualified saddle points from multiple real roots is given in Appendix C.

It is found that for each mode there is a unique saddle point $n_{\rho s\pm}$ identified to satisfy Equation (5.10) according to the limits principle. Then using the formula (5.6), the asymptotic expression of Equation (5.5) is given by

$$\mathbf{A}_{0\pm}(\mathbf{r}) \Rightarrow \hat{\mathbf{Z}}_S \frac{\mu_0 \omega I_A}{2\pi k_0^4} \sum_{m=0}^{\infty} d_{m\pm}(n_{\rho s\pm}) \cos m\beta \left(\frac{n_{\rho s\pm}}{n_{zs}'' \sin \alpha \cos \alpha} \right)^{1/2} \frac{1}{q_s n_{zs}} \frac{e^{-jk_0 n_s r}}{k_0 r} \quad (5.17)$$

where

$$\begin{aligned} q_s &\equiv q(n_{\rho s\pm}) \\ n_{zs} &\equiv n_z(n_{\rho s\pm}) \\ n_s &\equiv n_{zs} |\cos \alpha| + n_{\rho s\pm} \sin \alpha \\ n_{zs}'' &\equiv \left. \frac{d^2 n_z(n_\rho)}{dn_\rho^2} \right|_{n_\rho = n_{\rho s\pm}} \end{aligned} \quad (5.18)$$

Recalling the Fourier expansion in Equation (4.25b), the series in Equation (5.17) is closed,

$$\sum_{m=0}^{\infty} d_{m\pm}(n_{\rho s\pm}) \cos m\beta = \frac{\gamma}{\gamma^2 - (n_{\rho s\pm} \cos \beta \sin \psi + \text{sgn}(\pi/2 - \alpha) n_{zs} \cos \psi)^2}, \quad (5.19)$$

and the asymptotic expression can be rewritten as

$$\mathbf{A}_{0\pm}(\mathbf{r}) \Rightarrow \hat{\mathbf{Z}}_S \frac{\mu_0 \omega I_A}{2\pi k_0^4} \frac{\gamma}{\gamma^2 - (n_{\rho s\pm} \cos \beta \sin \psi + \text{sgn}(\pi/2 - \alpha) n_{zs} \cos \psi)^2} \left(\frac{n_{\rho s\pm}}{n_{zs}'' \sin \alpha |\cos \alpha|} \right)^{1/2} \frac{1}{q_s n_{zs}} \frac{e^{-jk_0 n_s r}}{k_0 r} \quad (5.20)$$

Since for spherical coordinates of the points $\mathbf{r}_1 = (r_1, \alpha_1, \beta)$ and $\mathbf{r}_2 = (r_2, \alpha_2, \beta)$ in the far region,

$$\begin{aligned}
r_1 &\Rightarrow r - \frac{\mathbf{r} \cdot \mathbf{L}}{r}, \quad \alpha_1 \Rightarrow \alpha \\
r_2 &\Rightarrow r + \frac{\mathbf{r} \cdot \mathbf{L}}{r}, \quad \alpha_2 \Rightarrow \alpha
\end{aligned} \tag{5.21}$$

the asymptotic expressions of the general vector potential at these two points take the form

$$\begin{aligned}
\mathbf{A}_{0\pm}(\mathbf{r}_1) &\Rightarrow \hat{\mathbf{Z}}_s \frac{\mu_0 \omega I_A}{2\pi k_0^4} \frac{\gamma}{\gamma^2 - (n_{\rho s \pm} \cos \beta \sin \psi + \text{sgn}(\pi/2 - \alpha) n_{zs} \cos \psi)^2} \left(\frac{n_{\rho s \pm}}{n_{zs} \sin \alpha \cos \alpha} \right)^{1/2} \frac{1}{q_s n_{zs}} \frac{e^{-jk_0 n_s r_1}}{k_0 r_1} \\
\mathbf{A}_{0\pm}(\mathbf{r}_2) &\Rightarrow \hat{\mathbf{Z}}_s \frac{\mu_0 \omega I_A}{2\pi k_0^4} \frac{\gamma}{\gamma^2 - (n_{\rho s \pm} \cos \beta \sin \psi + \text{sgn}(\pi/2 - \alpha) n_{zs} \cos \psi)^2} \left(\frac{n_{\rho s \pm}}{n_{zs} \sin \alpha \cos \alpha} \right)^{1/2} \frac{1}{q_s n_{zs}} \frac{e^{-jk_0 n_s r_2}}{k_0 r_2}
\end{aligned} \tag{5.22}$$

Noting that

$$\begin{aligned}
\frac{1}{2} \left(\frac{e^{-jk_0 n_s r_1}}{r_1} + \frac{e^{-jk_0 n_s r_2}}{r_2} \right) &\Rightarrow \frac{1}{2} \left(\frac{e^{-jk_0 n_s (r - \frac{\mathbf{r} \cdot \mathbf{L}}{r})}}{r} + \frac{e^{-jk_0 n_s (r + \frac{\mathbf{r} \cdot \mathbf{L}}{r})}}{r} \right) = \frac{e^{-jk_0 n_s r}}{2r} \left(e^{+jk_0 n_s \frac{\mathbf{r} \cdot \mathbf{L}}{r}} + e^{-jk_0 n_s \frac{\mathbf{r} \cdot \mathbf{L}}{r}} \right) \\
&= \frac{e^{-jk_0 n_s r}}{r} \cos(k_0 L n_s (\sin \psi \sin \alpha \cos \beta + \cos \psi \cos \alpha))
\end{aligned} \tag{5.23}$$

according to Equation (4.29), the asymptotic expression of the general vector potential is

$$\begin{aligned}
\mathbf{A}_{\pm}(\mathbf{r}) &\Rightarrow \hat{\mathbf{Z}}_s \frac{\mu_0 \omega I_0}{\pi k_0^5} F_1(\alpha) F_3(\alpha, \beta) \frac{e^{-jk_0 n_s r}}{r} \\
n_s &= n_{zs} |\cos \alpha| + n_{\rho s \pm} \sin \alpha, \quad (-\pi/2 \leq \arg(n_s) \leq 0) \\
n_{zs} &\equiv \sqrt{\frac{2\epsilon_1 \epsilon_3 - (\epsilon_1 + \epsilon_1)^2 n_{\rho s \pm}^2 + q_s^2}{2\epsilon_3}}, \quad (-\pi < \arg(n_{zs}) < 0) \\
q_s &\equiv \sqrt{(\epsilon_1 - \epsilon_1)^2 n_{\rho s \pm}^4 - 4\epsilon_2^2 \epsilon_3 n_{\rho s \pm}^2 + 4\epsilon_2^2 \epsilon_3^2} \\
(-\pi/2 \leq \arg(q_s(n_{\rho s+})) < \pi/2, \quad \pi/2 \leq \arg(q_s(n_{\rho s-})) < 3\pi/2) \\
F_1(\alpha) &= \frac{1}{q_s n_{zs}} \left(\frac{n_{\rho s \pm}}{n_{zs} \sin \alpha |\cos \alpha|} \right)^{1/2}, \quad n_{zs} \equiv \left. \frac{d^2 n_z(n_\rho)}{dn_\rho^2} \right|_{n_\rho = n_{\rho s \pm}} \\
F_3(\alpha, \beta) &= \frac{\gamma [\cos(k_0 n_s L (\sin \psi \sin \alpha \cos \beta + \cos \psi \cos \alpha)) - \cos(k_0 \gamma L)]}{\sin(k_0 \gamma L) [\gamma^2 - (n_{\rho s \pm} \sin \psi \cos \beta + \text{sgn}(\pi/2 - \alpha) n_{zs} \cos \psi)^2]}
\end{aligned} \tag{5.24}$$

The factor $F_3(\alpha, \beta)$ in the above equation depends on the antenna parameters and is referred to as the antenna factor.

For a given direction, the value of $n_{\rho s+}$ is different from $n_{\rho s-}$ because they are associated with different saddle points. Thus the amplitudes of q_s for the two modes are different. As shown in

Equation (5.24), q_s for the “+” mode should be on the right half plane, q_s for the “−” mode on the left half plane, and n_{zs} for both modes on the lower half plane. The calculated refractive index of spherical wave must be in the fourth quadrant. This necessary requirement is called radiation condition and it is set to make it sure that the transmitted far field is going away from the antenna possibly with attenuation in the collisional plasma. Equation (5.24) is valid for collisional plasma and it also gives the solution for collision-free plasma when the collision approaches zero.

The above result is derived using the asymptotic approach. It should be pointed out that asymptotic results do not imply any approximations. The asymptotic form of a function gives its precise limit when the argument approaches infinity, and therefore Equation (5.24) accurately represents the vector potential in the far region.

6. Radiation Field in the Far Region

6.1 Expression for the far field

The transmitted electromagnetic field in the far region is derived in this subsection using Equation (2.9). At first, the components in the Cartesian coordinate systems are derived and then transformed into the components in the spherical coordinate system. In the course of the derivation attention is paid to the far field, and thus all the terms with higher orders of attenuation with distance have been ignored. The detailed derivation is described in Appendix D. Given here is the far field expressed in the spherical coordinate system:

$$\begin{aligned}
 E_{r\pm}(r, \alpha, \beta) &= \frac{Z_0 I_0}{2\pi} F_{1\pm}(\alpha) F_{Er\pm}(\alpha, \beta) F_{3\pm}(\alpha, \beta) \frac{\exp(-jk_0 n_s r)}{r} \\
 E_{\alpha\pm}(r, \alpha, \beta) &= \frac{Z_0 I_0}{2\pi} F_{1\pm}(\alpha) F_{E\alpha\pm}(\alpha, \beta) F_{3\pm}(\alpha, \beta) \frac{\exp(-jk_0 n_s r)}{r} \\
 E_{\beta\pm}(r, \alpha, \beta) &= \frac{Z_0 I_0}{2\pi} F_{1\pm}(\alpha) F_{E\beta\pm}(\alpha, \beta) F_{3\pm}(\alpha, \beta) \frac{\exp(-jk_0 n_s r)}{r} \\
 H_{r\pm}(r, \alpha, \beta) &= \frac{I_0}{2\pi} F_{1\pm}(\alpha) F_{Hr\pm}(\alpha, \beta) F_{3\pm}(\alpha, \beta) \frac{\exp(-jk_0 n_s r)}{r} \\
 H_{\alpha\pm}(r, \alpha, \beta) &= \frac{I_0}{2\pi} F_{1\pm}(\alpha) F_{H\alpha\pm}(\alpha, \beta) F_{3\pm}(\alpha, \beta) \frac{\exp(-jk_0 n_s r)}{r} \\
 H_{\beta\pm}(r, \alpha, \beta) &= \frac{I_0}{2\pi} F_{1\pm}(\alpha) F_{H\beta\pm}(\alpha, \beta) F_{3\pm}(\alpha, \beta) \frac{\exp(-jk_0 n_s r)}{r}
 \end{aligned} \tag{6.1}$$

where $Z_0 = \sqrt{\epsilon_0 / \mu_0} = 377 \, \Omega$; the factors $F_{Er\pm}(\alpha, \beta)$, etc. have the form

$$\begin{aligned}
F_{Er}(\alpha, \beta) &= \left[\begin{aligned} & \left(n_{\rho\pm}^2 - \varepsilon_3 \right) \left(n_{\rho\pm}^2 + n_{zs}^2 - \varepsilon_1 \right) \sin\psi \sin\alpha \cos\beta \\ & + \left[n_{zs}^2 \left(n_{\rho\pm}^2 + n_{zs}^2 \right) - \varepsilon_1 \left(n_{\rho\pm}^2 + 2n_{zs}^2 \right) + \varepsilon_1^2 - \varepsilon_2^2 \right] \cos\psi \cos\alpha \\ & + n_{\rho\pm} \|n_{zs}\| \left(n_{\rho\pm}^2 + n_{zs}^2 - \varepsilon_1 \right) \left(\sin\psi \cos\alpha \cos\beta + \cos\psi \sin\alpha \right) \\ & + j\varepsilon_2 \left[\left(n_{\rho\pm}^2 - \varepsilon_3 \right) \sin\alpha + n_{\rho\pm} \|n_{zs}\| \cos\alpha \right] \sin\psi \sin\beta \end{aligned} \right] \\
F_{E\alpha}(\alpha, \beta) &= \left[\begin{aligned} & \left(n_{\rho\pm}^2 - \varepsilon_3 \right) \left(n_{\rho\pm}^2 + n_{zs}^2 - \varepsilon_1 \right) \sin\psi \cos\alpha \cos\beta \\ & - \left[n_{zs}^2 \left(n_{\rho\pm}^2 + n_{zs}^2 \right) - \varepsilon_1 \left(n_{\rho\pm}^2 + 2n_{zs}^2 \right) + \varepsilon_1^2 - \varepsilon_2^2 \right] \cos\psi \sin\alpha \\ & - n_{\rho\pm} \|n_{zs}\| \left(n_{\rho\pm}^2 + n_{zs}^2 - \varepsilon_1 \right) \left(\sin\psi \sin\alpha \cos\beta - \cos\psi \cos\alpha \right) \\ & + j\varepsilon_2 \left[\left(n_{\rho\pm}^2 - \varepsilon_3 \right) \cos\alpha - n_{\rho\pm} \|n_{zs}\| \sin\alpha \right] \sin\psi \sin\beta \end{aligned} \right] \\
F_{E\beta}(\alpha, \beta) &= \left[\begin{aligned} & \left(\varepsilon_1 n_{\rho\pm}^2 + \varepsilon_3 n_{zs}^2 - \varepsilon_1 \varepsilon_3 \right) \sin\psi \sin\beta \\ & + j\varepsilon_2 \left[\left(n_{\rho\pm}^2 - \varepsilon_3 \right) \sin\psi \cos\beta + n_{\rho\pm} \|n_{zs}\| \cos\psi \right] \end{aligned} \right] \\
F_{Hr}(\alpha, \beta) &= F_{E\beta}(\alpha, \beta) \left(n_{\rho\pm} \cos\alpha - \|n_{zs}\| \sin\alpha \right) \\
F_{H\alpha}(\alpha, \beta) &= F_{E\beta}(\alpha, \beta) \left(n_{\rho\pm} \sin\alpha + \|n_{zs}\| \cos\alpha \right) \\
F_{H\beta}(\alpha, \beta) &= \left[\begin{aligned} & -\|n_{zs}\| \left[\varepsilon_3 \left(n_{\rho\pm}^2 + n_{zs}^2 - \varepsilon_1 \right) \cos\beta + j\varepsilon_2 \varepsilon_3 \sin\beta \right] \sin\psi \\ & - n_{\rho\pm} \left[-\varepsilon_1 \left(n_{\rho\pm}^2 + n_{zs}^2 \right) + \varepsilon_1^2 - \varepsilon_2^2 \right] \cos\psi \end{aligned} \right] \\
\|n_{zs}\| &\equiv n_{zs} \operatorname{sgn}(\pi/2 - \alpha)
\end{aligned} \tag{6.2}$$

The above expressions accurately represent the transmitted electromagnetic field in the far region. The far field is composed to two mode waves. There is also a radial component but computations show that the two transverse components are dominant. As indicated by Equation (4.29), each mode is a superposition of waves which look like plane waves along the ambient magnetic field and cylindrical waves in the perpendicular direction, and these waves interfere with each other to form the far field. Now as revealed by Equation (6.1), the interference results in a reconstruction of waves in the far region for each mode, which looks like a spherical wave as the amplitude is decreasing inversely proportional to distance; however the propagation speed varies with the polar angle so that the wave front is essentially not a sphere, but is characterized by the anisotropic medium.

Equation (6.1) is valid for any plasma parameters (except for cut off and resonance) and any antenna length and orientation.

The far fields for parallel and perpendicular antenna orientation are special cases and the expressions can easily be derived by letting the antenna orientation angle $\psi = 0$ and $\psi = \pi/2$,

respectively. It should be stressed that, because the antenna factor cannot be decomposed into two parts relating to parallel and perpendicular directions, a discussion limited to these two special cases cannot lead to the far field expression for a general orientation even for short antennas unless it is infinitesimally short.

6.2 Refractive index surface

As shown in Equation (6.1), the far field represents a spherical wave. The propagation of the far field is completely determined by the refractive index of spherical wave. In each CMA region, there are two wave modes. Given typical plasma parameters the refractive index surfaces of both plane and spherical waves have been calculated and are plotted in Figure 7. In the figure the dashed lines are for plane waves and the solid lines for spherical waves; and the red lines are for the real part of the indices while the green lines represent the imaginary part with a negative sign. This figure illustrated the general features of the refractive index of spherical waves:

(1) In the direction of the ambient magnetic field and perpendicular to it, the refractive indices of spherical waves are equal to that of plane waves. In any other direction they are different. Similar to the refractive index of plane waves, the refractive index of spherical wave is symmetrical relative to the perpendicular direction of the magnetic field which means that the propagation property will not change when the field takes the inverse direction.

(2) When a mode of plane waves is able to propagate in a magnetoplasma with parameters for a given CMA region, the same mode of spherical waves is also able to propagate. For example, both modes of plane and spherical waves can propagate for Regions 1 and 6. When a mode of plane waves is vanishing for a region, the same mode of spherical waves is also vanishing. For example, neither wave can propagate in a magnetoplasma with parameters in Region 5.

(3) For Region 1 the difference between the refractive indices of plane and spherical waves is very small, but is getting larger for other CMA regions when X and/or Y increases as the plasma anisotropy becomes stronger.

(4) For Regions 3, 7, and 8, the “-” mode of plane waves (extraordinary mode for Region 3 and whistler mode for Regions 7 and 8) can propagate within the resonance cone. It is interesting that the propagation of spherical wave is confined in a so-called radiation cone. It has been proved in Appendix C that the radiation cone angle is equal to the 90 degree co-angle of the resonance cone angle. The whistler mode of plane waves with very low frequency can propagate in a large direction around the ambient magnetic field line, while the spherical waves concentrate in a very small cone around the field.

(5) Similar to plane waves, in a CMA region the refractive index surface of spherical waves is changing with plasma parameters but the shape is varying smoothly, in a manner called “creep deformation” in topological terminology. When transit from Region 1 to 2, the surface of the “+” wave remains creep deformed and the transition is called “intact”, while for the “-” wave the surface is destroyed and reconstructed and the transition is called “destructive”. From Region 3 to 6, the surface for the “-” wave is not completely destroyed but reshaped and the transition

is called “reshaping”. It is important to distinguish three topology types of transition if the computation relates to changes of plasma parameters from one CMA region to another. The transition types are summarized in Table 1.

Table 1. Transition types

	“+” Mode	“−” Mode
Region 1-Region 2	intact	destructive
Region 2-Region 3	intact	destructive
Region 3-Region 4	destructive	reshaping
Region 3-Region 6	intact	reshaping
Region 4-Region 5	intact	destructive
Region 4-Region 7	destructive	reshaping
Region 5-Region 8	intact	destructive
Region 6-Region 7	intact	reshaping
Region 7-Region 8	destructive	intact

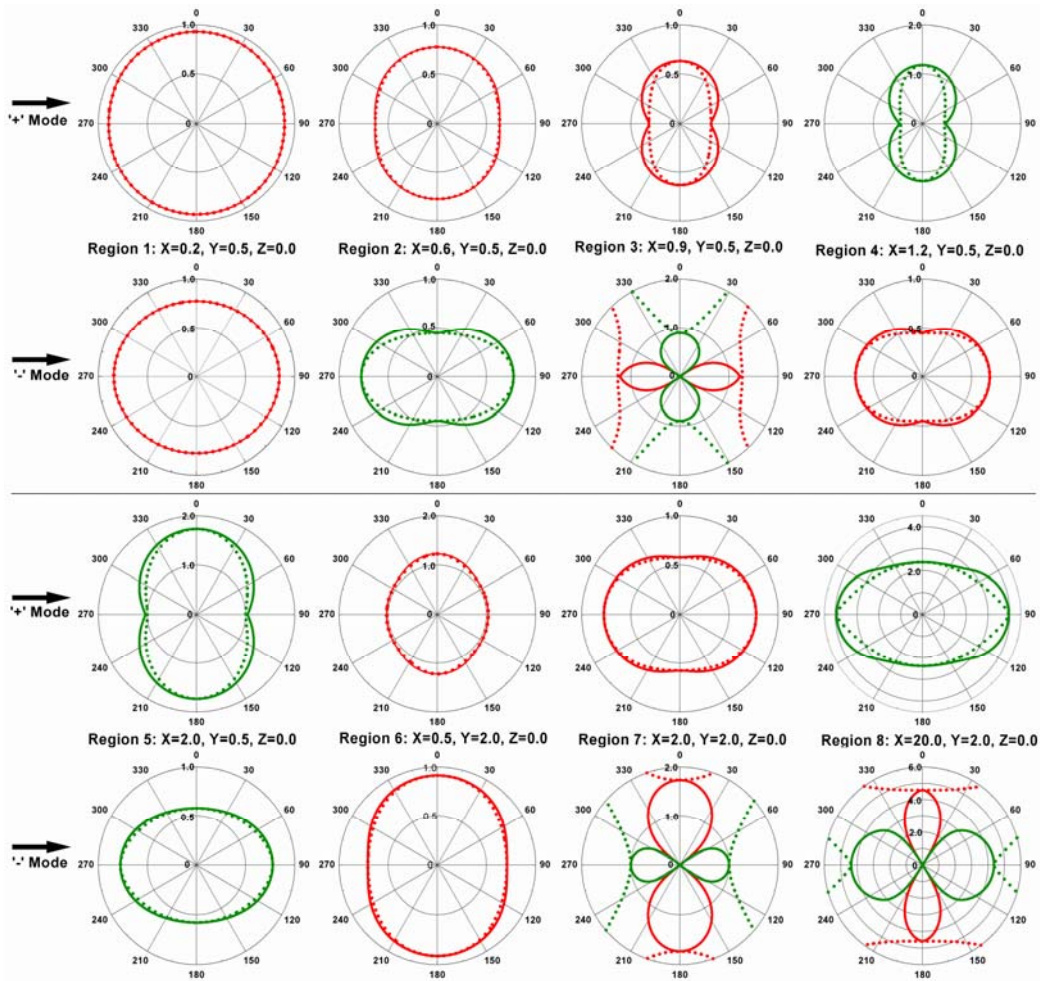


Figure 7. Refractive indices for typical parameters

As proved in Appendix C, for the whistler mode the refractive index of spherical waves is real in the radiation cone and the transmitted far field is progressive in it, and evanescent outside the cone. The radiation cone angle, α_{SRC} , and the resonance cone angle, α_{RC} , are complementary,

$$\alpha_{SRC} + \alpha_{RC} = \pi / 2 \quad (6.3)$$

It is easy to find that

$$\alpha_{SRC} \begin{cases} > \alpha_{RC}, & \text{if } X < 2 \frac{1-Y^2}{2-Y^2} \\ = \alpha_{RC} = \pi / 4, & \text{if } X = 2 \frac{1-Y^2}{2-Y^2} \\ < \alpha_{RC}, & \text{if } X > 2 \frac{1-Y^2}{2-Y^2} \end{cases} \quad (6.4)$$

Examples for the three cases are shown in Figure 8. The refractive indices for spherical waves and plane waves are plotted in the figure. The purple/red lines indicate that the index is real and the green/blue lines indicate that the index is negative imaginary.

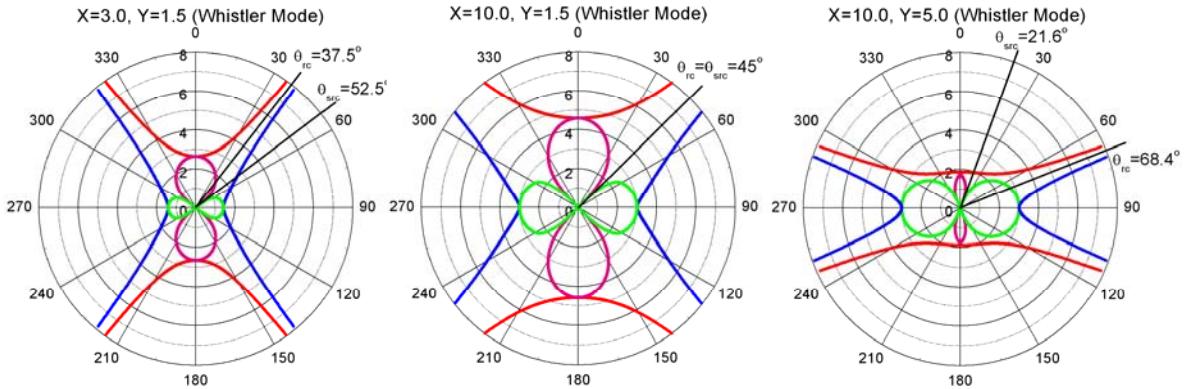


Figure 8. The radiation cone angle for spherical waves and the resonance cone angle are complementary.

It should be pointed out that the refractive index surfaces are not radiation patterns of an antenna, but they really plays important role in determination of them that will be discussed later.

6.3 Polarization

As shown in Equation (6.1), there is, in general, a non-zero component in the radial direction but the major components are transverse. The polarization for the two transverse components is described by a factor [Budden, 1985]

$$\Upsilon_{\pm}(\alpha, \beta) = \frac{E_{\alpha\pm}(r, \alpha, \beta)}{E_{\beta\pm}(r, \alpha, \beta)} \quad (6.5)$$

From Equations (6.1) and (6.2), it is found that

$$\Upsilon_{\pm}(\alpha, \beta) = \frac{F_{E\alpha\pm}(\alpha, \beta)}{F_{E\beta\pm}(\alpha, \beta)} \quad (6.6)$$

The polarization factor contains the information of amplitude ratio and phase difference. It is generally a complex number representing elliptical polarization. The sign of the imaginary part determines the rotating direction. The vector of electric field is rotating with left or right hand direction once in a cycle. If the factor is real the polarization is linear and if it is pure imaginary the polarization is circular. Because of the symmetrical property of the far field, the rotation direction remains unchanged with respect to the ambient magnetic field.

It is found that the polarization of left (L) or right (R) hand rotation is the same as plane wave propagation in the same radial direction. The polarization types for progressive modes for the 8 CMA regions are summarized in Table 2.

Table 2. Polarization type of spherical waves

	“+” Mode	“−” Mode
Region 1	L	R
Region 2	L	/
Region 3	L	R
Region 4	/	L
Region 5	/	/
Region 6	R	L
Region 7	L	R
Region 8	/	R

6.4 Convergence to Free Space

When the ambient magnetic field approaches zero ($Y \rightarrow 0$), the plasma reduces to an isotropic medium, and when the electron density can be ignored ($X \rightarrow 0$) it is reduced to free space. In these cases, the derived expressions of the far field, Equation (6.1), cannot be directly applied to give the solution because that the characteristic parameter of wave mode, q , is zero, indicating the two modes are no longer independent. In Appendix E the behavior of the far field expression is examined for the limits when $Y \rightarrow 0$ and/or $X \rightarrow 0$ and it is proved that the far field as expressed in Equation (6.1) converges to the well known solution for isotropic/free space.

When $Y \rightarrow 0$, the plasma is an isotropic medium with the refractive index $n = \sqrt{\epsilon_3}$. It has been proved in Appendix E that the limiting far fields of the two modes represent two transverse spherical waves, circular polarized with equal amplitudes and opposite sense of rotation. Since the limiting far field of the two modes in isotropic medium are propagating with the same speed they superpose a linear polarized wave. When the electron density is very small or the frequency is very high so that $X \rightarrow 0$, the far field is exactly reduced to the well known expression of the far field for an antenna in free space.

7. Radiation Patterns

The transmitted electromagnetic wave carries energy from the antenna to the far region. The Poynting vector describes the flow direction and power density. The far field as shown by Equation (6.1) is the complex amplitude of a sinusoidal varying electromagnetic wave and only the real part of the field is physically meaningful. The time average of the real part of the Poynting vector is,

$$\mathbf{S} = \frac{1}{T} \int_0^T dt \left(\frac{\mathbf{E}e^{j\omega t} + \mathbf{E}^*e^{-j\omega t}}{2} \times \frac{\mathbf{H}e^{j\omega t} + \mathbf{H}^*e^{-j\omega t}}{2} \right) = \frac{1}{2} \text{Re}(\mathbf{E} \times \mathbf{H}^*) \quad (7.1)$$

where $(\mathbf{E}, \mathbf{E}^*)$ and $(\mathbf{H}, \mathbf{H}^*)$ denote conjugate pairs. In collisional plasma the refractive index of spherical wave is complex and in the course of propagation part of the transmitted energy is consumed in heating particles. In collisionless plasma one mode wave (CMA Regions 2, 4 and 8), or both modes (Region 5) are evanescent, and in Regions 3, 7, and 8, the progressive waves are limited by the radiation cone. For evanescent waves no energy is transmitted to the far region, and the Poynting vector vanishes. Our discussion is limited to progressive mode waves in collisionless plasma.

Since the far field can be decomposed to two mode waves which propagate independently, the Poynting vector of the total far field is the summation of the two mode components, and in the spherical coordinate system it takes the form

$$\begin{aligned} \mathbf{S}(r, \alpha, \beta) &= (S_r(r, \alpha, \beta), S_\alpha(r, \alpha, \beta), S_\beta(r, \alpha, \beta)) \\ S_r(r, \alpha, \beta) &= S_{r+}(r, \alpha, \beta) + S_{r-}(r, \alpha, \beta) \\ S_\alpha(r, \alpha, \beta) &= S_{\alpha+}(r, \alpha, \beta) + S_{\alpha-}(r, \alpha, \beta) \\ S_\beta(r, \alpha, \beta) &= S_{\beta+}(r, \alpha, \beta) + S_{\beta-}(r, \alpha, \beta) \end{aligned} \quad (7.2)$$

The expressions for the three components are

$$\begin{aligned} S_{r\pm}(r, \alpha, \beta) &= \frac{Z_0 |I_0|^2}{8\pi^2 r^2} |F_{1\pm}(\alpha)|^2 |F_{3\pm}(\alpha, \beta)|^2 \cdot \text{Re} \begin{pmatrix} +F_{E\alpha\pm}(\alpha, \beta) F_{H\beta\pm}^*(\alpha, \beta) \\ -F_{E\beta\pm}(\alpha, \beta) F_{H\alpha\pm}^*(\alpha, \beta) \end{pmatrix} \\ S_{\alpha\pm}(r, \alpha, \beta) &= \frac{Z_0 |I_0|^2}{8\pi^2 r^2} |F_{1\pm}(\alpha)|^2 |F_{3\pm}(\alpha, \beta)|^2 \cdot \text{Re} \begin{pmatrix} +F_{E\beta\pm}(\alpha, \beta) F_{Hr\pm}^*(\alpha, \beta) \\ -F_{Er\pm}(\alpha, \beta) F_{H\beta\pm}^*(\alpha, \beta) \end{pmatrix} \\ S_{\beta\pm}(r, \alpha, \beta) &= \frac{Z_0 |I_0|^2}{8\pi^2 r^2} |F_{1\pm}(\alpha)|^2 |F_{3\pm}(\alpha, \beta)|^2 \cdot \text{Re} \begin{pmatrix} +F_{Er\pm}(\alpha, \beta) F_{H\alpha\pm}^*(\alpha, \beta) \\ -F_{E\alpha\pm}(\alpha, \beta) F_{Hr\pm}^*(\alpha, \beta) \end{pmatrix} \end{aligned} \quad (7.3)$$

It can be proved that, for collisionless plasma,

$$\begin{aligned} \text{Re} \left(F_{E\beta\pm}(\alpha, \beta) F_{Hr\pm}^*(\alpha, \beta) - F_{Er\pm}(\alpha, \beta) F_{H\beta\pm}^*(\alpha, \beta) \right) &= 0 \\ \text{Re} \left(F_{Er\pm}(\alpha, \beta) F_{H\alpha\pm}^*(\alpha, \beta) - F_{E\alpha\pm}(\alpha, \beta) F_{Hr\pm}^*(\alpha, \beta) \right) &= 0 \end{aligned} \quad (7.4)$$

and thus the two transverse components for either mode are exactly equal to zero,

$$\begin{aligned} S_{\alpha\pm}(r, \alpha, \beta) &= 0 \\ S_{\beta\pm}(r, \alpha, \beta) &= 0 \end{aligned} \quad (7.5)$$

indicating that the transmitted energy flows along the radial direction. Since the transmitted whistler is limited to the radiation cone, the Poynting vector is zero outside of the cone.

The time average of the transmitted power per unit solid angle, from Equations (7.3) and (7.5), is

$$\begin{aligned} \frac{dP}{d\Omega} &= \frac{Z_0 |I_0|^2}{8\pi^2} G(\alpha, \beta) \\ G(\alpha, \beta) &= G_+(\alpha, \beta) + G_-(\alpha, \beta) \\ G_{\pm}(\alpha, \beta) &= |F_{1\pm}(\alpha)|^2 |F_{3\pm}(\alpha, \beta)|^2 \cdot \text{Re} \left(\begin{aligned} &+F_{E\alpha\pm}(\alpha, \beta) F_{H\beta\pm}^*(\alpha, \beta) \\ &-F_{E\beta\pm}(\alpha, \beta) F_{H\alpha\pm}^*(\alpha, \beta) \end{aligned} \right) \end{aligned} \quad (7.6)$$

When the function $G_{\pm}(\alpha, \beta)$ or $G(\alpha, \beta)$ is calculated for all directions and plotted, it forms a three dimensional surface. This surface represents the angular distribution of the transmitted energy in various directions and is called radiation pattern.

For some CMA regions, such as Region 1, there are some singular points in the antenna factor for collisionless plasma and very narrow peaks appear in the radiation pattern. Allowing for a very small collision rate can remove them.

The radiation patterns for typical plasma parameters in CMA region1 are plotted in Figure 9a. The radiation patterns for the antenna with the same length and orientation in free space are also plotted in the figure for reference.

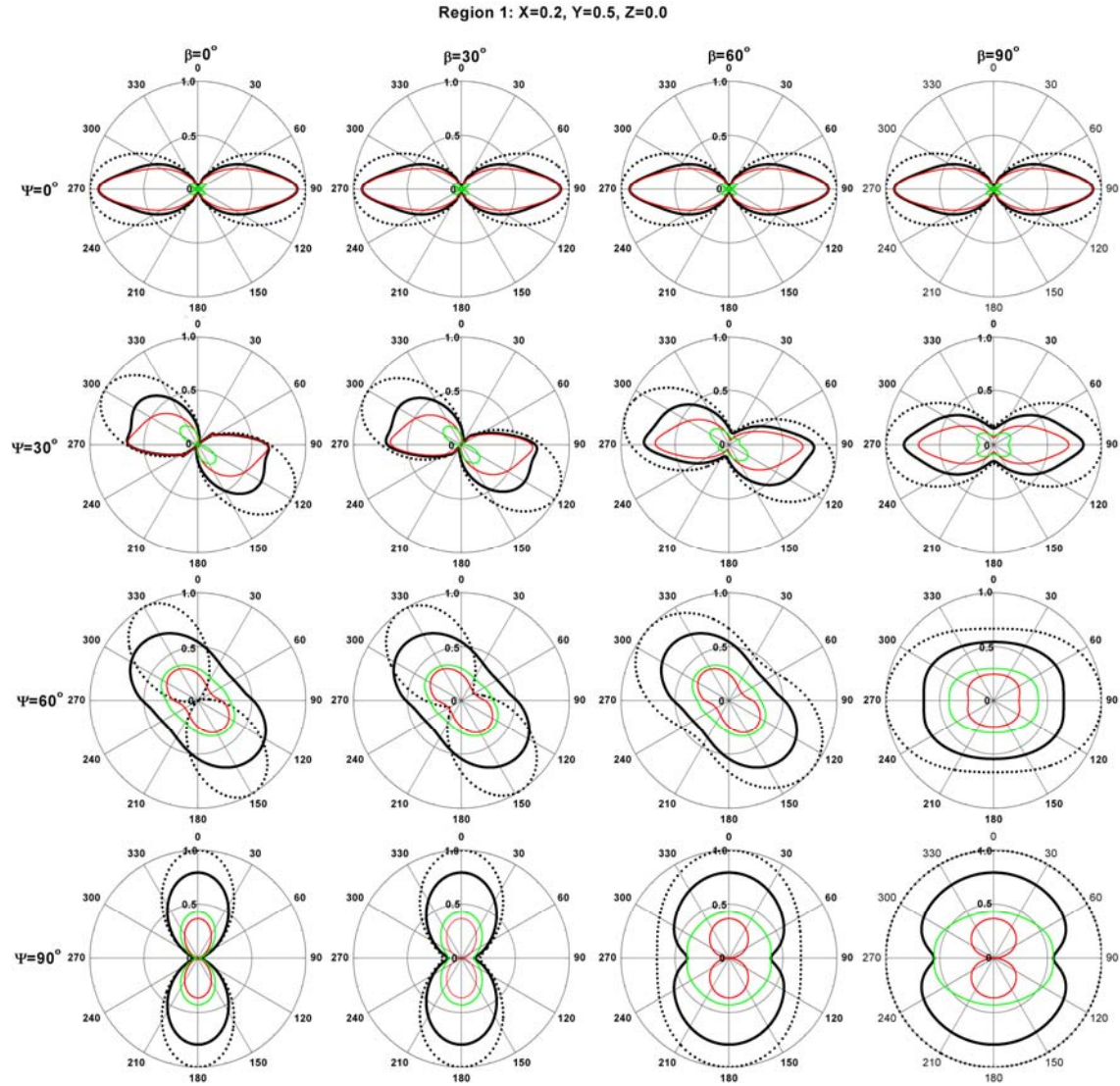


Figure 9a. Typical radiation patterns of half-wave antenna in CMA Region 1: Red for “+” mode, Green for “-” mode. Black line=summation of two modes; black dots=antenna in free space.

Figure 9b shows an example of radiation patterns for whistler transmission.

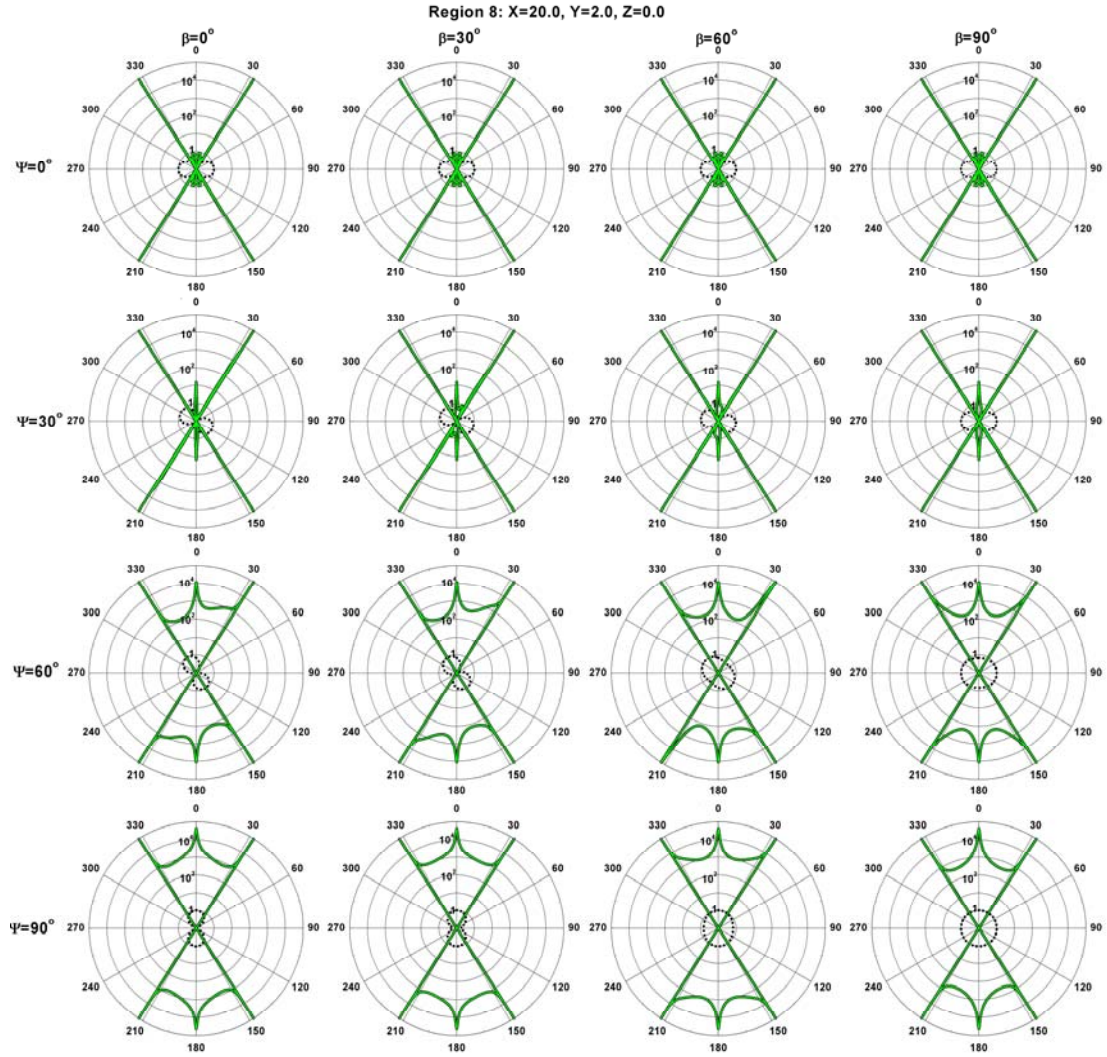


Figure 9b. Typical radiation patterns of half-wave antenna in CMA Region 8: Green for whistler mode. The black dots are for free space.

The far field is extremely strong at the edge of radiation cone, as shown in Figure 9b. This feature was observed in the laboratory experiments conducted in Caltech in the late 1960's [Fisher and Gould, 1969]. Computation results for various parameters indicate that more than half of the transmitted energy is in the outer half of the radiation cone as illustrated in Figure 10.

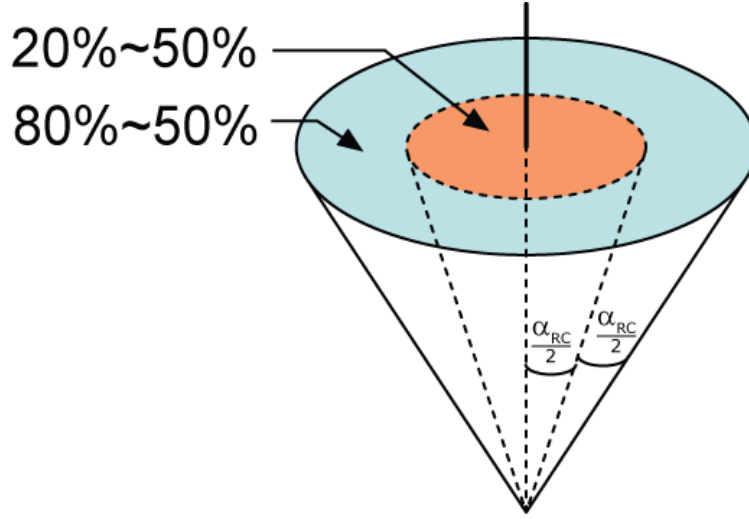


Figure 10. Most of transmitted energy distribute in the region near the edge of radiation cone

8. Radiation Resistance

8.1 Expression for the Radiation Resistance

Electromagnetic wave is excited by the driving current along the antenna, and viewed at the feed point the antenna appears as a two-terminal circuit element having an impedance with a resistance component. This resistance describes the energy consumption outside of the transmitting system. In practice, there may be several physics mechanisms to be responsible for the energy consumption. Putting any other possible energy loss aside, the radiation resistance associated with the transmitted power carried by the far field is defined by

$$\langle P \rangle = R_{RAD} \cdot \frac{1}{T} \int_0^T dt (|I_0| \cos \omega t)^2 = \frac{1}{2} |I_0|^2 R_{RAD} \quad (8.1)$$

where $\langle P \rangle$ is the time average of the total transmitted power according to Equation (7.6),

$$\langle P \rangle = \langle P_+ \rangle + \langle P_- \rangle$$

$$\langle P_{\pm} \rangle = \frac{Z_0 |I_0|^2}{8\pi^2} \int d\beta \int d\alpha \left[\sin \alpha |F_{1\pm}(\alpha)|^2 |F_{2\pm}(\alpha, \beta; \psi)|^2 |F_{3\pm}(\alpha, \beta; L, \psi)|^2 \right] \quad (8.2)$$

Thus the radiation resistance is calculated with

$$R_{RAD} = R_{RAD+} + R_{RAD-}$$

$$R_{RAD\pm} = \frac{Z_0}{4\pi^2} \int d\beta \int d\alpha \left[\sin \alpha |F_{1\pm}(\alpha)|^2 |F_{2\pm}(\alpha, \beta; \psi)|^2 |F_{3\pm}(\alpha, \beta; L, \psi)|^2 \right] \quad (8.3)$$

The radiation resistance is separated into two parts just to show the radiation ability for the two wave modes. The integration range in Equation (8.3) extends to all the directions in which the far field wave is progressive. In general, the range is $\beta \in [0, 2\pi]$ and $\alpha \in [0, \pi]$. But for whistler mode in CMA Regions 7 and 8, and for extraordinary wave mode in Region 3, the polar angle is limited in the radiation cone. If the far field for a mode is evanescent in all directions, the radiation resistance for this mode is zero. For example, in CMA Region 5 both mode waves are evanescent and the total radiation resistance is zero indicating that no energy is transmitted by the antenna in Region 5.

8.2 Computation of Radiation Resistance

As shown by Equation (8.3), the radiation resistance depends on the operating frequency, f , the plasma parameters, f_{pe} and f_{ce} , and the antenna parameters, L and ψ ,

$$R_{RAD\pm} = F(f; f_{pe}, f_{ce}; L, \psi) \quad (8.4)$$

Some parameters can be normalized by the operating frequency so that

$$R_{RAD\pm} = F\left(X, Y; \frac{2L}{\lambda_0}, \psi\right) \quad (8.5)$$

where the total antenna length is normalized by the wave length in free space,

$$\lambda_0 = \frac{c}{f} \quad (8.6)$$

The radiation resistance is calculated numerically carrying out the two dimensional integration in Equation (8.3). Attention is drawn for the radiation cone treatment where abnormal integration is needed as the power density approaches infinite at the edge of the radiation cone. In computation, one parameter can be taken as the variable and the others as parameters so as to examine the dependence of the radiation resistance with a parameter. This can be done either according to Equation (8.4) or (8.5). It may be required to do a series of plots or charts for different applications, but this work is not completed at this time. Next we show some examples.

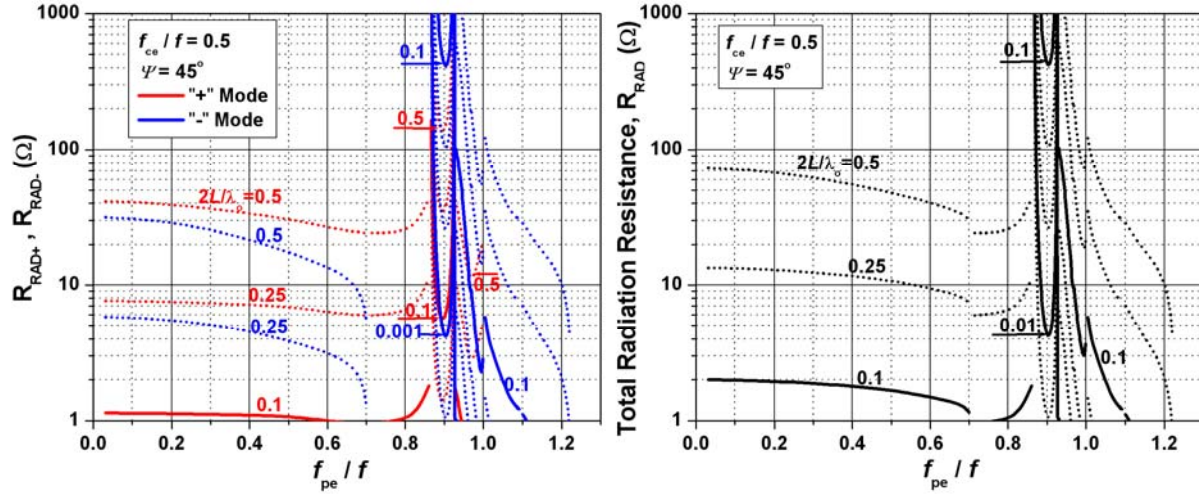


Figure 11. Radiation resistance for $Y < 1$.

Since the radiation resistance varies more with X than with Y , the radiation resistance is plotted as a function with X as the variable. The typical case for $Y < 1$ and $\psi = 45^\circ$ is shown in Figure 11. The values for γ are calculated using Equation (3.6). The radiation resistance for each mode is shown on the left, and the total resistance on the right. For a half-wave antenna ($2L/\lambda_0 = 0.5$), the total radiation resistance is equal to 73 ohms for very small values of f_{pe}/f . This result is no surprising since the convergence of the solution to free space has been proved previously and the property of the plasma in this occasion is actually close to free space. Except for CMA Region 3, the radiation resistance is smaller and the transmission efficiency of the antenna is degraded compared to free space. This suggests that the design of a transmit antenna for topside sounding of the ionosphere should take this fact into account.

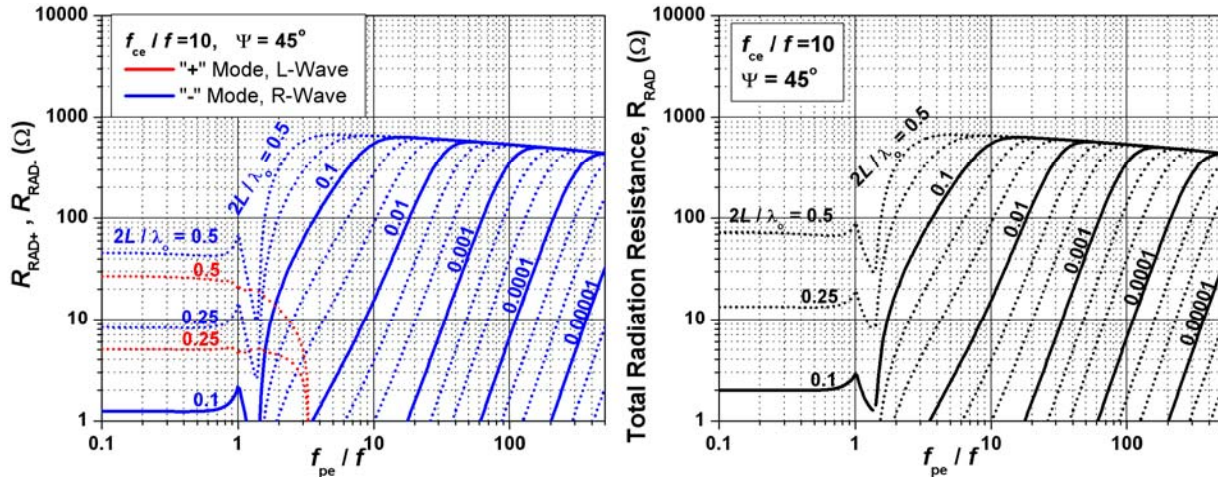


Figure 12. Radiation resistance for $Y > 1$.

Another example for $Y > 1$ and $\psi = 45^\circ$ is shown in Figure 12. The values for γ are also calculated using Equation (3.6). Note that if $\left(\sqrt{f_{pe}^2 + 4f_{pe}^2} - f_{pe} \right) / 2 < f < f_{pe}$, the L -wave is transmitted in addition to the whistler mode. Again for a half-wave antenna ($2L / \lambda_0 = 0.5$), the total radiation resistance is equal to 73 ohms for very small values of f_{pe} / f . When $f_{pe} / f < 1$, i.e., in Region 6, the radiation resistance varies very little with the ratio f_{pe} / f except for the small range near the plasma resonance line. The radiation resistance for whistler waves is large, and longer antennas have larger radiation resistance.

The current propagation constant, γ , in the antenna current model can be understood as the factor of effective antenna length. When γ is real and smaller than one, as it is in CMA Region 1, it makes the effective antenna length in plasma shorter so that the radiation resistance appears smaller compared to free space. As shown in Figure 3, γ is complex in Region 3, 7, and 8, therefore it is the absolute value that must be considered the factor of effective antenna length, and it is much larger than one, meaning that the radiation resistance is large in these regions. And when $|\gamma|$ becomes larger and larger, the curves for the radiation resistance are increasing with f_{pe} / f . On the other hand, the imaginary part of γ makes the current along the antenna decay, and this current decay effectively shortens the antenna reducing the radiation resistance. Both real and imaginary parts need to be considered for the design of the optimum power transmission of whistler mode waves.

The relationship of the radiation resistance and the antenna parameters is important. The antenna factor determines the dependence of the radiation resistance with the antenna length. Since in practice the length of a satellite-borne antenna is generally electrically short, especially for whistler transmission with VLF, the short antenna approximation of the antenna factor given in Equation (5.24) can be used,

$$F_3(\alpha, \beta) \approx \frac{k_0 L}{2} \frac{\gamma^2 - (n_s (\sin \psi \sin \alpha \cos \beta + \cos \psi \cos \alpha))^2}{\gamma^2 - (n_{ps\pm} \sin \psi \cos \beta + \text{sgn}(\pi/2 - \alpha) n_{zs} \cos \psi)^2} \quad (8.7)$$

Therefore, from Equation (8.3), the radiation resistance is proportional to the square of the antenna length,

$$R_{RAD} \propto \left(\frac{2L}{\lambda_0} \right)^2 \quad (8.8)$$

It is the same as the relation for antennas in free space.

Another example for the radiation resistance varying with the antenna length is given in Figure 13. For a dipole antenna with a total length of 80 meters, the radiation resistance ranges from 10 to 50 ohms for the range of operating frequency and plasma parameters shown in the figure.

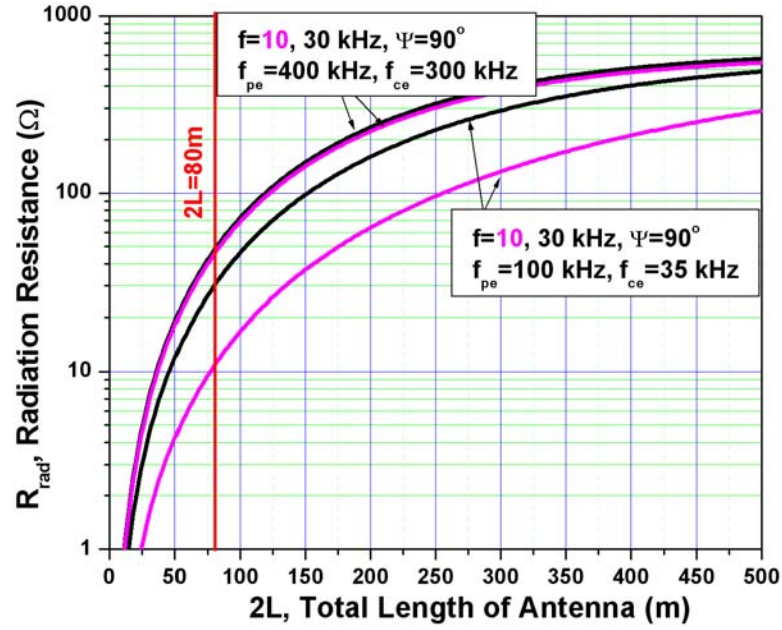


Figure 13. Predictions for a 80m antenna.

The dependence of the radiation resistance with the antenna orientation is, as an example, illustrated in Figure 14. It shows that the radiation resistance does not change much if $\psi > 45^\circ$.

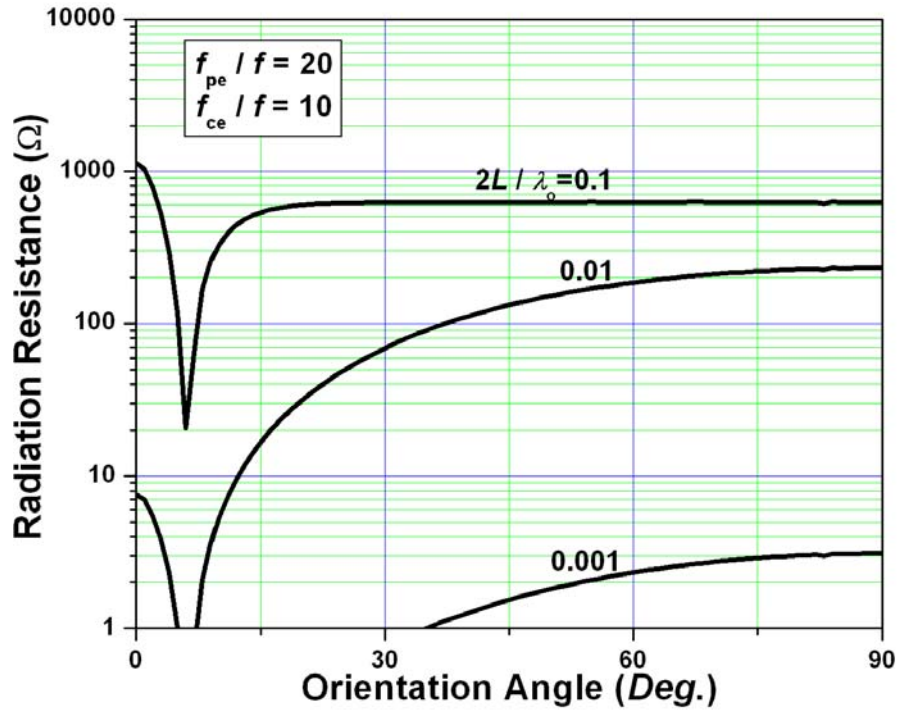


Figure 14. Radiation resistance versus antenna orientation.

8.4 Discussing the linear distribution of the antenna current

The model of a sinusoidal distribution of antenna current, given in Equation (3.4) is used for this study. For the convenience of discussion, it is rewritten here,

$$I(z') = \frac{I_0}{\sin(k_0 \gamma L)} \sin(k_0 \gamma (L - |z'|)), \quad |z'| \leq L \quad (8.9)$$

And the Fourier transform is

$$\mathbf{J}(\mathbf{n}) = \hat{\mathbf{z}}_s \frac{2\gamma I_0}{k_0 \sin(k_0 \gamma L)} \frac{\cos(k_0 n_z L) - \cos(k_0 \gamma L)}{\gamma^2 - n_z^2} \quad (8.10)$$

If the antenna is electrically short, Equation (8.9) is expanded as a Taylor series and the first term is dominant so that the current model is reduced to a linear distribution,

$$I(z') = \frac{I_0}{L} (L - |z'|), \quad (-L \leq z' \leq L) \quad (8.11)$$

Its Fourier transform takes the form

$$\mathbf{J}(\mathbf{n}) = \hat{\mathbf{z}}_s \frac{2I_0}{k_0^2 L} \frac{1 - \cos(k_0 L n_z)}{n_z^2} \quad (8.12)$$

It is true that Equation (8.11) gives a very good approximation to the sinusoidal model for short antennas. This looks like a reasonable argument, however, it is not the current itself but its Fourier transform that is used in the analysis. The short antenna approximation of Equation (8.10) does not lead to Equation (8.12), whereas the latter is the limit of the former when $\gamma \rightarrow 0$. Therefore it is no surprising that, if the linear distribution model is used, it will lead to a quite different result than our general solution.

9. Sheath Effects

When the antenna stimulates the electromagnetic field, the charged particles in the surrounding magnetoplasma will move in response to the varying fields. Because of the mass difference of electrons and ions and the fact that the whistler wave periods are between the ion and electron response times, a plasma sheath forms around the antenna. A theory to describe this complicated physical process was given, analytically, by Song et al. [2007] and, numerically, by Tu et al. [2008]. The existence of the plasma sheath breaks down the charge neutrality condition of the plasma. Our assumption is not valid and hence our theory is not applicable in the sheath. Fortunately, the dimension of the plasma sheath surrounding the antenna is generally limited in space. The inner boundary for our theory, in this case, should be located at the boundary of the sheath and the plasma. Since the size of the sheath is expected to vary within each wave cycle, we place our inner boundary at the outermost of the sheath boundary in a cycle. A more careful examination of the current at this boundary shows that it is radial to the antenna surface and nearly 90° out of phase with the antenna voltage. This is the same as the direction and phase relation with voltage for the current near the antenna in free space. Therefore, we conclude that the capacitance that is created by the sheath can be used to replace the capacitance for a transmitting antenna in free space and the size of the antenna can be replaced with the size of the sheath.

10. References

- Budden, K.G., The Propagation of Radio Waves, Cambridge University Press, 1985.
- Felsen, L.B., Radiation and Scattering of Waves, IEEE Press, 1995.
- Fisher, R. K. and R. W. Gould, Resonance Cones in the Field Pattern of A Short Antenna in an Anisotropic Plasma, Physical Review Letters, 22, 21, 1969.
- Ishizone, T, S. Adachi, and Y. Mushiake, Propagation constants of Electromagnetic Waves Along an Infinitely Long Conducting Wire in a General Magnetoplasma, Electronics And Communications, Vol.54-B, No. 8, 1971.
- Kogelnik, H., On electromagnetic radiation in magnetoionic media, J. Res. NBS, sec. D (Radio Propagation), 64, 515-523, 1960.
- Song, P., B. W. Reinisch, V. Paznukhov, G. Sales, D. Cooke, J.-N. Tu, X. Huang, K. Bibl, and I. Galkin, High-voltage antenna-plasma interaction in whistler wave transmission: Plasma sheath effects, *J. Geophys. Res.*, 112(A3), A03205, doi:10.1029/2006JA011683, 2007.
- Stratton, J.A., Electromagnetic Theory, McGraw-Hill Book Company, Inc., 1941.
- Tu, J., P. Song, and B. W. Reinisch, Plasma sheath structures around a radio frequency antenna, *J. Geophys. Res.*, 113(A7), A07223, doi:10.1029/2008JA013097, 2008.

Appendix A. Green's function for Radiation in Uniform Plasma

The radiation equation (1.1) can be solved with the Green's function method. The Green's function \mathbf{G} satisfies the following equation

$$\nabla \times (\nabla \times \mathbf{G}(\mathbf{r}, \mathbf{r}')) - k_0^2 \mathbf{\kappa} \cdot \mathbf{G}(\mathbf{r}, \mathbf{r}') = -j\mu_0 \omega \mathbf{I} \delta(\mathbf{r} - \mathbf{r}') \quad (\text{A1})$$

where \mathbf{I} is a unit tensor. The solution for Equation (1.1) is then

$$\mathbf{E}(\mathbf{r}, \omega) = \int_s \mathbf{G}(\mathbf{r}, \mathbf{r}') \cdot \mathbf{J}(\mathbf{r}', \omega) d\mathbf{r}' \quad (\text{A2})$$

The solution of Equation (A1) plus any solution of the equation

$$\nabla \times (\nabla \times \mathbf{G}(\mathbf{r}, \mathbf{r}')) - k_0^2 \mathbf{\kappa} \cdot \mathbf{G}(\mathbf{r}, \mathbf{r}') = 0 \quad (\text{A3})$$

still satisfies Equation (A1). However, the resulting “background field” does not originate from our current source and will be disregarded. For a uniform plasma when both the source and the observing points are shifted by a vector \mathbf{r}'' , the field produced by the source remains the same, or

$$\mathbf{G}(\mathbf{r}, \mathbf{r}') = \mathbf{G}(\mathbf{r} + \mathbf{r}'', \mathbf{r}' + \mathbf{r}'') \quad (\text{A4})$$

This holds for any vector \mathbf{r}'' and, in particular when $\mathbf{r}'' = -\mathbf{r}'$, it leads to

$$\mathbf{G}(\mathbf{r}, \mathbf{r}') = \mathbf{G}(\mathbf{r} - \mathbf{r}', 0) = \mathbf{G}(\mathbf{r} - \mathbf{r}') \quad (\text{A5})$$

Equation (A1) can then be written as

$$[\nabla \nabla - \nabla^2 \mathbf{I} - k_0^2 \mathbf{\kappa}] \cdot \mathbf{G}(\mathbf{r} - \mathbf{r}') = -j\mu_0 \omega \mathbf{I} \delta(\mathbf{r} - \mathbf{r}') \quad (\text{A6})$$

The Fourier transformation for any vector $\mathbf{A}(\mathbf{r})$ in the space domain is defined by

$$\begin{aligned} \mathbf{A}(\mathbf{k}) &= \int \mathbf{A}(\mathbf{r}) e^{j\mathbf{k} \cdot \mathbf{r}} d\mathbf{r} \\ \mathbf{A}(\mathbf{r}) &= \frac{1}{(2\pi)^3} \int \mathbf{A}(\mathbf{k}) e^{-j\mathbf{k} \cdot \mathbf{r}} d\mathbf{k} \end{aligned} \quad (\text{A7})$$

The physics meaning of Equation (A7) is to show that any field in space can be regarded as the superposition of monochromatic plane waves. Note that, according to the convention of theoretical physics, the same notation but with different argument is used to represent the Fourier transform of a vector field just to avoid introducing extra symbols. With this definition, the Fourier transform of Equation (A6) in the space domain can be easily obtained by using the operator formula $\nabla \Leftrightarrow -j\mathbf{k}$,

$$[\mathbf{k}\mathbf{k} - k^2 \mathbf{I} + k_0^2 \mathbf{\kappa}] \cdot \mathbf{G}(\mathbf{k}) = \mathbf{\Gamma} \cdot \mathbf{G}(\mathbf{k}) = j\mu_0 \omega \mathbf{I}, \quad (\text{A8})$$

where

$$\mathbf{\Gamma} \equiv \mathbf{k}\mathbf{k} - k^2 \mathbf{I} + k_0^2 \mathbf{\kappa} \quad (\text{A9})$$

In the observing Cartesian coordinate system it can be expressed in a matrix form

$$\mathbf{\Gamma} = \begin{bmatrix} k_x^2 - k^2 + k_0^2 \varepsilon_1 & k_x k_y - jk_0^2 \varepsilon_2 & k_x k_z \\ k_x k_y + jk_0^2 \varepsilon_2 & k_y^2 - k^2 + k_0^2 \varepsilon_1 & k_y k_z \\ k_x k_z & k_y k_z & k_z^2 - k^2 + k_0^2 \varepsilon_3 \end{bmatrix} \quad (\text{A10})$$

Using the refractive index vector defined by

$$\mathbf{k} = k_0 \mathbf{n} \quad (\text{A11})$$

the vector can also be expressed as

$$\mathbf{\Gamma} = k_0^2 (\mathbf{n}\mathbf{n} - n^2 \mathbf{I} + \mathbf{\kappa}) \quad (\text{A12})$$

The matrix form is

$$\mathbf{\Gamma} = k_0^6 \begin{bmatrix} n_x^2 - n^2 + \varepsilon_1 & n_x n_y - j\varepsilon_2 & n_x n_z \\ n_x n_y + j\varepsilon_2 & n_y^2 - n^2 + \varepsilon_1 & n_y n_z \\ n_x n_z & n_y n_z & n_z^2 - n^2 + \varepsilon_3 \end{bmatrix} \quad (\text{A13})$$

From Equation (A8), the Fourier transform of the Green's function is then

$$\mathbf{G}(\mathbf{k}) = j\mu_0\omega\mathbf{\Gamma}^{-1} \quad (\text{A14})$$

The Green's function is

$$\mathbf{G}(\mathbf{r} - \mathbf{r}') = \frac{j\mu_0\omega}{(2\pi)^3} \int \mathbf{\Gamma}^{-1} e^{-j\mathbf{k} \cdot (\mathbf{r} - \mathbf{r}')} d\mathbf{k} \quad (\text{A15})$$

In Equations (A14) and (A15) the inverse matrix $\mathbf{\Gamma}^{-1} = \text{adj}(\mathbf{\Gamma}) / \det(\mathbf{\Gamma})$. Here the adjoint matrix of matrix $\mathbf{\Gamma}$ is denoted by $\text{adj}(\mathbf{\Gamma})$, and $\det(\mathbf{\Gamma})$ denotes the determinant of matrix $\mathbf{\Gamma}$. Next we find the expressions for the determinant and the adjoint matrix.

It takes some algebra but without difficulties one gets the expression for the determinant in the spherical coordinate system

$$\det(\mathbf{\Gamma}) = k_0^6 \left[\begin{aligned} &(\varepsilon_1 \sin^2 \theta + \varepsilon_3 \cos^2 \theta) n^4 \\ &+ ((\varepsilon_2^2 - \varepsilon_1^2) \sin^2 \theta - \varepsilon_1 \varepsilon_3 (1 + \cos^2 \theta)) n^2 \\ &+ (\varepsilon_1^2 - \varepsilon_2^2) \varepsilon_3 \end{aligned} \right] \quad (\text{A16})$$

Note that $\det(\mathbf{\Gamma})=0$ is the dispersion relation of cold plasma, leading to the refractive index of plane wave for the modes,

$$\begin{aligned} n^2 &= \frac{(\varepsilon_1^2 - \varepsilon_2^2) \sin^2 \theta + \varepsilon_1 \varepsilon_3 (1 + \cos^2 \theta) + q_{\pm}}{2(\varepsilon_1 \sin^2 \theta + \varepsilon_3 \cos^2 \theta)} \\ q_{\pm} &= \pm \sqrt{(\varepsilon_1^2 - \varepsilon_2^2 - \varepsilon_1 \varepsilon_3)^2 \sin^4 \theta + 4\varepsilon_2^2 \varepsilon_3^2 \cos^2 \theta} \\ &(-\pi/2 \leq \arg(q_+) < \pi/2, \quad \pi/2 \leq \arg(q_-) < 3\pi/2) \end{aligned} \quad (\text{A17})$$

Using the relation of the cylindrical and spherical coordinates

$$n_{\rho} = n \sin \theta, \quad n_z = n \cos \theta, \quad n^2 = n_{\rho}^2 + n_z^2 \quad (\text{A18})$$

the expression of the determinant in the cylindrical coordinate system is obtained

$$\det(\mathbf{\Gamma}) = k_0^6 \left[\begin{aligned} &\varepsilon_3 n_z^4 + ((\varepsilon_1 + \varepsilon_3) n_{\rho}^2 - 2\varepsilon_1 \varepsilon_3) n_z^2 \\ &+ \varepsilon_1 n_{\rho}^4 + (\varepsilon_2^2 - \varepsilon_1^2 - \varepsilon_1 \varepsilon_3) n_{\rho}^2 \\ &+ (\varepsilon_1^2 - \varepsilon_2^2) \varepsilon_3 \end{aligned} \right] \quad (\text{A19})$$

And the refractive index of plane waves becomes

$$\begin{aligned}
n_z^2 &= \frac{2\varepsilon_1\varepsilon_3 - (\varepsilon_1 + \varepsilon_3)n_\rho^2 + q_\pm}{2\varepsilon_3} \\
q_\pm &= \sqrt{(\varepsilon_1 - \varepsilon_3)n_\rho^4 - 4\varepsilon_2^2\varepsilon_3n_\rho^2 + 4\varepsilon_2^2\varepsilon_3^2} \\
(-\pi/2 \leq \arg(q_+) < \pi/2, \quad \pi/2 \leq \arg(q_-) < 3\pi/2)
\end{aligned} \tag{A20}$$

Especially in the parallel direction, $\theta = 0$,

$$n_\rho = 0, \quad n_z^2 = \frac{2\varepsilon_1\varepsilon_3 + q_\pm}{2\varepsilon_3} \tag{A21}$$

$$q_\pm = \pm 2\sqrt{\varepsilon_2^2\varepsilon_3^2}, \quad (-\pi/2 \leq \arg(q_+) < \pi/2, \quad \pi/2 \leq \arg(q_-) < 3\pi/2)$$

and in the perpendicular direction, $\theta = \pi/2$,

$$n_z = 0, \quad n_\rho^2 = \frac{\varepsilon_1^2 - \varepsilon_2^2 + \varepsilon_1\varepsilon_3 + q_\pm}{2\varepsilon_1} \tag{A22}$$

$$q_\pm = \pm \sqrt{(\varepsilon_1^2 - \varepsilon_2^2 - \varepsilon_1\varepsilon_3)^2}, \quad (-\pi/2 \leq \arg(q_+) < \pi/2, \quad \pi/2 \leq \arg(q_-) < 3\pi/2)$$

The adjoint matrix is

$$\begin{aligned}
\text{adj}(\Gamma) &= k^2 \mathbf{k} \mathbf{k} + k_0^2 \Gamma_1 + k_0^4 \text{adj}(\kappa) \\
\Gamma_1 &= \begin{bmatrix} \begin{pmatrix} -(k_x^2 + k_y^2)\varepsilon_1 \\ -(k_x^2 + k_z^2)\varepsilon_3 \end{pmatrix} & \begin{pmatrix} -k_x k_y \varepsilon_3 \\ -j(k_x^2 + k_y^2)\varepsilon_2 \end{pmatrix} & \begin{pmatrix} -k_x k_z \varepsilon_1 \\ -jk_y k_z \varepsilon_2 \end{pmatrix} \\ \begin{pmatrix} -k_x k_y \varepsilon_3 \\ +j(k_x^2 + k_y^2)\varepsilon_2 \end{pmatrix} & \begin{pmatrix} -(k_x^2 + k_y^2)\varepsilon_1 \\ -(k_y^2 + k_z^2)\varepsilon_3 \end{pmatrix} & \begin{pmatrix} -k_y k_z \varepsilon_1 \\ +jk_x k_z \varepsilon_2 \end{pmatrix} \\ \begin{pmatrix} -k_x k_z \varepsilon_1 \\ +jk_y k_z \varepsilon_2 \end{pmatrix} & \begin{pmatrix} -k_y k_z \varepsilon_1 \\ -jk_x k_z \varepsilon_2 \end{pmatrix} & -(k^2 + k_z^2)\varepsilon_1 \end{bmatrix} \\
\text{adj}(\kappa) &= \begin{bmatrix} \varepsilon_1\varepsilon_3 & j\varepsilon_2\varepsilon_3 & 0 \\ -j\varepsilon_2\varepsilon_3 & \varepsilon_1\varepsilon_3 & 0 \\ 0 & 0 & \varepsilon_1^2 - \varepsilon_2^2 \end{bmatrix}
\end{aligned} \tag{A23}$$

The Green's function (A15) can be rewritten as

$$\mathbf{G}(\mathbf{r} - \mathbf{r}') = \frac{j\mu_0\omega}{(2\pi)^3} \int \frac{\text{adj}(\Gamma)}{\det(\Gamma)} e^{-j\mathbf{k} \cdot (\mathbf{r} - \mathbf{r}')} d\mathbf{k} \tag{A24}$$

where the expressions for the determinant and the adjoint are given by Equations (A16) or (A19), and (A23), respectively.

Note that the Green's function is a matrix and Equation (A24) involves 9 integrations. Each element is different and complicated. The analysis has been much simplified using the method developed by Kogelnik [1960]. The idea is to change the integrand using the operator formula $\nabla \Leftrightarrow -j\mathbf{k}$. In fact, part of the integrand can be replaced by the result after a differential operation because

$$\text{adj}(\mathbf{\Gamma})e^{-j\mathbf{k}\cdot(\mathbf{r}-\mathbf{r}')} = \mathbf{\Lambda}e^{-j\mathbf{k}\cdot(\mathbf{r}-\mathbf{r}')} \quad (\text{A25})$$

where the differential operator is a tensor acting on the observing coordinates and it can be written as a matrix,

$$\mathbf{\Lambda} = \begin{bmatrix} \Lambda_{11} & \Lambda_{12} & \Lambda_{13} \\ \Lambda_{21} & \Lambda_{22} & \Lambda_{23} \\ \Lambda_{31} & \Lambda_{32} & \Lambda_{33} \end{bmatrix}$$

$$\begin{aligned} \Lambda_{11} &= \frac{\partial^2}{\partial x^2} \left(\frac{\partial^2}{\partial x^2} + \frac{\partial^2}{\partial y^2} + \frac{\partial^2}{\partial z^2} \right) + k_0^2 \left(\varepsilon_1 \left(\frac{\partial^2}{\partial x^2} + \frac{\partial^2}{\partial y^2} \right) + \varepsilon_3 \left(\frac{\partial^2}{\partial x^2} + \frac{\partial^2}{\partial z^2} \right) \right) + k_0^4 (\varepsilon_1 \varepsilon_3) \\ \Lambda_{12} &= \frac{\partial^2}{\partial x \partial y} \left(\frac{\partial^2}{\partial x^2} + \frac{\partial^2}{\partial y^2} + \frac{\partial^2}{\partial z^2} \right) + k_0^2 \left(\varepsilon_3 \frac{\partial^2}{\partial x \partial y} + j\varepsilon_2 \left(\frac{\partial^2}{\partial x^2} + \frac{\partial^2}{\partial y^2} \right) \right) + k_0^4 (j\varepsilon_2 \varepsilon_3) \\ \Lambda_{13} &= \frac{\partial^2}{\partial x \partial z} \left(\frac{\partial^2}{\partial x^2} + \frac{\partial^2}{\partial y^2} + \frac{\partial^2}{\partial z^2} \right) + k_0^2 \left(\varepsilon_1 \frac{\partial^2}{\partial x \partial z} + j\varepsilon_2 \frac{\partial^2}{\partial y \partial z} \right) \\ \Lambda_{21} &= \frac{\partial^2}{\partial y \partial x} \left(\frac{\partial^2}{\partial x^2} + \frac{\partial^2}{\partial y^2} + \frac{\partial^2}{\partial z^2} \right) + k_0^2 \left(\varepsilon_3 \frac{\partial^2}{\partial x \partial y} - j\varepsilon_2 \left(\frac{\partial^2}{\partial x^2} + \frac{\partial^2}{\partial y^2} \right) \right) + k_0^4 (-j\varepsilon_2 \varepsilon_3) \\ \Lambda_{22} &= \frac{\partial^2}{\partial y^2} \left(\frac{\partial^2}{\partial x^2} + \frac{\partial^2}{\partial y^2} + \frac{\partial^2}{\partial z^2} \right) + k_0^2 \left(\varepsilon_1 \left(\frac{\partial^2}{\partial x^2} + \frac{\partial^2}{\partial y^2} \right) + \varepsilon_3 \left(\frac{\partial^2}{\partial y^2} + \frac{\partial^2}{\partial z^2} \right) \right) + k_0^4 (\varepsilon_1 \varepsilon_3) \\ \Lambda_{23} &= \frac{\partial^2}{\partial y \partial z} \left(\frac{\partial^2}{\partial x^2} + \frac{\partial^2}{\partial y^2} + \frac{\partial^2}{\partial z^2} \right) + k_0^2 \left(\varepsilon_1 \frac{\partial^2}{\partial y \partial z} - j\varepsilon_2 \frac{\partial^2}{\partial x \partial z} \right) \\ \Lambda_{31} &= \frac{\partial^2}{\partial z \partial x} \left(\frac{\partial^2}{\partial x^2} + \frac{\partial^2}{\partial y^2} + \frac{\partial^2}{\partial z^2} \right) + k_0^2 \left(\varepsilon_1 \frac{\partial^2}{\partial x \partial z} - j\varepsilon_2 \frac{\partial^2}{\partial y \partial z} \right) \\ \Lambda_{32} &= \frac{\partial^2}{\partial z \partial y} \left(\frac{\partial^2}{\partial x^2} + \frac{\partial^2}{\partial y^2} + \frac{\partial^2}{\partial z^2} \right) + k_0^2 \left(\varepsilon_1 \frac{\partial^2}{\partial y \partial z} + j\varepsilon_2 \frac{\partial^2}{\partial x \partial z} \right) \\ \Lambda_{33} &= \frac{\partial^2}{\partial z^2} \left(\frac{\partial^2}{\partial x^2} + \frac{\partial^2}{\partial y^2} + \frac{\partial^2}{\partial z^2} \right) + k_0^2 \left(\varepsilon_1 \left(\frac{\partial^2}{\partial x^2} + \frac{\partial^2}{\partial y^2} + \frac{\partial^2}{\partial z^2} + \frac{\partial^2}{\partial z^2} \right) \right) + k_0^4 (\varepsilon_1^2 - \varepsilon_2^2) \end{aligned} \quad (\text{A26})$$

Using Equation (A25) to replace part of the integrand in (A24), and exchanging the order of differentiation and integration, the Green's function is finally found

$$\mathbf{G}(\mathbf{r}-\mathbf{r}') = \frac{j\mu_0\omega}{(2\pi)^3} \mathbf{\Lambda} \int \frac{1}{\det(\mathbf{\Gamma})} e^{-j\mathbf{k}\cdot(\mathbf{r}-\mathbf{r}')} d\mathbf{k} \quad (\text{A27})$$

And changing the variable with Equation (A11), it can also be written as

$$\mathbf{G}(\mathbf{r} - \mathbf{r}') = \frac{j\mu_0\omega k_0^3}{(2\pi)^3} \Lambda \int \frac{1}{\det(\mathbf{\Gamma})} e^{-j\mathbf{k} \cdot (\mathbf{r} - \mathbf{r}')} d\mathbf{n} \quad (\text{A28})$$

The integration is performed over the whole n-space. Note that now only a single integration is to be performed and, with the aid of the differential operator, 9 elements of the Green's function tensor are produced.

Appendix B: Fourier Cosine Expansion

This Appendix determines the coefficients in the Fourier cosine expansion

$$\frac{\gamma}{\gamma^2 - (n_\rho \sin \psi \cos \varphi + n_{z\pm} \operatorname{sgn}(z) \cos \psi)^2} = \sum_{m=0}^{\infty} d_{m\pm} \cos m\varphi \quad (\text{B1})$$

Since

$$\frac{\gamma}{\gamma^2 - (n_\rho \sin \psi \cos \varphi + \operatorname{sgn}(z) n_{z\pm} \cos \psi)^2} = \frac{1}{2} \left[\frac{1}{n_\rho \sin \psi \cos \varphi + \gamma + \operatorname{sgn}(z) n_{z\pm} \cos \psi} - \frac{1}{n_\rho \sin \psi \cos \varphi - \gamma + \operatorname{sgn}(z) n_{z\pm} \cos \psi} \right] \quad (\text{B2})$$

one need only discuss the expansion

$$\frac{1}{a \cos \varphi + b} = \sum_{m=0}^{\infty} c_m \cos m\varphi, \quad (a \neq b, b \neq 0) \quad (\text{B3})$$

When $a = 0$, there is only one non-zero coefficient c_0 . Using Kronecker's notation

$$\delta_{ij} = \begin{cases} 1, & \text{if } i = j; \\ 0, & \text{otherwise.} \end{cases} \quad (\text{B4})$$

the coefficients can be expressed as

$$c_m = \delta_{m0} \frac{1}{b}, \quad (a = 0, m = 0, 1, 2, \dots) \quad (\text{B5})$$

When $a \neq 0$, the coefficients are calculated by

$$c_m = \frac{1}{(1 + \delta_{m0})a\pi} \int_0^{2\pi} \frac{\cos m\varphi}{\cos \varphi + \frac{b}{a}} d\varphi \quad (\text{B6})$$

With the variable change $\tau = e^{j\varphi}$, the integration becomes an integral along a unit circle

$$c_m = \frac{1}{j(1 + \delta_{m0})a\pi} \oint \frac{1 + \tau^{2m}}{\left(\tau^2 + 2\frac{b}{a}\tau + 1\right)\tau^m} d\tau \quad (\text{B7})$$

The integrand has two simple poles

$$\tau^{(1,2)} = -\frac{b}{a} \pm \sqrt{\left(\frac{b}{a}\right)^2 - 1} \quad (\text{B8})$$

And, if $m > 0$, a third pole of the m -th order

$$\tau^{(3)} = 0 \quad (\text{B9})$$

Since $a \neq b$, only one of the first two poles is inside the unit circle, which is denoted by $\tau^{(1)}$, and the other, $\tau^{(2)}$, is outside of it. The integration can be performed using the residue theorem to yield

$$c_m = \frac{4}{(1 + \delta_{m0})a} \frac{(\tau^{(1)})^m}{(\tau^{(1)} - \tau^{(2)})}, \quad (a \neq 0, m = 0, 1, 2, \dots) \quad (\text{B10})$$

It is found that, from Equation (B8),

$$\lim_{a \rightarrow 0} \tau^{(1,2)} = \begin{cases} 0, \\ \infty \end{cases} \quad (\text{B11})$$

and from Equation (B7),

$$\begin{aligned} \lim_{a \rightarrow 0} c_m (a \neq 0, m = 0) &= \lim_{a \rightarrow 0} \frac{4}{(1 + \delta_{m0})a} \frac{1}{(\tau^{(1)} - \tau^{(2)})} = \frac{1}{b} = c_m (a = 0, m = 0) \\ \lim_{a \rightarrow 0} c_m (a \neq 0, m > 0) &= \lim_{a \rightarrow 0} \frac{4}{(1 + \delta_{m0})a} \frac{(\tau^{(1)})^m}{(\tau^{(1)} - \tau^{(2)})} = 0 = c_m (a = 0, m > 0) \end{aligned} \quad (\text{B12})$$

This indicates that the case shown by Equation (B5) is in fact included in the general case shown by Equation (B10), and thus the above derivation can be summarized with the expressions

$$\begin{aligned} \frac{1}{a \cos \varphi + b} &= \sum_{m=0}^{\infty} c_m \cos m\varphi, \quad (a \neq b, b \neq 0) \\ c_m &= \frac{4}{(1 + \delta_{m0})a} \frac{(\tau^{(1)})^m}{(\tau^{(1)} - \tau^{(2)})} \xrightarrow{a \rightarrow 0} \delta_{m0} \frac{1}{b} \\ \tau^{(1,2)} &= -\frac{b}{a} \pm \sqrt{\left(\frac{b}{a}\right)^2 - 1}, \quad |\tau^{(1)}| < 1 \end{aligned} \quad (\text{B13})$$

Applying this formula to Equation (B2) and noting that for collisional plasma the condition $(a \neq b, b \neq 0)$ is always satisfied, the coefficients in the expansion (B1) are found in the form

$$\begin{aligned} d_{m\pm} &= \frac{2}{(1 + \delta_{m0})n_\rho \sin \psi} \left[\frac{(\tau_1^{(1)})^m}{\tau_1^{(1)} - \tau_1^{(2)}} - \frac{(\tau_2^{(1)})^m}{\tau_2^{(1)} - \tau_2^{(2)}} \right] \xrightarrow{\sin \psi n_\rho \rightarrow 0} \frac{\delta_{m0}}{(n_{z\pm} \cos \psi)^2 - \gamma^2} \\ \tau_1^{(1,2)} &= -\frac{\gamma + \text{sgn}(z)n_{z\pm} \cos \psi}{n_\rho \sin \psi} \pm \sqrt{\left(\frac{\gamma + \text{sgn}(z)n_{z\pm} \cos \psi}{n_\rho \sin \psi}\right)^2 - 1}, \quad |\tau_1^{(1)}| < 1 \\ \tau_2^{(1,2)} &= +\frac{\gamma - \text{sgn}(z)n_{z\pm} \cos \psi}{n_\rho \sin \psi} \pm \sqrt{\left(\frac{\gamma - \text{sgn}(z)n_{z\pm} \cos \psi}{n_\rho \sin \psi}\right)^2 - 1}, \quad |\tau_2^{(1)}| < 1 \end{aligned} \quad (\text{B14})$$

Note that the Fourier cosine series (B1) is valid for any complex variable and uniformly converges in the whole complex n_ρ -plane. It is easy to prove that the coefficients have the symmetrical property of the form

$$\begin{aligned} d_{m\pm}(-n_\rho) &= (-1)^m d_{m\pm}(+n_\rho) \\ d_{m\pm}(z < 0) &= (-1)^m d_{m\pm}(z > 0) \end{aligned} \quad (\text{B15})$$

Equation (B15) plays an important role in the analysis of the general vector potential.

Appendix C: Computation of Refractive index of Spherical Wave

The computation of the refractive index of spherical waves is based on the saddle points. The objective of Appendix C includes: (1) Showing the difficulties to find roots of the saddle point equation; (2) Developing a method of determining the saddle points.

The refractive index of spherical waves is defined as

$$n_s = n_z(n_\rho) |\cos \alpha| + n_\rho \sin \alpha$$

$$n_z(n_\rho) = \sqrt{\frac{2\varepsilon_1\varepsilon_3 - (\varepsilon_1 + \varepsilon_3)n_\rho^2 + q(n_\rho)}{2\varepsilon_3}} \quad (C1)$$

$$q(n_\rho) = \sqrt{(\varepsilon_1 - \varepsilon_3)^2 n_\rho^4 - 4\varepsilon_2^2 \varepsilon_3 n_\rho^2 + 4\varepsilon_2^2 \varepsilon_3^2}$$

The saddle points, $n_{\rho S\pm}$, are selected from the roots of the equation

$$\frac{dn_s(n_\rho)}{dn_\rho} = 0 \quad (C2)$$

It can be written as

$$n_\rho \left[-(\varepsilon_1 + \varepsilon_3)q(n_\rho) + (\varepsilon_1 - \varepsilon_3)^2 n_\rho^2 - 2\varepsilon_2^2 \varepsilon_3 \right] |\cos \alpha| + 2\varepsilon_3 n_z(n_\rho) q(n_\rho) \sin \alpha = 0 \quad (C3)$$

For both modes the saddle points $n_{\rho S\pm}$ are the functions of the polar angle α ,

$$n_{\rho S\pm} = n_{\rho S\pm}(\alpha) \quad (C4)$$

Because of the symmetry property, we need to solve Equation (C3) only in the range $0 \leq \alpha \leq \pi/2$.

According to Equation (4.29), for collisional plasma the saddle points must satisfy the requirements

$$\begin{aligned} -\pi < \arg(n_z) < 0 \\ -\pi/2 \leq \arg(q_+) < \pi/2 \\ \pi/2 \leq \arg(q_-) < 3\pi/2 \end{aligned} \quad (C5a)$$

and

$$-\pi/2 \leq \arg(n_s) \leq 0 \quad (C5b)$$

The so-called radiation condition in (C5b) is set to make sure that the transmitted far field is going away from the antenna possibly with attenuation in collisional plasma, and it is very important in view of physics. The equality in Equation (C5b) gives two special cases: one when the refractive index is a positive number describing a progressive wave without attenuation, and the other when it is negative imaginary representing an evanescent wave.

For given plasma parameters and direction, the multi-valued function n_s given in Equation (C1) defines a four-sheet Riemann surface with eight branch points, where individual sheets join

together. The four branch points are derived from $q(n_\rho) = 0$, referred to as the q -branch points, and the other four from $n_z(n_\rho) = 0$, referred to as the n_z -branch points. The eight branch points on the complex n_ρ -plane depend on the plasma parameters but are independent of the polar angle,

$$\begin{aligned} n_\rho \Big|_{n_z=0}^{(1,2)} &= \pm \sqrt{\varepsilon_3}, & n_\rho \Big|_{n_z=0}^{(3,4)} &= \pm \sqrt{\frac{\varepsilon_1^2 - \varepsilon_2^2}{\varepsilon_1}} \\ n_\rho \Big|_{q=0}^{(1,2,3,4)} &= \pm \frac{\sqrt{2\varepsilon_2\varepsilon_3}}{\varepsilon_1 - \varepsilon_3} \sqrt{\varepsilon_2 \pm \sqrt{\varepsilon_2^2 - (\varepsilon_1 - \varepsilon_3)^2}} \end{aligned} \quad (\text{C6})$$

indicating that all Riemann surfaces for various variable α share the same branch points.

For collisional plasma, the eight branch points are distinct and none of them is located on the real or imaginary axis. In the limiting case when collision approaches zero, they may locate on the real or imaginary axis. As illustrated in Figure C-1, their locations are different for the eight CMA regions but the relative positions of the branch points are similar for all parameters in the same region. In Region 1, all the branch points are on the real axis, and the q -branch points are larger than the n_z -branch points. In Region 2, all four q -branch points and one pair of the n_z -branch points are on the real axis, and the other pair is on the imaginary axis. In Region 3, they are all on the real axis and the q -branch points are always located between the n_z -branch points. In Region 4, one pair of the n_z -branch points is located on the real axis, and another pair on the imaginary axis; four more q -branch points are located far from the origin on the imaginary axis. In Region 5, all the branch points are on the imaginary axis and the q -branch points are larger than the n_z -branch points. In Region 6, the n_z -branch points are located on the real axis, and the four q -branch points are symmetrically located on the plane. In Region 7, one pair of the n_z -branch points is located on the real axis, and another pair on the imaginary axis, and the four q -branch points are symmetrically located on the plane. In Region 8, all n_z -branch points are on the imaginary axis and the q -branch points are symmetrically located on the plane.

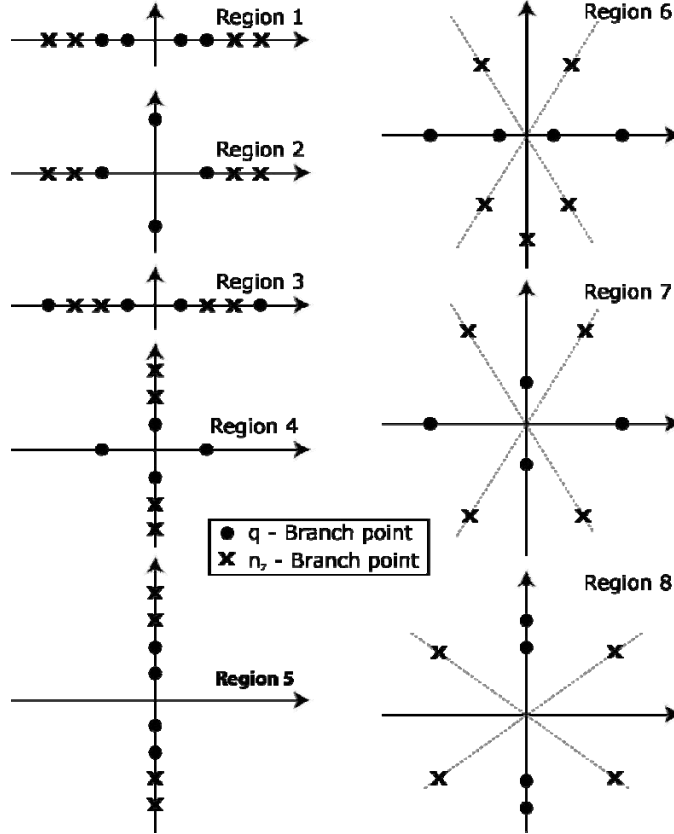


Figure C-1. Branch points in the n_ρ -plane for collisionless plasma

The four sheets of the Riemann surface can be disconnected by properly setting branch cut lines and the disconnected sheets are referred to as “ n_{z+}/q_+ ”, “ n_{z-}/q_+ ”, “ n_{z+}/q_- ” and “ n_{z-}/q_- ”, respectively,

$$\begin{aligned}
 \text{Sheet } n_{z+}/q_+ : & -\pi/2 \leq \arg(q) < \pi/2; \quad 0 < \arg(n_z) < +\pi \\
 \text{Sheet } n_{z-}/q_+ : & -\pi/2 \leq \arg(q) < \pi/2; \quad -\pi \leq \arg(n_z) \leq 0 \\
 \text{Sheet } n_{z+}/q_- : & \pi/2 \leq \arg(q) < 3\pi/2; \quad 0 < \arg(n_z) < +\pi \\
 \text{Sheet } n_{z-}/q_- : & \pi/2 \leq \arg(q) < 3\pi/2; \quad -\pi \leq \arg(n_z) \leq 0
 \end{aligned} \tag{C7}$$

The typical topological structure of the Riemann surface is illustrated in Figure C-2. The two sheets n_{z+}/q_+ and n_{z+}/q_- , and the other two sheets n_{z-}/q_+ and n_{z-}/q_- are connected at the branch points $n_\rho|_{q=0}^{(1,2)}$ and $n_\rho|_{q=0}^{(3,4)}$, respectively. When crossing any of these branch points it may go from one sheet to another and the propagation converts from one mode to another. The two sheets n_{z+}/q_+ and n_{z+}/q_- , and the other two sheets n_{z-}/q_+ and n_{z-}/q_- are connected at the branch points $n_\rho|_{n_z=0}^{(1,2)}$ and $n_\rho|_{n_z=0}^{(3,4)}$, respectively. When crossing any of these branch points it may go from one sheet to another and the wave vector component along the magnetic field changes to the opposite direction.

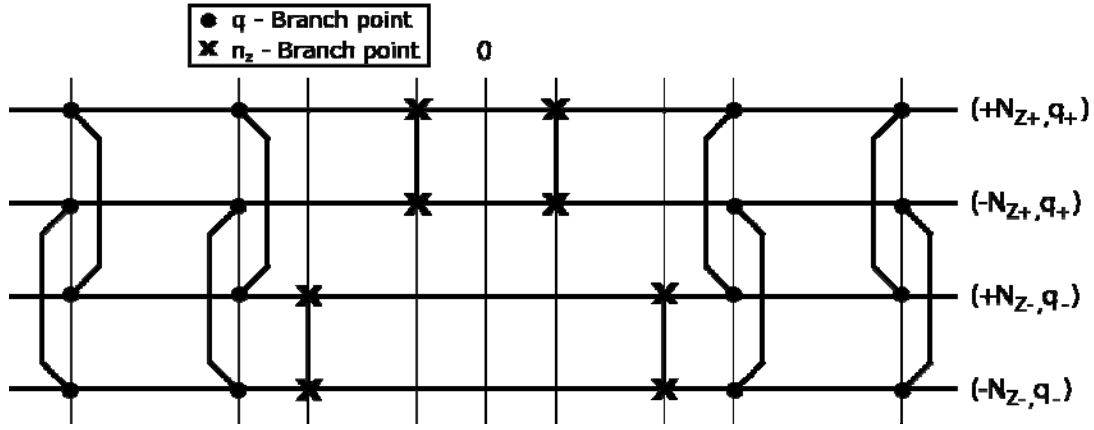


Figure C-2. Structure of the Riemann surface

In general, it is difficult to find an explicitly analytical expression for the roots of Equation (C3), but the solution can be found numerically. Since the required saddle points are located on the “ n_{z-}/q_+ ” or “ n_{z-}/q_- ” sheet of the Riemann surface, if using the direct method, every step of the numerical analysis must be carried out on the right sheet and it takes a lot of attentive care to do it.

To avoid the difficulty an alternative method is introduced. Doing square operations for $q(n_\rho)$ and $n_z(n_\rho)$, Equation (C3) can be transformed to a sextic equation (sixth-order polynomial)

$$a_6 \tau^6 + a_5 \tau^5 + a_4 \tau^4 + a_3 \tau^3 + a_2 \tau^2 + a_1 \tau + a_0 = 0 \quad (C8)$$

$$\tau = n_\rho^2$$

with the coefficients

$$\begin{aligned}
a_6 &= \varepsilon_1 (\varepsilon_1 - \varepsilon_3)^4 (\varepsilon_1 \cos^2 \alpha + \varepsilon_3 \sin^2 \alpha) \\
a_5 &= -(\varepsilon_1 - \varepsilon_3)^2 \left\{ \begin{aligned} &8\varepsilon_1^2 \varepsilon_2^2 \varepsilon_3 \cos^4 \alpha \\ &+ \left[-\varepsilon_2^2 (\varepsilon_1 + \varepsilon_3) (\varepsilon_1^2 + \varepsilon_3^2 - 10\varepsilon_1 \varepsilon_3) + \varepsilon_1 (\varepsilon_1 - \varepsilon_3)^2 (\varepsilon_1^2 + \varepsilon_3^2) \right] \sin^2 \alpha \cos^2 \alpha \\ &+ \varepsilon_3 \left[-\varepsilon_2^2 (\varepsilon_1^2 + \varepsilon_3^2 - 10\varepsilon_1 \varepsilon_3) + \varepsilon_1 (\varepsilon_1 + \varepsilon_3) (\varepsilon_1 - \varepsilon_3)^2 \right] \sin^4 \alpha \end{aligned} \right\} \\
a_4 &= \left\{ \begin{aligned} &2\varepsilon_2^2 \left[\varepsilon_1 \varepsilon_3 (\varepsilon_1^2 - \varepsilon_3^2)^2 - \varepsilon_2^2 \varepsilon_1 \varepsilon_3 (\varepsilon_1^2 + \varepsilon_3^2 - 10\varepsilon_1 \varepsilon_3) \right] \cos^4 \alpha \\ &+ \varepsilon_2^2 \varepsilon_3 \left[\begin{aligned} &(\varepsilon_1 - \varepsilon_3)^2 (7\varepsilon_1^3 + 17\varepsilon_1 \varepsilon_3^2 + 9\varepsilon_1^2 \varepsilon_3 - \varepsilon_3^3) \\ &- \varepsilon_2^2 (\varepsilon_1 + \varepsilon_3) (7\varepsilon_1^2 + 7\varepsilon_3^2 - 30\varepsilon_1 \varepsilon_3) \end{aligned} \right] \sin^2 \alpha \cos^2 \alpha \\ &+ \varepsilon_3^2 \left[\varepsilon_1^2 (\varepsilon_1 - \varepsilon_3)^4 + \varepsilon_2^2 (\varepsilon_1 - \varepsilon_3)^2 (7\varepsilon_1^2 + 18\varepsilon_1 \varepsilon_3 - \varepsilon_3^2) - 8\varepsilon_2^4 (\varepsilon_1^2 + \varepsilon_3^2 - 4\varepsilon_1 \varepsilon_3) \right] \sin^4 \alpha \end{aligned} \right\} \\
a_3 &= 2\varepsilon_2^2 \varepsilon_3 \left\{ \begin{aligned} &\left[-4\varepsilon_1 \varepsilon_3 \varepsilon_2^2 (\varepsilon_1 + \varepsilon_3)^2 + 4\varepsilon_2^4 \varepsilon_1 \varepsilon_3 \right] \cos^4 \alpha \\ &+ \left[\begin{aligned} &-\varepsilon_1 \varepsilon_3 (\varepsilon_1 - \varepsilon_3)^2 (3\varepsilon_1^2 + 3\varepsilon_3^2 + 2\varepsilon_1 \varepsilon_3) \\ &- \varepsilon_2^2 \varepsilon_3 (3\varepsilon_1^3 + 20\varepsilon_1^2 \varepsilon_3 + 31\varepsilon_1 \varepsilon_3^2 - 6\varepsilon_3^3) + 6\varepsilon_2^4 \varepsilon_3 (\varepsilon_1 + \varepsilon_3) \end{aligned} \right] \sin^2 \alpha \cos^2 \alpha \\ &+ 4\varepsilon_3^2 \left[-\varepsilon_1 (\varepsilon_1 - \varepsilon_3)^2 (2\varepsilon_1 + \varepsilon_3) + 2\varepsilon_2^2 \varepsilon_3 (\varepsilon_3 - 5\varepsilon_1) + 2\varepsilon_2^4 \right] \sin^4 \alpha \end{aligned} \right\} \\
a_2 &= \varepsilon_2^2 \varepsilon_3^2 \left\{ \begin{aligned} &\varepsilon_2^2 \left[(\varepsilon_1 + \varepsilon_3)^4 + \varepsilon_2^4 - 2\varepsilon_2^2 (\varepsilon_1 + \varepsilon_3)^2 \right] \cos^4 \alpha \\ &+ 4\varepsilon_2^2 \varepsilon_3 \left[(5\varepsilon_1^3 + 9\varepsilon_1^2 \varepsilon_3 + 11\varepsilon_1 \varepsilon_3^2 - \varepsilon_3^3) - \varepsilon_2^2 (5\varepsilon_1 + 7\varepsilon_3) \right] \sin^2 \alpha \cos^2 \alpha \\ &+ 8\varepsilon_3^2 \left[\varepsilon_1^2 (\varepsilon_1 - \varepsilon_3)^2 + \varepsilon_2^2 (5\varepsilon_1^2 + 8\varepsilon_1 \varepsilon_3 - \varepsilon_3^2) - 6\varepsilon_2^4 \right] \sin^4 \alpha \end{aligned} \right\} \\
a_1 &= 8\varepsilon_2^4 \varepsilon_3^4 \left\{ \left[\varepsilon_2^2 (\varepsilon_1 + 2\varepsilon_3) - \varepsilon_1 (\varepsilon_1 + \varepsilon_3)^2 \right] \cos^2 \alpha + 2\varepsilon_3 \left[3\varepsilon_2^2 - 3\varepsilon_1^2 - \varepsilon_1 \varepsilon_3 \right] \sin^2 \alpha \right\} \sin^2 \alpha \\
a_0 &= 16\varepsilon_2^4 \varepsilon_3^6 (\varepsilon_1^2 - \varepsilon_2^2) \sin^4 \alpha
\end{aligned} \tag{C9}$$

In the parallel direction, $\alpha = 0$, and thus $a_1 = a_0 = 0$, the equation becomes a quartic (fourth-order polynomial) equation. And in the perpendicular direction, $\alpha = \pi/2$, the equation can also be simplified. Except for these two special cases, no explicitly analytical solution can be found, in general, for a sixth-order polynomial equation such as Equation (C8), but in any case the six roots, τ_i ($i = 1, 2, \dots, 6$), can be evaluated by any available numerical method, providing twelve values of $n_\rho = \pm\sqrt{\tau_i}$, ($i = 1, 2, \dots, 6$). The required saddle points must be included in them and the remaining task is to identify which of them qualify as the saddle points to give physically meaningful solutions.

For collisionless plasma, all the coefficients in Equation (C9) are real numbers, and at least two real roots exist, positive or negative, and the others are conjugate pairs for such an even order polynomial equation. The conjugate pair result in progressive waves with attenuation along the propagation path.

This is physically unreasonable for collision-free plasma and all the roots in a conjugate pair should be abandoned. It remains to find out whether all the real roots are qualified.

Note that, in the course of transformation from Equation (C3) to (C8), the square operations cause the loss of designation of wave mode type. Each of the real roots is checked to see if it satisfies the original equation (C3) with an assumed mode type. The requirements given in Equation (C5a) is for the general collisional plasma. With consideration of the limit to collisionless plasma, the argument for n_z should extend to including the real axis, and for collisionless plasma the requirements are revised taking the form

$$\begin{aligned} -\pi &\leq \arg(n_z) \leq 0 \\ \pi/2 &\leq \arg(q_+) < \pi/2 \\ \pi/2 &\leq \arg(q_-) < 3\pi/2 \end{aligned} \tag{C10}$$

This procedure can successfully identify the mode type for all the real roots. It is found that, for a given direction, the two modes are always associated with different real roots unless the two roots are equal to each other. Consequently, the amplitudes of q-value for the two modes are not equal, in general, for the same polar angle α

The saddle point from the positive real root gives a positive real value for the spherical refractive index n_s , which represents a wave to propagate in the given direction α , while the saddle point from the negative real root results in a negative pure imaginary of spherical refractive index, which indicates that the wave is evanescent in the given direction. According to the theory of polynomials, the numbers of the positive and negative real roots are determined by the sign of $a_6 a_0$: If $a_6 a_0 > 0$, at least two real single roots are both positive or both negative and, if $a_6 a_0 < 0$, one is positive and the other negative. It is easy to prove that

$$\begin{aligned} a_6 a_0 > 0, & \begin{cases} \text{If } 0 < \alpha < \pi/2, \text{ for CMA Regions 1, 5 and 6;} \\ \text{If } \alpha_{\text{SRC}} < \alpha < \pi/2, \text{ for CMA Region 3;} \\ \text{If } 0 < \alpha < \alpha_{\text{SRC}}, \text{ for CMA Regions 7. and 8.} \end{cases} \\ a_6 a_0 < 0, & \begin{cases} \text{If } 0 < \alpha < \pi/2, \text{ for CMA Regions 2 and 4;} \\ \text{If } 0 < \alpha < \alpha_{\text{SRC}}, \text{ for CMA Region 3I;} \\ \text{If } \alpha_{\text{SRC}} < \alpha < \pi/2, \text{ for CMA Regions 7 and 8.} \end{cases} \end{aligned} \tag{C11}$$

$$\alpha_{\text{SRC}} = \arctan \sqrt{\frac{-\varepsilon_1}{\varepsilon_3}}$$

Therefore both mode waves can be transmitted and propagate in CMA Regions 1 and 6, but only one mode wave can propagate in Regions 2 and 4 and the other mode wave is evanescent. In Region 5, the transmitted waves of both modes are evanescent. It is interesting to note that one mode waves transmitted in Regions 3 (Extraordinary wave mode), 7 and 8 (Whistler wave mode) are confined in a cone. This cone is referred to as the radiation cone. The cone for the extraordinary wave in Region 3 is extended around the direction perpendicular to the ambient

magnetic field, and the whistler waves are confined in the cone around the direction of the ambient magnetic field. Since the resonance cone angle for plane wave is

$$\alpha_{RC} = \arctan \sqrt{\frac{-\varepsilon_3}{\varepsilon_1}} \quad (C12)$$

the radiation cone angle, α_{SRC} , and the resonance cone angle, α_{RC} , are complementary,

$$\alpha_{SRC} + \alpha_{RC} = \pi / 2 \quad (C13)$$

When crossing the border of the radiation cone, the refractive index of spherical waves jumps from a positive real number to a negative imaginary number.

It still remains determined whether all real roots are qualified as saddle points. For example, in the parallel direction $\alpha = 0$, Equation (C3) is reduced to

$$n_\rho \left[-(\varepsilon_1 + \varepsilon_3)q(n_\rho) + (\varepsilon_1 - \varepsilon_3)^2 n_\rho^2 - 2\varepsilon_2^2 \varepsilon_3 \right] = 0 \quad (C14)$$

The roots are

$$n_\rho^2 = \begin{cases} 0 \\ \frac{2\varepsilon_1 \varepsilon_2^2 \varepsilon_3 \pm \sqrt{\Delta}}{\varepsilon_2 (\varepsilon_1 - \varepsilon_3)^2}, \end{cases} \quad \Delta \equiv \varepsilon_1 \varepsilon_2^2 \varepsilon_3 (\varepsilon_1 + \varepsilon_3)^2 (\varepsilon_2 + \varepsilon_1 - \varepsilon_3)(\varepsilon_2 - \varepsilon_1 + \varepsilon_3) \quad (C15)$$

In the case of $\Delta \geq 0$, there are two more real roots and these two roots are also zero provided that

$$\begin{aligned} X &= 2 \frac{1-Y}{2-Y} \equiv X_1 \\ X &= 2 \frac{1+Y}{2+Y} \equiv X_2 \end{aligned} \quad (C16)$$

It is found, not only exactly along the direction of the ambient magnetic field but also around it, that more real roots exist:

- (1) In CMA Region 2, if $1 > X \geq X_2$;
- (2) In CMA Region 4, if $1 < X \leq X_2$;
- (3) In CMA Region 7, if $X \leq X_2$ and $X \geq X_1, Y > 2$;
- (4) In CMA Region 8, if $X \geq X_1, Y > 2$;
- (5) It can be proved that, around the perpendicular direction, in CMA Region 3, more real roots exist if $X \geq X_3 \equiv \sqrt{1-Y^2}$.

The areas in which multiple real roots exist are shaded in the CMA diagram in Figure C-3.

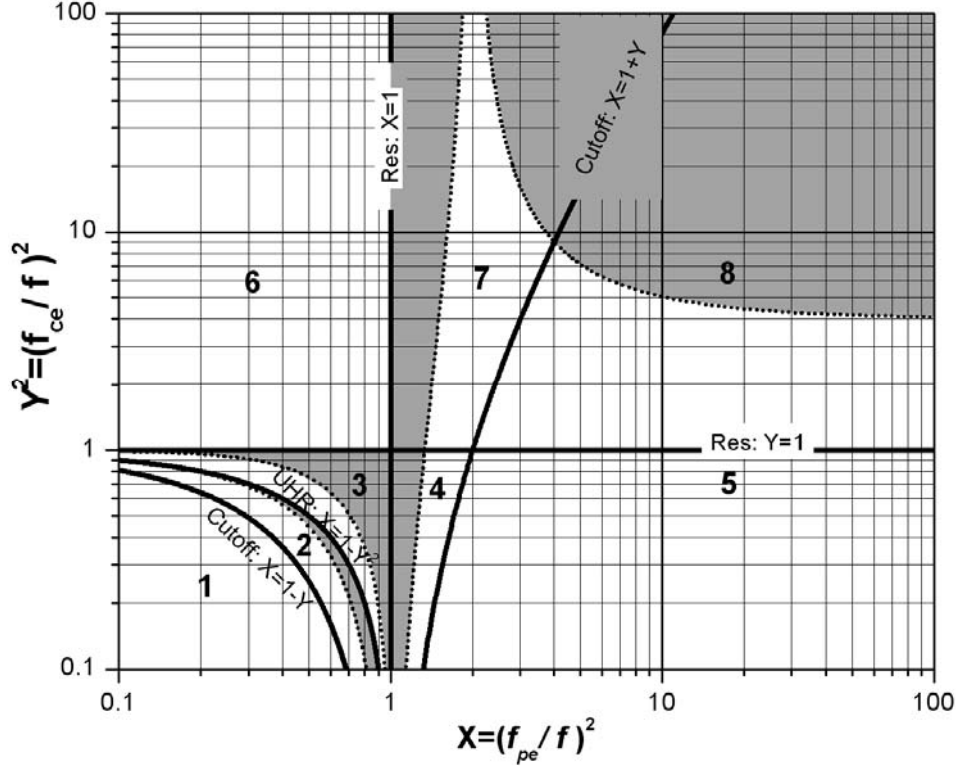


Figure C-3. Multiple real roots exist in the shaded area.

When multiple real roots exist in the shaded area, one needs to determine whether all or some of them are qualified. The general vector potential is derived for collisional plasma and it is acknowledged that, according to the limitation principle, its limit when the collision approaches zero is the true solution for collision-free plasma. When the check is done as described above, the requirements given in Equation (10) and (C5b) have to be checked. Figure C-4 can help to resolve the questions. In the figure, the open circles denote the solutions for collisional plasma when the collision rate is getting smaller and smaller, and finally arrive at the positions marked by black dots which denote the solutions for collision-free plasma. When doing the check as describe above, in the course of limitation from collisional to collisionless case, it is not clear whether the n_s point goes to the real or imaginary axis from outside of the fourth quadrant or from inside. If the former is the case, the associated root is obviously not qualified because the requirement given in Equation (C5b) is not satisfied, as illustrated in Figure C-4a.

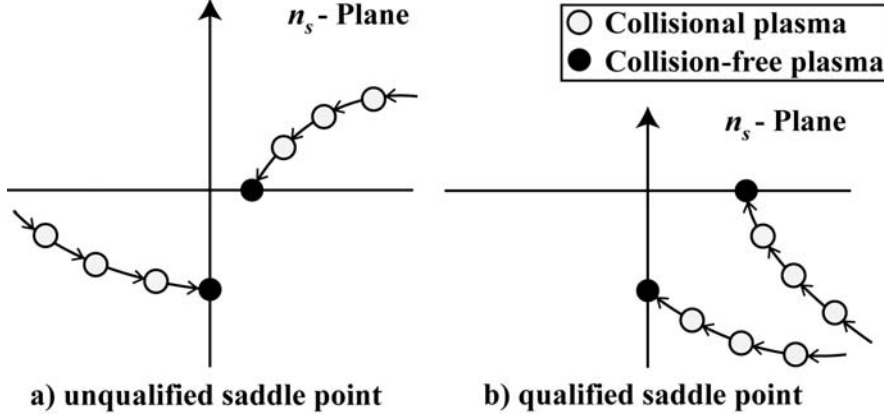


Figure C-4. Check with limitation principle.

For collisional plasma, the coefficients given in Equation (C9) are all complex and, in general, the roots of Equation (C8) are complex. Letting the collision rate get smaller and smaller, a sequence of the six roots can be obtained,

$$\{\tau_{1i}, \tau_{2i}, \tau_{3i}, \tau_{4i}, \tau_{5i}, \tau_{6i}\}, \quad i = 1, 2, 3, \dots \quad (\text{C17})$$

When the collision rate is zero, the multiple real roots appear in the last row of the sequence. The step used to change the collision should be properly selected so as to assure the accuracy of the found roots. A check must be done to see whether the corresponding “historical roots” from non-zero collision rates satisfy the Equations (C8), (C5a) and (C5b). The check is done for the two values as to determine which one should be used,

$$n_\rho = \pm \sqrt{\tau} \quad (\text{C18})$$

It is found that for each mode only one real root is qualified as the saddle point.

As an example, Figure C-5 shows this check of limitation principle for whistler mode in CMA Region 8. In Figure C-5a, the parameters are $X = 12, Y = 1.5$. There is only one positive root for any given value of α and it is easy to calculate the refractive index as shown in the figure. But as shown in Figures C-5b, C-5c and C-5d, the parameter ($X > X_1, Y > 2$) is located in the shaded area and three positive roots exist in the direction range of $\alpha \in (0, \alpha_m)$. Note that in Figure C-5d the value of α_m is even larger than the radiation cone angle. If the check of limitation principle is not done, the three submodes, shown as black dotted lines in the figure, would be accepted as the solution. In fact, once the check of limitation principle is done, the solid red lines denote the true solution of the refractive index. The curve of the refractive index jumps at the direction $\alpha = \alpha_T$ where two real roots are qualified. In the range $0 \leq \alpha \leq \alpha_T$ the smallest root is qualified and in the range $\alpha_T \leq \alpha \leq \pi/2$ the largest root is qualified. It is obvious that in this case the solution is overestimated without the check of limitation principle.

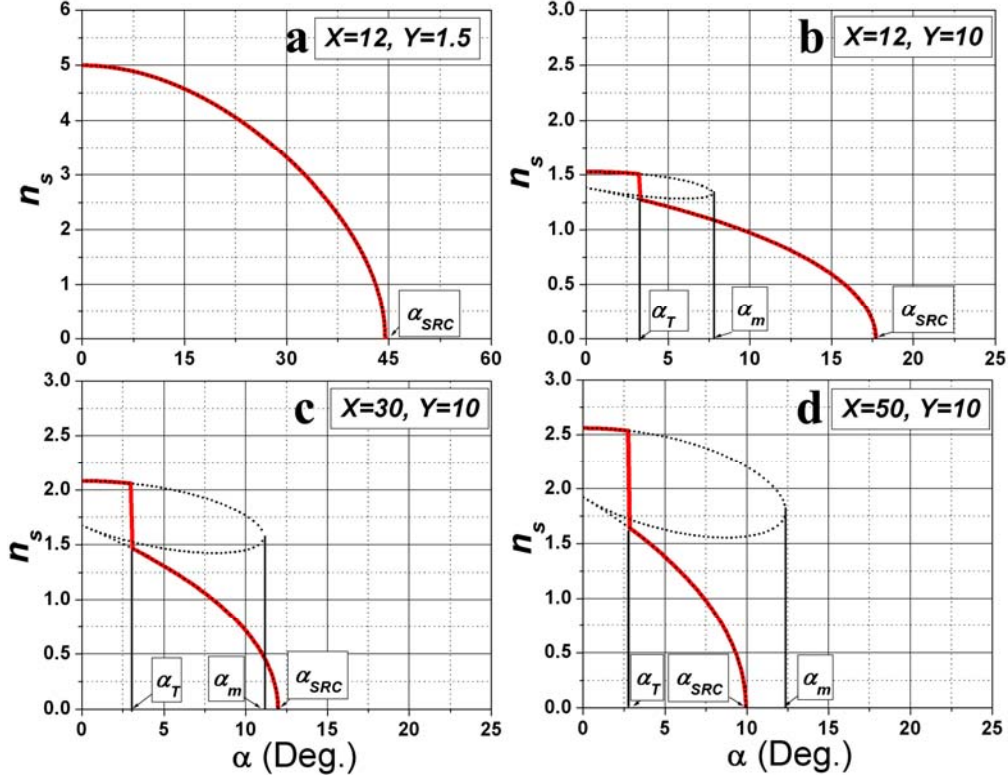


Figure C-5. Qualified saddle points for whistler modes.

As indicated by Equation (C14), in the parallel direction multiple real roots possibly exist. Only the root $= 0$ is always qualified. It is no surprising to have this result because this root always exists for collisional plasma with any value of collision. Therefore, the refractive index in the parallel direction is identical with that for plane wave,

$$\begin{aligned}
 \alpha &= 0 \\
 q_{\pm} &= \pm 2\sqrt{\varepsilon_2^2 \varepsilon_3^2} \\
 (-\pi/2 \leq \arg(q_+) < \pi/2, \quad \pi/2 \leq \arg(q_-) < 3\pi/2) \\
 n_{\rho s \pm} &= 0, \quad n_{z \pm} = \sqrt{\frac{2\varepsilon_1 \varepsilon_2 + q_{\pm}}{2\varepsilon_2}}, \quad (-\pi/2 \leq \arg(n_{z+}) \leq 0) \\
 n_{s \pm} &= n_{z \pm}
 \end{aligned} \tag{C19}$$

In the perpendicular direction, Equation (C3) is reduced to the same equation as to derive the branch points,

$$n_z(n_\rho)q(n_\rho) = 0 \tag{C20}$$

The q -branch points and the n_z -branch points are to be checked with the limitation principle. It is obvious that for CMA Regions 6, 7, and 8, the q -branch points are not qualified because they will make the refractive index of spherical waves complex with non-zero real and non-zero

imaginary parts, and it is physically unreasonable for collision-free plasma. In fact, in any case only one of the n_z -branch points is qualified as the saddle point, yielding

$$\begin{aligned}
\alpha &= \pi/2 \\
q_{\pm} &= \pm \sqrt{(\varepsilon_1^2 - \varepsilon_2^2 - \varepsilon_1 \varepsilon_3)^2} \\
(-\pi/2 \leq \arg(q_+) < \pi/2, \quad \pi/2 \leq \arg(q_-) < 3\pi/2) \\
n_{\rho s \pm} &= \sqrt{\frac{\varepsilon_1^2 - \varepsilon_2^2 + \varepsilon_1 \varepsilon_3 + q_{\pm}}{2\varepsilon_1}}, \quad (-\pi/2 \leq \arg(n_{\rho s+}) \leq 0) \\
n_{z \pm} &= 0 \\
n_{s \pm} &= n_{\rho s \pm}
\end{aligned} \tag{C21}$$

This equation shows that the refractive indices for both plane waves and spherical waves are identical in the perpendicular direction. Except for the above two special directions as given in Equations (C19) and (C21), the refractive index of spherical waves differ from that of plane waves.

In summary, it takes the following steps to calculate the refractive index of spherical waves:

- (1) For the parallel and perpendicular directions, the refractive index of spherical waves is identical with that of plane waves, as given by Equations (C19) and (C21).
- (2) For other directions, the roots of (C8) are calculated.
- (3) Each root is checked with an assumed mode to see whether it satisfies Equation (C3), (C5a), and (C5b). For the collisional plasma, the refractive index is calculated using the qualified roots.
- (4) For collisionless plasma, only the real roots need to be checked, and the values of q and n_z are calculated according to Equation (C10). When multiple real roots exist, the values of α_m and α_T are to be found. Then the qualified roots are determined and the refractive index is calculated.

Appendix D: Derivation of the Far Field Expression

The asymptotic form of the general vector potential can be written as

$$\mathbf{A}_{\pm}(\mathbf{r}) = (\hat{\mathbf{X}} \sin \psi + \hat{\mathbf{Z}} \cos \psi) A_{\pm}(r, \alpha, \beta)$$

$$A_{\pm}(r, \alpha, \beta) = \frac{\mu_0 \omega I_0}{2\pi k_0^5} F_{1\pm}(\alpha) F_{3\pm}(\alpha, \beta) \frac{\exp(-jk_0 n_s r)}{r} \quad (\text{D1})$$

Here $\hat{\mathbf{X}}$ and $\hat{\mathbf{Z}}$ stand for the unit vectors along the x- and z-axis, respectively, of the observing coordinate system. The electric field is determined by

$$\mathbf{E}_{\pm}(\mathbf{r}) = \mathbf{\Lambda} \cdot \mathbf{A}_{\pm}(\mathbf{r}) \quad (\text{D2})$$

and the components are

$$E_{x\pm}(\mathbf{r}) = (\sin \psi \Lambda_{11} + \cos \psi \Lambda_{13}) A_{\pm}(r, \alpha, \beta)$$

$$E_{y\pm}(\mathbf{r}) = (\sin \psi \Lambda_{21} + \cos \psi \Lambda_{23}) A_{\pm}(r, \alpha, \beta) \quad (\text{D3})$$

$$E_{z\pm}(\mathbf{r}) = (\sin \psi \Lambda_{31} + \cos \psi \Lambda_{33}) A_{\pm}(r, \alpha, \beta)$$

The expression of the differential operator is derived in Appendix A. The differentiation operation deals with variables in the Cartesian coordinate system while the general vector potential is expressed in terms of variables in the spherical coordinates. The derivation needs to use the Jacobian of the coordinate transformation,

$$J = \frac{\partial(x, y, z)}{\partial(r, \alpha, \beta)} = \begin{bmatrix} \sin \alpha \cos \beta & r \cos \alpha \cos \beta & -r \sin \alpha \sin \beta \\ \sin \alpha \sin \beta & r \cos \alpha \sin \beta & r \sin \alpha \cos \beta \\ \cos \alpha & -r \sin \alpha & 0 \end{bmatrix} \quad (\text{D4})$$

$$J^{-1} = \frac{\partial(r, \alpha, \beta)}{\partial(x, y, z)} = \begin{bmatrix} \sin \alpha \cos \beta & \sin \alpha \sin \beta & \cos \alpha \\ \cos \alpha \cos \beta / r & \cos \alpha \sin \beta / r & -\sin \alpha / r \\ -\sin \beta / (r \sin \alpha) & \cos \beta / (r \sin \alpha) & 0 \end{bmatrix}$$

Now the partial derivatives of the first order can be found

$$\begin{aligned}
\frac{\partial}{\partial x} A_{\pm}(r, \alpha, \beta) &= \left(\sin \alpha \cos \beta \frac{\partial}{\partial r} + \frac{1}{r} \cos \alpha \cos \beta \frac{\partial}{\partial \alpha} - \frac{\sin \beta}{r \sin \alpha} \frac{\partial}{\partial \beta} \right) A_{\pm}(r, \alpha, \beta) \\
&= \sin \alpha \cos \beta \left(-jk_0 n_s - \frac{1}{r} \right) A_{\pm}(r, \alpha, \beta) \\
&\quad + \frac{1}{r} \cos \alpha \cos \beta \left(\frac{1}{F_{1\pm}(\alpha)} \frac{\partial F_{1\pm}(\alpha)}{\partial \alpha} + \frac{1}{F_{3\pm}(\alpha, \beta)} \frac{\partial F_{3\pm}(\alpha, \beta)}{\partial \alpha} - jk_0 r \frac{dn_s}{d\alpha} \right) A_{\pm}(r, \alpha, \beta) \\
&\quad - \frac{\sin \beta}{r \sin \alpha} \frac{1}{F_{3\pm}(\alpha, \beta)} \frac{\partial F_{3\pm}(\alpha, \beta)}{\partial \beta} A_{\pm}(r, \alpha, \beta) \\
\frac{\partial}{\partial y} A_{\pm}(r, \alpha, \beta) &= \left(\sin \alpha \sin \beta \frac{\partial}{\partial r} + \frac{1}{r} \cos \alpha \sin \beta \frac{\partial}{\partial \alpha} + \frac{\cos \beta}{r \sin \alpha} \frac{\partial}{\partial \beta} \right) A_{\pm}(r, \alpha, \beta) \\
&= \sin \alpha \sin \beta \left(-jk_0 n_s - \frac{1}{r} \right) A_{\pm}(r, \alpha, \beta) \\
&\quad + \frac{1}{r} \cos \alpha \sin \beta \left(\frac{1}{F_{1\pm}(\alpha)} \frac{\partial F_{1\pm}(\alpha)}{\partial \alpha} + \frac{1}{F_{3\pm}(\alpha, \beta)} \frac{\partial F_{3\pm}(\alpha, \beta)}{\partial \alpha} - jk_0 r \frac{dn_s}{d\alpha} \right) A_{\pm}(r, \alpha, \beta) \\
&\quad + \frac{\cos \beta}{r \sin \alpha} \frac{1}{F_{3\pm}(\alpha, \beta)} \frac{\partial F_{3\pm}(\alpha, \beta)}{\partial \beta} A_{\pm}(r, \alpha, \beta) \\
\frac{\partial}{\partial z} A_{\pm}(r, \alpha, \beta) &= \left(\cos \alpha \frac{\partial}{\partial r} - \frac{\sin \alpha}{r} \frac{\partial}{\partial \alpha} \right) A_{\pm}(r, \alpha, \beta) \\
&= \cos \alpha \left(-jk_0 n_s - \frac{1}{r} \right) A_{\pm}(r, \alpha, \beta) \\
&\quad - \frac{\sin \alpha}{r} \left(\frac{1}{F_{1\pm}(\alpha)} \frac{\partial F_{1\pm}(\alpha)}{\partial \alpha} + \frac{1}{F_{3\pm}(\alpha, \beta)} \frac{\partial F_{3\pm}(\alpha, \beta)}{\partial \alpha} - jk_0 r \frac{dn_s}{d\alpha} \right) A_{\pm}(r, \alpha, \beta)
\end{aligned} \tag{D5}$$

Since we are interested in the far field, the faster evanescent terms with higher orders of $1/r$ can be dropped and the above partial derivatives become

$$\begin{aligned}
\frac{\partial}{\partial x} A_{\pm}(r, \alpha, \beta) &= -jk_0 \cos \beta \left(n_s \sin \alpha + \cos \alpha \frac{dn_s}{d\alpha} \right) A_{\pm}(r, \alpha, \beta) \\
\frac{\partial}{\partial y} A_{\pm}(r, \alpha, \beta) &= -jk_0 \sin \beta \left(n_s \sin \alpha + \cos \alpha \frac{dn_s}{d\alpha} \right) A_{\pm}(r, \alpha, \beta) \\
\frac{\partial}{\partial z} A_{\pm}(r, \alpha, \beta) &= -jk_0 \left(n_s \cos \alpha - \sin \alpha \frac{dn_s}{d\alpha} \right) A_{\pm}(r, \alpha, \beta)
\end{aligned} \tag{D6}$$

Note that the refractive index of spherical waves is a function of $n_{\rho s}$ and α , and $n_{\rho s}$ itself is also a function of α . Then we have

$$\frac{dn_s}{d\alpha} = \frac{\partial n_{zs}}{\partial n_{\rho s}} \frac{dn_{\rho s}}{d\alpha} \operatorname{sgn}(\pi/2 - \alpha) \cos \alpha - n_{zs} \operatorname{sgn}(\pi/2 - \alpha) \sin \alpha + \sin \alpha \frac{dn_{\rho s}}{d\alpha} + n_{\rho s} \cos \alpha \tag{D7}$$

Since $n_{\rho s}$ for either wave mode is a root of the equation

$$\frac{\partial n_{zs}}{\partial n_{\rho s}} \operatorname{sgn}(\pi/2 - \alpha) \cos \alpha + \sin \alpha = 0 \tag{D8}$$

Equation (D7) is simplified to

$$\frac{dn_s}{d\alpha} = -n_{zs} \operatorname{sgn}(\pi/2 - \alpha) \sin \alpha + n_{\rho s} \cos \alpha \quad (\text{D9})$$

Then Equation (D6) becomes

$$\begin{aligned} \frac{\partial}{\partial x} A_{\pm}(r, \alpha, \beta) &= -jk_0 n_{\rho s} \cos \beta A_{\pm}(r, \alpha, \beta) \\ \frac{\partial}{\partial y} A_{\pm}(r, \alpha, \beta) &= -jk_0 n_{\rho s} \sin \beta A_{\pm}(r, \alpha, \beta) \\ \frac{\partial}{\partial z} A_{\pm}(r, \alpha, \beta) &= -jk_0 \|n_{zs}\| A_{\pm}(r, \alpha, \beta) \end{aligned} \quad (\text{D10})$$

where we introduced the notation $\|n_{zs}\|$

$$\|n_{zs}\| \equiv n_{zs} \operatorname{sgn}(\pi/2 - \alpha) . \quad (\text{D11})$$

Equation (D10) shows that, in order to find the far field, the computation rule of the first order derivatives of the vector potential can simply be expressed as a factor,

$$\begin{aligned} \frac{\partial}{\partial x} &\Rightarrow -jk_0 n_{\rho s} \cos \beta \\ \frac{\partial}{\partial y} &\Rightarrow -jk_0 n_{\rho s} \sin \beta \\ \frac{\partial}{\partial z} &\Rightarrow -jk_0 \|n_{zs}\| \end{aligned} \quad (\text{D12})$$

Applying this operation rule to the derivatives of higher orders, we can derive

$$\begin{aligned} \Lambda_{11} A_{\pm} &= k_0^4 \left[n_{\rho s}^2 (n_{\rho s}^2 + n_{zs}^2) \cos^2 \beta - \varepsilon_1 n_{\rho s}^2 - \varepsilon_3 (n_{\rho s}^2 \cos^2 \beta + n_{zs}^2) + \varepsilon_1 \varepsilon_3 \right] A_{\pm} \\ \Lambda_{13} A_{\pm} &= k_0^4 n_{\rho s} \|n_{zs}\| \left[(n_{\rho s}^2 + n_{zs}^2 - \varepsilon_1) \cos \beta - j \varepsilon_2 \sin \beta \right] A_{\pm} \\ \Lambda_{21} A_{\pm} &= k_0^4 \left[n_{\rho s}^2 (n_{\rho s}^2 + n_{zs}^2) \sin \beta \cos \beta - n_{\rho s}^2 (\varepsilon_3 \sin \beta \cos \beta - j \varepsilon_2) - j \varepsilon_2 \varepsilon_3 \right] A_{\pm} \\ \Lambda_{23} A_{\pm} &= k_0^4 n_{\rho s} \|n_{zs}\| \left[(n_{\rho s}^2 + n_{zs}^2 - \varepsilon_1) \sin \beta + j \varepsilon_2 \cos \beta \right] A_{\pm} \\ \Lambda_{31} A_{\pm} &= k_0^4 n_{\rho s} \|n_{zs}\| \left[(n_{\rho s}^2 + n_{zs}^2 - \varepsilon_1) \cos \beta + j \varepsilon_2 \sin \beta \right] A_{\pm} \\ \Lambda_{33} A_{\pm} &= k_0^4 \left[n_{zs}^2 (n_{\rho s}^2 + n_{zs}^2) - \varepsilon_1 (n_{\rho s}^2 + 2n_{zs}^2) + (\varepsilon_1^2 - \varepsilon_2^2) \right] A_{\pm} \end{aligned} \quad (\text{D13})$$

Then the components of the electric field in the Cartesian coordinate system are in the form

$$\begin{aligned}
E_{x\pm}(\mathbf{r}) &= k_0^4 \left[\left[n_{\rho s\pm}^2 (n_{\rho s\pm}^2 + n_{zs}^2 - \varepsilon_3) \cos^2 \beta - \varepsilon_1 n_{\rho s\pm}^2 - \varepsilon_3 n_{zs}^2 + \varepsilon_1 \varepsilon_3 \right] \sin \psi \right. \\
&\quad \left. + n_{\rho s\pm} \|n_{zs}\| \left[(n_{\rho s\pm}^2 + n_{zs}^2 - \varepsilon_1) \cos \beta - j \varepsilon_2 \sin \beta \right] \cos \psi \right] A_{\pm} \\
E_{y\pm}(\mathbf{r}) &= k_0^4 \left[\left[n_{\rho s\pm}^2 (n_{\rho s\pm}^2 + n_{zs}^2 - \varepsilon_3) \sin \beta \cos \beta + j \varepsilon_2 (n_{\rho s\pm}^2 - \varepsilon_3) \right] \sin \psi \right. \\
&\quad \left. + n_{\rho s\pm} \|n_{zs}\| \left[(n_{\rho s\pm}^2 + n_{zs}^2 - \varepsilon_1) \sin \beta + j \varepsilon_2 \cos \beta \right] \cos \psi \right] A_{\pm} \\
E_{z\pm}(\mathbf{r}) &= k_0^4 \left[n_{\rho s\pm} \|n_{zs}\| \left[(n_{\rho s\pm}^2 + n_{zs}^2 - \varepsilon_1) \cos \beta + j \varepsilon_2 \sin \beta \right] \sin \psi \right. \\
&\quad \left. + \left[n_{zs}^2 (n_{\rho s\pm}^2 + n_{zs}^2) - \varepsilon_1 (n_{\rho s\pm}^2 + 2n_{zs}^2) + \varepsilon_1^2 - \varepsilon_2^2 \right] \cos \psi \right] A_{\pm}
\end{aligned} \tag{D14}$$

The components of the magnetic field in the Cartesian coordinate system are determined by

$$\mathbf{H}(\mathbf{r}) = \frac{j}{\mu_0 \omega} \nabla \times \mathbf{E}(\mathbf{r}). \tag{D15}$$

And the results are

$$\begin{aligned}
H_{x\pm} &= \frac{k_0^5}{\mu_0 \omega} \left[\|n_{zs}\| \left[n_{\rho s\pm}^2 ((\varepsilon_3 - \varepsilon_1) \sin \beta \cos \beta - j \varepsilon_2 \cos^2 \beta) + j \varepsilon_2 \varepsilon_3 \right] \sin \psi \right. \\
&\quad \left. + n_{\rho s\pm} \left[(-\varepsilon_1 (n_{\rho s\pm}^2 + n_{zs}^2) + \varepsilon_1^2 - \varepsilon_2^2) \sin \beta - j \varepsilon_2 n_{zs}^2 \cos \beta \right] \cos \psi \right] A_{\pm} \\
H_{y\pm} &= \frac{k_0^5}{\mu_0 \omega} \left[\|n_{zs}\| \left[-n_{\rho s\pm}^2 (\varepsilon_1 \sin^2 \beta + j \varepsilon_2 \sin \beta \cos \beta + \varepsilon_3 \cos^2 \beta) - \varepsilon_3 (n_{zs}^2 - \varepsilon_1) \right] \sin \psi \right. \\
&\quad \left. + n_{\rho s\pm} \left[-j \varepsilon_2 n_{zs}^2 \sin \beta + (\varepsilon_1 (n_{\rho s\pm}^2 + n_{zs}^2) - \varepsilon_1^2 + \varepsilon_2^2) \cos \beta \right] \cos \psi \right] A_{\pm} \\
H_{z\pm} &= \frac{k_0^5}{\mu_0 \omega} \left[(\varepsilon_1 n_{\rho s\pm}^2 + \varepsilon_3 n_{zs}^2 - \varepsilon_1 \varepsilon_3) \sin \beta + j \varepsilon_2 (n_{\rho s\pm}^2 - \varepsilon_3) \cos \beta \right] \sin \psi \\
&\quad + j \varepsilon_2 n_{\rho s\pm} \|n_{zs}\| \cos \psi \tag{D16}
\end{aligned}$$

Transform of the coordinate systems leads to the far field expression in the spherical coordinate system

$$\begin{aligned}
E_{r\pm}(r, \alpha, \beta) &= \frac{Z_0 I_0}{2\pi} F_{1\pm}(\alpha) F_{Er\pm}(\alpha, \beta) F_{3\pm}(\alpha, \beta) \frac{\exp(-jk_0 n_s r)}{r} \\
E_{\alpha\pm}(r, \alpha, \beta) &= \frac{Z_0 I_0}{2\pi} F_{1\pm}(\alpha) F_{E\alpha\pm}(\alpha, \beta) F_{3\pm}(\alpha, \beta) \frac{\exp(-jk_0 n_s r)}{r} \\
E_{\beta\pm}(r, \alpha, \beta) &= \frac{Z_0 I_0}{2\pi} F_{1\pm}(\alpha) F_{E\beta\pm}(\alpha, \beta) F_{3\pm}(\alpha, \beta) \frac{\exp(-jk_0 n_s r)}{r} \\
H_{r\pm}(r, \alpha, \beta) &= \frac{I_0}{2\pi} F_{1\pm}(\alpha) F_{Hr\pm}(\alpha, \beta) F_{3\pm}(\alpha, \beta) \frac{\exp(-jk_0 n_s r)}{r} \\
H_{\alpha\pm}(r, \alpha, \beta) &= \frac{I_0}{2\pi} F_{1\pm}(\alpha) F_{H\alpha\pm}(\alpha, \beta) F_{3\pm}(\alpha, \beta) \frac{\exp(-jk_0 n_s r)}{r} \\
H_{\beta\pm}(r, \alpha, \beta) &= \frac{I_0}{2\pi} F_{1\pm}(\alpha) F_{H\beta\pm}(\alpha, \beta) F_{3\pm}(\alpha, \beta) \frac{\exp(-jk_0 n_s r)}{r}
\end{aligned} \tag{D17}$$

Here the so-called impedance of free space is $Z_0 = \sqrt{\varepsilon_0/\mu_0} = 377$ ohms, and the coefficients $F_{E\alpha\pm}(\alpha, \beta)$, etc. take the form

$$\begin{aligned}
F_{Er\pm}(\alpha, \beta) &= \begin{bmatrix} (n_{\rho s\pm}^2 - \varepsilon_3)(n_{\rho s\pm}^2 + n_{zs}^2 - \varepsilon_1) \sin \psi \sin \alpha \cos \beta \\ + \left[(n_{zs}^2 - \varepsilon_1)(n_{\rho s\pm}^2 + n_{zs}^2 - \varepsilon_1) - \varepsilon_2^2 \right] \cos \psi \cos \alpha \\ + n_{\rho s\pm} \|n_{zs}\| (n_{\rho s\pm}^2 + n_{zs}^2 - \varepsilon_1) (\sin \psi \cos \alpha \cos \beta + \cos \psi \sin \alpha) \\ + j\varepsilon_2 \left[(n_{\rho s\pm}^2 - \varepsilon_3) \sin \alpha + n_{\rho s\pm} \|n_{zs}\| \cos \alpha \right] \sin \psi \sin \beta \end{bmatrix} \\
F_{E\alpha\pm}(\alpha, \beta) &= \begin{bmatrix} (n_{\rho s\pm}^2 - \varepsilon_3)(n_{\rho s\pm}^2 + n_{zs}^2 - \varepsilon_1) \sin \psi \cos \alpha \cos \beta \\ - \left[(n_{zs}^2 - \varepsilon_1)(n_{\rho s\pm}^2 + n_{zs}^2 - \varepsilon_1) - \varepsilon_2^2 \right] \cos \psi \sin \alpha \\ - n_{\rho s\pm} \|n_{zs}\| (n_{\rho s\pm}^2 + n_{zs}^2 - \varepsilon_1) (\sin \psi \sin \alpha \cos \beta - \cos \psi \cos \alpha) \\ + j\varepsilon_2 \left[(n_{\rho s\pm}^2 - \varepsilon_3) \cos \alpha - n_{\rho s\pm} \|n_{zs}\| \sin \alpha \right] \sin \psi \sin \beta \end{bmatrix} \\
F_{E\beta\pm}(\alpha, \beta) &= \begin{bmatrix} (\varepsilon_1 n_{\rho s\pm}^2 + \varepsilon_3 n_{zs}^2 - \varepsilon_1 \varepsilon_3) \sin \psi \sin \beta \\ + j\varepsilon_2 \left[(n_{\rho s\pm}^2 - \varepsilon_3) \sin \psi \cos \beta + n_{\rho s\pm} \|n_{zs}\| \cos \psi \right] \end{bmatrix} \\
F_{Hr\pm}(\alpha, \beta) &= F_{E\beta\pm}(\alpha, \beta) (n_{\rho s\pm} \cos \alpha - \|n_{zs}\| \sin \alpha) \\
F_{H\alpha\pm}(\alpha, \beta) &= F_{E\beta\pm}(\alpha, \beta) (n_{\rho s\pm} \sin \alpha + \|n_{zs}\| \cos \alpha) \\
F_{H\beta\pm}(\alpha, \beta) &= \begin{bmatrix} -\|n_{zs}\| \left[\varepsilon_3 (n_{\rho s\pm}^2 + n_{zs}^2 - \varepsilon_1) \cos \beta + j\varepsilon_2 \varepsilon_3 \sin \beta \right] \sin \psi \\ + n_{\rho s\pm} \left[\varepsilon_1 (n_{\rho s\pm}^2 + n_{zs}^2 - \varepsilon_1) + \varepsilon_2^2 \right] \cos \psi \end{bmatrix}
\end{aligned} \tag{D18}$$

Remember that $\|n_{zs}\|$ is not the absolute value but is defined by Equation (D11).

Appendix E: Convergence to the Isotropic/Free Space Solution

In this Appendix, the behavior of the derived expression of the far field, Equation (6.1), is examined for the limits when $Y \rightarrow 0$ and/or $X \rightarrow 0$ to reveal the convergence of the derived solution for magnetoplasma to the isotropic/free space case.

For collisionless plasma the first and the second order of the derivatives of the plasma parameters are

$$\begin{aligned} \frac{d\varepsilon_1}{dY} &= -\frac{2XY}{(1-Y^2)^2}, \quad \frac{d^2\varepsilon_1}{dY^2} = -\frac{2X(1+3Y^2)}{(1-Y^2)^3} \\ \frac{d\varepsilon_2}{dY} &= \frac{X(1+Y^2)}{(1-Y^2)^2}, \quad \frac{d^2\varepsilon_2}{dY^2} = \frac{2XY(3+Y^2)}{(1-Y^2)^3} \\ \frac{d\varepsilon_3}{dY} &= 0, \quad \frac{d^2\varepsilon_3}{dY^2} = 0 \end{aligned} \quad (E1)$$

For very weak magnetized plasma, the parameters can be expressed by a Taylor series approximation

$$\begin{aligned} \varepsilon_1 &= \varepsilon_3 - XY^2 + O(Y^4) \\ \varepsilon_2 &= XY + O(Y^3) \\ \varepsilon_3 &= 1 - X \end{aligned} \quad (E2)$$

where the remaining terms are denoted by, for example, $O(Y^4)$, indicating the omitted terms of the lowest order is $\sim Y^4$. As a result one can find the approximations for the mode discriminator

$$q_{\pm} = \pm 2 \left(\varepsilon_3^2 - \varepsilon_3 n_{\rho}^2 \right)^{1/2} XY + O(Y^2). \quad (E3)$$

And for the function

$$n_z = \sqrt{\varepsilon_3 - n_{\rho}^2} + \frac{-\varepsilon_3 n_{\rho}^2 \pm 2X \sqrt{\varepsilon_3^2 - \varepsilon_3 n_{\rho}^2}}{4\varepsilon_3 \sqrt{\varepsilon_3 - n_{\rho}^2}} Y + O(Y^2). \quad (E4)$$

This gives

$$n_z' \equiv \frac{dn_z}{dn_{\rho}} = \frac{-n_{\rho}}{\sqrt{\varepsilon_3 - n_{\rho}^2}} + \frac{Y}{4\varepsilon_3} \frac{\left[-\left(2\varepsilon_3 \left(\varepsilon_3^2 - \varepsilon_3 n_{\rho}^2 \right)^{1/2} \pm 2\varepsilon_3 X \right) \left(\varepsilon_3 - n_{\rho}^2 \right) + \left(-\varepsilon_3 n_{\rho}^2 \left(\varepsilon_3^2 - \varepsilon_3 n_{\rho}^2 \right)^{1/2} \pm 2X \left(\varepsilon_3^2 - \varepsilon_3 n_{\rho}^2 \right) \right) \right]}{\left(\varepsilon_3 - n_{\rho}^2 \right)^{3/2} \left(\varepsilon_3^2 - \varepsilon_3 n_{\rho}^2 \right)^{1/2}} n_{\rho} + O(Y^2) \quad (E5)$$

$$n_z'' \equiv \frac{d^2 n_z}{dn_{\rho}^2} = \frac{-\varepsilon_3}{\left(\varepsilon_3 - n_{\rho}^2 \right)^{3/2}} + O(Y)$$

Then the saddle points for the two modes can be found from the equation $n_z' = -\sin \alpha / |\cos \alpha|$, i.e.

$$\frac{-n_\rho}{\sqrt{\varepsilon_3 - n_\rho^2}} + \frac{Y}{4\varepsilon_3} \frac{\left\{ \begin{aligned} & -\left(2\varepsilon_3(\varepsilon_3^2 - \varepsilon_3 n_\rho^2)^{1/2} \pm 2\varepsilon_3 X\right)(\varepsilon_3 - n_\rho^2) \\ & + \left(-\varepsilon_3 n_\rho^2 (\varepsilon_3^2 - \varepsilon_3 n_\rho^2)^{1/2} \pm 2X(\varepsilon_3^2 - \varepsilon_3 n_\rho^2)\right) \end{aligned} \right\}}{(\varepsilon_3 - n_\rho^2)^{3/2} (\varepsilon_3^2 - \varepsilon_3 n_\rho^2)^{1/2}} n_\rho + O(Y^2) = -\frac{\sin \alpha}{|\cos \alpha|} \quad (\text{E6})$$

The zero order of approximation is

$$n_{\rho s}^2 = \varepsilon_3 \sin^2 \alpha \quad (\text{E7})$$

And the first order of approximation

$$n_{\rho s}^2 = \varepsilon_3 \frac{\sin^2 \alpha |\cos \alpha|^2 + \frac{Y}{2\varepsilon_3^2} \left[-\varepsilon_3 \varepsilon_3 (1 + |\cos \alpha|^2) \pm 2X^2 |\cos \alpha| \right] \sin^2 \alpha}{|\cos \alpha|^4 + \sin^2 \alpha |\cos \alpha|^2 + \frac{Y}{2\varepsilon_3^2} \left[-\varepsilon_3 \varepsilon_3 (1 + |\cos \alpha|^2) \pm 2X^2 |\cos \alpha| \right] \sin^2 \alpha} \quad (\text{E8})$$

Therefore the Taylor expansion of the saddle points takes the form

$$\begin{aligned} n_{\rho s}^2 &= \varepsilon_3 \sin^2 \alpha + \frac{\sin^2 \alpha}{2\varepsilon_3} \left[-\varepsilon_3^2 (1 + |\cos \alpha|^2) \pm 2X^2 |\cos \alpha| \right] Y + O(Y^2) \\ n_{\rho s} &= \sqrt{\varepsilon_3} \sin \alpha + \frac{\sin \alpha}{4\varepsilon_3^{3/2}} \left[-\varepsilon_3^2 (1 + |\cos \alpha|^2) \pm 2X^2 |\cos \alpha| \right] Y + O(Y^2) \end{aligned} \quad (\text{E9})$$

leading to

$$\begin{aligned} q_s &= \pm 2\varepsilon_3 |\cos \alpha| XY + O(Y^2) \\ n_{zs}^2 &= \varepsilon_3 \cos^2 \alpha - \frac{\sin^2 \alpha}{2\varepsilon_3} \left[-\varepsilon_3^2 (1 + \cos^2 \alpha) \pm 2|\cos \alpha| X \right] Y \pm |\cos \alpha| XY + O(Y^2) \\ n_{zs} &= \varepsilon_3^{1/2} |\cos \alpha| - \frac{\sin^2 \alpha}{4\varepsilon_3^{1/2}} \left[-\varepsilon_3^2 (1 + \cos^2 \alpha) \pm 2|\cos \alpha| X \right] Y \pm \frac{XY}{2\varepsilon_3^{1/2}} + O(Y^2) \\ n_s &= \varepsilon_3^{1/2} + O(Y) \\ n_{zs}'' &= \frac{-1}{\varepsilon_3^{1/2} |\cos \alpha|^3} + O(Y) \end{aligned} \quad (\text{E10})$$

Now it is easy to find the limits

$$\begin{aligned} F_1(\alpha) q_s &\equiv \frac{1}{n_{zs}} \left(\frac{n_{\rho s \pm}}{n_{zs}'' \sin \alpha |\cos \alpha|} \right)^{1/2} \xrightarrow{Y \rightarrow 0} j \\ \gamma &\xrightarrow{Y \rightarrow 0} \sqrt{\varepsilon_3} \end{aligned} \quad (\text{E11})$$

$$F_3(\alpha, \beta; L, \psi) \xrightarrow{Y \rightarrow 0} \frac{\cos(k_0 \sqrt{\varepsilon_3} L (\sin \psi \sin \alpha \cos \beta + \cos \psi \cos \alpha)) - \cos(k_0 \sqrt{\varepsilon_3} L)}{\sin(k_0 \sqrt{\varepsilon_3} L) \left[1 - (\sin \psi \sin \alpha \cos \beta + \cos \psi \cos \alpha)^2 \right]}$$

and

$$\begin{aligned}
\frac{(n_{\rho s \pm}^2 + n_{zs}^2 - \varepsilon_1)}{q_s} &\xrightarrow{Y \rightarrow 0} \frac{1}{2\varepsilon_3} \\
\frac{(\varepsilon_1 n_{\rho s \pm}^2 + \varepsilon_3 n_{zs}^2 - \varepsilon_1 \varepsilon_3)}{q_s} &\xrightarrow{Y \rightarrow 0} \frac{1}{2} \\
\frac{\varepsilon_2}{q_s} &\xrightarrow{Y \rightarrow 0} \frac{\mp 1}{2\varepsilon_3 |\cos \alpha|} \\
\frac{\varepsilon_2^2}{q_s} &\xrightarrow{Y \rightarrow 0} 0
\end{aligned} \tag{E12}$$

Using the expression of the far field and noting that $\|\cos \alpha\| = \cos \alpha$, the limits of the propagation factor can be found

$$\begin{aligned}
\frac{F_{Er \pm}(\alpha, \beta)}{q_{s \pm}} &\xrightarrow{Y \rightarrow 0} 0 \\
\frac{F_{E\alpha \pm}(\alpha, \beta)}{q_{s \pm}} &\xrightarrow{Y \rightarrow 0} \frac{1}{2} \begin{cases} -\sin \psi \cos \alpha \cos \beta + \cos \psi \sin \alpha \pm j \sin \psi \sin \beta, & 0 \leq \alpha \leq \pi/2 \\ -\sin \psi \cos \alpha \cos \beta + \cos \psi \sin \alpha \mp j \sin \psi \sin \beta, & \pi/2 < \alpha \leq \pi \end{cases} \\
\frac{F_{E\beta \pm}(\alpha, \beta)}{q_{s \pm}} &\xrightarrow{Y \rightarrow 0} \begin{cases} \frac{1}{2} \{ \sin \psi \sin \beta \mp j [-\sin \psi \cos \alpha \cos \beta + \cos \psi \sin \alpha] \}, & 0 \leq \alpha \leq \pi/2 \\ \frac{1}{2} \{ \sin \psi \sin \beta \pm j [-\sin \psi \cos \alpha \cos \beta + \cos \psi \sin \alpha] \}, & \pi/2 < \alpha \leq \pi \end{cases} \\
\frac{F_{Hr \pm}(\alpha, \beta)}{q_{s \pm}} &\xrightarrow{Y \rightarrow 0} 0 \\
\frac{F_{H\alpha \pm}(\alpha, \beta)}{q_{s \pm}} &\xrightarrow{Y \rightarrow 0} -\sqrt{\varepsilon_3} \frac{F_{E\beta \pm}(\alpha, \beta)}{q_{s \pm}} \\
\frac{F_{H\beta \pm}(\alpha, \beta)}{q_{s \pm}} &\xrightarrow{Y \rightarrow 0} \begin{cases} \frac{1}{2} \sqrt{\varepsilon_3} [-\sin \psi \cos \alpha \cos \beta + \cos \psi \sin \alpha \pm j \sin \psi \sin \beta], & 0 \leq \alpha \leq \pi/2 \\ \frac{1}{2} \sqrt{\varepsilon_3} [-\sin \psi \cos \alpha \cos \beta + \cos \psi \sin \alpha \mp j \sin \psi \sin \beta], & \pi/2 < \alpha \leq \pi \end{cases} \tag{E13}
\end{aligned}$$

In the limit, the far fields of the two modes in an isotropic medium with the refractive index $n = \sqrt{\varepsilon_3}$ are therefore represented by two transverse spherical waves, circular polarized with equal amplitudes and opposite sense of rotation. Since the limiting far fields of the two modes in isotropic medium are propagating with the same speed, the sum of the two modes results in a linear polarized wave,

$$\begin{aligned}
E_r(r, \alpha, \beta) &= 0 \\
E_\alpha(r, \alpha, \beta) &= \frac{jZ_0 I_0}{2\pi} \begin{pmatrix} -\sin \psi \cos \alpha \cos \beta \\ +\cos \psi \sin \alpha \end{pmatrix} F_3(\alpha, \beta; L, \psi) \frac{\exp(-jk_0 \sqrt{\varepsilon_3} r)}{r} \\
E_\beta(r, \alpha, \beta) &= \frac{jZ_0 I_0}{2\pi} (\sin \psi \sin \beta) F_3(\alpha, \beta; L, \psi) \frac{\exp(-jk_0 \sqrt{\varepsilon_3} r)}{r} \\
H_r(r, \alpha, \beta) &= 0 \\
H_\alpha(r, \alpha, \beta) &= \frac{jI_0}{2\pi} \sqrt{\varepsilon_3} (\sin \psi \sin \beta) F_3(\alpha, \beta; L, \psi) \frac{\exp(-jk_0 \sqrt{\varepsilon_3} r)}{r} \\
H_\beta(r, \alpha, \beta) &= \frac{jI_0}{2\pi} \sqrt{\varepsilon_3} \begin{pmatrix} -\sin \psi \cos \alpha \cos \beta \\ +\cos \psi \sin \alpha \end{pmatrix} F_3(\alpha, \beta; L, \psi) \frac{\exp(-jk_0 \sqrt{\varepsilon_3} r)}{r}
\end{aligned} \tag{E14}$$

This shows the far field for an antenna located in an isotropic medium with refractive index $n = \sqrt{\varepsilon_3}$. Without losing generality we can set the orientation angle $\psi = 0$ for isotropic medium, and the expressions reduce to

$$\begin{aligned}
E_r(r, \alpha, \beta) &= 0 \\
E_\alpha(r, \alpha, \beta) &= \frac{jZ_0 I_A}{2\pi} \frac{\cos(k_0 \sqrt{\varepsilon_3} L \cos \alpha) - \cos(k_0 \sqrt{\varepsilon_3} L)}{\sin \alpha} \frac{\exp(-jk_0 \sqrt{\varepsilon_3} r)}{r} \\
E_\beta(r, \alpha, \beta) &= 0 \\
H_r(r, \alpha, \beta) &= 0 \\
H_\alpha(r, \alpha, \beta) &= 0 \\
H_\beta(r, \alpha, \beta) &= \frac{jI_A}{2\pi} \frac{\cos(k_0 \sqrt{\varepsilon_3} L \cos \alpha) - \cos(k_0 \sqrt{\varepsilon_3} L)}{\sin \alpha} \frac{\exp(-jk_0 \sqrt{\varepsilon_3} r)}{r} \\
I_A &\equiv \frac{I_0}{\sin(k_0 L)}
\end{aligned} \tag{E15}$$

This expression represents the far field in isotropic medium for an antenna along the z-axis. When the electron density is very small or the frequency is very high so that $X \rightarrow 0$ and $\varepsilon_3 \rightarrow 1$, Equation (E15) is exactly reduced to the well known expression of the far field for an antenna in free space,

$$\begin{aligned}
E_r(r, \alpha, \beta) &= 0 \\
E_\alpha(r, \alpha, \beta) &= \frac{jZ_0 I_A}{2\pi} \frac{\cos(k_0 L \cos \alpha) - \cos(k_0 L)}{\sin \alpha} \frac{\exp(-jk_0 r)}{r} \\
E_\beta(r, \alpha, \beta) &= 0 \\
H_r(r, \alpha, \beta) &= 0 \\
H_\alpha(r, \alpha, \beta) &= 0 \\
H_\beta(r, \alpha, \beta) &= \frac{jI_A}{2\pi} \frac{\cos(k_0 L \cos \alpha) - \cos(k_0 L)}{\sin \alpha} \frac{\exp(-jk_0 r)}{r} \\
I_A &\equiv \frac{I_0}{\sin(k_0 L)}
\end{aligned} \tag{E16}$$

In the above discussion, the limiting procedure is done first for $Y \rightarrow 0$ and then $X \rightarrow 0$. It should be pointed out that the limiting can also be treated in one step $X \rightarrow 0$ and $Y \rightarrow 0$, and a similar derivation yields the same result as given above, indicating the convergence of the general results to free space case.

Appendix F: Comments on Previously Published Papers

Below we outline our attempts to reproduce some previous VLF radiation theories. Wang and Bell concentrated their efforts on the VLF radiation problem in the late 1960s and early 1970s. Three major papers were published:

- [1] On VLF radiation fields along the static magnetic field from sources immersed in a magneto plasma, IEEE Trans. Ant. And Prop. November 1969.
- [2] On VLF radiation resistance of an electric dipole in a cold magnetoplasma, Radio Science, 5, 3, 1970.
- [3] VLF/ELF radiation patterns of arbitrary oriented electric and magnetic dipoles in a cold lossless multicomponent magnetoplasma, JGR, March 1, 1972.

Wang and Bell treated a short antenna which leads simple integration over the source. Based on Wang and Bell [1], the far-field radiated from a short antenna with a linear current distribution fed at the antenna center, the radiation resistance and the radiation patterns were analyzed as described in papers [2] and [3], respectively.

We found some mathematical errors in the derivation of paper [1]. When the time factor $\exp(j\omega t)$ is used, the relative dielectric matrix of a magnetoplasma with the magnetized field along the z-axis can be written as:

$$\mathbf{\kappa} = \begin{bmatrix} \varepsilon_1 & -j\varepsilon_2 & 0 \\ j\varepsilon_2 & \varepsilon_1 & 0 \\ 0 & 0 & \varepsilon_3 \end{bmatrix} \quad (\text{F1})$$

The k-space (n-space) integration to derive the Green's function is

$$I(\mathbf{r}) = \frac{j}{2\pi k_0} \int_0^\pi \int_0^{2\pi} \int_0^\infty \left\{ \frac{n^2 \sin \theta e^{-jk_0 \mathbf{n} \cdot \mathbf{r}}}{(\varepsilon_1 \sin^2 \theta + \varepsilon_3 \cos^2 \theta)(n^2 - n_+^2)(n^2 - n_-^2)} \right\} dnd\varphi d\theta \quad (\text{F2})$$

where $k_0 = \omega/c$ is the wave number in free space, and n_\pm are the refractive indices of the two modes,

$$n_\pm^2 = \frac{(\varepsilon_1^2 - \varepsilon_2^2) \sin^2 \theta + \varepsilon_1 \varepsilon_3 (1 + \cos^2 \theta) + q_\pm(\theta)}{2(\varepsilon_1 \sin^2 \theta + \varepsilon_3 \cos^2 \theta)} \quad (\text{F3})$$

$$q_\pm(\theta) = \pm \sqrt{(\varepsilon_1^2 - \varepsilon_2^2 - \varepsilon_1 \varepsilon_3)^2 \sin^4 \theta + 4\varepsilon_2^2 \varepsilon_3^2 \cos^2 \theta}$$

The observing vector can be expressed in the Cartesian coordinate, spherical, or cylindrical coordinate system

$$\mathbf{r} = (x, y, z) = (r, \alpha, \beta) = (\rho, \beta, z) \quad (\text{F4})$$

Similarly, the refractive index vector

$$\mathbf{n} = (n_x, n_y, n_z) = (n, \theta, \varphi) = (n_\rho, \varphi, n_z). \quad (\text{F5})$$

Equation (F2) is identical to Equation (F3) given in [1] except for some notations and the point source position. Before the source analysis is involved, without losing generality it can be assumed that the point source is located at the origin of the coordinate system. According to paper [1], the contour integration with respect to the variable n and the integration with respect to azimuthal angle φ can be performed to yield (see Equation (5) in [1])

$$I(\mathbf{r}) = -\frac{2\pi}{k_0} \int_0^{\pi/2, \theta_r} d\theta \frac{\sin \theta}{q_+(\theta)} n_-^{(1)} J_0(k_0 n_-^{(1)} \rho \sin \theta) e^{-jk_0 n_-^{(1)} \cos \theta |z|} \quad (\text{F6})$$

This result is critical to the analysis of the far field to derive the radiation resistance and the features in radiation patterns. No detailed derivation that shows how to get Equation (F6) from Equation (F2) was given in [1]. In other words, Equation (F6) above, or Equation (5) in [1], are in question. As the integrations in Equation (F2) over the variables n and φ have been performed to derive (F6), there are two possible integration orders to follow: (a) integrating over φ first and then over n , or (b) integrating over n first and then over φ . Below we test both approaches in a rigorous manner.

The integration in Equation (F2) can be separated into two parts I_1 and I_2 ,

$$I(\mathbf{r}) = I_1 + I_2$$

$$I_1 = \frac{j}{2\pi k_0} \int_0^{\pi/2} d\theta \int_0^{2\pi} d\varphi \int_0^\infty dn \left\{ \frac{n^2 \sin \theta e^{-jk_0 n r \cos \tau}}{(\varepsilon_1 \sin^2 \theta + \varepsilon_3 \cos^2 \theta)(n^2 - n_+^2)(n^2 - n_-^2)} \right\} \quad (\text{F7})$$

$$I_2 = \frac{j}{2\pi k_0} \int_{\pi/2}^\pi d\theta \int_0^{2\pi} d\varphi \int_0^\infty dn \left\{ \frac{n^2 \sin \theta e^{-jk_0 n r \cos \tau}}{(\varepsilon_1 \sin^2 \theta + \varepsilon_3 \cos^2 \theta)(n^2 - n_+^2)(n^2 - n_-^2)} \right\}$$

where τ is the angle between the observing vectors \mathbf{r} and the refractive index vector \mathbf{n} , and $\mathbf{n} \cdot \mathbf{r} = nr \cos \tau = n_\rho \rho \cos(\varphi - \beta) + n_z z = n(\rho \sin \theta \cos(\varphi - \beta) + z \cos \theta)$

$$\cos \tau \equiv \sin \alpha \sin \theta \cos(\varphi - \beta) + \cos \alpha \cos \theta \quad (\text{F8})$$

For the second integration I_2 changing variables with

$$n' = -n, \quad \theta' = \pi - \theta, \quad \varphi' = \varphi - \pi,$$

it is easy to prove that

$$I_2 = \frac{j}{2\pi k_0} \int_0^{\pi/2} d\theta' \int_{-\pi}^\pi d\varphi' \int_{-\infty}^0 dn' \left\{ \frac{(n')^2 \sin \theta' e^{-jk_0 n' r \cos \tau'}}{(\varepsilon_1 \sin^2 \theta' + \varepsilon_3 \cos^2 \theta')((n')^2 - (n_+')^2)((n')^2 - (n_-')^2)} \right\} \quad (\text{F9})$$

where τ' corresponds to θ' and φ' in the definition of τ in (F8). Noting that the integration of φ' is over a whole cycle, which can be shifted to from 0 to 2π , $n \cos \tau = n' \cos \tau'$, and $n_{\pm} = n'_{\pm}$, the integral (F2) can be expressed in the form

$$I(\mathbf{r}) = \frac{j}{2\pi k_0} \int_0^{\pi/2} d\theta \frac{\sin \theta}{(\varepsilon_1 \sin^2 \theta + \varepsilon_3 \cos^2 \theta)} \int_{-\infty}^{+\infty} dn \frac{n^2 e^{-jk_0 n z \cos \theta}}{(n^2 - n_+^2)(n^2 - n_-^2)} \int_0^{2\pi} d\varphi e^{-jk_0 n \rho \sin \theta \cos(\varphi - \beta)} \quad (\text{F10})$$

or in the form

$$I(\mathbf{r}) = \frac{j}{2\pi k_0} \int_0^{\pi/2} d\theta \frac{\sin \theta}{(\varepsilon_1 \sin^2 \theta + \varepsilon_3 \cos^2 \theta)} \int_0^{2\pi} d\varphi \int_{-\infty}^{+\infty} dn \left\{ \frac{n^2 e^{-jk_0 n r \cos \tau}}{(n^2 - n_+^2)(n^2 - n_-^2)} \right\} \quad (\text{F11})$$

Since both Equations (F10) and (F11) are derived from Equation (F2), we can use either one to evaluate the integration as given by Equation (F2).

Exercise (a): Integrating over φ first and then over n .

Equation (10) is used to evaluate the integration. The function $e^{-jk_0 n \rho \sin \theta \cos(\varphi - \beta)}$ can be expanded with Bessel functions

$$e^{-jk_0 n \rho \sin \theta \cos(\varphi - \beta)} = J_0(k_0 n \rho \sin \theta) + 2 \sum_{m=1}^{\infty} (-j)^m J_m(k_0 \rho \sin \theta) \cos(m(\varphi - \beta)) \quad (\text{F12})$$

Replacing it in Equation (10) and integrating over φ yields

$$I(\mathbf{r}) = \frac{j}{k_0} \int_0^{\pi/2} d\theta \frac{\sin \theta}{(\varepsilon_1 \sin^2 \theta + \varepsilon_3 \cos^2 \theta)} \int_{-\infty}^{+\infty} dn \frac{n^2}{(n^2 - n_+^2)(n^2 - n_-^2)} J_0(k_0 n \rho \sin \theta) e^{-jk_0 n z \cos \theta} \quad (\text{F13})$$

The integral over n is

$$I_n = \int_{-\infty}^{+\infty} dn F(n) \quad (\text{F14})$$

$$F(n) = \frac{n^2}{(n^2 - n_+^2)(n^2 - n_-^2)} J_0(k_0 n \rho \sin \theta) e^{-jk_0 n z \cos \theta}$$

It remains to integrate over n with the residue theorem. For a magnetoplasma with heat dissipation there are four simple poles in the integrand on the complex n -plane,

$$\begin{aligned} n_+^{(1)} &= \mu_+ - j\chi_+, & n_+^{(2)} &= -n_+^{(1)} = -\mu_+ + j\chi_+ \\ n_-^{(1)} &= \mu_- - j\chi_-, & n_-^{(2)} &= -n_-^{(1)} = -\mu_- + j\chi_- \end{aligned} \quad (\text{F15})$$

where $\mu_{\pm} > 0$ and $\chi_{\pm} > 0$. Figure 1 shows the complex n -plane. The poles $n_+^{(1)}$ and $n_-^{(1)}$ are located on the lower half plane and the other two poles $n_+^{(2)}$ and $n_-^{(2)}$ on the upper half plane. For

a dissipation-free magnetoplasma, the poles are located symmetrically either on the real axis for propagating modes or the imaginary axis for vanishing modes. However, the dissipation-free case is not realistic and the physically meaningful solution for a dissipation-free magnetoplasma should be considered as the limiting case of the general solution when the dissipation approaches zero.

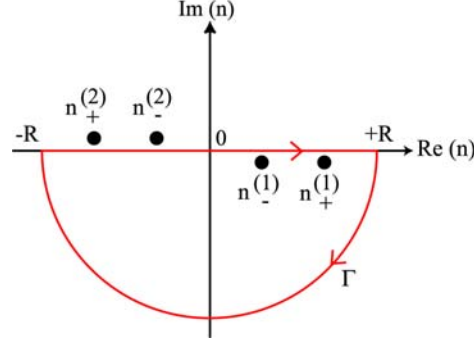


Figure 1. Complex n -plane

A contour is constructed to enclose the two poles on the lower half plane (when $z \geq 0$). It consists of two parts: the linear section on the real axis from $-R$ to $+R$ and the semicircle Γ . The integrand function, $F(n)$, is analytical in the domain enclosed by the contour except for the two simple poles in the lower half plane. The residue values of the two poles can be obtained,

$$\begin{aligned} \text{res}(n_+^{(1)}) &= \lim_{n \rightarrow n_+^{(1)}} \left[(n - n_+^{(1)}) \frac{n^2}{(n^2 - n_+^{(2)2})(n^2 - n_-^{(2)2})} J_0(k_0 n \rho \sin \theta) e^{-jk_0 n \cos \theta z} \right] \\ &= \frac{(n_+^{(1)})^2}{(n_+^{(1)} + n_+^{(1)})(n_+^{(1)} - n_-^{(1)})} J_0(k_0 n_+^{(1)} \rho \sin \theta) e^{-jk_0 n_+^{(1)} z \cos \theta} = \frac{\varepsilon_1 \sin^2 \theta + \varepsilon_3 \cos^2 \theta}{2q_+(\theta)} n_+^{(1)} J_0(k_0 n_+^{(1)} \rho \sin \theta) e^{-jk_0 n_+^{(1)} z \cos \theta} \\ \text{res}(n_-^{(1)}) &= -\frac{\varepsilon_1 \sin^2 \theta + \varepsilon_3 \cos^2 \theta}{2q_+(\theta)} n_-^{(1)} J_0(k_0 n_-^{(1)} \rho \sin \theta) e^{-jk_0 n_-^{(1)} z \cos \theta} \end{aligned}$$

According to the residue theorem, the contour integration is determined by the summation of the residue values of the enclosed poles:

$$\int_{-R}^R dn F(n) + \int_{\Gamma} dn F(n) = 2\pi j \frac{\varepsilon_1 \sin^2 \theta + \varepsilon_3 \cos^2 \theta}{2q_+(\theta)} \begin{bmatrix} n_+^{(1)} J_0(k_0 n_+^{(1)} \rho \sin \theta) e^{-jk_0 n_+^{(1)} z \cos \theta} \\ -n_-^{(1)} J_0(k_0 n_-^{(1)} \rho \sin \theta) e^{-jk_0 n_-^{(1)} z \cos \theta} \end{bmatrix} \quad (\text{F16})$$

Taking the limit as R approaches infinity:

$$\int_{-\infty}^{+\infty} dn F(n) + \lim_{R \rightarrow \infty} \int_{\Gamma} dn F(n) = 2\pi j \frac{\varepsilon_1 \sin^2 \theta + \varepsilon_3 \cos^2 \theta}{2q_+(\theta)} \begin{bmatrix} n_+^{(1)} J_0(k_0 n_+^{(1)} \rho \sin \theta) e^{-jk_0 n_+^{(1)} z \cos \theta} \\ -n_-^{(1)} J_0(k_0 n_-^{(1)} \rho \sin \theta) e^{-jk_0 n_-^{(1)} z \cos \theta} \end{bmatrix} \quad (\text{F17})$$

If one could prove that

$$\boxed{\lim_{R \rightarrow \infty} \int_{\Gamma} dn F(n) = 0} \quad (\text{F18})$$

then the integration over n would be successfully performed yielding

$$I(\mathbf{r}) = -\frac{\pi}{k_0} \int_0^{\pi/2} d\theta \frac{\sin \theta}{q_+(\theta)} \begin{bmatrix} n_+^{(1)} J_0(k_0 n_+^{(1)} \rho \sin \theta) e^{-jk_0 n_+^{(1)} z \cos \theta} \\ -n_-^{(1)} J_0(k_0 n_-^{(1)} \rho \sin \theta) e^{-jk_0 n_-^{(1)} z \cos \theta} \end{bmatrix} \quad (\text{F19})$$

In the condition that only the whistler mode is able to propagate while the other mode is vanishing, the integration is reduced to

$$I(\mathbf{r}) = \frac{\pi}{k_0} \int_0^{\pi/2} d\theta \frac{\sin \theta}{q_+(\theta)} n_-^{(1)} J_0(k_0 n_-^{(1)} \rho \sin \theta) e^{-jk_0 n_-^{(1)} \cos \theta |z|} \quad (\text{F20})$$

When $z < 0$, the contour integral should be over the upper half plane and the result remains the same. Therefore, Equation (F20) is valid for both $z \geq 0$ and $z \leq 0$ and an absolute sign can be added. This result differs from Equation (F6) with only a constant factor of -2 .

Unfortunately, we are unable to confirm Equation (F18), the major difference between our derivation and that of Wang and Bell. It is true that the Bessel function in the integrand $F(n)$ approaches zero when n approaches infinity along the real axis. However, the Bessel function approaches infinity along any other direction on the complex n -plane when n approaches infinity. This property of the Bessel function makes the integrand function diverging at the infinity point even when the effect of the factor $e^{-jk_0 n z \cos \theta}$ is taken into account. Therefore, if integrating over φ first and then over n , one should not have derived Equation (F6) from Equation (F2).

Exercise (b): integrating over n first and then over φ .

Equation (F11) is used to evaluate the integration. It is found that, when integrating over n first, the mathematical difficulty that the integration along the arc on the complex plane is not converging as described above, can in fact be avoided. The integral over n in Equation (F11) is

$$I_n = \int_{-\infty}^{+\infty} dn F(n) \quad (\text{F21})$$

$$F(n) = \frac{n^2 e^{-jk_0 n r \cos \tau}}{(n^2 - n_+^2)(n^2 - n_-^2)}$$

The integrand function, $F(n)$, now uniformly approaches zero at the infinite point on the complex n -plane because no Bessel function or sin/cos function of n is involved. The necessary condition given by the Jordan Lemma is satisfied and the Cauchy residue theorem can be employed to evaluate the integral (F21). The integration contour along the real axis is deformed to a contour at the lower or upper half plane depending on the sign of $\cos \tau$. Using the relations of the poles as given in Equation (F15), the integration result can be written as

$$I_n = \begin{cases} 2\pi j \frac{\varepsilon_1 \sin^2 \theta + \varepsilon_3 \cos^2 \theta}{2q_+(\theta)} \left[n_+^{(1)} e^{-jk_0 n_+^{(1)} r |\cos \tau|} - n_-^{(1)} e^{-jk_0 n_-^{(1)} r |\cos \tau|} \right], & (\cos \tau \neq 0) \\ 0, & (\cos \tau = 0) \end{cases} \quad (\text{F22})$$

Substituting (F22) back into Equation (F11) yields

$$I(\mathbf{r}) = -\frac{1}{2k_0} \int_0^{\pi/2} d\theta \frac{\sin \theta}{q_+(\theta)} \int_0^{2\pi} d\varphi \left[n_+^{(1)} e^{-jk_0 n_+^{(1)} r |\cos \tau|} - n_-^{(1)} e^{-jk_0 n_-^{(1)} r |\cos \tau|} \right] \quad (\text{F23})$$

Note that the absolute value of $\cos \tau$ is required because of the convergence condition for the lower half complex plane contour integration. It is shown below that Wang and Bell's result can be reproduced when the absolute value signs are dropped. However, we should point out that in the domain where $\cos \tau < 0$, the integral of the arc goes to infinity if taking the lower half-plane integration. Similarly, if taking the upper half plane, the integral will not converge in the domain where $\cos \tau > 0$. It is then interesting to understand where $\cos \tau$ can change sign. As

illustrated in Figure 2, the sign of $\cos \tau$ may change when the refractive index vector rotates in the upper half space ($0 \leq \theta \leq \pi/2$ and $0 \leq \varphi \leq 2\pi$) even when the observing vector is also located in the upper half space but not along the z-axis. In other words, without the absolute sign, the contour integral does not converge on a half plane except for the case of $\alpha = 0$.

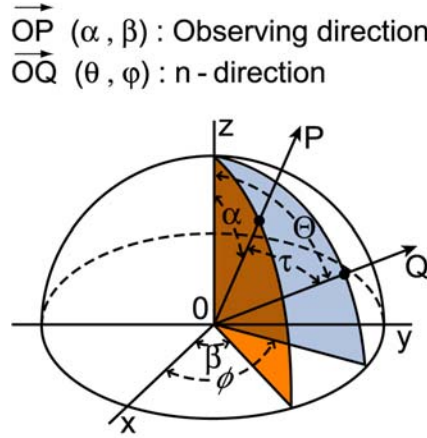


Figure 2. Upper Half Space

In order to integrate over the variable φ , the spherical Bessel and Legendre expansion is used [Stratton, J.A., Electromagnetic Theory, p.409, 1941]

$$e^{-jk_0nr|\cos \tau|} = \sum_{i=0}^{\infty} a_i j_i(k_0nr) P_i(\cos \tau) \quad (\text{F24})$$

The coefficients can be determined in the following way:

$$a_i j_i(k_0nr) = \frac{2i+1}{2} \int_0^{\pi} e^{jk_0nr|\cos \tau|} P_i(\cos \tau) \sin \tau d\tau \quad (\text{F25})$$

Differentiating both sides i times with respect to variable r and using the formula

$$\left[\frac{d^i j_i(r)}{dr^i} \right]_{r=0} = \frac{2^i (i!)^2}{(2i+1)!} \quad (\text{F26})$$

we have

$$a_i \frac{2^i (i!)^2}{(2i+1)!} = \frac{2i+1}{2} (-j)^i \int_0^{\pi} (|\cos \tau|)^i P_i(\cos \tau) \sin \tau d\tau = \frac{2i+1}{2} (-j)^i \times \begin{cases} 0, & i = 1, 3, 5, \dots \\ 2^{i+1} \frac{(i!)^2}{(2i+1)!}, & i = 0, 2, 4, \dots \end{cases}$$

Hence, the coefficients are

$$a_i = \frac{1+(-1)^i}{2} (2i+1)(-j)^i, \quad i = 0, 1, 2, 3, \dots \quad (\text{F27})$$

Using the Addition Theorem [Stratton, 1941], the expansion (24) takes the form of

$$e^{-jk_0nr|\cos\tau|} = j_0(k_0nr) + \sum_{i=1}^{\infty} \frac{1+(-1)^i}{2} (-j)^i (2i+1) j_i(k_0nr) \left[\begin{aligned} &P_i(\cos\theta)P_i(\cos\alpha) \\ &+ 2 \sum_{m=1}^i \frac{(i-m)!}{(i+m)!} P_i^m(\cos\theta)P_i^m(\cos\alpha) \cos m(\varphi-\beta) \end{aligned} \right] \quad (\text{F28})$$

The series (F28) uniformly converges for all variables. Integration over φ leads to

$$I(\mathbf{r}) = -\frac{\pi}{k_0} \int_0^{\pi/2} d\theta \frac{\sin\theta}{q_+(\theta)} \left\{ \begin{aligned} &n_+^{(1)} \left[j_0(k_0n_+^{(1)}r) + \sum_{i=1}^{\infty} \frac{1+(-1)^i}{2} (-j)^i (2i+1) j_i(k_0n_+^{(1)}r) P_i(\cos\theta)P_i(\cos\alpha) \right] \\ &-n_-^{(1)} \left[j_0(k_0n_-^{(1)}r) + \sum_{i=1}^{\infty} \frac{1+(-1)^i}{2} (-j)^i (2i+1) j_i(k_0n_-^{(1)}r) P_i(\cos\theta)P_i(\cos\alpha) \right] \end{aligned} \right\} \quad (\text{F29})$$

If only one mode $n_-^{(1)}$ is propagating and the other mode does not contribute to the far field, the integration becomes

$$I(\mathbf{r}) = \frac{\pi}{k_0} \int_0^{\pi/2} d\theta \frac{\sin\theta}{q_+(\theta)} n_-^{(1)} \left[j_0(k_0n_-^{(1)}r) + \sum_{i=1}^{\infty} \frac{1+(-1)^i}{2} (-j)^i (2i+1) j_i(k_0n_-^{(1)}r) P_i(\cos\theta)P_i(\cos\alpha) \right] \quad (\text{F30})$$

This result is quite different from Equation (F6).

Next we show that, if the absolute sign of $\cos\tau$ in Equation (F22) could be ignored, the same result as Equation (F6) can be obtained. In fact, if the sign of $\cos\tau$ is ignored Equation (F22) becomes

$$\begin{aligned} I_n &= 2\pi j \times \frac{\varepsilon_1 \sin^2\theta + \varepsilon_3 \cos^2\theta}{2q_+(\theta)} \left[n_+^{(1)} e^{-jk_0n_+^{(1)}r\cos\tau} - n_-^{(1)} e^{-jk_0n_-^{(1)}r\cos\tau} \right] \\ &= 2\pi j \times \frac{\varepsilon_1 \sin^2\theta + \varepsilon_3 \cos^2\theta}{2q_+(\theta)} \left[n_+^{(1)} e^{-jk_0n_+^{(1)}[\rho\sin\theta\cos(\varphi-\beta)+z\cos\theta]} - n_-^{(1)} e^{-jk_0n_-^{(1)}[\rho\sin\theta\cos(\varphi-\beta)+z\cos\theta]} \right] \end{aligned} \quad (\text{F31})$$

Substituting the above into Equation (F11) and using expansion (F12), the integration over φ gives

$$I(\mathbf{r}) = \frac{\pi}{k_0} \int_0^{\pi/2} d\theta \frac{\sin\theta}{q(\theta)} \left[n_+^{(1)} J_0(k_0n_+^{(1)}\rho\sin\theta) e^{-jk_0n_+^{(1)}\cos\theta|z|} - n_-^{(1)} J_0(k_0n_-^{(1)}\rho\sin\theta) e^{-jk_0n_-^{(1)}\cos\theta|z|} \right] \quad (\text{F32})$$

It is the same as Equation (F19), and similar to (F6) when the n_+ term is dropped but with a factor -2 difference.

As shown above, our solution for the integration (F2) with respect to the variables n and φ is Equation (F30). Then the question arises how far Equation (F6) differs from it. The analysis can start from Equation (F23) by ignoring the absolute sign of $\cos\tau$ in Exercise (b). If the absolute sign of $\cos\tau$ in Equation (F23) is ignored, the expansion with the spherical Bessel function and the Legendre polynomial will take the form

$$e^{-jk_0nr\cos\tau} = j_0(k_0nr) + \sum_{i=1}^{\infty} (-j)^i (2i+1) j_i(k_0nr) \left[\begin{aligned} &P_i(\cos\theta)P_i(\cos\alpha) \\ &+ 2 \sum_{m=1}^i \frac{(i-m)!}{(i+m)!} P_i^m(\cos\theta)P_i^m(\cos\alpha) \cos m(\varphi-\beta) \end{aligned} \right] \quad (\text{F33})$$

Now the integration over φ for the propagating mode takes the form

$$I(\mathbf{r}) = \frac{\pi}{k_0} \int_0^{\pi/2} d\theta \frac{\sin \theta}{q_+(\theta)} n_-^{(1)} \left[j_0(k_0 n_-^{(1)} r) + \sum_{i=1}^{\infty} (-j)^i (2i+1) j_i(k_0 n_-^{(1)} r) P_i(\cos \theta) P_i(\cos \alpha) \right] \quad (\text{F34})$$

Comparison of Equation (F34) with Equation (F30) reveals that the former contains more terms with odd orders and the question is answered.

Summary:

1. Exhaustive efforts have been made to re-derive the results of Wang and Bell, especially equation (F6). Because the original paper skipped the procedure for a two-fold integration to derive (F6), we made attempts for two different procedures.
2. In one procedure, Exercise (a), a divergent contour integral is involved and the derivation provides no solution. In the other procedure, Exercise (b), the integral converges, but the result is substantially different from Wang and Bell.
3. In both Exercises, Wang and Bell's result can be recovered under invalid assumptions, with a difference of the factor -2 which we consider not substantial. In Exercise (a), one has to assume the diverged contour integral to be 0. In Exercise (b), one has to ignore an absolute sign.
4. The spherical coordinate system is used in the above derivation. It should be pointed out that the convergence speed of the involved series in Equation (F30) is very slow and it seems difficult to get the far field from it. In our study we use the cylindrical coordinate system and all the troubles are removed as shown in the text.

APPENDIX D

Impedance Characteristics of an Active Antenna Transmitting in the Whistler Mode

V.V. Paznukhov, G.S. Sales, K. Bibl, B.W. Reinisch, P. Song, and X. Huang
Center for Atmospheric Research, University of Massachusetts Lowell

Impedance Characteristics of an Active Antenna Transmitting in the Whistler Mode

Abstract

We use the Radio Plasma Imager on the IMAGE satellite to investigate the characteristics of whistler wave transmission by an electric antenna in space plasma. A dedicated experiment was carried out on 21-22 September 2005, for two orbits in the plasmasphere. The input impedance characteristics of the dipole antenna submerged in plasma is determined for whistler mode transmission. These results are consistent with a physical model in which the plasma around each antenna element forms an ion sheath with a time-varying radius while the antenna itself is negatively charge to a large voltage. Within the plasmasphere, these sheaths are a part of the antenna-plasma system and represent a capacitive component of the tuned antenna circuit. It is shown that inside the plasmasphere the RPI antenna capacitance varied from 430 pF to 480 pF. Comparison to model calculations shows good agreement with a relative error smaller than 5%. Measurements of the antenna input resistance showed that inside the plasmasphere its value was between 200 Ω and 500 Ω , varying considerably with changes in the ambient electron density and cyclotron frequency. A comparison to model calculations suggests that a large part of the antenna input resistance represents the antenna radiation resistance.

1. Introduction

Recently, there has been a growing interest in placing radiowave transmitters onboard earth-orbiting satellites in order to study Earth's magnetospheric environment. Transmitters operating in the very low frequency (VLF) band may potentially be used to modify the pitch angle distribution of energetic particles in the magnetosphere through wave-particle interaction [Lyons *et al.*, 1971, 1972; Abel and Thorne, 1998a,b]. In order to achieve significant pitch-angle diffusion of the radiation belt particles, a transmitter has to be able to transmit a high power VLF wave. For designs of high power space-borne transmitters operating in a plasma environment it is important to understand the interaction of the antenna at high voltage with the surrounding plasma. The Radio Plasma Imager (PRI) instrument designed by the Center for Atmospheric Research of University of Massachusetts Lowell [Reinisch *et al.*, 2000] was used for such studies. RPI was the most powerful active magnetospheric radar operating in the radio frequency bands covering the plasma resonance frequencies characteristic of Earth's magnetosphere (3 kHz to 3 MHz). In 2004 and 2005 several studies were carried out to assess the characteristics of the plasma sheath formed around the instrument antennas during whistler wave transmissions. These efforts resulted in a much better understanding of the antenna-plasma interaction and were important for the development of future space radars operating in this frequency range. In this paper we present results of a dedicated experiment aimed at investigating the characteristics of VLF transmission in the magnetospheric plasma.

For an active whistler wave transmission antenna in plasma, a substantial space-charge sheath (dependent on the applied RF voltage) forms around the antenna elements, *i.e.*, plasma in the vicinity of the antenna is not charge neutral. The formation of the sheaths is caused by the different responses of the electrons and ions to the changing antenna charge. In the whistler frequency range, the electrons can respond to the changing electric field surrounding the antenna nearly instantaneously while the ions cannot move fast enough to follow the wave oscillations. The sheath properties vary with time as the antenna voltage and current oscillate during a wave cycle and with plasma conditions as the satellite travels in space. The presence of the plasma sheath seriously affects the antenna electrical characteristics during the transmission.

A number of theoretical studies of radiowave transmission from a short dipole antenna surrounded by plasma have been carried out starting from the 1960s [e.g., *Mlodnosky and Garriott*, 1963, *Despain* 1966, *Shkarofksy*, 1972]. Experimental investigations of this problem, however, are quite scarce [e.g., *Oliver et al.*, 1973]. While these works have brought a conceptual understanding of the antenna-plasma interaction, the models lacked self-consistency, since in most cases electrostatic condition was assumed and the radiation resistance was not considered. A significantly more self consistent model has recently been proposed by *Song et al.*, [2007] and numerically investigated by *Tu et al.* [2008]. In the former work an analytical solution for a time-dependent one-dimensional situation was presented while assuming immobile ions. Some preliminary experimental results obtained with the RPI-IMAGE instrument were also used to demonstrate the validity of the model. The achieved inaccuracy in comparison between the modeled and measured sheath capacitance was about 20%. The reason for this relatively large error is likely the fact that some information used in the analysis was not directly obtained from in-space measurements but derived from the RPI engineering unit under various assumptions. In order to improve the comparison of the theory with observation, we carefully designed a series of operations and measurements through which all critical parameters were directly measurable within the limit of the RPI capability. The experiment, which was given the name “V71”, in accordance with the internal RPI programming convention, was successfully carried out in September 2005.

2. RPI Antenna-in-Plasma Tuning Experiment

2.1. Experiment set-up

The IMAGE satellite [*Burch et al.*, 2001], launched in March 2000, was the first NASA mission dedicated to remote imaging of Earth’s magnetosphere. The satellite was on a polar orbit with an apogee of ~ 7.5 Re, perigee of < 1000 km, and an orbit period of 14.5 hours. Among imaging instruments onboard the satellite was the Radio Plasma Imager (RPI) tasked to characterize the magnetospheric plasma using the radio frequency sounding technique. The RPI instrument consisted of an electronics unit, two 500-m tip-to-tip wire dipole antennas in the spin plane (referred to as x - and y - antennas) and a 20-m dipole along the spin axis. RPI transmitted and received coded pulse signals in the frequency range between 3 kHz and 3 MHz. The long wire antennas were connected to the transmitter through a “tuner” consisting of a set of inductors and capacitors that were adjustable with frequency in order to match the reactance of the RPI output circuit to the reactance of antenna-plasma system. When the match occurred, or the circuit was in tune, maximum transmitted power was achieved, which was monitored by the

measurements of the voltage at the antenna and the current in the power supply. The system allowed programmable parameters of the tuners for each frequency used in the sounding (Reinisch *et al.*, 2000). Figure 1 is a basic schematic diagram of the RPI sounder which includes a separate tuner for each element of the dipole antenna. It is important to mention that DC current measurements were made in the power supply, and AC voltage measurements were made at the two input terminals, marked as V_{a1} and V_{a2} in Figure 1. Only the x -antenna was used for transmission in this experiment (a power supply in the y -transmitter had failed earlier in the mission). By the time of this experiment one of x -antenna elements was shortened, likely by a meteorite impact. Resonance measurements had determined the length of the remaining section as 125 m. At the time of the V71 experiment, only the voltage measurements at the shorter element were reliable.

In our earlier experiment that was reported by Song *et al.* [2007], since the range of the input impedance of the antenna-plasma system was unknown, the tuners were operated over a very large range of the inductances at various frequencies, the combination of which resulted in a large range of reactances. With the knowledge of the range of the input impedance gained from the first experiment, in the V71 experiment the tuning algorithm was simplified by using a set of fixed inductors in each tuner. The RPI operating frequency was then stepped through a large frequency range to find the best tuning frequency indicated by a voltage maximum at the antenna input. The two tuning inductors selected for this experiment were equal to $L_t = 22.4$ mH. It was determined in the laboratory that each inductor had a parallel stray capacitance of approximately 83 pF, and 50 Ω internal resistance. In addition, there was a 100 Ω resistor connected in series with each tuning inductor. The frequency range covered by the V71 experiment was 18 to 80 kHz in 300 Hz steps with a dwell time on each frequency of ~ 0.125 s. Each V71 scan was followed by routine sounding measurements, from which the plasma frequency and electron gyro frequency were derived; the program repeated every 4 minutes.

The power supply currents and antenna voltages were measured for every frequency once every four minutes for portions of two complete satellite orbits. The data from both passes of the satellite were very similar, and the first pass from 2200 UT on 21 September 2005 to 0230 UT on 22 September 2005 is presented in this paper. During this pass, the measurements began in the outer magnetosphere before IMAGE entered the dayside plasmasphere; the measurements continued in the plasmasphere, over the southern polar cap region, and finally in the nightside plasmasphere as illustrated in Figure 2. The approximate plasmasphere boundary in the figure is at $L=5$. The observations can be divided into five nominal regions, according to the satellite positions as shown in Figure 2. These regions are listed in Table 1.

As part of its routine sounding program RPI also measured the local plasma resonance frequencies such as the plasma frequency f_{pe} and electron-cyclotron frequency f_{ce} [Galkin *et al.*, 2004], making it possible to determine the local plasma parameters $X = f_{pe}^2 / f^2$ and $Y = f_{ce} / f$ at the satellite position, which are plotted in Figure 3. Using the values of X and Y the propagation modes in terms of the regions in the standard CMA diagram [e.g., Budden, 1985] are determined and marked in Figure 2. A good portion between 2320 UT (when $Y=1$) and 0110 UT (when $Y=1$ again), except for the time interval over the polar cap, represents whistler mode propagation region VIII (*i.e.*, $f \leq f_{ce} \leq f_{pe}$) which is our primary interest in this work. For

periods $X < 1$, *i.e.*, before 2250 UT and after 0147 UT the IMAGE satellite was in regions of very low electron densities outside the plasmasphere and the propagation mode is O-X mode (CMA regions I-III). In these regions the plasma conditions can be approximated by that of the free-space environment.

2.2 Antenna Voltage Measurements

The voltage measurements on the short antenna element are shown in Figure 4 as a function of sounding frequency and time, demonstrating the effects of the plasma environment on the antenna parameters.

The tuned frequencies at which the maximum voltages occurred, *i.e.*, the antenna-tuner resonance frequencies, are indicated in Figure 4 by black dots. As the satellite passed through the plasmasphere, significant changes in the tuned frequency are clearly visible, indicating changes in the antenna input impedance, resulted from the variations of the plasma sheath properties surrounding the antenna. As the IMAGE satellite entered the plasmasphere, the tuned frequency decreased quickly from 37.2 kHz (relatively constant in the low electron density region of the outer magnetosphere) to 34.3 kHz within the plasmasphere and then continued to decrease more slowly to 33.0 kHz before entering the polar cap region. The tuned frequency variation on the other side of the plasmasphere was similar. This decrease in the tuned frequency within the plasmasphere corresponds to an increase in local electron density (*i.e.*, the X parameter as seen in Figure 3) as the IMAGE satellite moved to lower altitudes. In Section 4, this variation is discussed in terms of the characteristics of the ion sheaths that surround the antenna elements.

Referring again to Figure 4, it is clear that the RPI transmitting system was “tuned” well (*i.e.*, it shows a relatively sharp resonance and high voltage) practically in all regions except in the polar cap (region VII). The system was not tuned well (low maximum antenna voltage) at the times when the satellite was in an environment with $X = 1$ (around 2247 UT and 0145 UT), indicating a smaller Q -factor. Since the quality-factor Q equals the ratio of the reactance to the resistance, a lower Q -factor signals increased resistive loss in the system, likely indicating that a portion of the system energy is lost to the local particle resonance absorption of the waves. In the low electron density regions outside the plasmasphere the system was tuning very well (very narrow resonance with very high voltage or Q). In the whistler mode regions, inside the plasmasphere, the resonance was relatively sharp, but the maximum voltage was smaller compared to that outside the plasmasphere.

Below, we derive the two main characteristics of the RPI transmitting system: the antenna input resistance and reactance. These two parameters were determined using the measured resonance (tuned) frequency and the antenna voltage at the resonance frequency.

3. Antenna impedance measurements

3.1 Antenna reactive component

To determine the RPI antenna impedance, the antenna-circuit system is represented by a simplified equivalent circuit shown in Figure 5.

The antenna, sheath, and radiation effects are now represented by the antenna capacitance C_a and antenna input resistance R_a . Elements L_t^* and R_t^* shown in the figure represent the tuner inductors/capacitors and resistors modified by the effect of the parallel stray capacitance of 83 pF, and the internal resistance of the inductor of 50 Ω and 100 Ω additional resistor. Their effect makes the effective inductance approximately 6% larger and is taken into account when calculating the tuner reactance. The voltage source V_s^* shown in the figure represents the voltage in the secondary circuit of the transformer shown in Figure 1. This voltage was not directly measured in the experiment; however, it is known that the source primary voltage V_s was at a relatively constant value of 20 V varying with the frequency by not more than $\pm 10\%$. Therefore, the secondary voltage V_s^* is assumed to be constant, independent of frequency.

The antenna reactance is calculated from the RPI system resonance condition according to which a maximum voltage occurs when the capacitive antenna reactance equals the total inductive reactance of the two tuners, i.e., $\omega_{res}(t)L_{t1} + \omega_{res}(t)L_{t2} = 1/\omega_{res}(t)C_a(t)$ where ω_{res} is the angular frequency for which the maximum voltage is measured in each frequency scan (i.e., the resonance frequency). Thus, it is straightforward to calculate the antenna capacitance, $C_a(t) = [\omega_{res}^2(t)(L_{t1} + L_{t2})]^{-1}$. The calculated antenna capacitances are shown in Figure 6. Outside the plasmopause, where the electron density was very low representing essentially free space conditions, the measured capacitance was 350 pF to 370 pF and can be interpreted as the dipole antenna capacitance in vacuum.

Inside the plasmasphere the input capacitance varied from 430 pF to 480 pF. These variations are mainly associated with the plasma frequency variations. It is interesting to compare these results to the model calculations. The plasma sheath model proposed by Song et al. [2007] allows calculation of the antenna-sheath system capacitance in plasma. The results of the model calculation for the antenna-sheath capacitance for the conditions of the V71 experiment are shown in Figure 6 as a blue line. The local plasma densities (the main input to the model) were determined from the local sounding resonance frequencies. Inside the plasmasphere the difference between the experimental results and the model is less than 5%. There is a larger difference in the polar cap region, since the model neglects the effects of the magnetic field, while in the polar cap region f_{ce} is greater than f_{pe} and the magnetic field effect must be taken into account.

Song et al. [2007] also discussed the structure of the ion sheaths surrounding the antenna elements in the plasmasphere. The relationship between the radius of a cylindrical sheath and its capacitance, assuming a sheath that is long relative to its radius, r_{si} , is:

$$C_{ai}(t) = \frac{2\pi\epsilon_0 l_i}{\ln\left[\frac{r_{si}(t)}{r_a}\right] - \frac{1}{2}}, \quad (1)$$

where ε_0 is the permittivity of free space, e the electron charge, l_i the length of the antenna element i , and r_a the radius of the antenna wire (0.0002 m for RPI). Subscript i denotes each of the two antenna elements. The measured capacitance corresponds to the serial combination of the antenna/sheath capacitances of the two unequal antenna elements. Assuming equal charge on each of the antenna elements and a 2:1 length ratio, the ratio of the average sheath capacitances is close to a 2:1. Figure 7 shows the time variation of the radii of these sheaths based on the calculated antenna capacitance. The radius varied from about 10 m as the satellite entered the plasmasphere and decreased to 3 m as the ambient plasma density increased until the satellite entered the polar cap region. Under the conditions of low electron density found outside the plasmasphere and in the polar cap, because the electron characteristic frequencies are less than the tuned frequency, the electrons have no time to respond to the wave and no significant antenna sheath is formed.

In reality, the sheath radius also varies within a wave cycle following the sinusoidal variation of RPI antenna voltage [Song *et al.*, 2007]. However, because no instantaneous measurements of antenna voltage were available in the experiment, the RMS voltages are used. Therefore, the derived antenna capacitance should be regarded as a time average over a wave cycle, as it is defined in any resonance circuit analysis. The perception that a circuit can resonate only when the inductance varies with the varying sheath capacitance on a sub-cycle level is a misconception of the circuit tuning. The time variable used in our analysis refers to time scales longer than many wave cycles.

3.2 Antenna input resistance measurements

Determination of the antenna input resistance is more complicated as compared to the antenna reactance measurements because it is an order smaller than the reactance. We determine it using the RMS voltage measurements which are shown in Figure 8. Inside the plasmasphere, the voltages measured on the short antenna element varied between 500 V and 800 V.

Referring to the equivalent circuit shown in Figure 5, since $V_a \gg V_s^*$ the measured antenna voltages are approximately equal to the voltages across the corresponding tuner elements (e.g., $V_{a1} \approx V_{t1}$, $V_{a2} \approx V_{t2}$). The RMS amplitude of the voltage on tuner 1 (no phase measurements were made in the V71 experiment) can be written as:

$$\begin{aligned}
 |V_{a1}(t)| &= |I_a(t)Z_{t1}(t)| = \left| \frac{V_s^*}{Z_{t1}(t) + Z_{t2}(t) + Z_a(t)} Z_{t1}(t) \right| \\
 &= \left| \frac{V_s^*}{2R_t + j\omega(t)L_{t1} + j\omega(t)L_{t2} + R_a(t) - j\frac{1}{\omega(t)C_a(t)}} Z_{t1}(t) \right| \\
 &= \frac{|V_s^*|}{2R_t + R_a(t)} |Z_{t1}(t)|
 \end{aligned} \tag{2}$$

where V_s^* is again the RMS source voltage in the secondary circuit of the transformer. The last expression results from the resonance condition.

In principle, it is possible to determine the value of $R_a(t)$ from the above expression. However, since the voltage V_s^* in the secondary circuit of the transformer was not directly measured in our experiment, it is preferable to eliminate this term from the calculation. This can be done by comparing the measurements made at different periods of time, namely, the observations made outside and inside of the plasmasphere (regions 1, 5 and 2, 4 shown in Figure 2), which are denoted by superscripts o and i , respectively. The voltages are then written as:

$$|V_{a1}^o(t)| = \frac{|V_s^*|}{2R_t + R_a^o(t)} |Z_{t1}(t)| \quad (3)$$

$$|V_{a1}^i(t)| = \frac{|V_s^*|}{2R_t + R_a^i(t)} |Z_{t1}(t)| \quad (4)$$

Note that outside the plasmasphere the plasma conditions corresponded to the propagation regions I-III (see Figure 3). Since the resonance frequency was much greater than the local plasma frequency, these conditions were very close to the “free space” conditions ($X \ll 1$). Under such conditions, the RPI antenna is effectively very short (wavelength of the order 10 km compared to the antenna length of 375 m) and therefore, the antenna resistance can be assumed to be negligibly small in comparison to the tuner resistance, (i.e., $R_a^o(t) \rightarrow 0$). With this approximation, the antenna resistance $R_a^i(t)$ inside the plasmasphere is

$$R_a(t) = 2R_t^* \left(\frac{|Z_{t1}^i(t)| |V_{t1}^o(t)|}{|Z_{t1}^o(t)| |V_{t1}^i(t)|} - 1 \right) \quad (5)$$

We note that $|Z_{t1}(t)| \equiv \sqrt{(\omega_{res}(t)L_{t1})^2 + R_t^2} \approx \omega_{res}(t)L_{t1}$, as $\omega_{res}(t)L_{t1} \gg R_t$, and obtain

$$R_a(t) = 2R_t^* \left(\frac{\omega_{res}^i(t)}{\omega_{res}^o} \frac{|V_{t1}^o|}{|V_{t1}^i(t)|} - 1 \right) \quad (6)$$

where ω_{res}^o is the average tuned angular frequency outside the plasmasphere (relatively constant at 37.2 kHz) and $\omega_{res}^i(t)$ is the time-varying tuned angular frequency inside the plasmasphere. The results for the antenna input resistance are shown in Figure 9. For times when IMAGE/RPI was inside the plasmasphere, the antenna input resistance varied considerably from 250 Ω to 500 Ω . When the satellite was near the $X = 1$ point (at about 2245 UT), the input resistance was very large, indicating energy loss due to the local plasma resonance. As the IMAGE satellite descended to lower altitudes into denser plasmas, the resistance increased

steadily. Finally, in the polar cap region (around 0030 UT) the antenna input resistance increased to an even higher value of 600 Ω .

3.3 Power Balance

Using our measurements made during the V71 experiment, it is possible to estimate the power dissipated by the transmitting system including losses in the dipole antenna. The power dissipated in the antenna-tuner system can be calculated in two independent ways:

$$P_1(t) = V_s^* |I_a(t)| = \frac{(V_s^*)^2}{R_a(t) + 2R_t^*}$$

$$P_2(t) = |I_a(t)|^2 (R_a(t) + 2R_t^*) = \left| \frac{V_{a1}(t)}{Z_{t1}(t)} \right|^2 (R_a(t) + 2R_t^*)$$
(6)

As mentioned above, the power supply voltage V_s was a relatively constant 20 V, varying by not more than $\pm 10\%$ over the frequencies used in the V71 experiment. The results of the calculations made using the above formulas are shown in Figure 10. The agreement between the two calculations is remarkable. The power dissipated in the high density regions is 9-12 W, while in the free space region, outside the plasmasphere it is about 20 W. We should point out that our results cannot distinguish the power lost to the local plasma from that to radiation.

4. Summary and Discussion

Using the RPI-IMAGE satellite transmission system, we conducted an experiment to determine the impedance of a dipole antenna for transmission of whistler mode waves in the plasmasphere. Despite the fact that the RPI instrument was not designed for such an operation, and a number of complications in the experiment and data analysis, we have been able to determine the input impedance characteristics of a high voltage transmitting dipole antenna in space plasma. Measurements of the RPI antenna reactance/capacitance have demonstrated the effect of the ion sheath formation when the satellite was inside the plasmasphere with high ambient electron densities. Our experimental data for the antenna capacitance is in good agreement with the theoretical calculations (see Figure 6) made using the model proposed by *Song et al.* [2007]. The fact that the RPI transmitting system was able to tune very well during the V71 experiment (Figure 4) also suggests that the model of the antenna sheath capacitance and the logarithmic dependence on the radius are valid.

The calculated antenna input resistance R_a varied significantly during the time of the experiment and it can be assumed to be close to zero outside the plasmasphere in very low-electron density and weak-field regions ($f \gg f_{pe}; f \gg f_{ce}$). This assumption of a small radiation resistance in the low density regions is consistent with the well known results for free-space transmission [e.g., *Balanis*, 2005]. Inside the plasmasphere, in the whistler mode transmission region ($f < f_{pe}; f < f_{ce}$) the antenna input resistance varies from 200 Ω to 500 Ω . When the sounding (resonance) frequency is close to the local plasma resonance frequency (i.e., $X=1$) the antenna resistance can be between 600 Ω and 800 Ω . We attribute the enhanced loss

near the local plasma frequency to local wave particle resonances, i.e., waves that are absorbed by electron plasma oscillations. The radiation resistance in the whistler mode is crucial knowledge for potential space weather applications. A very important question is how much of the measured input antenna resistance in the whistler mode of operation is due to the antenna radiation resistance and how much is dissipated locally near the antenna. Unfortunately, in our experiment it is not possible to directly distinguish the losses near the antenna from those in the true far field, i.e. from the radiation losses. However, there are indications that suggest that the major part of the measured antenna resistance represents the radiation resistance. First of all, it is not debatable that whistler mode waves can be radiated in plasma, meaning that the sheath does not completely shield the antenna from the plasma. For example, *Sonwalkar et al.* [2007] reported RPI observations of whistler wave echoes reflected in the plasmasphere, suggesting a significant amount of whistler wave power radiated during the transmission. It is also possible to compare the measured RPI antenna input resistance with the theoretical values of the radiation resistance. An advanced new theory for the radiated fields in plasma from a dipole antenna of arbitrary length has been developed by *Huang et al.* [2008]. We now compare our measurements with the theoretical calculations of the radiation resistance made using this model. Figure 11 shows the measured antenna input resistances as red dots, and the theoretical calculations in the range of the Y -values during the experiment when the whistler modes were transmitted. During the V71 experiment, the Y -values varied from 2 to about 10 (see Figure 3).

Within the whistler mode region (VIII) the agreement between experiment and theoretical calculations is very good. This suggests that in the whistler mode region, a major part of the measured antenna input resistance in fact represents the antenna radiation resistance, and local losses are negligible.

Acknowledgement

This research was supported by USAF Grant FA8718-05-C-0070 of the AF Research Laboratory.

References

- Abel, B. and R. M. Thorne, Electron scattering loss in the Earth's inner magnetosphere: 1. Dominant physical processes, *J. Geophys. Res.*, *103*, 2385, 1998a
- Abel, B. and R. M. Thorne, Electron scattering loss in the Earth's inner magnetosphere: 2. Sensitivity to model parameters, *J. Geophys. Res.*, *103*, 2397, 1998b
- Balanis, C.A., Antenna Theory: Analysis and Design, 3rd Edition, John Wiley & Sons, 2005
- Balmain, K. G., The impedance of a short dipole antenna in a magnetoplasma, *IEEE, Trans Antennas Propag.*, *12*, 605, 1964
- Benson, R. F., P. A. Webb, J. L. Green, L. Garcia, and B. W. Reinisch, Magnetospheric electron densities inferred from upper-hybrid band emissions, *Geophys. Res. Lett.*, *31*(20), L20803, doi:10.1029/2004GL020847, 2004
- Budden, K.G., The propagation of radio waves. The theory of radio waves of low power in the ionosphere and magnetosphere. Cambridge University Press, Cambridge- New York, 1985
- Burch, J.L. et al., Views of Earth's magnetosphere with the IMAGE satellite, *Science*, *291*, 541, 2001

- Despain, A. M., Antenna impedance in the ionosphere, Rep. 3, AFCRL-66-412, Upper Air Res. Lab., Univ. of Utah, Salt Lake City, Utah, 1966
- Galkin, I., B. W. Reinisch, G. Grinstein, G. Khmyrov, A. Kozlov, X. Huang, and S. F. Fung, Automated exploration of the radio plasma imager data, *J. Geophys. Res.*, 109(A12), A12210, doi:10.1029/2004JA010439, 2004
- Huang, X., B. W. Reinisch, P. Song, and G. P. Ginat, Far Field of Linear Antennas in an anisotropic plasma, Proceedings of the XXIX URSI General Assembly, Chicago, IL, USA, 7-16 August 2008, 2008
- Lyons, L. R., R. M. Thorne, and C. F. Kennel, Pitch-angle diffusion of radiation belt electrons within the plasmasphere. *J. Geophys. Res.*, 77, 3455 – 3474, 1972
- Lyons, L. R., R. M. Thorne, and C. F. Kennel, Electron pitch-angle diffusion driven by oblique whistler-mode turbulence., *J. Plasma Phys.*, 6, 589 – 606, 1971
- Mlodnosky R.F. and O.K. Garriott, The V.L.F. admittance of a dipole in the lower ionosphere. 1962 *Proc. Int. Conf. Ionosphere* (Inst. Phys. and Physical Soc. London), 1963, 484-491.
- Oliver, B. M., Clements, R. M., and P. R. Smy, Experimental investigation of the low-frequency capacitive response of a plasma sheath. *Journal of Applied Physics*, 44, 1973, 4511-4517
- Reinisch, B.W. et al., The radio plasma imager investigation on the IMAGE spacecraft, *Space Sci. Rev.*, 91, 319, 2000
- Reinisch, B.W. et al., First results from the radio plasma imager in IMAGE, *Geophys. Res. Lett.*, 28, 1167, 2001
- Shkarofsky, I. P., Nonlinear sheath admittance, currents, and charges associated with high peak voltage driven on a VLF/ELF dipole antenna moving in the ionosphere, *Radio Science*, 7, 503, 1972
- Song, P., B. W. Reinisch, V. Paznukhov, G. Sales, D. Cooke, J.-N. Tu, X. Huang, K. Bibl, and I. Galkin, High-voltage antenna-plasma interaction in whistler wave transmission: Plasma sheath effects, *J. Geophys. Res.*, 112(A3), A03205, doi:10.1029/2006JA011683, 2007
- Sonwalkar, V. S., Reddy, A., Carpenter, D. L., and Reinisch, B.W., Observations of Magnetospherically Reflected (MR), Specularly Reflected (SR), and Back Scattered (BS) Whistler Mode (WM) Echoes Observed by Radio Plasma Imager (RPI) on IMAGE: Diagnostics of Electron Density, Density Structure, and Ion Composition. American Geophysical Union, Fall Meeting 2007, abstract #SM32A-04, 2007
- Tu, J., P. Song, and B. W. Reinisch, Plasma sheath structures around a radio frequency antenna, *J. Geophys. Res.*, 113(A7), A07223, doi:10.1029/2008JA013097, 2008

FIGURE CAPTIONS

Figure 1. Schematic diagram of the RPI transmitting system. The “tuning inductor” is a combination of inductors and capacitors with a total reactance L_t that is inductive. The power supply current I_{ps} was measured in the primary circuit of the transformer while the voltages V_{a1} and V_{a2} were measured at the antenna.

Figure 2. The RPI/IMAGE orbit for the V71 experiment. The red curve indicates the IMAGE orbit. Labels 1 to 5 indicate the regions listed in Table 1.

Figure 3. The plasma parameters X and Y during the V71 experiment determined by measured plasma frequency and electron gyro frequency with the tuned transmission frequency. The Roman numbers denote the regions in the standard CMA diagram. The regions defined in Table 1 are indicated on top of the figure.

Figure 4. The measured antenna voltages as a function of time and frequency during the V71 experiment made on 21-22 September, 2005. The RPI transmitting system was stepped in frequency at 300 Hz intervals. Black dots indicate the frequency of the maximum voltage, *i.e.*, resonance, or tuned, frequency. The five regions listed in Table 1 are labeled.

Figure 5. Simplified tuner-antenna-plasma circuit. Tuner elements L_t^* and R_t^* denote the original tuner elements adjusted by the parallel stray capacitance (see Figure 1). V_s^* is the source voltage in the secondary of the transformer. The antenna/plasma sheath system is represented by an input impedance Z_a with a capacitance C_a and resistance R_a .

Figure 6. RPI antenna capacitance (black) calculated using the known tuner inductances and the tuned (resonance) frequency yielding the maximum antenna voltage. Blue line shows the modeled RPI antenna capacitance [Song *et al.*, 2007].

Figure 7. The effective radii of the RPI antenna sheaths as a function of time. The red curve is for the short (125m) antenna element and the black curve for the long (250m) one.

Figure 8. Measured RMS voltage on the short antenna element at the tuned frequency.

Figure 9. Calculated antenna input resistance as a function of time during the V71 passage through the plasmasphere.

Figure 10. Power dissipated by the transmitting/antenna system, calculated using Eq. 6.

Figure 11. V71 whistler data points (red) (2320UT – 0110UT) superposed on the theoretical radiation resistance for Y -values from 2 to 10 as shown in the legend [Huang *et al.* 2008]. The polar cap data points (0015 - 0030UT) were not included.

UNEVEN DIPOLE TRANSMIT ANTENNA

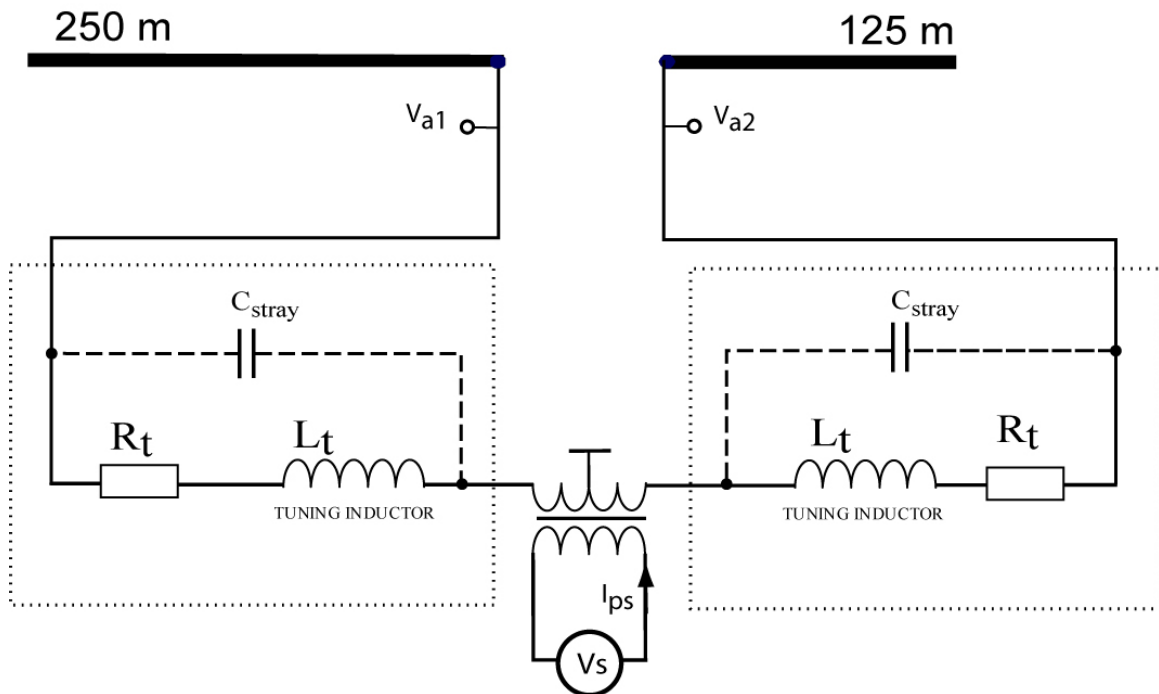


Figure 1. Schematic diagram of the RPI transmitting system. The “tuning inductor” is a combination of inductors and capacitors with a total reactance L_t that is inductive. The power supply current I_{ps} was measured in the primary circuit of the transformer while the voltages V_{a1} and V_{a2} were measured at the antenna.

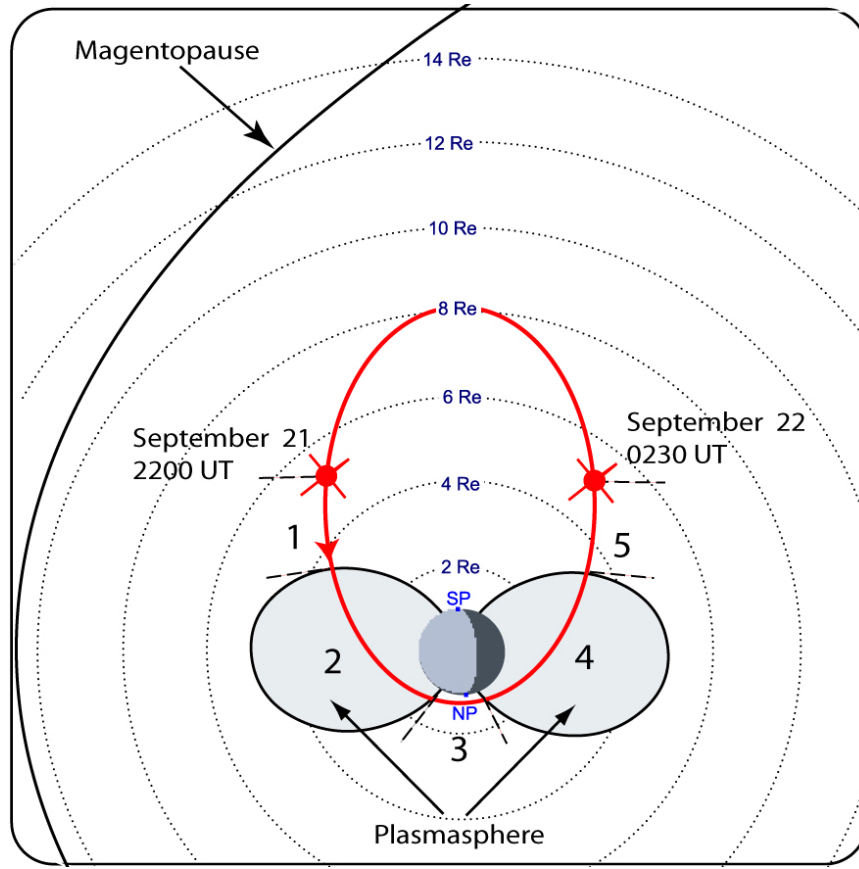


Figure 2. The RPI/IMAGE orbit for the V71 experiment. The red curve indicates the IMAGE orbit. Labels 1 to 5 indicate the regions listed in Table 1.

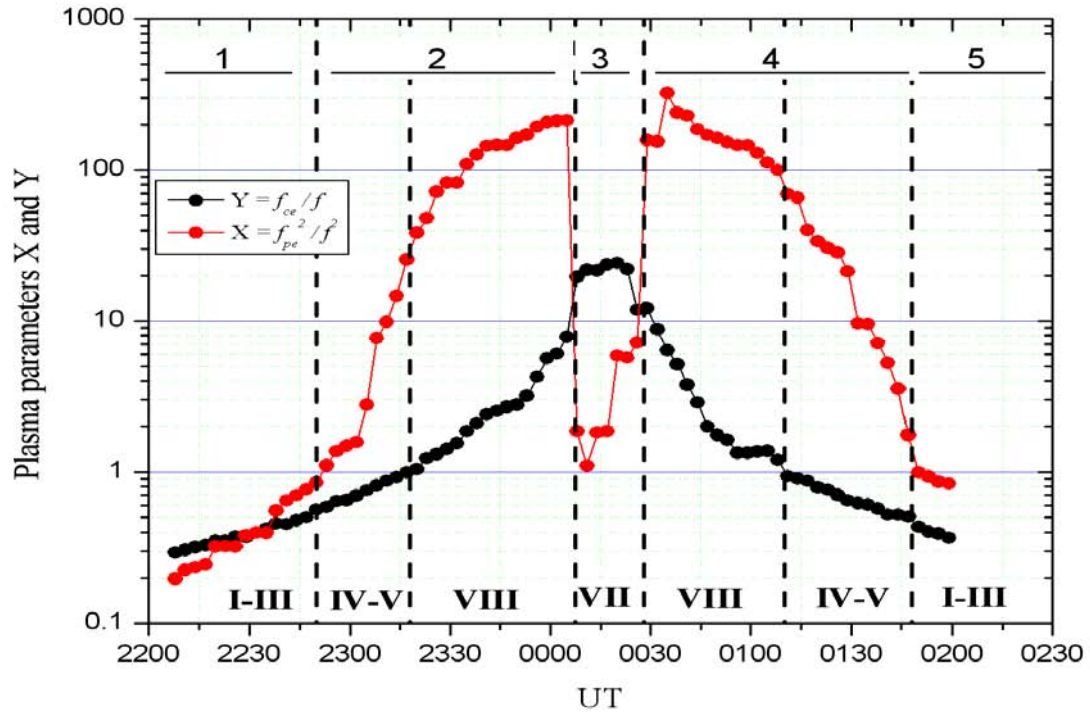


Figure 3. The plasma parameters X and Y during the V71 experiment determined by measured plasma frequency and electron gyro frequency with the tuned transmission frequency. The Roman numerals denote the regions in the standard CMA diagram. The regions defined in Table 1 are indicated on top of the figure.

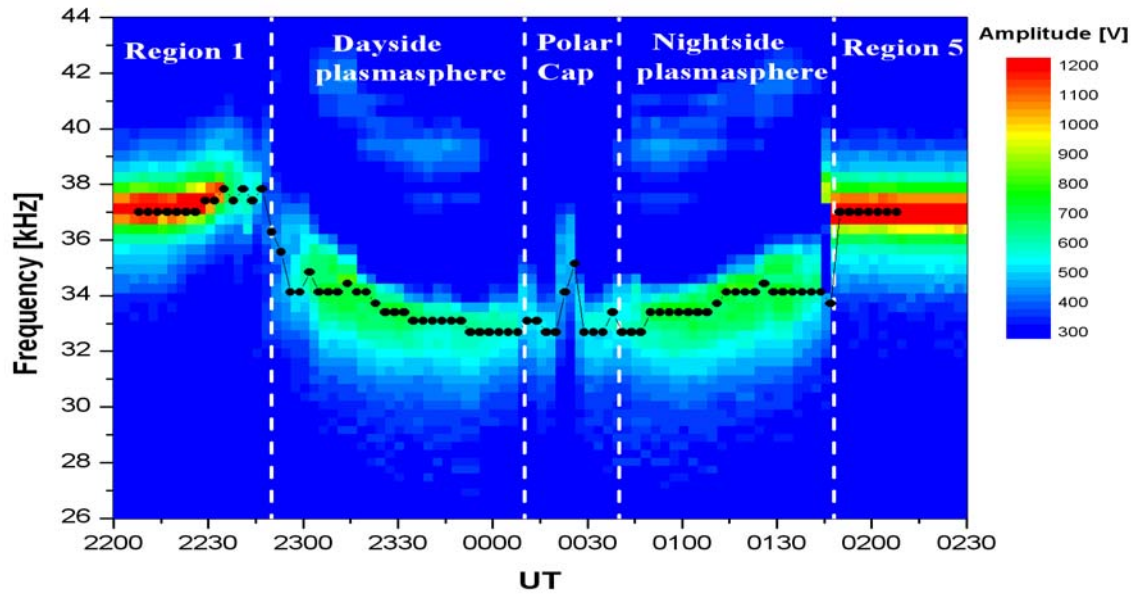


Figure 4. The measured antenna voltages as a function of time and frequency during the V71 experiment made on 21-22 September, 2005. The RPI transmitting system was stepped in frequency at 300 Hz intervals. Black dots indicate the frequency of the maximum voltage, *i.e.*, resonance, or tuned, frequency. The five regions listed in Table 1 are labeled.

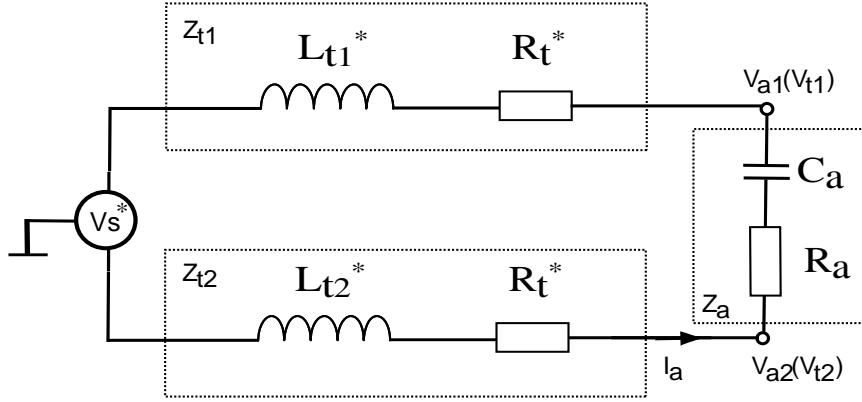


Figure 5. Simplified tuner-antenna-plasma circuit. Tuner elements L_t^* and R_t^* denote the original tuner elements adjusted by the parallel stray capacitance (see Figure 1). V_s^* is the source voltage in the secondary of the transformer. The antenna/plasma sheath system is represented by an input impedance Z_a with a capacitance C_a and resistance R_a .

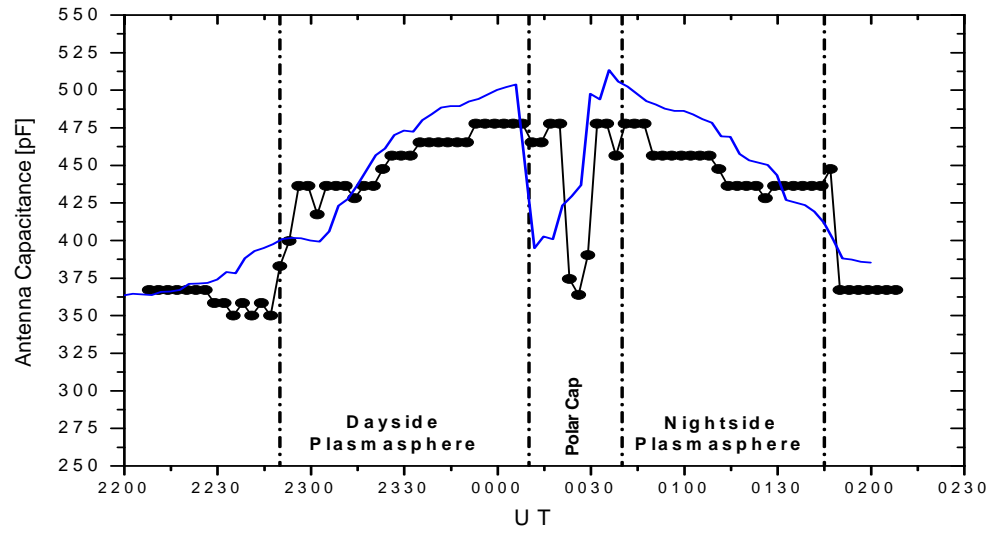


Figure 6. RPI antenna capacitance (black) calculated using the known tuner inductances and the tuned (resonance) frequency yielding the maximum antenna voltage. Blue line shows the modeled RPI antenna capacitance [Song *et al.*, 2007].

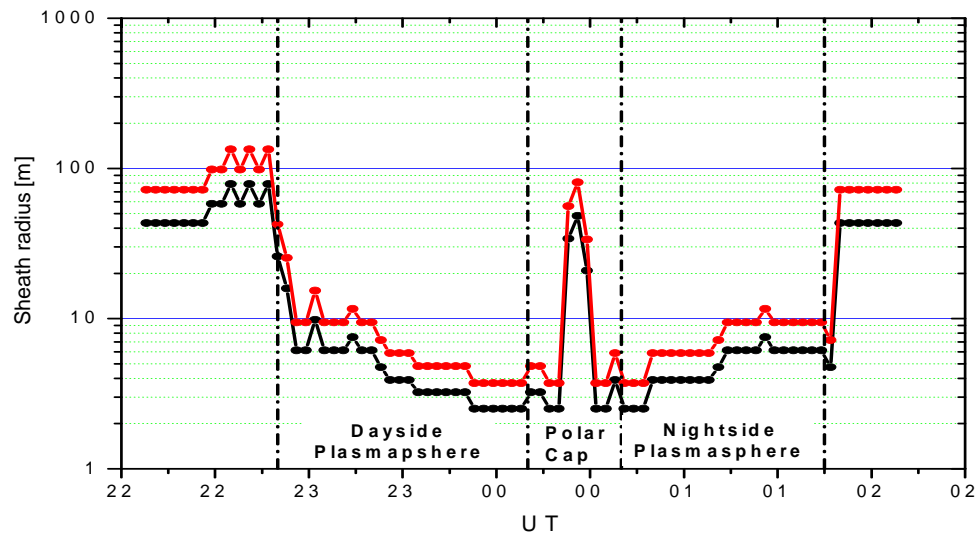


Figure 7. The effective radii of the RPI antenna sheaths as a function of time. The red curve is for the short (125m) antenna element and the black curve for the long (250m) one.

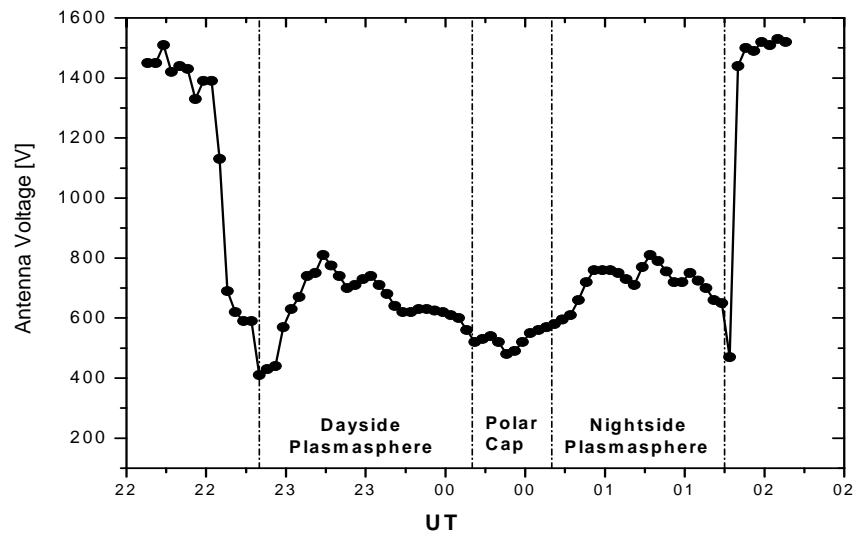


Figure 8. Measured RMS voltage on the short antenna element at the tuned frequency.

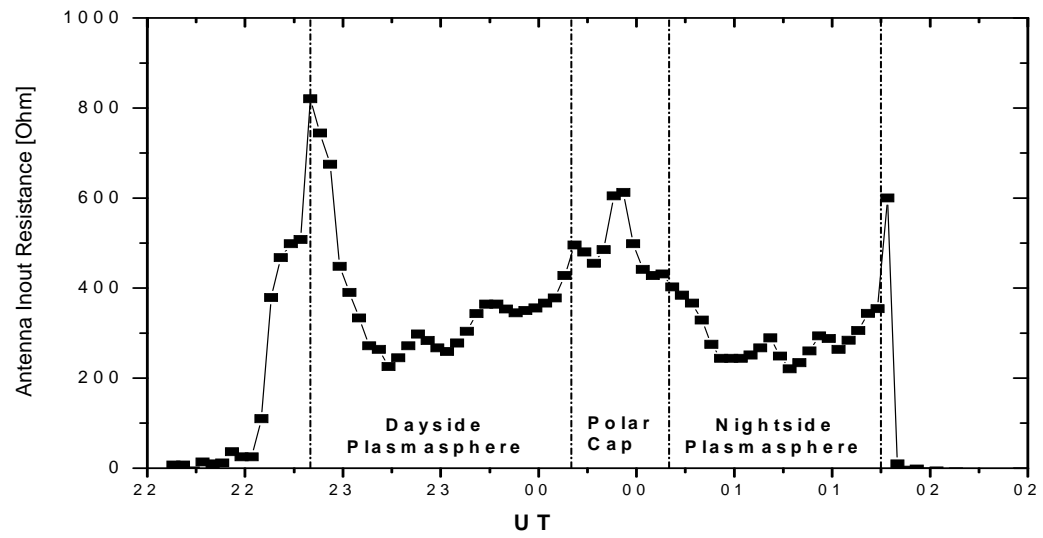


Figure 9. Calculated antenna input resistance as a function of time during the V71 passage through the plasmasphere.

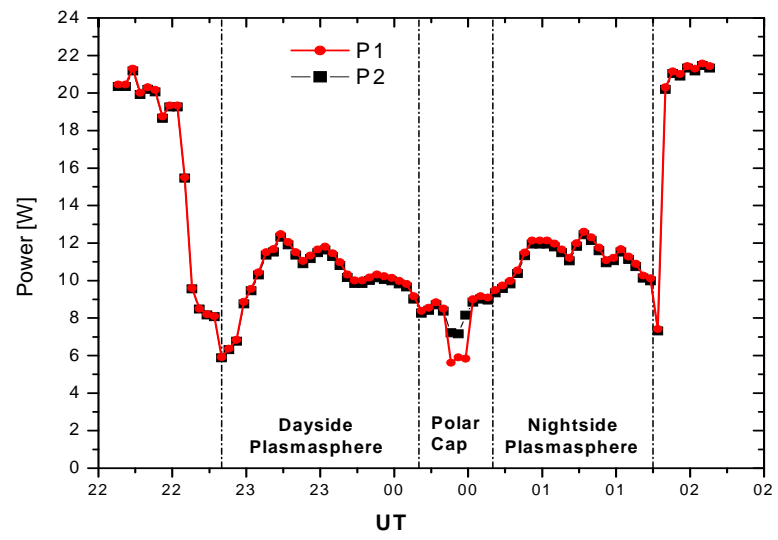


Figure 10. Power dissipated by the transmitting/antenna system, calculated using Eq. 6.

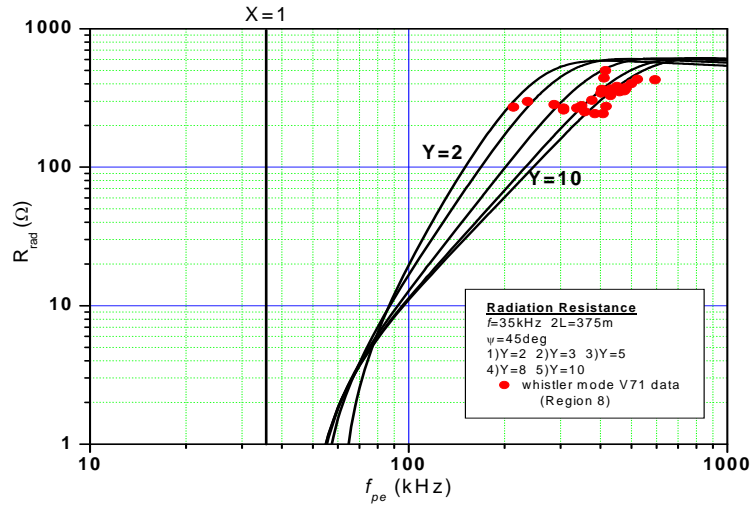


Figure 11. V71 whistler data points (red) (2320UT – 0110UT) superposed on the theoretical radiation resistance for Y -values from 2 to 10 as shown in the legend [Huang *et al.* 2008]. The polar cap data points (0015 - 0030UT) were not included.

Table 1. Regions during the V71 experiment.

Region	Description	Time interval (approx.)
1	Outside the plasmasphere	2200 UT – 2250 UT
2	Plasmasphere (on the dayside)	2250 UT – 0010 UT
3	Polar cap region	0010 UT – 0040 UT
4	Plasmasphere (on the nightside)	0040 UT – 0148 UT
5	Outside the plasmasphere	0145 UT – 0230 UT

